



Vysoké učení technické v Brně
Fakulta strojního inženýrství
Ústav konstruování

Brno University of Technology
Faculty of Mechanical Engineering
Institute of Machine and Industrial Design

STUDIUM MECHANICKÝCH VLASTNOSTÍ NUTNÝCH PRO POPIS RYCHLÉ DEFORMACE MIKRO-PRUTOVÉ STRUKTURY VYROBENÉ TECHNOLOGIÍ SLM

STUDY OF ENERGY ABSORPTION IN MICRO-STRUT LATTICE
STRUCTURE PRODUCED BY SELECTIVE LASER MELTING

Ing. Radek Vrána

Autor práce
Author

doc. Ing. David Paloušek, Ph.D.

Vedoucí práce
Supervisor

Disertační práce
Dissertation Thesis

Brno 2018

STATEMENT

I hereby declare that I have written the PhD thesis *Study of Energy Absorption in Micro-Strut Lattice Structure Produced by Selective Laser Melting* on my own according to advice of my supervisors doc. Ing. David Paloušek, Ph.D. and doc. Ing. Daniel Koutný, Ph.D., and using the sources listed in references.

Brno, _____

.....
Ing. Radek Vrána

BIBLIOGRAPHICAL REFERENCE

VRANA, R. *Study of Energy Absorption in Micro-Strut Lattice Structure Produced by Selective Laser Melting*. Brno, 2018, 101 p. PhD thesis. Brno University of Technology, Faculty of Mechanical Engineering, Institute of Machine and Industrial Design. Supervisor: doc. Ing. David Paloušek, Ph.D.

ACKNOWLEDGEMENT

I would like to express my thanks to my colleagues who supported and helped me during all my doctoral study. First of all, my thanks belong to my supervisors, doc. Ing. David Paloušek, Ph.D. and doc. Ing. Daniel Koutný, Ph.D., not only for many hours of useful consultations and a lot of great advice but also for ensuring of great conditions for my work, friendly workplace relationships and inspiring, long and loud listening to hard metal music during business trips by car. Further, I would like to thank to doc. Ing. Pavel Mañas, Ph.D. for many useful consultations in the field of finite element analysis and to all my colleagues from a REAT group.

Finally, I would like to express my thanks to my family, my parents and especially to my amazing girlfriend and future wife Zuzka, for her sustaining support, huge understanding for my work and just because she has always been here for me.

I could not have completed this thesis without help and support of all the above-mentioned people!

ABSTRACT

The present dissertation thesis is a part of the research project which is aimed to use the SLM produced lattice structures as an impact energy absorber with defined mechanical behaviour. The main goal of the thesis is the development of the numerical model of deformation behaviour of the SLM produced micro-strut lattice structure the made from AlSi10Mg. In order to achieve the main goal, it was necessary to analyse the influence of SLM process parameters on the formation of internal material defects and surface roughness during the SLM production of the micro-strut lattice structure; these defects degrade mechanical properties of the structure and their removal will improve the mechanical properties. The results show a significant influence of two main parameters – laser scanning speed and laser power. On the basis of these findings, the parameters of input energy E_{in} and linear energy E_{lin} , which include both above parameters, were defined and their limit values were determined to minimize the imperfections. The deformation behaviour of the manufactured micro-strut lattice structures was analysed on the developed drop-weight impact device that allows testing with an impact energy up to of 120 J. The deformation behaviour is evaluated using the image analysis of the high-speed camera record and force record from the strain gauge. The results of the mechanical testing were used for the validation of the developed numerical model in the ANSYS Explicit software where the real shape of the produced micro-strut lattice structure was implemented in the form of an elliptical geometry along with the information on the real mechanical properties in the form of the developed material model. The resulting comparison of the experimental results and the numerical model prediction show a good match at the maximum load F_{max} (deviation of 5 %) and also the entire course of sample deformation. These findings will be further used to design of energy absorber with defined mechanical properties.

KEYWORDS

Selective Laser Melting, micro-strut lattice structure, impact energy, numerical model, porosity, surface roughness, material AlSi10Mg, laser scanning strategy

ABSTRAKT

Předložená dizertační práce je součástí většího výzkumného projektu, který si klade za cíl využití mikro-prutové konstrukce vyrobené technologií SLM jako absorbér rázové energie s přesně navrženými vlastnostmi. Hlavním cílem práce je vývoj numerického modelu deformačního chování mikro-prutové konstrukce vyrobeného technologií Selective Laser Melting (SLM) z materiálu AlSi10Mg. Aby bylo možné dosáhnout hlavního cíle dizertační práce, bylo nutné analyzovat vliv procesních parametrů technologie SLM na tvorbu vnitřních materiálových vad a drsnost povrchu při výrobě mikro-prutové konstrukce. Tyto imperfekce degradují její mechanické vlastnosti a jejich odstranění zlepšují možnosti a přesnost numerické predikce. Výsledky ukazují významný vliv dvou hlavních parametrů – skenovací rychlosti laseru a výkonu laseru. Na základě těchto poznatků byly dále definovány parametry vstupní energie E_{in} a lineární energie E_{lin} , které zahrnují oba zmíněné parametry a byly definovány jejich limitní hodnoty pro minimalizaci vzniklých imperfekcí. Deformační chování vyrobené mikro-prutové konstrukce bylo analyzováno na navrženém pádové zařízení, které umožňuje testování s dopadovou energií až 120 J. Deformační chování je vyhodnocováno s využitím obrazové analýzy záznamu vysoko rychlostní kamery a silového průběhu z tenzometru. Výsledky analýzy byly využity pro validaci numerického modelu v programu ANSYS Explicit, do kterého byly implementovány poznatky o reálném tvaru vyrobeného mikro-prutového materiálu ve formě eliptického modelu geometrie a informace o reálných mechanických vlastnostech ve formě vyvinutého materiálového modelu. Výsledné porovnání výsledků experimentu s predikcí numerického modelu ukazují dobrou shodu v místě maximálního zatížení F_{max} (odchylka 5 %) i průběhu celé deformace vzorku. Tyto poznatky budou v budoucnu využity při návrhu absorbéru energie s definovanými mechanickými vlastnostmi.

KLÍČOVÁ SLOVA

Selective Laser Melting, mikro-prutová struktura, nárazová energie, numerický model, porozita, drsnost povrchu, materiál AlSi10Mg, skenovací strategie laseru

CONTENTS

1 Introduction	12
2 State of the Art	14
2.1 Selective Laser Melting technology	14
2.2 Powder material production.....	15
2.3 Fabrication of the SLM aluminium alloys lattice structure.....	16
2.4 Mechanical properties of the aluminium alloys produced by SLM.....	23
2.5 Low-velocity loading of lattice structure and experimental devices.....	27
3 Analysis and Conclusion of Literature Review	36
3.1 Process parameters of structured material.....	36
3.2 Mechanical properties of lattice structure	37
3.3 Description of deformation behaviour	38
3.4 Nonlinear dynamic FEM analysis of micro-strut lattice structure	38
4 Aim of Thesis	40
4.1 Scientific questions	40
4.2 Hypotheses	40
4.3 Thesis layout	41
5 Materials and Methods	42
5.1 Laser strategy for lattice structure fabrication (Paper A).....	42
5.2 Numerical model of low-velocity impact (Paper B).....	43
5.3 Used Analysis	43
5.4 Used SLM specimens	49
5.5 FEM numerical model	51
6 Results	54
6.1 Construction of experimental device – The drop weight impact tester	54
6.2 Laser strategy for lattice structure fabrication - Paper A.....	61
6.3 Script for designing of the strut contour strategy	66
6.4 Development of Low-velocity Impact Numerical Model - Paper B	70
6.5 Study about influence of the strut diameter size on the BCC lattice structure mechanical behaviour using FEA	75
6.6 Study of the lattice structure local impact	77
7 Discussion	80
7.1 Laser strategy for lattice structure fabrication	80
7.2 Low-velocity Impact Numerical Model and Its Application.....	83
8 Conclusions	86
9 List of Publications	89
10 Literature	91
List of Figures and Tables	95
List of Figures	95
List of Tables	98
List of Symbols and Abbreviations	99
List of Appendices	101

1 INTRODUCTION

In recent years, the additive technology has become a widespread and popular manufacturing technology that can quickly create a desired component from a variety of materials. This technology was primarily used in the prototype phase of the design cycle but currently it is also beginning to be involved in the production process, the so-called additive manufacturing. Special areas of additive technologies are based on the selective melting of the metal powder using high power laser - Selective Laser Melting (SLM) and Direct Metal Laser Sintering (DMLS). The onset of these technologies has been greatly dependent on the development of powerful lasers. While the first recorded patent in the field of plastic SLS additive technology dates to 1986 (University of Texas) [1] and the first recorded patent of SLM additive technology to 1995 (Fraunhofer ILT, Aachen) [2], the first machine which allows for complete and controlled melting of aluminium powder was developed in 2016 [3].



Fig. 1.1. (a) Absorbers of impact energy from metal foam [4]; (b) inner structure of bone [5]

SLM makes it possible to produce even complex parts with internal architecture that are hard to manufacture using other technologies. It can be topology optimized shape of the part or half-solid and half-structured part for which we can find an inspiration primarily in the nature. A good example is a human bone filled with structured part, the so-called spongiosa. It's density and architecture are arranged depending on the bone loading during whole life (Figure 1b). This spatial structure ensures a high strength and excellent mechanical properties of the whole bone (Figure 1.2a). [6, 7]

For engineering applications, simplification of the general structure to the micro-strut lattice structure, which is composed of periodically repeating micro-strut cells, is often used. These strut-lattice structures are already used in the industries such as space, aerospace [8] (Figure 1.2b) or automotive (motorsport) due to great weight-strength ratio or in medicine (prosthetics) for the natural connection between the joint replacement and the bones to ensure growing together [9].

Due to the micro-strut structure topology, these materials are also suitable for applications of impact energy absorption where the plastic deformation of the individual layers of the structure results in effective energy absorption. At present,

mainly conventional metallic foams are used for this type of protective elements (Figure 1.1a). A disadvantage of metal foams is primarily that the topology of the inner structure is not exactly defined and thereby also mechanical properties. The metal foams can be produced only from materials with a relatively low melting point and low viscosity [4], which is mostly aluminium. Compared to the SLM technology, this technology can produce a lattice structure with precisely controlled shape of special metal materials (e.g. high-strength titanium alloys). Thanks to this, the designed parts can withstand much higher loads or absorb higher impact energy. A precise control of the shape also allows for advanced computational methods to predict mechanical properties. This is especially important for the aerospace industry where a great emphasis is placed on the accuracy and reliability of parts [10–12].

One of the disadvantages of SLM technology is the number of process parameters that affect the resulting quality of the parts. These include laser power, scanning speed, single laser tracks spacing, surface scanning strategies (hatching, etc.), working atmosphere, and properties of supplied material. All these parameters affect the physical phenomena crucial for the resulting quality of the manufactured struts (especially the deviation from the required dimensions and material properties). In order to use the lattice structure in industry, it is necessary to find a suitable combination of process parameters for the respective material, which will allow for precise and repeatable production [13–15].

This thesis is focused on the development of a numerical model of the lattice structure deformation behaviour by FEM, as the first step on the way to design impact energy absorber. To reach this goal, it is necessary to deal with two related areas - the research of impact energy absorption in micro-strut lattice structure for validation of the numerical model and the study about influence of SLM process parameters on material imperfection for increase an accuracy of the numerical model.

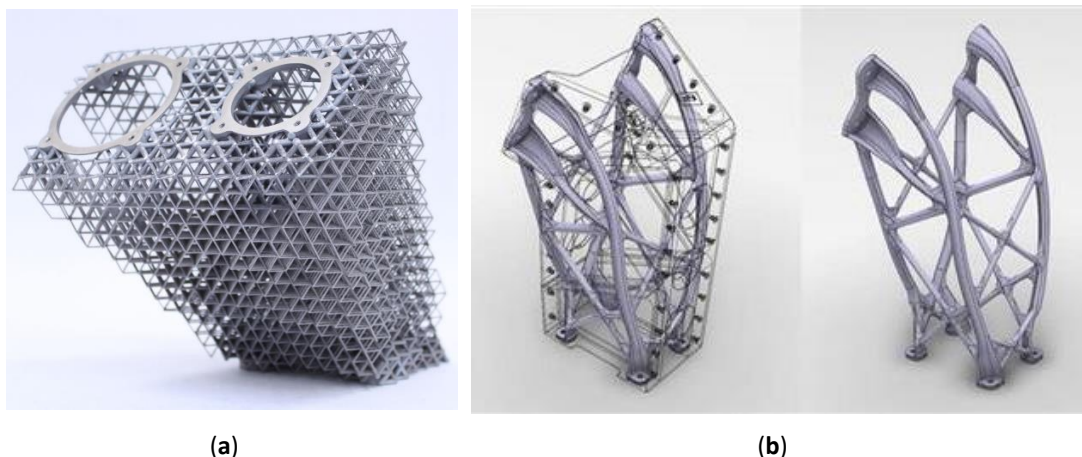


Fig. 1.2. Lattice structure bracket for space application (a) ESA, BUT, LKE; (b) Airbus [8]

2 STATE OF THE ART

2.1

2.1 Selective Laser Melting technology

Selective Laser Melting (SLM) is an additive manufacturing process developed by Dr. M. Fockele and Dr. D. Schwarze of F & S Stereolithographietechnik GmbH, and Dr. W. Meiners, Dr. K. Wissenbach, and Dr. G. Andres of Fraunhofer ILT to produce metal components from metallic powders [16].

SLM allows for production of metallic component - layer by layer - directly from 3D CAD data using a YLR high power fibre laser and a metal powder. The process starts by depositing of the metal powder on a substrate plate (platform). Then the powder is melted at Ar or N₂ atmosphere by a laser beam according the CAD. After production of the layer, the platform is lowered by its thickness and a new layer is deposited above. Again, this layer is melted by a laser beam and bonded with a previous layer using a high-power laser. This process is repeated until the whole component is finally fabricated (Figure 2.1) [17].

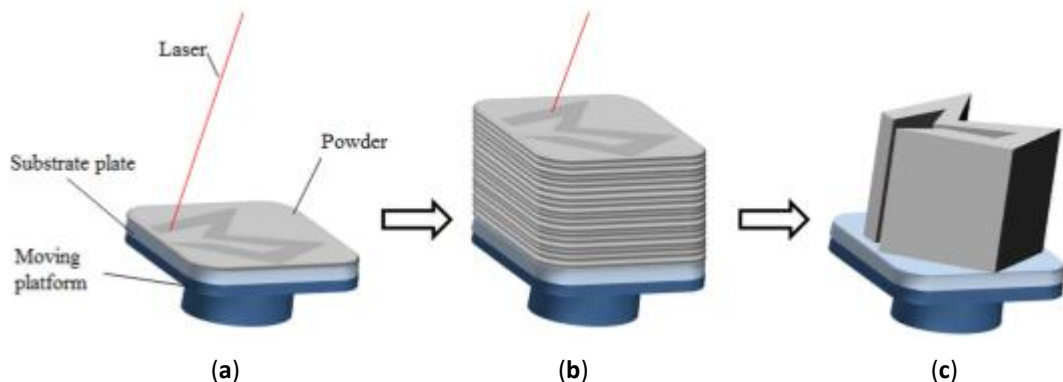


Fig. 2.1. Concept of SLM process. (a) High-power laser melts selective areas of the powder bed; (b) Process is repeated for successive layers; (c) Surrounding powder is removed [16].

SLM technology differs from previous Selective Laser Sintering technologies especially by the use of a high-power laser which allows for complete melting of the deposited metal powder. During the melting process, the local fully melted area, the so-called melt pool, is created; its behaviour is influenced by a number of physical processes such as surface tension of the liquid metal phase, different thermal conduction of the surrounding metal powder and already melted material, a liquid metal flowing etc. Therefore, the SLM technology is sensitive to setting of processing parameters [18].

Using the SLM process, a wide range of materials can be processed. They can be divided into five groups - steel and iron-based alloys, titanium and its alloys, Inconel and nickel-based alloys, aluminium and its alloys and other materials. Most of the research studies are focused on the steel and iron-based alloys and titanium and its alloys due to their high mechanical properties and therefore great assumptions to be used in high-end applications such as medicine implants, light-weight components for aero- or space industry or cooling applications. Another reason is a significantly higher laser power required for melting of Al alloys due to a significantly higher

reflectivity of the powder material ($> 91\%$) and higher thermal conductivity. However, nowadays, the SLM machines are usually equipped with high-power laser (1kW) or even multi-laser system, which allows for effective production of Al materials, and they also become popular for light-weight applications due to an appropriate density vs. strength ratio [16, 18].



Fig. 2.2. SLM 280^{HL} machine from SLM Solution GmbH [19]

2.2 Powder material production

2.2

The most common process of a metal powder production for SLM technology is the gas atomization (Figure 2.3). During this process, the base material is melted in inert atmosphere and extrudes through the nozzle under pressure. Then, the liquid material is sprayed by a high-velocity flow of Ar, N₂ or He atmosphere. Most of the formed particles have a spherical shape with occasional asymmetries or satellites [20].

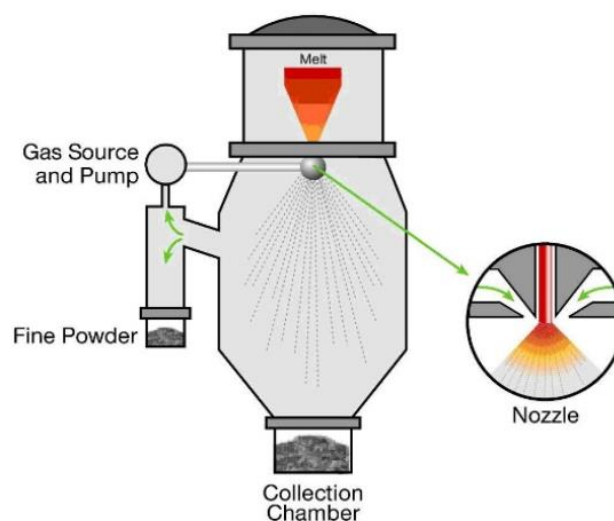


Fig. 2.3. Schema of the gas atomization [20]

2.3 Fabrication of the SLM aluminium alloys lattice structure

The aluminium alloys are popular and widespread materials in many areas of the industry mainly due to low density and weight of the final parts. The SLM technology generally allows to produce a lot of types of the alloys such as AlSi10Mg, AlSi12 with the same or even better mechanical properties compared to cast material in static loading; however, the wrong set up of the SLM process parameters or orientations of the specimens can significantly influence the final mechanical properties.

The main advantage of the additive production is the possibility to produce a complex geometry which cannot be achieved conventionally. Therefore, the additive technologies are perspective for production of cellular lattice structures which are composed of regularly repeated unit cells. The unit cells are usually thin struts constructions [15, 21–23] or any complex shape such as a gyroid (Figure 2.4) [24].

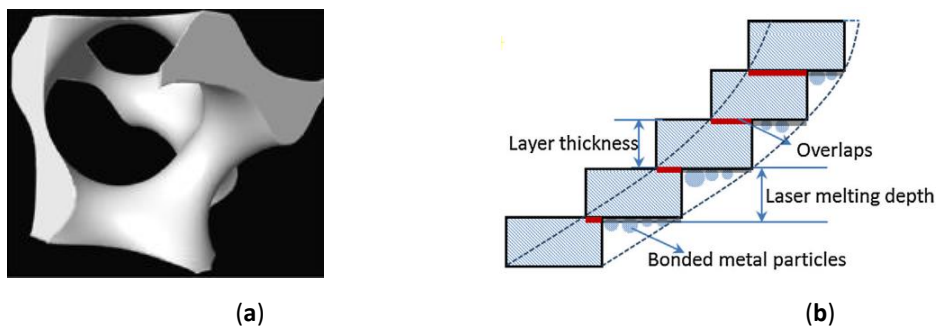


Fig. 2.4. (a) Gyroid unit; (b) Schematic illustration of the SLM manufacturing process of the circular strut [24]

Yan et al. [24] tested a manufacturability of the gyroid structure according to the size of the unit cell. This complex unit cell was chosen based on its self-supporting shape; therefore, it is not necessary to use the support structure and is suitable for large size of the unit cells. The authors explained the higher surface roughness on the down-skin surface by the “stair effect” after slicing of the strut to the single layers. This effect increases at a lower strut inclination, where only a small overlaps occur and a larger part of the single layer is produced directly on the powder. However, a lower height of layer thickness could decrease this effect.

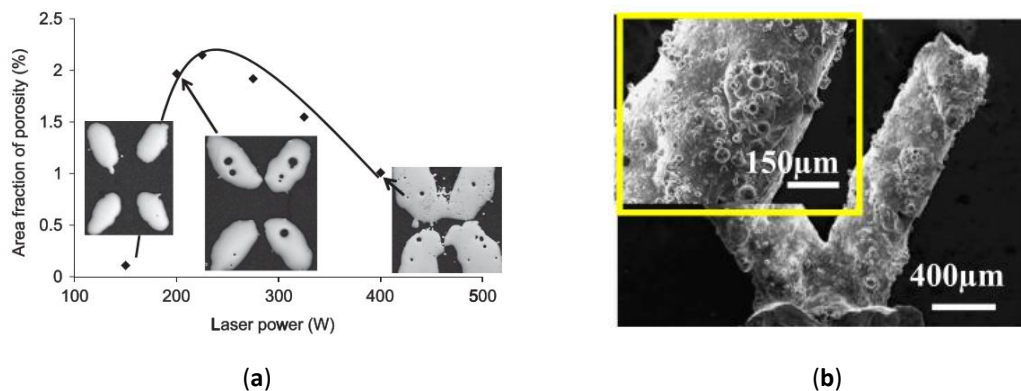


Fig. 2.5. (a) Variation of porosity within the struts as a function of laser power at a traverse speed of $7000 \text{ mm}\cdot\text{s}^{-1}$; (b) Magnified view of the strut surface [25]

Qiu et al. [25] investigated the influence of the laser power (**LP**) and the scanning (**LS**) speed on the diameter, shape, and porosity of the struts made of AlSi10Mg material. The linear dependence between the strut diameter and the increasing **LP** was found. The authors used **LS** of $3500 \text{ mm}\cdot\text{s}^{-1}$ while the **LP** was changed in the range from 150 W to 400 W. The results show that according to the used **LP**, the real diameter of strut changed from $260 \text{ }\mu\text{m}$ to $500 \text{ }\mu\text{m}$ for the nominal diameter of $300 \text{ }\mu\text{m}$. Due to the number of struts in the lattice structure, the mechanical properties of the whole structure were significantly changed. The dependence of the main process parameters on the strut porosity was evaluated, but only for one **LP** and **LS** level (Figure 2.5a).

Abele et al. [22] dealt with dimensional accuracy of the micro-strut lattice structure. The authors tested a laser strategy for lattice structure production focused on high dimensional accuracy of very thin struts ($d = 0.2 \text{ mm}$). These struts were produced by only one laser path (Figure 2.6); therefore, the authors investigated primarily the offset of laser contour paths. The linear energy E_{lin} ($\text{J}\cdot\text{mm}^{-1}$) and laser spot diameter were used as the control parameters. The authors defined the struts' size limitation for 1.4542 stainless steel material as two times laser spot diameter.

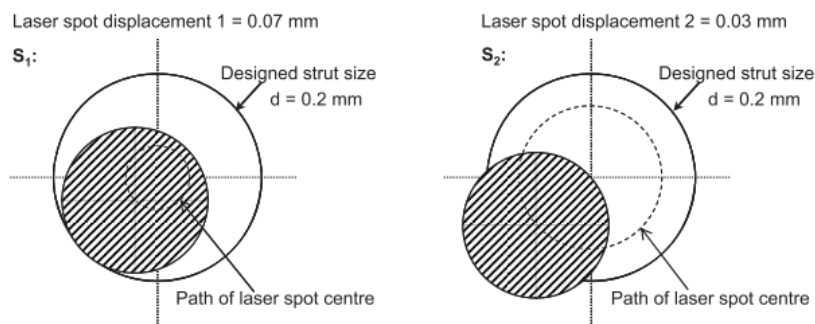


Fig. 2.6. Positioning of the laser spot relative to the nominal contour using different laser spot displacements [22]

Leary et al. [21] investigated a manufacturability and surface roughness of the struts with the orientation typical for micro-strut lattice structures. They found that the surface roughness on the strut down-skin surface is significantly higher due to a heat transfer and sticking of the surrounding powder on the strut down-skin. The surface roughness is strongly dependent on the strut orientation which was also described by other authors [21, 22, 24].

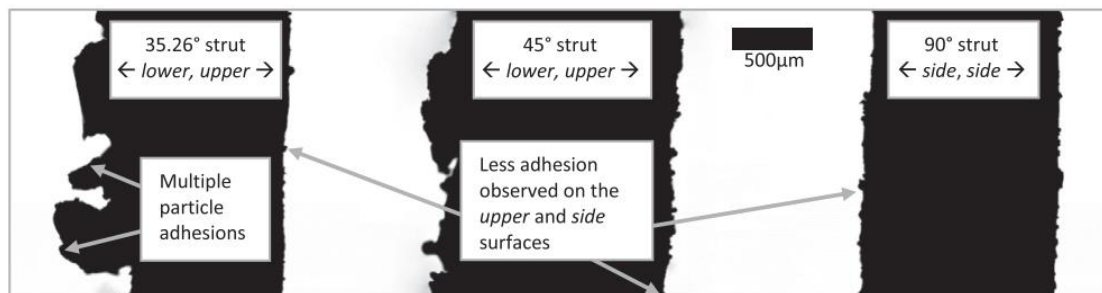


Fig. 2.7. Representative optical microscope image of the lower and upper faces of 35.26° , 45° and 90° struts [21]

They also tested the mechanical properties of the different shape-types of the strut-lattice structures to find out their energy absorption capacity. The results show a considerable variation due to a different shape of the unit cells and a significant decrease of the mechanical properties after progressive collapse of the structure (Figure 2.8a). The FBCCZ was demonstrated to provide a stable crushing behaviour and excellent energy absorption. The experimental results were compared with results of numerical analysis with constrained and unconstrained models. The conclusion is that the constrained model reaches higher stiffness and better corresponds with the experimental data (Figure 2.8b).

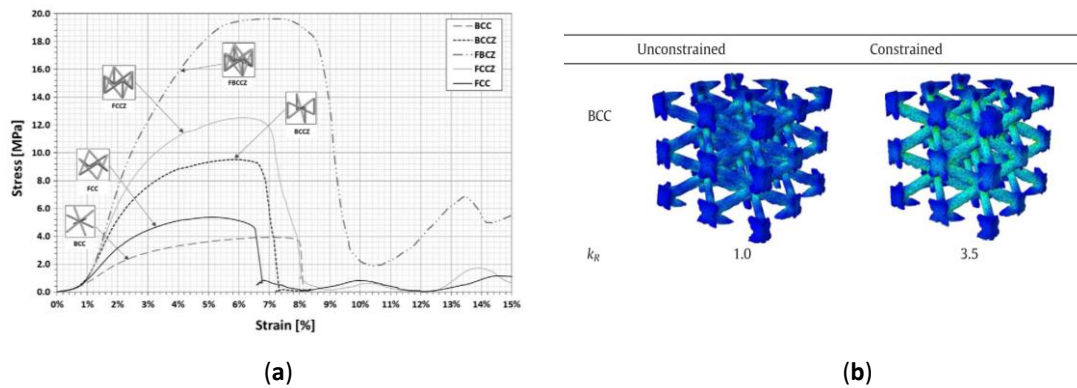
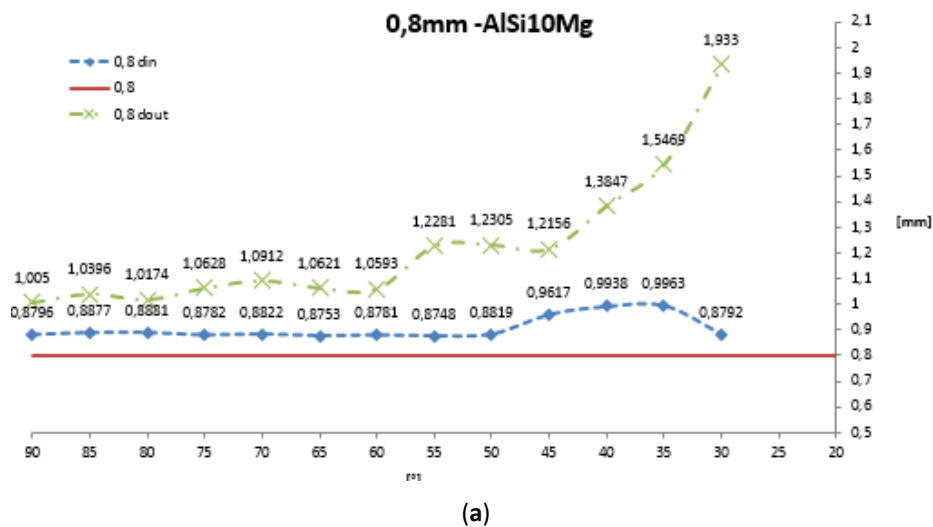


Fig. 2.8. (a) Uniaxial compression stress-strain responses of tested lattice specimens; (b) Von Mises stress and relative stiffness, k_R , both normalised to data for unconstrained BCC [21]

Koutny et al. [11] examined the influence of the strut orientation on the real strut diameter (Figure 2.9a). The strut specimens of AlSi10Mg and 316L materials were measured by a 3D optical scanner and evaluated by maximum inscribed cylinders inside the struts (Figure 2.9c,d). It represents the largest homogenous strut-diameter which is not influenced by high surface roughness on the strut down-skin. Correction parameters for the struts' production with the accurate size were proposed. The results show that the surface roughness rapidly increase at low strut inclination ($< 45^\circ$) and at low struts diameters.



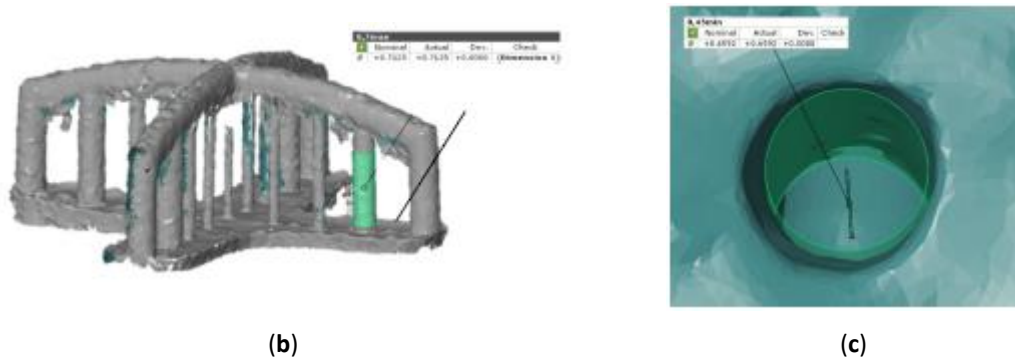


Fig. 2.9. (a) Real AlSi10Mg beam diameter in dependence on beam inclination; Evaluation of dimensional accuracy of individual beams, (b) minimum circumscribed cylinder, (c) maximum inscribed cylinder (left) [11]

Suard et al. [15] examined the differences between the ideal CAD structure geometry and the real geometry after EBM production. The specimens were digitized using μ CT. The surface data show high roughness and irregular strut surface; therefore, the “effective volume” which presents the largest homogenous strut-volume was defined (Equation 2.1). The V_{ef} of the 45°inclined struts is of 0.37.

$$V_{ef} = \frac{V_{inscribed\ cylinder}}{V_{strut}} \quad (2.1)$$

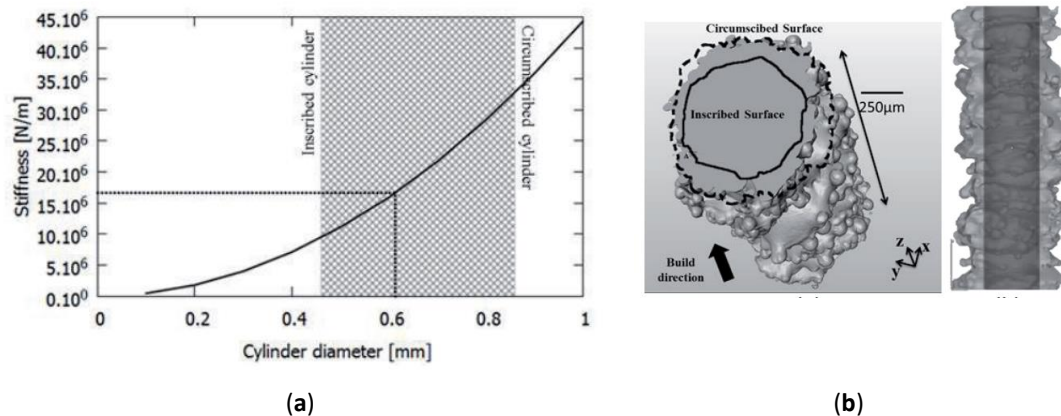


Fig. 2.10. (a) Comparison of FEA analysis using various strut diameter and the real CT shape; (b) Tomographic reconstruction of a 1mm strut with the inscribed cylinder (dark) inside the real strut (bright) [15]

The aim of this study was to simplify real shape of struts to the corresponding cylindrical geometry usable in the numerical model. According to the numerical analysis of the real shape of the strut obtained by μ CT, a suitable diameter for simplification was defined (Figure 2.10a). The results of the analysis also show that the real measured strut dimensions are needed for a precise analysis.

Yu et al. [26] used a numerical simulation to investigate the influence of the laser power and the scanning speed on the parameters of the single tracks. The numerical model was created with one layer of 30 μ m particles of AlSi10Mg material in argon atmosphere. The main conclusions were:

- Properly increasing laser power can increase wettability, improve the surface quality, and completely melt the metal powder; but high power (above 250 W) leads to pores and the balling effect, which make the surface rough (Figure 2.11a).
- Long-time irradiation leads to “self-balling” and affects the surface quality. A long liquid lifetime gives the melt a chance to form a lot of small balls to decrease their surface energy.
- The Z-direction shrinkage ratio is sensitive to the laser power. High laser power causes the high temperature and the viscosity tends to be low. Then, the low viscosity increases the melt flow ability. Then, it is easier for the liquid metal to flow from the top to the bottom, making each layer flatter. However, if the laser power exceeds 250 W, both the shrinkage ratio and the surface roughness decrease (Figure 2.11b).

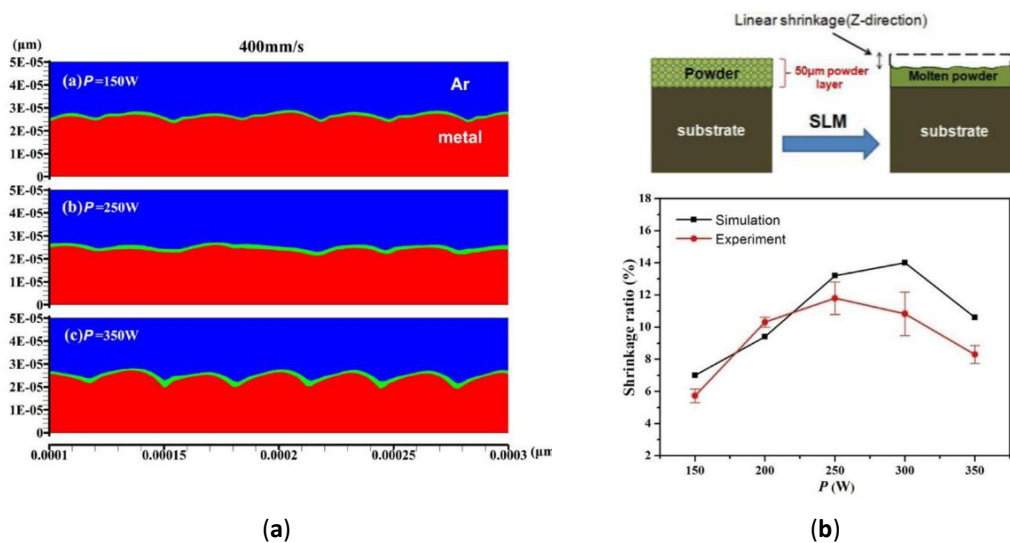


Fig. 2.11. (a) Comparison of surface roughness contour plots at different processing conditions; (b) The linear shrinkage ratio of different laser power in the simulation and experiments [26]

Yu et al. [27] continued their work and other numerical studies were aimed at the re-melting effect during layer by layer production. The results indicated that re-melting of previous fabricated layer induced by laser melting of current powder layer played a crucial role in the increase of densification level. During the re-melting process, the trapped gas pores in the previous layer rose up to the surface area, resulting in lower porosity level in the previous layer (Figure 2.12).

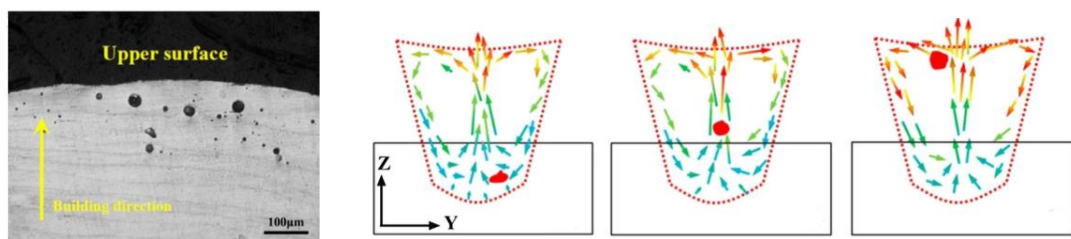


Fig. 2.12. Motion trail of single gas pore and the velocity vector plots around the pore in the molten pool at different time: (a) $t = 62\ \mu\text{s}$; (b) $t = 102\ \mu\text{s}$; (c) $t = 142\ \mu\text{s}$ [27]

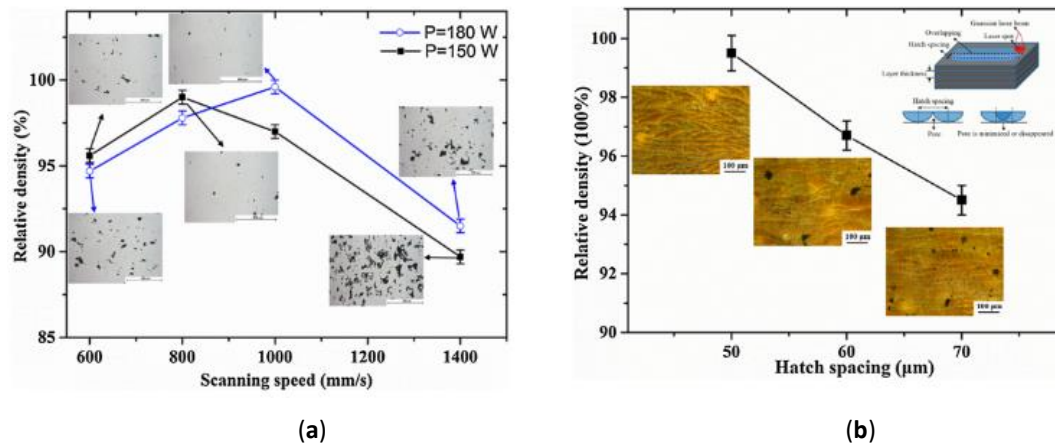


Fig. 2.13. (a) Influence of incident laser power and scanning speed on the relative density of SLM-processed specimens; (b) Influence of hatch spacing on the relative density of SLM-processed specimens under the laser power of $P = 180 \text{ W}$, scanning speed of $v = 1000 \text{ mm} \cdot \text{s}^{-1}$ and hatch spacing of $50 \mu\text{m}$ [23].

Wei et al. [23] showed that the single tracks produced in the linear energy density range of $1.5 - 1.875 \text{ J} \cdot \text{cm}^{-1}$ had a continuous scan track with a relatively smooth surface without intertrack pores (Figure 2.13). Delroisse et al. [28] studied the influence of strut orientation on the microstructure. The microstructure heterogeneities were compared between the inclined and vertical struts of AlSi10Mg lattices processed by SLM. While the vertical struts present a fully dense homogenous microstructure, large levels of porosities and heterogeneous microstructure are present in inclined struts (Figure 2.14b); especially a much larger level of porosities in the bottom part of the strut compared to the upper part. These differences are due to a larger time spent at high temperature in the bottom zone of the strut caused by worse heat transfer due to the strut inclination and low thermal conductivity of the surrounding powder.

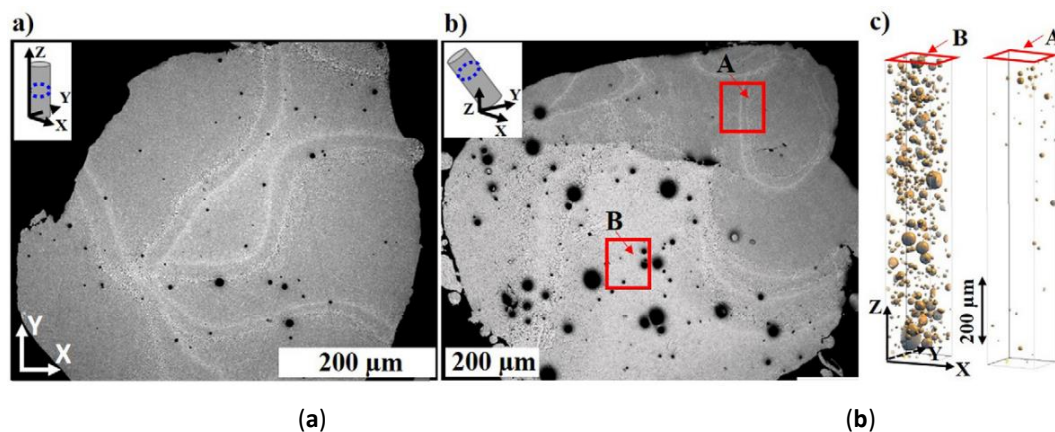


Fig. 2.14. Comparison of the microstructure of (a) a vertical and (b) an inclined strut (c) Porosity in zone A and B of (b) observed by 3D X-ray tomography along virtual parallelepiped oriented along the axis of the strut [28].

Amani et al. [29] produced a series of the BCC lattice structure specimens by SLM 250^{HL} and using the process parameters LP of 250 W , LS of $571 \text{ mm} \cdot \text{s}^{-1}$ and layer

thickness LT of 60 μm . The produced lattice specimens were analysed by high-resolution μCT equipped with double detector and as is shown on the [Figure 2.15](#), the resulting level of porosity is quite high of about 2.01 %.

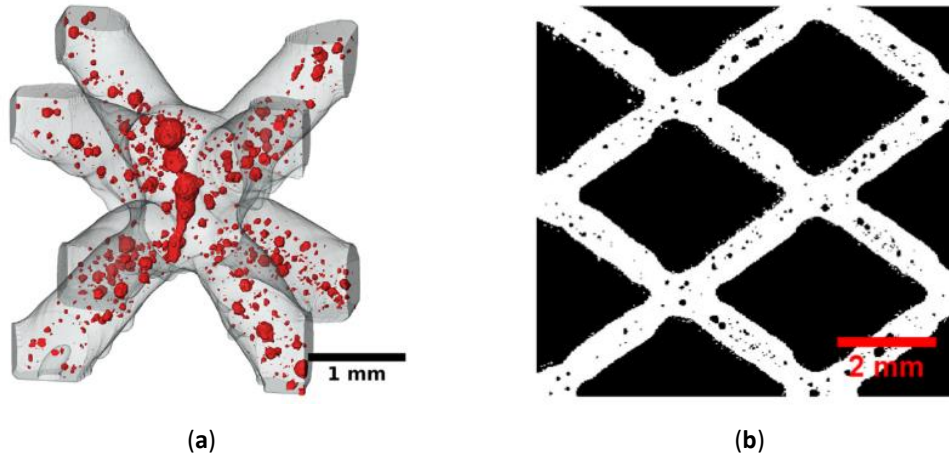


Fig. 2.15. (a) Local cavities in red and AlSi10Mg phase in transparent gray; (b) One diagonal slice of the 3D tomographic image [29]

Based on the porosity results, they prepared numerical model which reflects occurred internal porosity. For purpose of the numerical model, the porosity was divided to two groups, the group of porosity $< 31 \mu\text{m}$ (0.09 % from total 2.01 %) which was not reflected in numerical model and the group of porosity $> 31 \mu\text{m}$ (1.92 % from total 2.01 %) which was considered in the model. As the material model was used Gurson-Tvergaard-Needleman (GTN) which represent void nucleation and growth in the simulation within the Abaqus environment. The comparison of the simulation and the experimental results shows very nice results with only small deviations from experiment ([Figure 2.17](#)). A stress distribution of the numerical model including the internal porosity show the influence of the porosity on the mechanical properties of whole lattice structure ([Figure 2.16](#)).

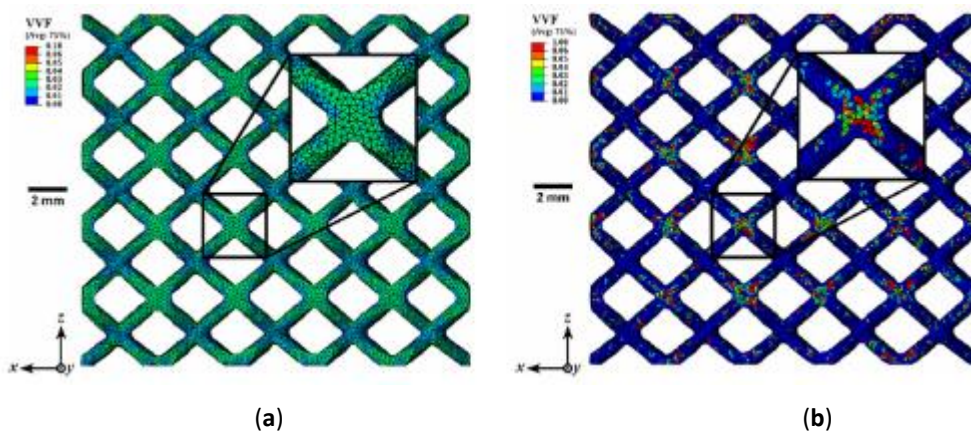


Fig. 2.16. Contour plots of VVF resulting from FE simulations of the homogeneous (a) or heterogeneous GTN models (b) of the thin-strut specimen, at a nominal strain of 0.066 corresponding to experimental plastic collapse strain [29]

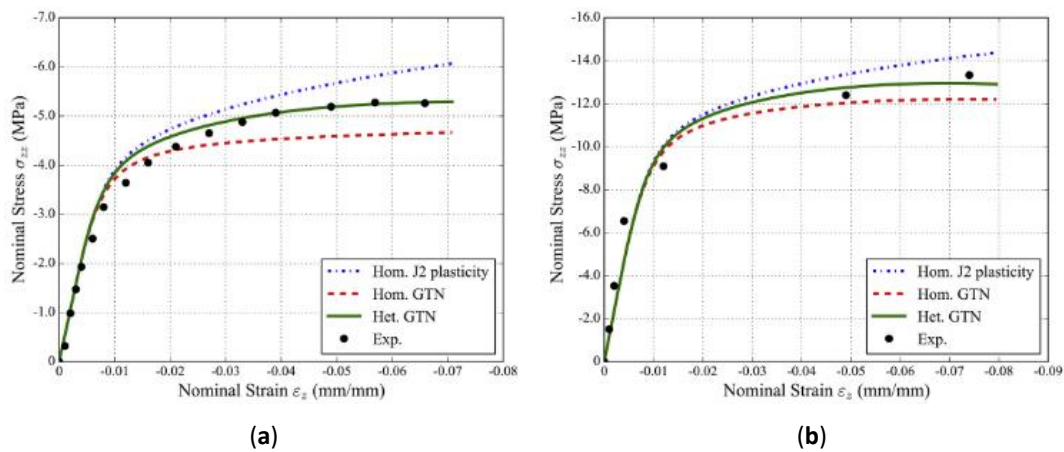


Fig. 2.17. Stress-strain curves obtained by in-situ/ex-situ compression, FE simulations of the (a) thin-strut and (b) thick-strut specimens. The dotted blue, dashed red and solid green lines correspond to FE simulations with non-porous J2 plasticity, homogeneous GTN and heterogeneous GTN models, respectively [29]

2.4 Mechanical properties of the aluminium alloys produced by SLM

2.4

2.5.1 Bulk material

Kempen et al. [12] examines the mechanical properties such as UTS, YTS, elongation at break, and hardness of the SLM produced specimens of the flat shape. The specimens were produced at three various orientations (Figure 2.18a) to find out their influence on the mechanical properties.

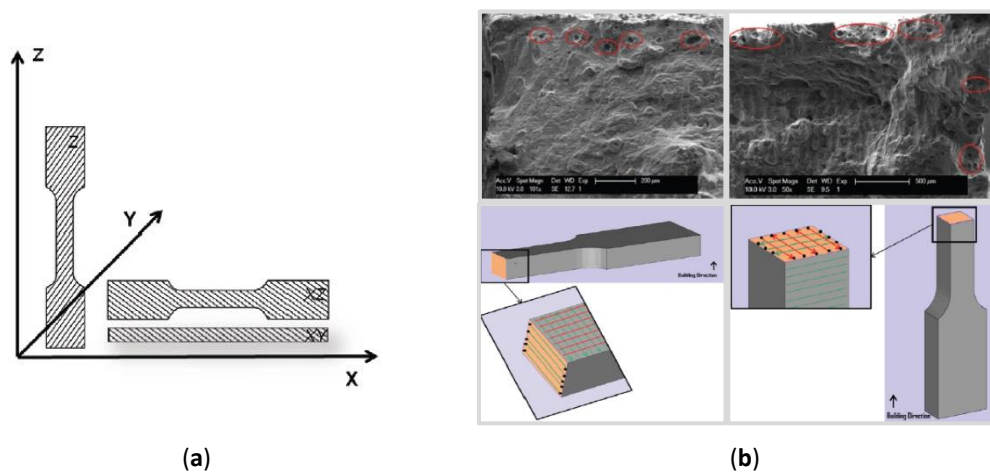


Fig. 2.18. (a) The specimens' orientation during SLM production; (b) SLM laser strategy and its influence on the close to surface porosity [12]

The results show that the quasi-static mechanical properties of the SLM produced specimens were the same or even higher than those of the cast material. It is caused by the fine microstructure of the SLM material and Si-phase distribution due to the fine powder material created by approximately 50 μm particles. The results also show that the specimens orientation influences an elongation parameter and the specimens produced in the XY plane (parallel to the platform) reached higher values. It is caused by the close to surface porosity at the end of the laser tracks which is

formed due to the laser slows down before reaching the border of the part and that the laser influences the material for a longer time (Figure 2.18b). This close to surface porosity initiates the damage of the specimens.

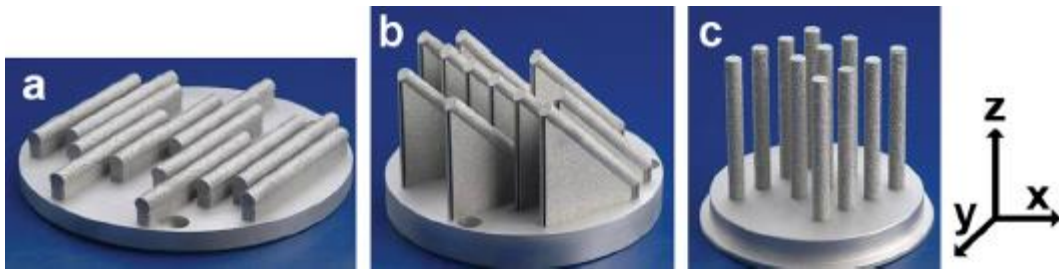


Fig. 2.19. The specimens' orientation during SLM production [10]

Brandl et al [10] dealt with a similar type of study. They also fabricated cylindrical specimens at various orientations according to Figure 2.19 but in this case, the specimens were used as semi-finished parts for machining of the final shape of the tensile specimens. The results show an isotropic mechanical behaviour. It is in line with the previous study, where only the close to the surface area was problematic; this porous area was machined in this study.

Hitzler et al. [30] performed an extensive study on the influence of the AISi10Mg specimens orientation during SLM production on their final mechanical properties (Figure 2.20). The results of mechanical testing of the non-heat-treated and machined specimens at and loading speed of $5 \text{ mm}\cdot\text{s}^{-1}$ are present in Table 2.1.

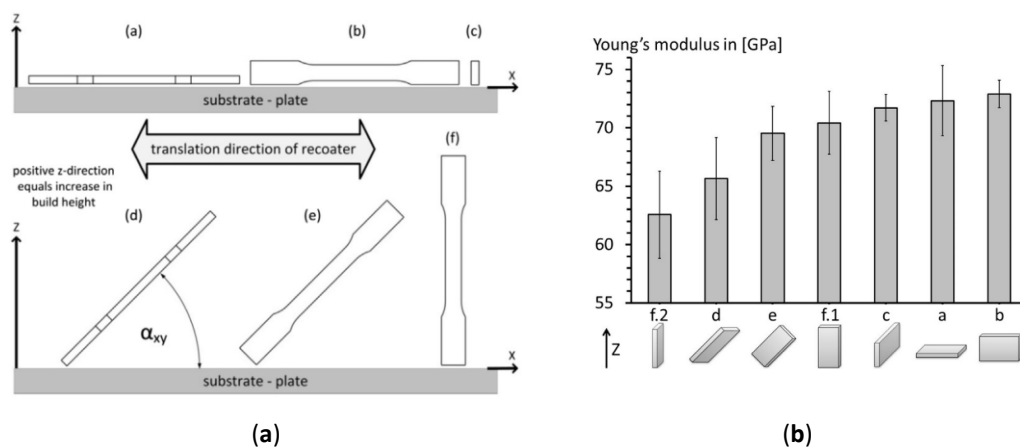


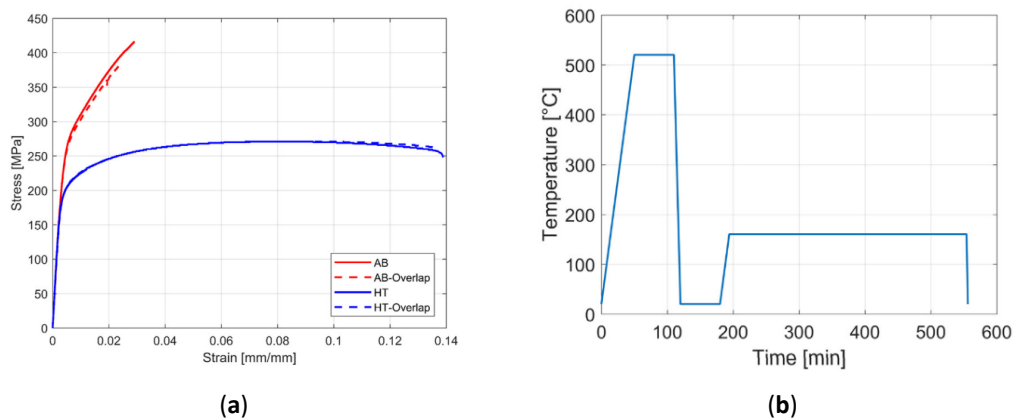
Fig. 2.20. (a) Schema of the configurations in the build space; (b) Young's modulus dependency of AISi10Mg for tensile loading in regard to the orientation during the SLM process [30]

The tensile specimens were designed in accordance to the standard DIN 50125:2009-07 as flat specimens of type E5 \times 10 \times 40 and produced with an oversize of 0.4 mm in width and thickness. As preparation for the tensile testing procedure, the specimens were milled to obtain the final shape and the required surface quality. Moreover, this machining step ensured equal conditioning in terms of the inherent specimen surfaces, regardless of their orientation in the SLM process. Hence, the surface quality dependency based on the inclination and orientation of the individual specimen within the fabrication [31] was removed as an influencing factor for crack initiation and propagation, which have a significant impact on the tensile strength.

Tab. 2.1 Averaged results for the mechanical properties, tensile test in accordance to the DIN EN ISO 6892-1:2009–12 [30]

Configuration	E (MPa)	$YTS_{0.2\%}$ (MPa)	$UTS_{\%}$ (MPa)	$Elongation$ $at Failure$ [%]	$Poisson's Ration \nu$ (-)
(a)	72.322	206.74	366.43	6.12	0.2901
(b)	72.888	241.15	399.10	6.47	0.3205
(c)	71.715	222.83	360.27	5.33	0.3619
(d)	65.640	188.15	330.11	4.47	0.3235
(e)	69.515	179.71	314.32	3.97	0.3448
(f1)	70.422	208.57	357.49	3.15	-
(f2)	62.560	198.13	344.73	3.20	0.3040
SLM metal powder reference	64±10	227±11	397±11	6±1	-
Die-cast material	71	172	324	3	-

The authors also concluded that the main differences in the mechanical properties of the High – vs. Low specimens were caused by the varying development of the precipitation- hardening process after consolidation and corresponded directly with the varying dwell times in the build environment at elevated temperatures.

**Fig. 2.21.** (a) The engineering stress-strain curves for AB and HT specimen's series; (b) the applied T6 heat treatment (HT) [32]

Bagherifard et al. [32] examined the influence of the post processing on the static and dynamic loading. In their study, the standard flat specimens for static testing and the hourglass specimens for fatigue testing were tested using different type of the post processing – T6 heat treatment (HT, Figure 2.21b), sand blasting (SB) or shot peening (SP).

Tab. 2.2 The mechanical properties for SLM specimens compared with convent. cast material [32]

#	AB	HT	Conventional cast and aged (EN1706, [33])
Young modulus (GPa)	72 ± 1.5	73 ± 1	71
Yield stress (MPa)	273 ± 3	201 ± 6	180
Ultimate stress (MPa)	393 ± 20	265 ± 9	300–317
Elongation at fracture (%)	2.5 ± 0.4	13 ± 1	2.5–3.5

The results show that the specimens fabricated by SLM exhibit a good static strength (Table 2.2), due to the very high thermal gradient that characterizes the

process; however, their performance under dynamic loading is somehow restricted due to the limited ductility, tensile residual stresses, defect density and inadequate surface morphology in the as built configuration (Table 2.3). The results highlight that appropriate post treatments can significantly enhance the fatigue and static performance of SLM specimens resulting in characteristics that are comparable and even better than those of conventionally manufactured material.

Tab. 2.3 Fatigue strength corresponding to 3 million cycles for all series [32]

<i>Specimen series</i>	<i>Fatigue strength (Hodge-Rosenblatt) (MPa)</i>	<i>Fatigue strength (ISO12017) (MPa)</i>
AB	36	50 ± 4
HT	83	75 ± 7
SB	161	173 ± 4
SP	176	185 ± 13
HT + SB	162	175 ± 4
HT + SP	101	102 ± 4
Cast A360-T6	-	76–115 ± 10
Wrought 6061 alloy	-	120

The results of the previous authors are summarized in the following Table 2.4.

Tab. 2.4 Comparison of averaged mechanical properties for AlSi10Mg; all results refer to specimens without additional post heat-treatment [30]

	this work	Buchbinder et al. (2015)	Kempen et al. (2012)	Fraunhofer ILT – Research Project (Buchbinder et al., 2010)
Laser power ¹³ [W]	350	240 960 960	200	250 250
Scan speed ¹⁴ [mm/s]	930	500 >1000 >1000	1400	50 500
Laser re-melting	no	no	yes	no
Preheating [°C]	200	-	220	300 300
Number of configurations investigated ¹⁵	6	2	2	3 3
Young's modulus <i>E</i> [GPa]	62.56–72.89	-	68	-
Yield strength <i>R</i> _{p0.2} [MPa]	180–241	210–240	125–150	90 125–140
Ultimate tensile strength <i>R</i> _m [MPa]	314–399	400–450	250–305	391–396 210 250–270
Elongation at failure <i>A</i> _t [%]	3.15–6.47	3.2–5.9 5.5–8.0	4.1–6.3	3.47–5.55 7 4.7–6.8
Poisson's ratio <i>ν</i> [-]	0.29–0.36	-	-	-
Hardness ¹⁶	as-built	105–122 [HBW 2.5/62.5]	-	-
	machined	101–131 [HBW 2.5/62.5]	130–140 [HV 0.1]	83–90 [HV 0.1] 127 [HV 0.5] 70 [HV 0.1] 75 [HV 0.1]

2.5.1 Micro-strut lattice structure material

As the previous studies show, the mechanical properties of the SLM produced parts depend on the level of the internal porosity and surface roughness. The porosity appears usually close to the surface area where the laser slows down at the end of the laser track. The influence of the area close to the surface is even greater in case of the thin strut where close to surface is higher, i.e. the tested specimen has a smaller cross-section than it is in the case of the lattice structure [14, 34].

Tsopanos et al. [14] deals with the mechanical properties of the lattice structure from the 316L material. In the study, two types of the experiments were performed: standard quasi-static mechanical testing of the lattice cubes and the tensile testing of very “wires” shape specimens which represented the struts in the lattice structure. The data recorded was hard to evaluate; therefore, the tensile test was re-simulated in LS-DYNA to obtain the stress – strain curve for evaluation of the mechanical properties.

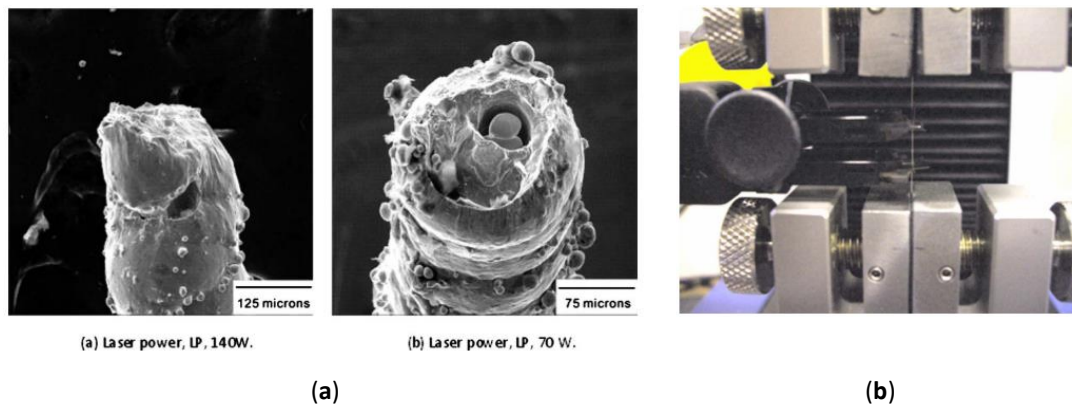


Fig. 2.22. (a) SEM micrographs of failure surfaces of 316L struts; (b) tensile mechanical testing of wire [14]

From the comparison of the bulk and thin-wire mechanical properties, it results that those of the thin-wire were of about 30% lower. It was caused mainly by internal defects in the wire specimens (Figure 2.22). These results were confirmed by Dong et al. [34] who deal with the mechanical properties of the AISi10Mg strut shape tensile specimens in the range of the diameters between 1 and 5 mm. The building orientation of the specimens was perpendicular to the platform, and the same process parameters were used for all the specimens. The results show that the mechanical properties and also the porosity level were changed up to the diameter $d = 4$ mm (Figure 2.23). Based on these results, it is obvious that the mechanical properties of the lattice structures must be evaluated on the specimens with a similar shape and dimensions.

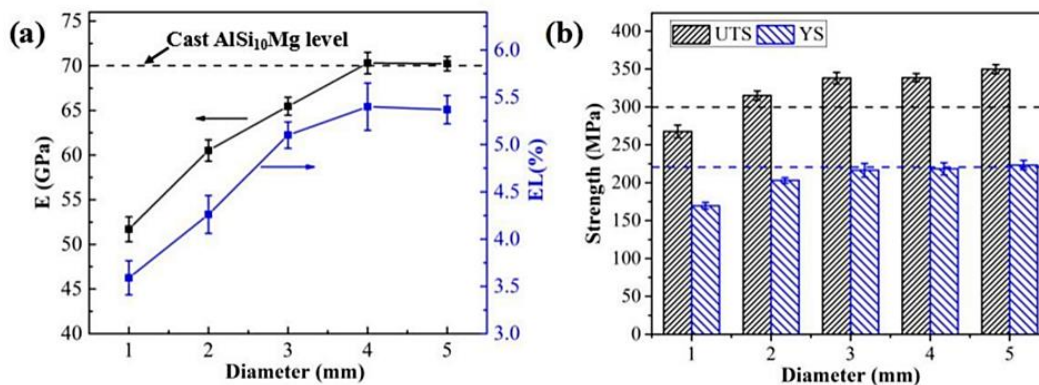


Fig. 2.23. Effect of build size on the mechanical performance of AISi10Mg specimens: (a) EM and EL; (b) UTS and YS [34]

2.5 Low-velocity loading of lattice structure and experimental devices

2.5

The previous studies aimed at the impact resistance show that the impact testers are divided into two categories according to the impact velocity. High impact speeds, above $50 \text{ m} \cdot \text{s}^{-1}$, are usually realised by horizontal testers which use a compressed gas such as nitrogen [35] or helium [36] with a pressure of about 10 MPa. These devices are used for testing of the elements for ballistic protection.

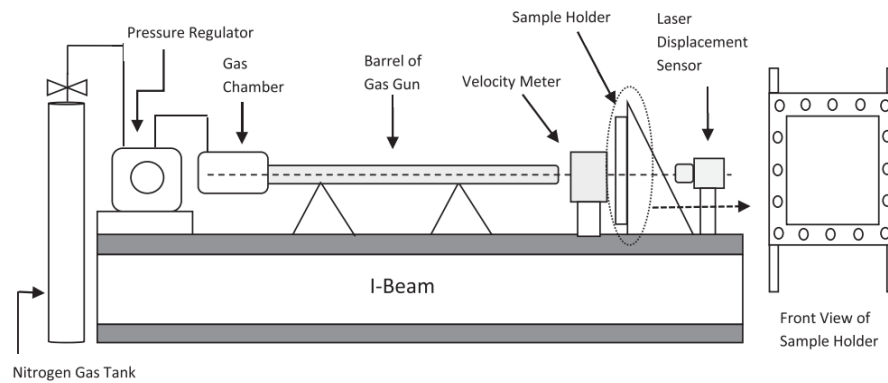


Fig. 2.24. Impact experimental set-up.[35]

For low impact speeds below $50 \text{ m}\cdot\text{s}^{-1}$, the tower testers based on the drop-weight principal are preferred (Figure 2.24). Shen [37] and Mines [38] used drop-weight testers to examine the ability of different types of the lattice structures to absorb the impact energy. Both devices employ the same method of force measurement using a strain gauge located between the indenter and the weights. Mines evaluates deformation using a laser-Doppler speedometer. Shen, on the contrary, uses a high-speed camera to measure speed and deformation. The specimens are placed on the base plate without any further clamping.

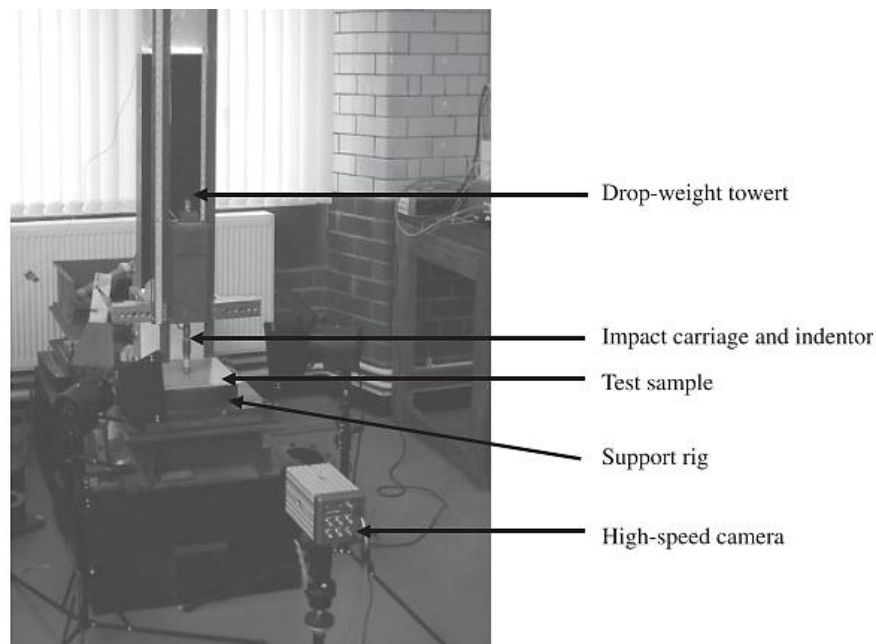


Fig. 2.25. The drop-weight rig used to characterise the dynamic properties of specimens [37]

In his study, Mines et al. [38] focused on the impact resistance of the Ti-6-4-BCC micro-lattice structure applied as the core material of the sandwich panel in comparison with the aluminium honeycomb and the SS316L micro-lattice structure. The specimens were placed on four spherical supports $d = 10 \text{ mm}$, and as the indenter, the hemisphere pin with diameter $d = 10 \text{ mm}$ was used. The results show

that, from SLM processing point of view, the SS316L micro-lattice structures are less sensitive to build conditions during the process; however, they have a low specific strength and higher density and so they are not suitable for high-performance applications in aerospace.

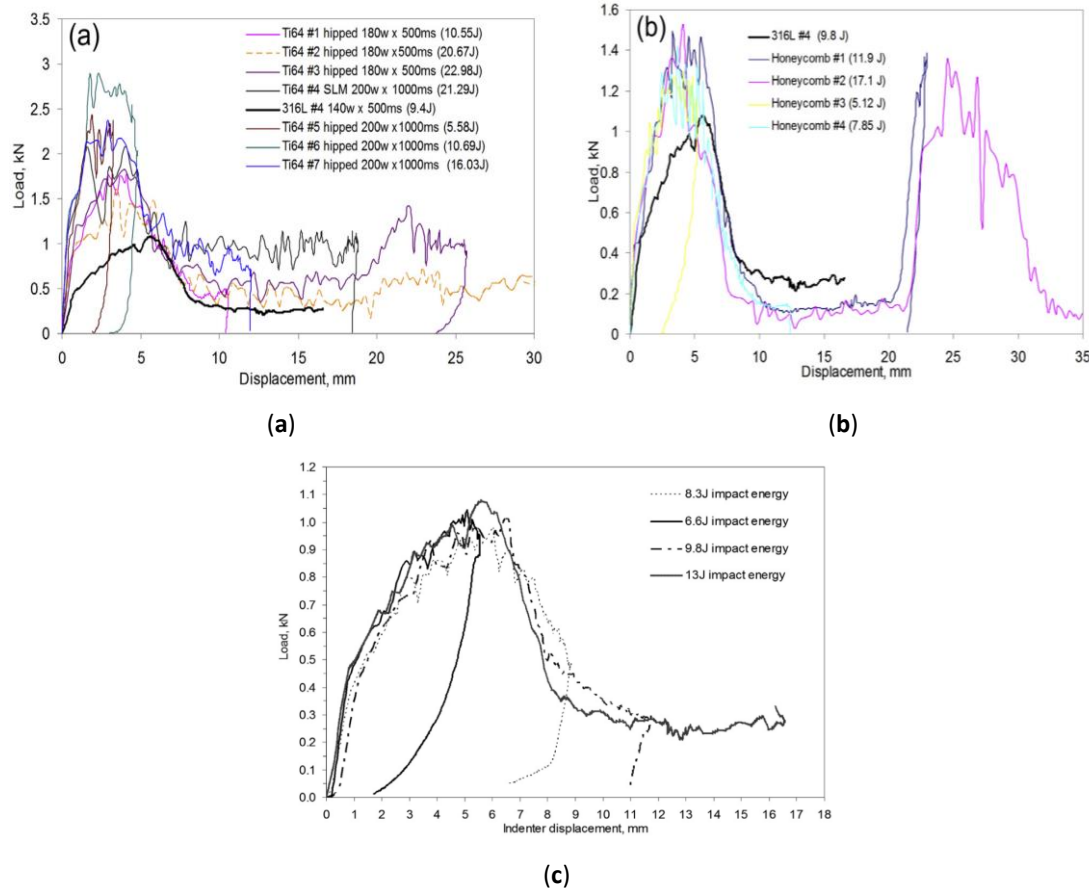


Fig. 2.26. Impactor load - displacement curves of sandwich panels based on (a) the Ti64 lattice core and (b) the aluminium honeycomb core for corner supported low velocity impact tests. Stainless steel 316L data shown for comparison; (c) Load vs impactor displacement for various impact energies for 316L stainless steel core sandwich panel under four-point support [38]

From the comparison of the Ti-6-4-BCC lattice structure and the SS316L lattice structure, it results that the impact performance of the Ti alloy is always above SS316L. The results also show that the impact behaviour of the BCC lattice structure from Ti alloy depends on the strain rate when, for different levels of the impact energy, the Ti lattice structure transfers various levels of load (Figure 2.26a, specimens Ti64#5 – Ti64#7). The SS316L material is not so strongly dependent on the strain rate due to a more ductile material behaviour (Figure 2.26b). From the comparison of the aluminium honeycomb structure and the SS316L lattice structure, the honeycomb structure shows a better impact performance, and the strain rate dependence was not observed (Figure 2.26c). The higher impact resistance is mainly caused by the suitable topology of the honeycomb structure in the direction of the load. The specific motivation for this study was the application of the SLM technology

and BCC structures in mitigating against a foreign object impact damage in sandwich panels, e.g. hail or rubber impact on twin-skinned aircraft fuselages.

Shen et al. [37] extended previous work about study on the influence of SLM processing parameters on the impact performing behaviour. He observed that the strut diameter changes according to the used laser energy level and struts orientation. It is in line with previous study [38]. Shen also shows that the influence of both parameters is not the same as is shown in [Figure 2.27](#), where different combinations of laser power and exposure time which results at the same applied energy were applied.

$$E = P \cdot T \quad (2.2)$$

where P is the laser power and T is the exposure time in single point system.

Shen also examined the differences between the quasi-static and low-velocity impact response of the SS316L lattice structure sandwich panels. In the experiment, the range of strain rate was changed from $2 \times 10^{-4} \text{ s}^{-1}$ to $3 \times 10^2 \text{ s}^{-1}$. It can be seen from [Figure 2.28](#) that there is no significant effect of strain rate on the impact response of the sandwich panels. This supports the Swanson's argument [39] that the response of the plate can be considered quasi-static if the impactor mass is more than 10 times higher than the mass of the panel. Thus, all of the impact tests conducted here can be considered as being in the quasi-static regime.

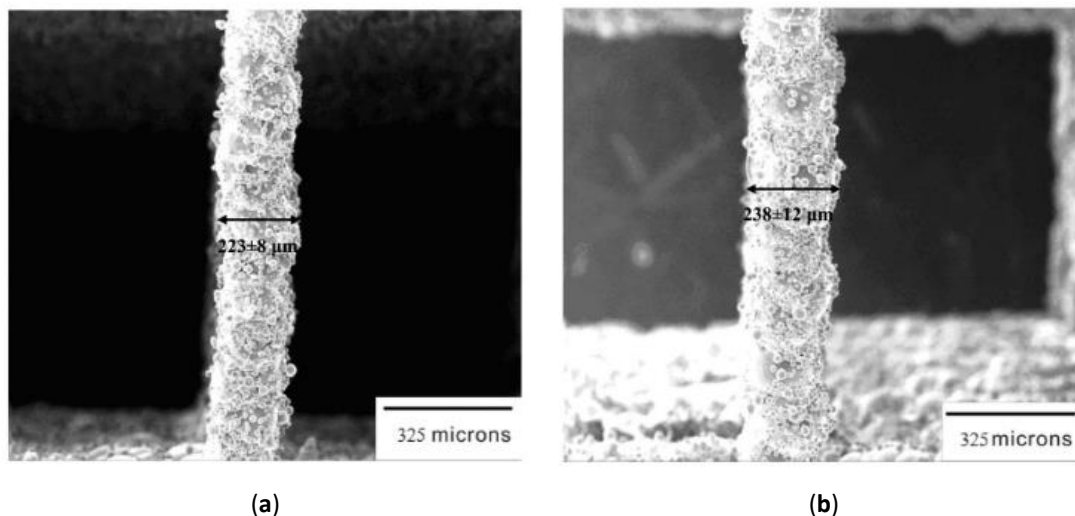


Fig. 2.27 Struts SEM images of SS316L lattice structure blocks manufactured using (a) $P=140\text{W}$, $T=500 \text{ ms}$ and (b) $P=70\text{W}$, $T=1000 \text{ ms}$ [37].

These results also show a relatively small variance in the F_{max} experimental data, with the maximum average force being 1510 N. The small differences in the maximum forces are likely to be due to variations of the elastic properties of the composite and the precise location of impact. This suggests that the impact response of these lattice core sandwich panels is highly reproducible.

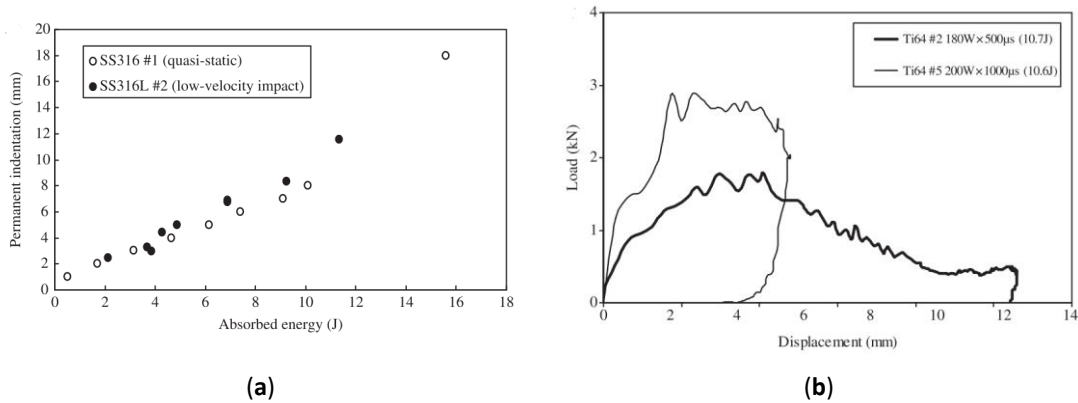


Fig. 2.28 (a) Permanent indentation vs. absorbed energy plots of SS316L lattice sandwich panels fully supported, strain rate ranged from $2 \times 10^{-4} \text{ s}^{-1}$ to $3 \times 10^2 \text{ s}^{-1}$; (b) Ti64 #2 and #5 following impact tests at velocity of 3 m.s^{-1} [37].

Mines et al. [40] used the SLM technology to fabricate the SS316L lattice structure as a twin-skinned composite material. One of the major structural performance requirements for such twin-skinned structures is a foreign object impact resistance; therefore, the numerical simulation of the impact performance was created. Two numerical models were created using default Hughes and Liu and B-S beam [41]. The geometry of the BCC lattice was created in in-house software which has a library of geometries available. Each strut of the unit-cell is represented by three beam elements. The constant bending moment formulation (Hughes Liu) allows for a simple failure criterion to be included in the material model and is used in simulations. This failure criterion simulates a strut rupture by reducing beam stiffness as gauss points achieve a critical effective stress and by deleting a beam element when all gauss points failed. The effective strain is set to the failure strain of a strut subject to uniaxial tension.

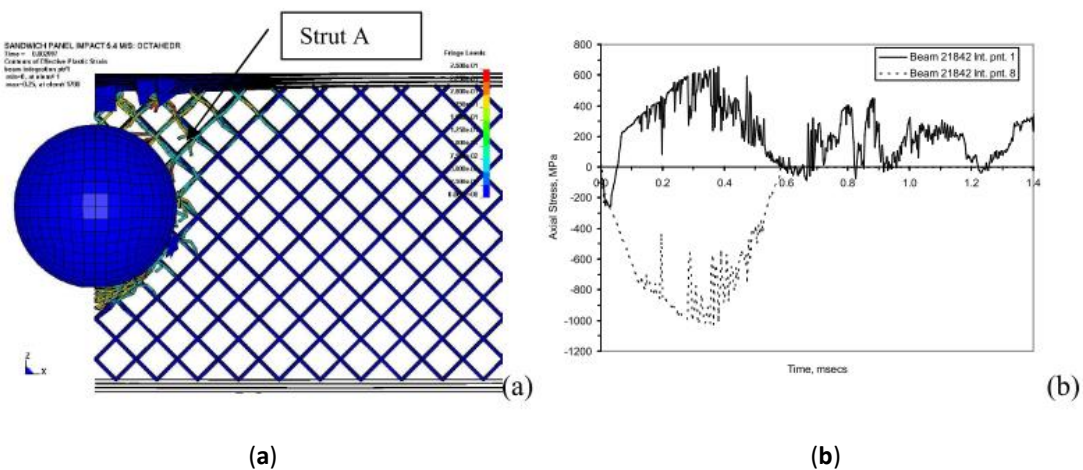


Fig. 2.29 (a) Perforation and simulation, (b) Behaviour of a specific micro strut (A) [40]

A series of experimental tests on lattice struts were performed to establish the mechanical properties of the stainless steel 316L struts and, in contrast to them, with bulk 316L properties. This mechanical behaviour was approximated using a bi-linear

elastic-plastic material model with failure. An important aspect of the lattice model is modelling of densification. Experimental observations show that increasing levels of localised crush lead to the contact between neighbouring struts of the lattice, which produces a rapid increase in stress at densification. To validate the numerical model, the uniaxial constrained compression tests were simulated and compared with the experiment. The simulations showed a good agreement with experiments. A skin and micro-strut failure model proved to be robust. The use of three beam elements per micro-strut enabled us to capture the basic physical phenomena.

The impact resistance was also dealt by Labeas et al. [42]. They focused on the impact resistance of the BCC lattice structure composites produced by SLM technology from SS361L. The skinned plates were made of carbon epoxide. The mechanical properties of the lattice structure were identified by quasi-static compressive mechanical test. To validate the numerical model, the low-velocity experiment was performed. The numerical model was created in PAM-Crash and contains the following boundary conditions:

- The lattice structure was represented by a beam type element
- In the numerical model, two areas were defined in the lattice structured core, the former near the indenter body which was created by finer beams composed of four elements and the latter was composed of two-element beam.
- The mechanical behaviour of the lattice structure was defined using a bi-linear plasticity material model
- The skinned plates were created by *shell 163* elements
- The contact *type 33* was defined between the indenter and the composite specimen
- The material properties were re-edited using calibration according to the performed experiment
- The quarter model was used to save the computing time ([Figure 2.30a](#))
- Another numerical model was created using a homogenised core to save computing time ([Figure 2.30b](#))
- The polygonal mesh of a homogenised core was created by the volumetric *solid 164* elements
- Default material model *Mat-54* was used for the upper and bottom skin plates. The material model was supplemented with the fracture model of damage
- Default material model *Mat-26 (honeycomb)* was used for the homogenised core

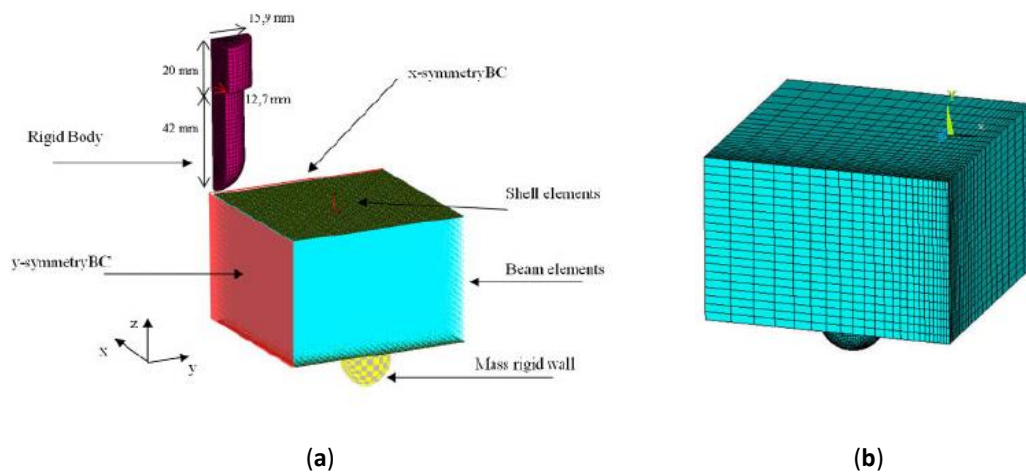


Fig. 2.30 (a) Quarter panel FE model with symmetrical boundary conditions; (b) Mesh (FE) of skin and core of homogenised core FE model [42]

During the mechanical impact testing, the specimen was loaded at three levels of the impact energy – 194 J, 99 J, 20 J. The comparison of the FE simulation and the mechanical testing results show a good agreement with the beam numerical model in all deformation processes. The homogenised numerical model is suitable for the first F_{max} prediction but during deformation (Figure 2.31).

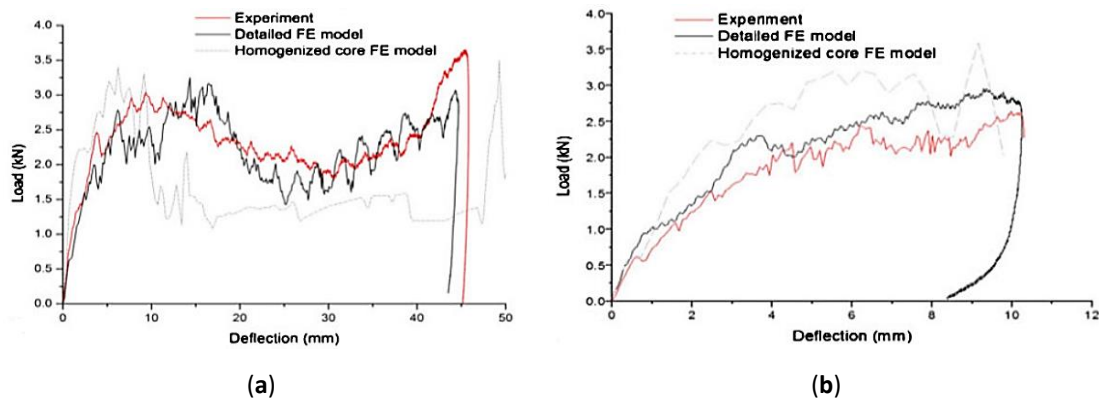


Fig. 2.31 (a) bcc-LV2 (99 J); (b) bcc-LV3 (20 J) [42]

Wang et al. [43] tested the ability of special absorbers made of steel sheet and metal foam to absorb energy. These absorbers should be used as an attachment element between the anti-explosive wall and the supporting parts of the building which will eventually absorb a part of the energy of explosion by its deformation, so the protective wall remained intact (Figure 2.32).

The authors describe the behaviour of the absorption connector and identify three phases of its deformation – elastic deformation phase, plastic deformation phase, ideally at the same level of stress (force), and densification phase, where the internal topology of the core material disappeared and the absorption connector loses its ability of energy absorption.

To describe the mechanical performance of the absorption connector the authors used the following critical indicators: average force, mean force, densification

displacement, energy absorption efficiency, energy absorption capacity, crush force efficiency.

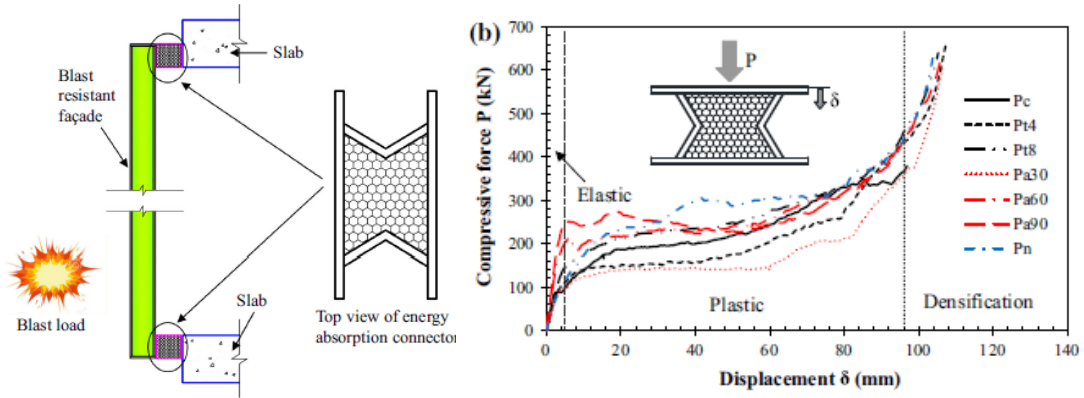


Fig. 2.32 Example of application of energy absorption connector [43]

Energy absorption efficiency is defined as follow:

$$\eta(x) = \frac{1}{F(x)H} \int_{x_y}^x F(\bar{x})d\bar{x} \quad (2.3)$$

where $F(x)$ is compressive force, H is height of aluminum foam and x_y is displacement at yield. Densification displacement of energy absorption connector, x_D , is determined as the displacement corresponding to the stationary point at the energy absorption efficiency – displacement curve where the efficiency reaches a maximum value, i.e.,

$$\left. \frac{d\eta(x)}{dx} \right|_{x=x_D} = 0 \quad (2.4)$$

Figure 2.33 illustrates the determination of densification displacement by a given compressive force–displacement curve. Then, the mean force is determined by:

$$F_p = \frac{\int_{x_y}^{x_D} F(\bar{x})d\bar{x}}{x_D - x_y} \quad (2.5)$$

The energy absorption capacity is obtained by integrating the force with displacement from 0 to x_D

$$E_a = \int_0^{x_D} F(\bar{x})d\bar{x} \quad (2.6)$$

Since the maximum force that will be transferred to the buildings is also a vital indicator, the crush force efficiency was adopted to evaluate the ratio of the mean force to maximum force, which is given as follow:

$$e_f = \frac{F_p}{F_{max}} \quad (2.7)$$

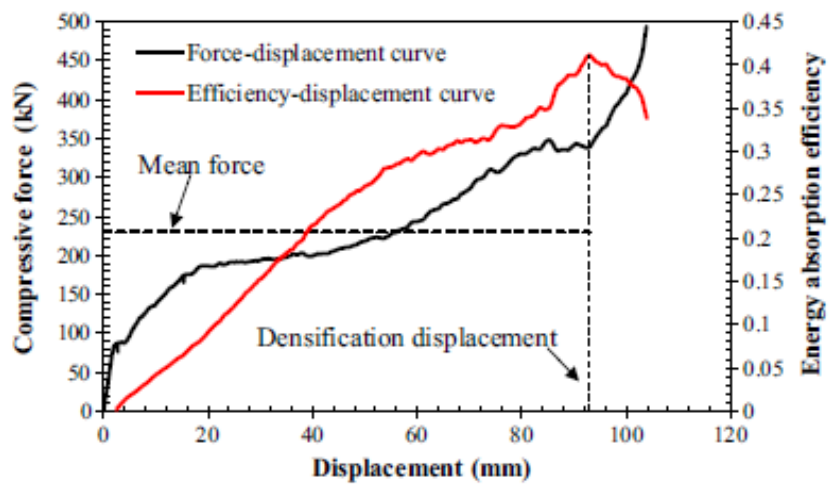


Fig. 2.33 Determination of densification displacement.[43]

3 ANALYSIS AND CONCLUSION OF LITERATURE REVIEW

The porous materials, e.g. a honeycomb or metal foams, are light-weight materials which are created with regular (honeycomb) or irregular (metal foams) internal material topology and air pores. They are characterized by low material vs. air ratio (porosity up to 95%) [44–46] and are divided into two groups – with opened or closed air gaps. The closed air gaps materials are usually metal foams used as the infill of the contraction elements e.g. tubes, square tubes and plates. The internal infill improves the mechanical properties without a significant increase in weight [47, 48]. The opened-air gaps materials are usually used as protective elements which are able to absorb high impact energy through self-deformation[43]

With the gradual development of the Selective Laser Melting (SLM) technology which brings a larger size of the build-envelope and possible use of high-strength powder materials, it seems to be a perspective way to produce highly-durable porous structures. The main advantage of the SLM lattice structure compared to other porous materials is a possibility to produce user-designed lattice structures with defined geometry which can be optimized for a specific application, e.g. by a local change of stiffness or the special shape of the lattice topology. It allows for the use of topology optimization and numerical modelling to design the impact energy absorber with defined mechanical properties or deformation behaviour.

In order to use the SLM micro-strut lattice structure as an energy absorber in protective applications, it is necessary to optimise the SLM processing parameters for production of micro-strut lattice structures without a high level of internal porosity or surface roughness, because, as was shown in previous studies, mechanical properties of SLM produced parts are strongly dependent on the used process parameters, especially in the case of the micro-strut lattice structure geometry [15, 23, 25, 30, 34].

A strut-shape and lattice structure cube specimens will be produced for quasi-static and low-velocity mechanical testing. Their specific mechanical properties will be obtained to create the lattice structure material model for FEM analysis. Finally, the FEM numerical model of lattice structure deformation will be created based on previous results. The model will be used to study the lattice structure behaviour under low-velocity dynamic loading according to the used micro-strut size.

3.1 Process parameters of structured material

The authors deal with setting of process parameters for the production of dimensionally accurate parts with a density approaching 100% of the material. The authors investigate the impact of major process parameters such as laser power, scanning speed, laser focus, hatch distance, and chamber heating. They mostly observe these properties on large-volume cube-type specimens [21, 49, 50]. As can be seen from other publications, the situation is significantly different when specimens with a small volume of material are produced [34]. In this case, even the appropriate setting of the process parameters for the full-volume specimen may not be optimal for thin struts the production. This is confirmed by Qiu et al. [25] who

examine the process parameters directly on structured parts. The results differ significantly from previous works where the volumetric specimens were used. Depending on the used process parameters, the size of diameter and also material properties of the lattice structure were changed. It was confirmed also by Delroisse et al. [28]. Sensitivity of the SLM process can be seen in [Figure 2.5a](#) that, when the scanning speed of the laser was increased from 2000 mm. s⁻¹ to 4000 mm.s⁻¹, the material porosity can be changed multiple times [14].

The mechanical properties of the SLM produced lattice structure are strongly depended on the internal imperfection, such as internal porosity and surface roughness. **Using the suitable combination of process parameter, their level is possible significantly decrease and so improve the mechanical properties.** It is also useful from a numerical simulation point of view because the internal porosity can cause random local damage of the lattice structure which cannot be reflected in the numerical model; therefore, **reducing of imperfections level will increase the prediction accuracy.**

3.2 Mechanical properties of lattice structure

3.2

Kempen et al. [12] investigate the influence of specimens orientation during the SLM production on their mechanical properties of the specimens. The authors found that, depending on the orientation, the pores that degrade mechanical properties arise close to the surface of the specimen. The authors use the flat shape of a tensile specimen. Hitzler et al. [30] also examine the influence of building orientation on mechanical properties. Contrary to Kempen [12], the authors used SLM only to produce a semi-product (flat plates), which are subsequently machined to the shape of a standard flat tensile specimens; therefore, most of close to the surface porosity was removed and only a low anisotropy was observed compared to the study [12]. It was also confirmed by Brandl et al. [10]. Hitzler et al. also observed significant changes in mechanical properties of the high- (in the Z axis) vs. low-height specimens (in the xy plane). It is caused by aging of the material during longer build jobs. Tsopanos et al. [14] examine the mechanical resistance of lattice structures from SS316L. To obtain real mechanical properties, the authors first perform a tensile test of thin wires. They find out that, with such a small volume of material, the mechanical values of thin steel struts 316L decreased of about 30% of the bulk material. It was also confirmed by Dong et al. [34] during mechanical testing of the struts tensile specimens with diameters between 1 mm and 5 mm. Therefore, it is clear that the mechanical properties of volume tensile specimens cannot be used as the input data for material model of the lattice structure. **It is necessary to test their behaviour directly on the thin-strut specimens.**

The authors of the articles [11, 15] draw attention to large inaccuracies in the production of thin struts. The strut is normally produced with a very rough surface and its cross section is variable ([Figure 2.10b](#)). In order to predict the mechanical properties of micro-strut lattice using FEM analysis, the geometry must be simplified; therefore, an alternative way is to use the *effective strut diameter*. This diameter enters the FEM calculation as the diameter of structure strut.

The real diameter is often significantly larger. This is due to heat transfer to the surrounding powder material and subsequent melting of the surrounding particles that stick to the strut surface. Koutny et al [11] further analyse a dimensional accuracy of the struts with different production orientation. The authors show that, at low production angles, the strut diameter fluctuations can be very significant, and **the strut can no longer be considered a cylindrical object**. The same conclusion is drawn by Leary et al. [21], who directly use different types of the lattice structure as a test specimen. The authors determine the material roughness and find out that its value differs in different areas of the struts. At the down-skin surface, the roughness is much higher than that at the upper side or on the side of the strut. This is confirmed by Yan et al. [51] who termed it a staircase effect. When preparing the data for additive technologies, the objects are cut into thin layers. This leads to the formation of overlapping parts on the down-skin side of the strut.

3.3

3.3 Description of deformation behaviour

Most authors compare the impact resistance of micro-lattice structure materials to conventionally produced structured materials that are already used in the aerospace industry, such as metal foams and the honeycomb structures. In the case of lattice materials produced by SLM technology, the authors emphasize the possibility to control the shape of the material structure and the possibility to produce structures made of more durable material than aluminium alloys suitable for the production of metal foams [42, 43, 52, 53].

To obtain the absorption behaviour of these materials, the authors use different types of test devices depending on the type of load. Yahava et al. [35] used horizontal high-speed impact tester with loading velocity above $50 \text{ m}\cdot\text{s}^{-1}$; Shen [37] and Mines [38] used “tower configuration” with lower impact velocity. The advantage of this configuration is an easy change of the impact energy using various mass or falling height of the loading element.

The analysed articles also show the parameters that are used for description of an energy absorption behaviour. Most authors compare the dependencies of force vs. deformation, deformation vs. time, absorbed energy vs. deformation, deformation speed vs. time. To reach all dependences above, the testing device must include a strain gauge and possibly a high-speed camera or another sensor capable of recording specimen deformation and impact velocity. For the design of an experimental device **the tower variant of device was chosen as suitable**.

3.4

3.4 Nonlinear dynamic FEM analysis of micro-strut lattice structure

For an efficient design of energy absorber, it is necessary to use FEM numerical model supplemented with the appropriate material model which define mechanical properties of the micro-strut lattice structure.

There are two main approaches to the numerical modelling of porous materials. The former uses a homogenised model of geometry and the latter uses a simplified model of real geometry [54–59]. The method of how to simplify the real shape of the lattice struts for FEA was described by Suard et al [15]. For application in FEA, the

geometry was simplified to circular cross-section with diameter which corresponds with the *effective volume* of the strut. Koutny et al. [11] measured the shape of struts specimens using optical measurement. Based on the results, the maximum inscribed diameter was used for evaluation of mechanical properties.

Porous materials have a specific deformation behaviour due to their core topology. Therefore, in the case of homogenised geometry, it is necessary to use a suitable material model which considers its deformation behaviour. Material models of porous structures, such as honeycomb or metal foam, are usually included in the material library of the FEA software, and it is possible to use them also for lattice structure [38, 42, 58, 59]. According to Mohmmed et al. [58], a crushable foam material model is suitable for simulation of penetration of porous foam blocks with a damage criterion describing the occurrence of breakdowns between the core and plates. Input material properties can be obtained from uniaxial compression tests according to ASTM D5308. Labeas et al. [42] used both methods; the material model Mat-26 Honeycomb (LS-Dyna) to create a dynamic FEM simulation with a homogenised micro-lattice core and the bilinear (multilinear) material model with micro-lattice BCC structure geometry. The results showed that the simplified core is only suitable for prediction of the first progressive collapse of the lattice structure while the beam geometry allows to predict the whole deformation process. Based on previous studies [38, 42, 58], boundary conditions of a numerical model, such as type and density of polygonal mesh, type of contact between bodies were determined. Base on previous author is also clear that is necessary to use different material model for core and skinned plates and the damage criterion must be implement to both of them.

The resulting FEM numerical model will be used to study the deformation of the micro-lattice structure core; therefore, the geometry including a real strut geometry will be used. To save computing time, the quarter model as in the case of [42] will be used.

4 4 AIM OF THESIS

The primary aim of the present dissertation thesis is the development of the numerical model of the SLM produced BCC lattice structure for prediction of its deformation behaviour under impact loading. For this purpose, the material model of the SLM lattice structure must be created using quasi-static mechanical testing of designed specimens. To improve the mechanical properties of the lattice material, the influence of the main SLM process parameters and lattice structure production strategy on the material and mechanical properties must be clarified. To achieve the main goal of this thesis, the solution to the following sub-aims are necessary:

- Development of an experimental device for testing absorption behaviour of the BCC lattice structure.
- Development of software for the analysis of the measured data and evaluation of lattice structure behaviour under low-velocity deformation in MATLAB.
- Experimental testing of BCC lattice structure behaviour under low-velocity loading
- Research of the influence of main SLM process parameters on the material and mechanical properties of lattice structure
- Development of a laser strategy for lattice structure fabrication.
- Design of experiments and approaches for obtaining of SLM produced mechanical properties for FEA material model.
- Creation of the numerical model of a BCC lattice structure deformation using a dynamic nonlinear solver (ANSYS Explicit).

4.1

4.1 Scientific questions

- Q1.** *It is possible to define a relationship between main process parameters and formation of the material imperfection for strut geometry, such as an internal porosity and a surface roughness?*
- Q2.** *Do the struts-shape changes affect a deformation behaviour of the lattice structures?*

4.2

4.2 Hypotheses

- H1.** *Formation of material porosity is affected by strut orientation during SLM production.*
- H2.** *In case of strut, the porosity and roughness level are dependent on used laser energy.*
- H3.** *The changes in the strut-shape cross-section mainly depend on the strut orientation*
- H4.** *The mechanical properties of the multi-strut tensile specimens produced in orientation 90° have lower mechanical properties than specimens produced in orientation 45°.*

4.3 Thesis layout

The present dissertation thesis is a part of the research project which is aimed to use the SLM produced lattice structures as an energy absorber which will be used as a protective element with defined mechanical behaviour. The thesis deals with three sub-parts of this project which are needed to achieve the above global aim in the future.

The first research area was the development of the SLM contour strategy for lattice structure production. The aim of the new strategy was to stabilize the material and mechanical properties which are easily degradable using an incorrect setup of the laser. Incurred imperfections decrease mechanical properties of lattice structure and also decrease agreement of a simulation and experiment because it is complicated to include them to the numerical model. The designed script is able to propose an appropriate combination of the process parameters to keep the input and linear energy in the proper range. The results of this area were published in [Paper A](#).

The second research area was the study of the lattice structure mechanical properties during absorption of the impact energy. For this purpose, a drop-weight impact device was designed and produced. Together with the device, the software for effective evaluation of the experiments was developed in MATLAB. The results of the impact testing provided fundamental information for another research area which deals with a numerical model of low-velocity dynamic loading. A numerical model was created in software Ansys, module Explicit, to allow for the analysis of BCC lattice structure behaviour. This numerical model uses the geometry with elliptical shape of the struts and the bi-linear material model of lattice structure which was developed within this thesis. The results of this area were presented in [Paper B](#).

The full-text [Paper A](#) and [Paper B](#) are attached as a part of this thesis; therefore, the results of both of them will be present in a brief version.

Paper A

VRÁNA, R.; KOUTNÝ, D., PALOUŠEK, D., PANTĚLEJEV, L., JAROŠ, J., ZIKMUND, T. and KAISER, J. Selective Laser Melting Laser Strategy for Fabrication of Thin Struts Usable in Lattice Structures. *Materials* **2018**, 11 (9), DOI: 10.3390/ma11091763. ISSN 1996-1944.

- *Materials MDPI* - **IF 2.467**, Q2

-Authors contribution 65%



Paper B

VRÁNA, R.; ČERVINEK, O., MAŇAS, P., KOUTNÝ, D. and PALOUŠEK, D. Dynamic Loading of Lattice Structure Made by Selective Laser Melting - Numerical Model with Substitution of Geometrical Imperfections. *Materials* **2018**, 11(11), DOI: 10.3390/ma11112129. ISSN 1996-1944.

- *Materials MDPI* - **IF 2.467**, Q2

-Authors contribution 60%



5 MATERIALS AND METHODS

In order to answer the scientific questions presented in the previous chapter, experimental investigations of the influence of the main SLM process parameters on material, shape and mechanical properties were performed.

5.1 Laser strategy for lattice structure fabrication (Paper A)

In the case of SLM process parameters optimization for the lattice structure production, a number of follow-up experiments were performed using the SLM280^{HL} machine.

To verify the quality of the AlSi10Mg powder material, the base analysis of the particle size distribution and spherical shape of the metal particles was performed. Depending on the results, suitable layer thickness (**LT**) was applied.

First, a *single tracks weld test* was performed with a wide range of the laser speed (**LS**) and laser power (**LP**) combinations. The aim of the experiment was to find the perspective areas where the used combination of parameters provides continuous and uniform laser welds. The perspective area was identified and described by the weld width (**w**) vs. **LS** dependences at constant **LP** parameters. It allows for a prediction of expected **w** for another, so far not tested, combination of process parameters. Also, the limit level of linear energy E_{lin} was defined for continuous and uniform single welds without a balling effect.

In the following *strut experiment I*, the contour strategy was applied for the first time. The experiment was divided into two parts – to find out the suitable overlap (**OL**) of neighbouring contour welds parameters for a different strut inclination and to compare the internal porosity and surface roughness of different struts inclinations. Due to a high number of the produced specimens, only basic analyses of porosity and roughness performed to find general trends. To express the trends, the input energy E_{in} , which considers a different strut inclination through length of laser tracks and resulting strut cross-section, was defined and applied. Based on the results, the **OL** parameter suitable for the inclinations of 90° and 35.26° was found.

Another *strut experiment II* aimed at a deeper analysis of internal porosity and surface roughness only for the inclination of 35.26° because the results of those struts showed a higher predisposition for significantly worse level of material imperfections and also this strut inclination is included in the most common BCC shape of the lattice structure. For porosity analysis in the whole volume of the strut, the computed tomography was used. The μ CT was also used to digitize the whole surface of the struts; therefore, the down-skin surface roughness could be evaluated. The results allowed to create dependences of porosity and surface roughness vs. input and linear energies. Due to this, it is possible to predict the expected level of the above parameters.

The results from all the experiments were used in the script which can manually design a suitable contour strategy and choose the best combination of process parameters for the required diameter of the struts. In the case of strut diameter $d = 2$ mm, the script also allows to predict the surface roughness and porosity. The future aim is to continue with the same analysis on the thinner struts and to create

complex own software for generation of the contour strategy which can automatically design the best combination of the process parameters for various strut diameters based on the criterion chosen by the user (porosity, dimension accuracy, roughness, mechanical properties, speed of the process, etc).

5.2 Numerical model of low-velocity impact (Paper B)

5.2

In the case of development of the lattice structure material and the numerical model, a shape analysis and a number of the quasi-static and low-velocity mechanical tests were performed. First, all the specimens for shape and mechanical testing were produced from AlSi10Mg powder in one build job to ensure the same condition during SLM production.

To evaluate the real shape and dimensions of the lattice structure, the specimens for shape analysis and tensile testing were analysed using the Atos optical system. The dimensions were measured by fitting ideal shapes into the digitized surface geometry in GOM Inspect software. The measured data were used for precise evaluation of mechanical properties and as the background for creation of geometry for a numerical model.

To obtain the necessary mechanical properties of the lattice structure material, the special specimens were designed - for tensile testing, the multi-strut tensile specimens; for compression testing, the lattice structure cube covered with thin plates on the bottom and upper side. They were tested using standard quasi-static testing and the resulting mechanical properties were used for definition of bilinear isotropic hardening model.

The numerical model was designed based on previous studies as a quarter model composed of 5 bodies where two types of material model were used. The main part, the lattice structure core, was made of solid tetrahedron elements. Boundary conditions were defined according to the real drop-weight test.

The final impact testing was performed by drop-weight impact tester designed within this thesis. Mechanical properties were measured using two main sensors – a strain gauge in loading “falling head” part and a high-speed camera in front of the device.

In the future, the numerical model will be used for a detailed description of the deformation mechanism of the lattice structure depending on various shapes of lattice structure unit cells.

5.3 Used Analysis

5.3

5.3.1 Metal powder analysis

The AlSi10Mg aluminium alloy metal powder (TLS Technik GmbH, Germany) was used in all experiments. The powder was produced using a gas atomization in nitrogen atmosphere and its particles had almost a spherical shape (Figure 5.1b). A particle size distribution was analysed (Horiba LA – 960) for powder quality verification. The results can be seen in the chart (Figure 5.1a). The particle mean size was 41.41 μm , median size was 40.7 μm and standard deviation was 12.9 μm . The particle size up to 25.2 μm represents 10 % and the particle size up to 58 μm

represents 90 % of particle size distribution. Depending on the particle size distribution, a 50 μm layer thickness was applied.

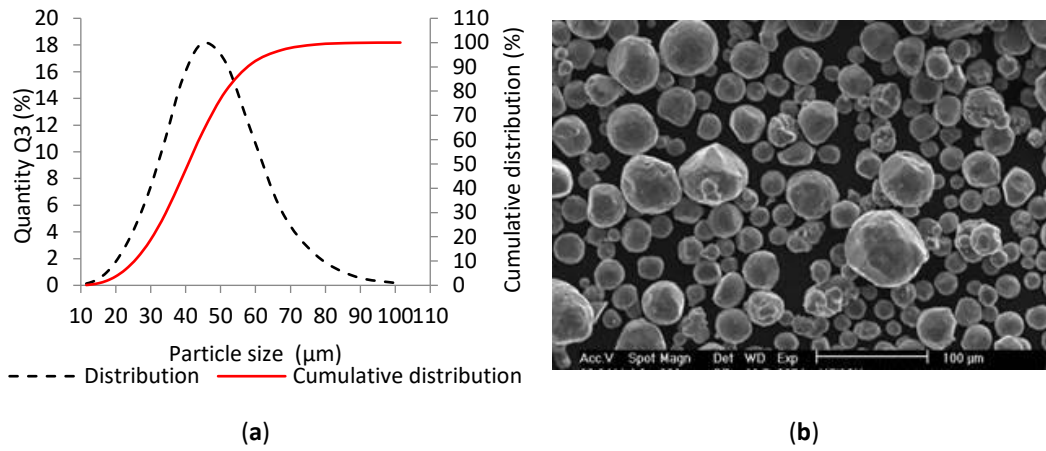


Fig. 5.1. SLM powder characteristics - (a) particle size distribution chart; (b) shape of particles (SEM)

5.3.2 Roughness analysis

The specimens of the *strut experiment 1* were digitized using the optical measurement system (Atos Triple Scan III, GOM GmbH) to find out the surface roughness on the strut side. The optical system was equipped with two 8 Mpx cameras and MV60 lens (resolution 0.017 mm). The specimens were coated with a thin layer of TiO_2 powder (thickness around 0.003 mm; [60]) prior to digitation. After measuring, the data were polygonised using a “more detailed” option. Using optical measurement, the down-skin surface cannot be sufficiently digitized. Therefore, the data of computed tomography (μCT) were used

The GOM Inspect software was used to evaluate the surface roughness by comparing the section line of digitized strut surface and best-fitted CAD in the GOM software. (Figure 5.3a). Obtained values were used for calculation of the Ra surface roughness according to equation 5.1.

$$Ra = \frac{1}{n} \sum_{i=1}^n |z_i| = \frac{|z_1| + |z_2| + \dots + |z_n|}{n} \quad (5.1)$$

5.3.3 Porosity analysis

Software ImageJ was used to initiate the porosity analysis of the top view specimens' images (8-bites) after basic grinding to the mid-plane of the specimens using CP-2 Grinder, Sinowon. The images were converted to black and white colours using an automatic threshold to reach a repeatability for all specimens. The results of porosity were evaluated as the percentage of black in white colour. (Figure 5.2b).

The internal porosity was also analysed using the computed tomography (μCT , GE phoenix v|tome|x L240). The main parameters of the X-ray tube were voltage of 130 kV, current of 100 μA , and a filter of 0.5 mm thin copper plate. Within two μCT measurements, two groups of 4 specimens were jointly analysed (Figure 5.3b). The measured data were obtained with 15 μm linear voxel size accuracy and were reconstructed (using the back-projection algorithm) in the Datos reconstruction

software. All subsequent post-processing was performed in the software VGStudio MAX 3.1.

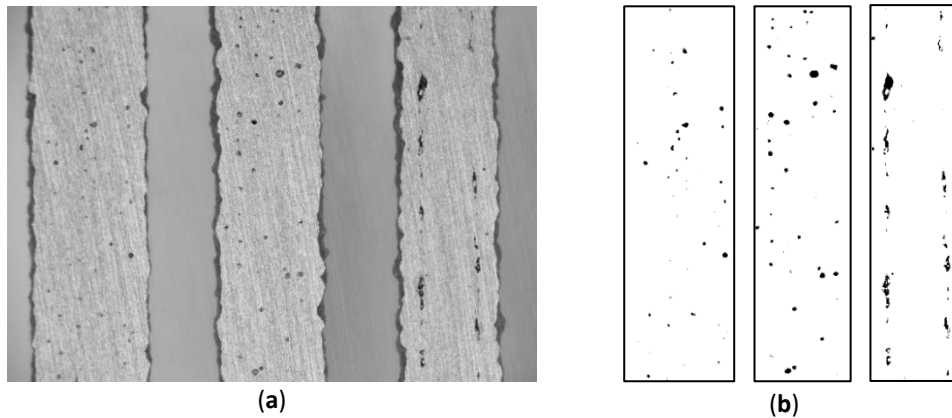


Fig. 5.2. The specimen after basic grinding; (a) the top view images captured by lighting microscope; (b) three areas of the struts after converting of the colours in ImageJ software

During the software analysis, the reconstructed data were divided into single struts and then each specimen was independently analysed by the porosity analysis software module. The threshold for detection of air pores was calculated automatically by software to reach the compatibility between both measurements. The results of the porosity analysis were between 0.17 – 2.93% (Figure 5.3 c, d).

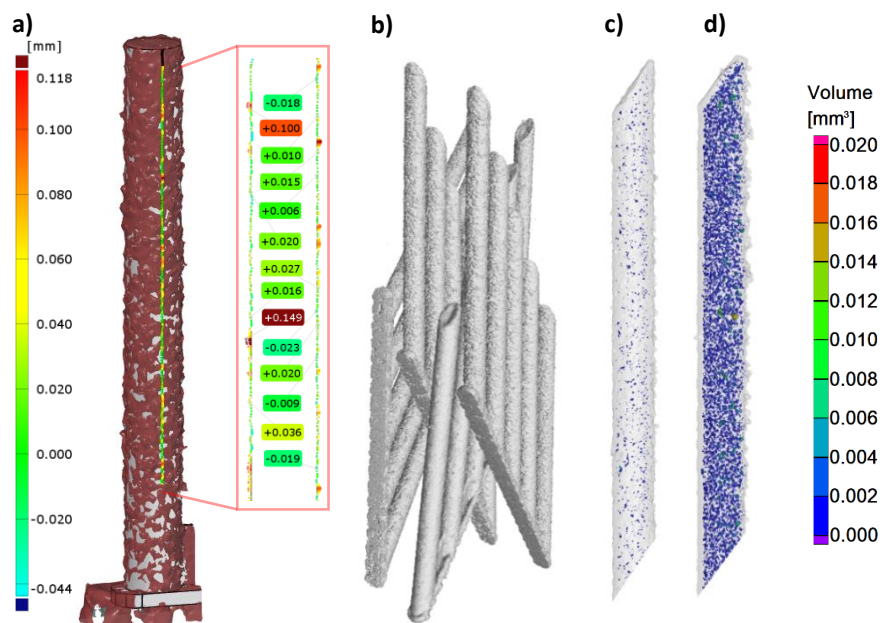


Fig. 5.3. Struts analysis - (a) surface roughness evaluation in GOM Inspect software; (b) group of four specimens measured together in VGStudio MAX software; (c) transparent 3D render of the strut with the lowest porosity of 0.17% (d) transparent 3D render of the strut with the highest porosity of 2.93%.

5.3.4 Input energy calculation

The input energy to the current layer E_{in} was obtained by [equation 5.2](#). It is based on the real laser track trajectory in the actual layer and the geometry of the tracks which was found out from the single welds test and is defined by the beam compensation (**BC**) and contour hatch (**CH**) parameters ([Figure 5.4](#)). The total length of the laser paths in the layer l was calculated based on the ellipse circumference o and numbers of laser tracks N ([equation 5.4](#)). This approach takes account of the different cross-section of inclined struts.

$$E_{in} = E_{lin} \cdot l \quad (5.2)$$

$$E_{lin} = \frac{LP}{LS} \quad (5.3)$$

$$l = \sum_{i=1}^n o_1 + o_2 + \dots + o_n \quad (5.4)$$

$$o \approx \frac{\pi}{2} \left[a + b + \sqrt{2(a^2 + b^2)} \right] \quad (5.5)$$

$$a = \frac{d}{2}; b = \left(\frac{d}{2} \right) \cdot \cos(54,74^\circ) \quad (5.6)$$

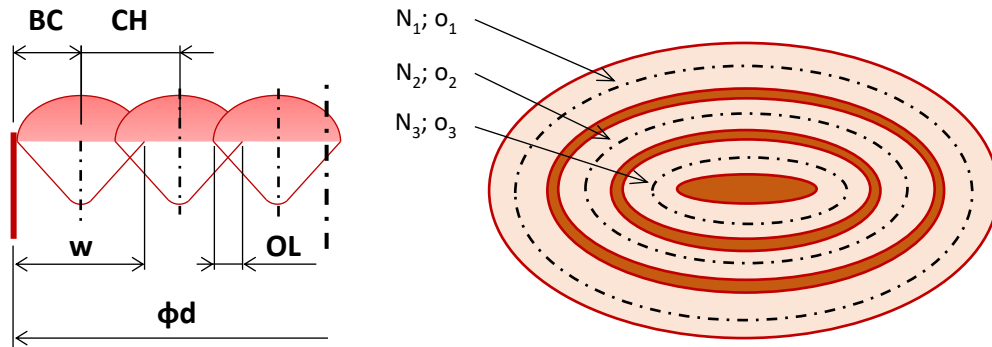


Fig. 5.4. Schema of the elliptic laser tracks trajectory

5.3.5 Strut shape analysis

To determine the real shape, dimensions and mechanical properties of the BCC lattice structure produced by SLM, O-series (lattice structure specimens) and TS-series (multi-strut tensile specimens) were analyzed by ATOS Triple Scan optical 3D scanner (GOM GmbH, Germany, MV170 lens). Due to the complex shape of lattice specimens, only four-corner struts could be digitized in the required quality.

The actual dimensions were measured by fitting the ideal cylinders and ellipses into the surface geometry in GOM Inspect software ([Figure 5.5](#)) - diameter d_{in} (inscribed cylinder) shows the largest diameter of homogeneous strut without geometrical imperfection and surface roughness; diameter d_{out} (circumscribed cylinder) defines the strut diameter including surface roughness and partially melted powder on the down skin strut surface; diameter d_{gauss} shows the value with the Gaussian distribution. To include the partially melted powder on the down skin side to the strut geometry, the ellipse geometry, which very well reflects the real shape of the strut cross-section, was used. Elliptical dimensions were measured in three

points on the single corner struts, and the average value was applied (Figure 5.5a). Measured diameters were used for the dimensional analysis of the lattice structure and for creation of real lattice structure geometry in FEA.

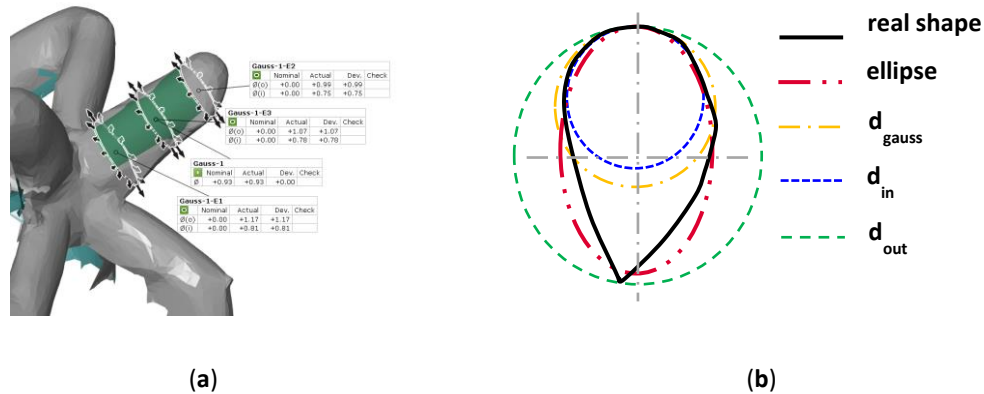


Fig. 5.5. (a) Measurement of the elliptical cross-section; (b) Visual 2D representation of elements used for dimensional struts analysis

5.3.6 Analysis of the strut inclination

The influence of the strut inclination on its cross-section dimensions was analysed using a special “cage” specimens (Figure 5.6). The shape is based on the micro-strut lattice unit cell which is composed of thin and short struts attached by two points to another unit cells. The cage specimens is composed of 13 struts in the diameter range between $d = 0.2$ and $d = 1.0$ mm in step 0.05 mm. The cage also protects struts during post-processing and measurement. The specimens were produced from AISi10Mg with inclination α in the range between of 0° and 90° . The specimens were digitized using Atos Triple Scan optical system and the struts dimensions were evaluated in GOM Inspect software, where the inscribe, Gfauss and circumscribed cylinders were fitted to digitized geometry.



Fig. 5.6. (a) Orientation of specimen with support structures; (b) Produced specimen fixed on the platform

5.3.7 Quasi-static mechanical properties analysis

Zwick Z020 device, a universal machine for mechanical testing with maximum force of 20 kN, was used for tensile (TS-series, TB-series) and compression testing (C-

series). Specimens were pre-loaded with of 20 N and further loaded with standard loading speed of $2 \text{ mm}\cdot\text{min}^{-1}$. During tensile testing, specimens were clamped into the jaws and loaded until all struts were broken. During compression testing, specimens were placed between two plates; the bottom one was fixed and the top one was sliding on the joint. Specimens were compressed to the first progressive collapse of the lattice structure. (Figure 5.7).

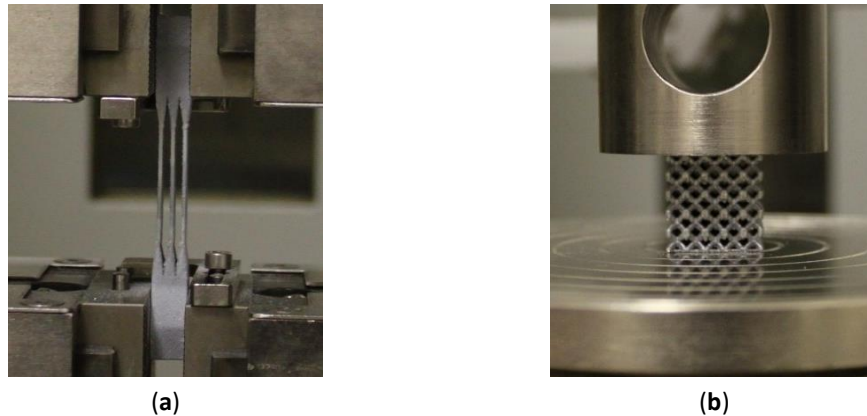


Fig. 5.7. Mechanical testing using Zwick Z020 machine (a) tensile test, (b) compression test

5.3.8 Low-velocity impact testing

Low-velocity impact testing of specimens of the IT-series was performed on the drop-weight impact tester developed at Brno University of Technology (Figure 5.8). The system is equipped with high-speed camera *Phantom V710* and strain-gauge (*XY31-3/120*). During impact testing, the weight of the falling head was $m = 7.252 \text{ kg}$ and the drop height was $h = 1 \text{ m}$. For these parameters, the falling head achieves the impact velocity $v_{in} = 3.2 \text{ m}\cdot\text{s}^{-1}$ with impact energy $E_I = 71.1 \text{ J}$.

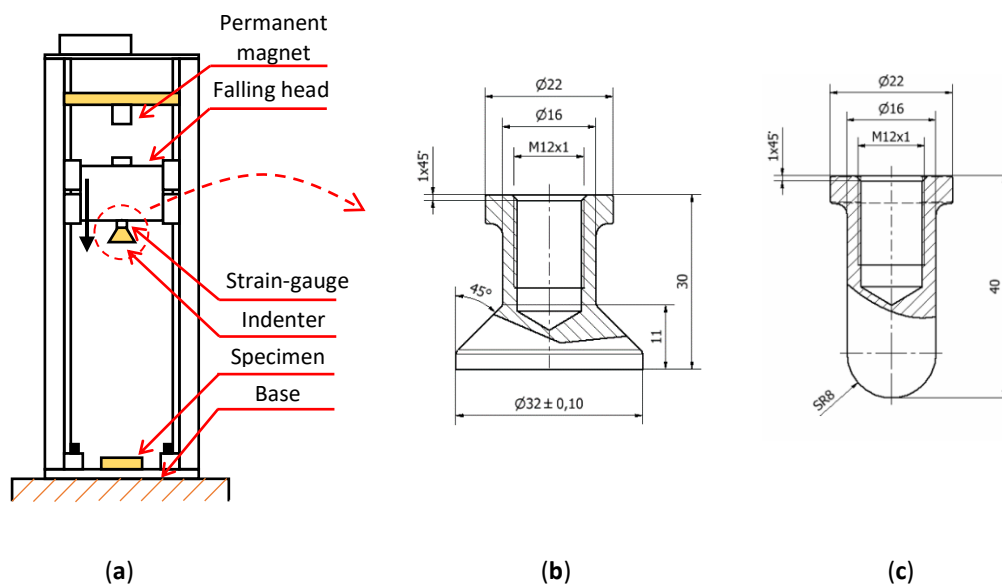


Fig. 5.8. (a) Low-velocity impact tester; (b) Geometry of the flat indenter; (c) Geometry of the ball indenter

5.4 Used SLM specimens

All specimens were manufactured using the SLM machine (SLM 280^{HL}, SLM Solution GmbH, Germany) equipped with 400 W YLR laser. The laser beam is focused to the diameter of 82 μm , has a Gaussian shape and works with a continuous wave. Laser scanning speed may reach up to 10.000 $\text{mm} \cdot \text{s}^{-1}$ and maximum build envelope is 280 x 280 x 350 mm. During the production process, N_2 atmosphere was used in the chamber and the oxygen level was kept under 0.2%. Before fabrication, the platform was pre-heated to 150 $^\circ\text{C}$.

5.4.1 Single welds specimens

To prepare real conditions during layer by layer production, single welds were produced on the top of 5 mm solid material block (Figure 5.9a). The influence of the laser direction on the single welds condition was also observed; therefore, all single welds were produced in and against atmosphere flow direction (Figure 5.9b). The top view images of the welds were obtained with a light microscope (Olympus SZX7, Olympus) for the visual evaluation of the continuity and uniformity and for the weld width measurement (Figure 5.9c). The weld width was measured in six points along each single weld and one average value was used. For the experiment, the following process parameters were changed – **LP** in the range from 175 to 400 W in steps 25 W and **LS** in the range from 200 to 2000 $\text{mm} \cdot \text{s}^{-1}$ in steps 100 $\text{mm} \cdot \text{s}^{-1}$. Finally, 120 pairs of single welds were analysed.

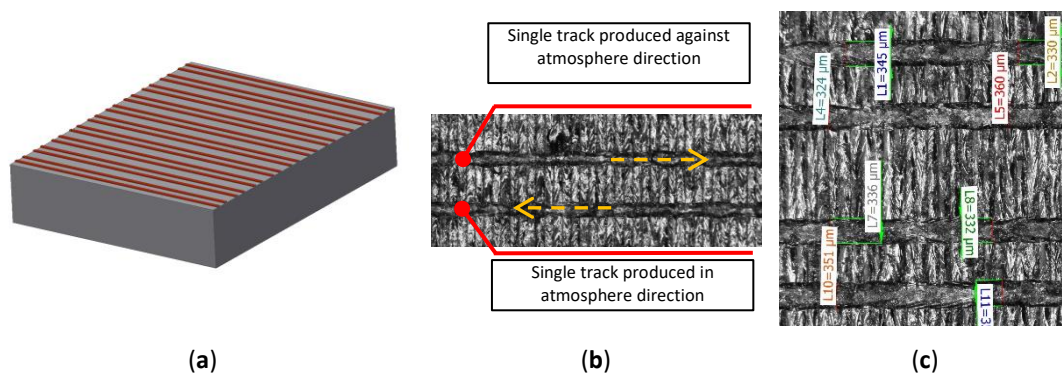


Fig. 5.9. (a) Shape of the single-track weld specimen; (b) measurement of the width of the single welds; (c) One combination of process parameters produced in and against atmosphere flow

5.4.2 Struts specimens I

The struts specimens were designed with respect of the future metallographic analysis as a group of 5 struts with a common base plate and a thin mid-wall in the bottom part. The mid-wall allows for control of the position of the grinding plane during metallographic analysis (Figure 5.10a). Based on the results of single welds in the range between 145 and 401 μm , a larger diameter $d = 2 \text{ mm}$ was chosen to ensure the possibility to analyse the overlap parameter in the range from **OL** -50% to **OL** 50% of width of the single weld (Figure 5.10b). The specimens were produced in two inclinations **OR** 90 $^\circ$ and **OR** 35.26 $^\circ$ compared to the platform. A beam compensation parameter (**BC**, Figure 5.4) was applied as a half of the weld width. Laser process parameters were changed as follows – **LP** in the range from

225 to 350 W and LS in the range from 400 to 2000 mm. s^{-1} . In this experiment, the laser contour strategy was tested. Table 5.1 shows a comparison with the standard laser strategy from SLM Solution company.

Tab. 5.1 Comparison of different laser strategies applied on thin struts - the developed contour strategy and standard SLM strategy

d (mm)/strategy	0.5 mm	0.6 mm	0.7 mm	0.8 mm	0.9 mm
Contour					
Standard					

5.4.3 Struts specimens II

For the second strut experiment, the same shape of the specimens as in the previous test was used. The process parameters were selected: LP in the range from 225 W to 400 W and LS in the range from 500 mm. s^{-1} to 2000 mm. s^{-1} . The process parameters were selected to obtain the influence of LS and LP on the porosity and surface roughness. The struts specimens with only OR 35.26° were used. The specimens were analysed using μ CT to obtain more accurate results of internal porosity in whole struts volume and full surface data for down-skin surface roughness evaluation.

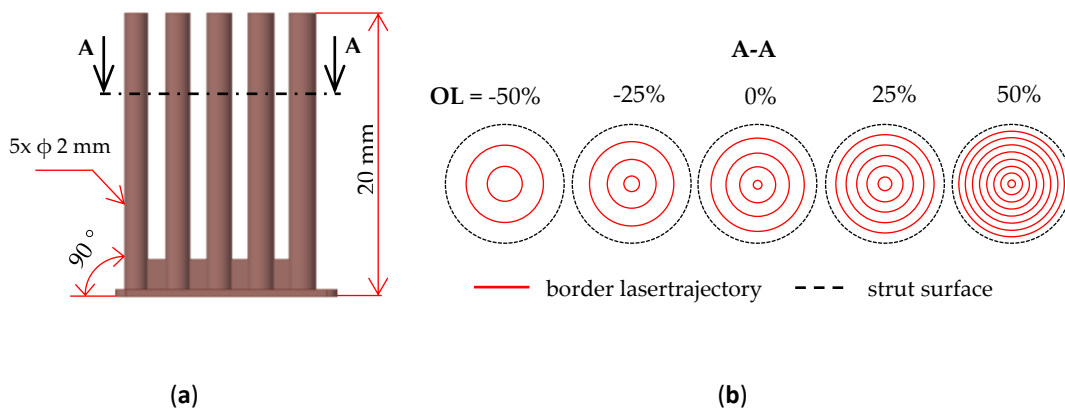


Fig. 5.10. (a) Shape of the specimen shapes with inclination of 90°; (b) used overlap strategy

5.4.4 Tensile specimens

Mechanical properties of thin struts (the base element of the lattice structure) are highly affected by the surface roughness and the internal material porosity which locally reduces the strut cross-section and mechanical properties [14]. To reflect it in the material model, the multi-strut shape of tensile specimens was designed for quasi-static mechanical testing (TS-series; Figure 5.11b). The multi-strut specimens

were composed of 12 struts with diameters of $d = 0.8$ mm and strut lengths of $l = 29$ mm and were fabricated in the inclinations of **OR** 90° and **OR** 45° relative to the platform. To compare the struts and bulk mechanical properties, standard bulk material specimens (TB-series; Figure 5.11a) were also fabricated in the same inclinations. All specimens were tested in the as-build condition.

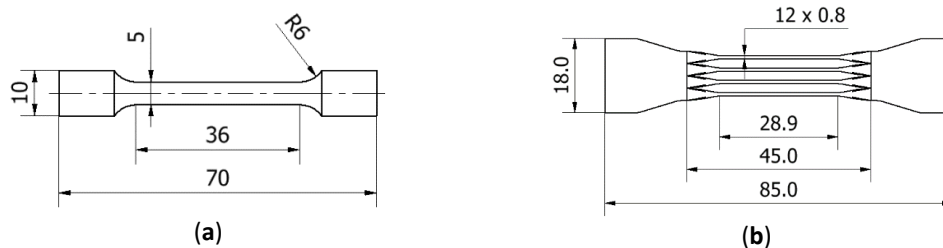


Fig. 5.11. Specimens for (a) quasi-static tensile testing of bulk material (TB-series); (b) quasi-static tensile testing of multi-strut specimens (TS-series)

5.4.5 Lattice structure specimens for quasi-static and low-velocity mechanical testing; Lattice structure specimens for shape and dimensions analysis

The BCC lattice structure specimens with dimensions of $20 \times 20 \times 20.8$ mm were used for quasi-static compression test (C-series; Figure 5.12a). The BCC unit cell was composed of eight struts with diameter $d = 0.8$ mm and side length $a_{BCC} = 4$ mm. On the bottom and the upper side, the specimens were covered with thin plates $t = 0.3$ mm. For low-velocity impact testing, specimens with dimensions of $20 \times 20 \times 16.8$ mm and with the same shape of the unit cell were used (IT-series; Figure 5.12a). To verify the material model based on mechanical properties found in quasi-static testing, the specimens for low-velocity impact testing with diameters of 0.6, 0.8, 1.0, 1.2 mm were also produced.

The specimens for the shape analysis were similar to those for mechanical testing, but without the upper plate for better access to the lattice structure core during the optical measurement process (O-series; Figure 5.12b).

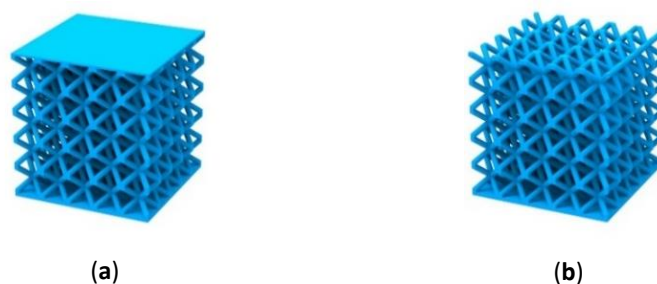


Fig. 5.12. Specimens for (a) quasi-static compressive (C-series) and low-velocity impact testing (IT-series); (b) optical analysis (O-series)

5.5 FEM numerical model

The numerical model of low-velocity impact test was created in ANSYS Workbench 18.2 software, module Explicit dynamic. Based on previous studies [37, 38, 42], the

material model *Bilinear isotropic hardening* was selected for definition of mechanical properties of lattice structure core. The geometry was composed of five bodies according to Figure 5.13 where the body (3) represents the lattice structure core; bodies (2) and (4) represent the bottom and upper plates of the specimen; the body (1) is the indenter, and the body (5) is a solid base. Input parameters for definition of the material model of lattice structure core were determined from quasi-static tensile and compression tests of TS- and C-series. The material model of plates was determined from the tensile test of bulk material (TB-series). The core material model was also supplemented with the criterion of damage obtained from the lattice quasi-static compression test. The used limit value corresponds with strain at the maximum stress point ($\epsilon_{\sigma_{max}}$) before the progressive collapse of the lattice structure. For the indenter and the base body, the standard *Structural Steel* material model was used; in the case of the indenter with rigid behaviour.

The constraints were based on a quarter symmetry in x and y directions. From the bottom to the top (Figure 5.13a), between the base (5) and the bottom plate (4), the frictional contact with static frictional coefficient (0.61) and dynamic frictional coefficient (0.47) were defined. The bottom and upper plates (4, 2) are connected with the lattice core (3) by the bonded contacts. Body self-interaction was involved. To achieve a comparable result with the experiment, only the base body (5), which represents the base plate in the testing device, was limited in x , y , z direction (rotation was not suppressed). To define the load, parameters of the low-velocity impact experiment were used. The falling head ($m = 7.25 \text{ kg}$) was represented by the indenter of equal weight. The impact velocity was determined using a high-speed camera as $v = 3.1 \text{ m} \cdot \text{s}^{-1}$. For all bodies, the standard gravity acceleration $g = 9.806 \text{ m} \cdot \text{s}^{-2}$ was adopted.

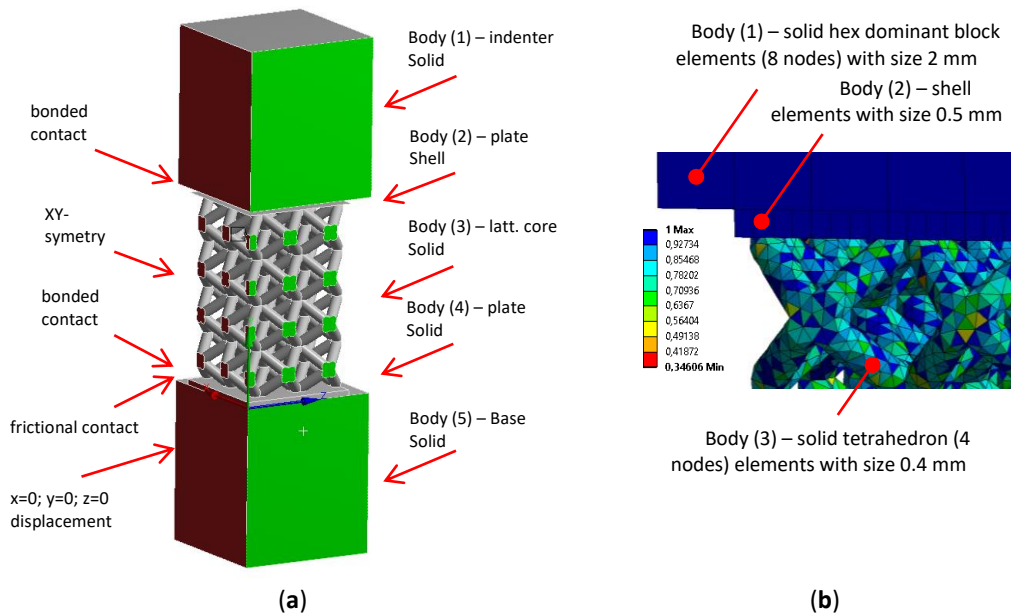


Fig. 5.13. Numerical model in the Ansys software (a) quarter model with bodies and constrains; (b) finite element mesh quality

A finite element mesh was created with several element types (Figure 5.13b) – the base and indenter bodies (1, 5) were formed by Hex dominant block elements (8 nodes) with the size of 2 mm, the bottom plate (4) with Hex Dominant block elements (8 nodes) with the size of 1 mm, the lattice core (3) with solid Tetrahedron elements (4 nodes), which also well represent surface roughness of the struts (Figure 5.13b). Their size was managed according to the nominal diameter of struts and the mesh quality parameter. In the case of circular cross-section with diameter $d_r = 0.95 \text{ mm}$, the tetrahedron element size was 0.4 mm. The shell elements with the size of 0.5 mm were used for the upper plate (2) because, if the solid Hex Dominant block elements (8 nodes) were used, the error energy (hourglass energy) caused by element nodes shifting can occurs.

6 RESULTS

6.1 Construction of experimental device – The drop weight impact tester

In order to use the SLM lattice structure as the energy absorber, it is necessary to understand the mechanism of deformation under different types of loading (local, surface) and to describe their mechanical properties.

For this purpose, based on the previous studies, a drop-weight impact test device was designed to measure all the necessary values during the impact test of lattice structure and to describe the deformation process of the lattice structure material. The advantages of the device are its compact dimensions and sufficient impact energy for testing purposes. A disadvantage, compared to other types, are energy losses in linear guides during the drop of the loading element.

6.1.1 Description of the experimental device

The above testing device was designed based on the studies [37, 38], where the authors tested the impact resistance of the porous material under local impact loading (break through the porous material). During penetration of the ball's indenter into the porous material, the reaction force was measured using a strain gauge.

The same drop-weight principle was used for our experimental device; therefore, it belongs to the low-velocity category. The impact energy is supplied by a simple change of potential energy to an impact energy of the falling head during its fall (equation 6.1).

$$\frac{1}{2}mv^2 + E_t = mgh \quad (6.1)$$

where m (kg) is the mass of the falling head, v ($m.s^{-1}$) is the falling head velocity just before the impact, E_t (J) is wasted energy due to friction, h (m) is the height of fall, and g ($m.s^{-2}$) is gravitational acceleration.

The impact tester consists of two main parts (Figure 6.1) – the frame and the falling head. *The frame* is composed of the bottom steel plate, aluminium profiles with linear guides and the upper aluminium plate. The bottom base plate is made of massive steel $t = 20$ mm which is also fixed to a steel fixing plate in the laboratory floor. The sufficient stiffness of the base plate is important to eliminate its deformation during impact testing of the specimens. The aluminium profiles ensure a lower stiffness which allows for a small deformation of the guides; therefore, during linear motion, high friction losses are not created.

The falling head (FH) consists of several parts (Figure 6.2) – the base, weights, strain - gauge (deformation member), indenter and carriage of the linear guides. The base is a machined aluminium part with two screwed pins for placement of weight. On the *FH*, it is possible to place 10 pieces of the sheet plate $t = 6$ mm weights; each of them weighs 0.5 kg. The deformation member is made of aluminium alloy EN AW 7075 and fitted with four full-bridge HBM XY31-3/120 strain gauges. The deformation member was designed for maximal load of 20 kN using FEA. The indenter is a hard steel part which is screwed directly into the strain gauge. Depending on the

performed test, "tip" or "plate" type of the indenter may be used. For the shape of the "tip" body, theoretical point load of the lattice structure will be observed. In the case of the "plate" body, the surface load will be observed (Figure 6.3b).

The impact energy of the device is managed by the number of weights along with the height adjustment of *FH*. The maximum theoretical impact energy of the experimental device is 120 J with the weight of 12.25 kg and the height of fall $h = 1\text{ m}$.

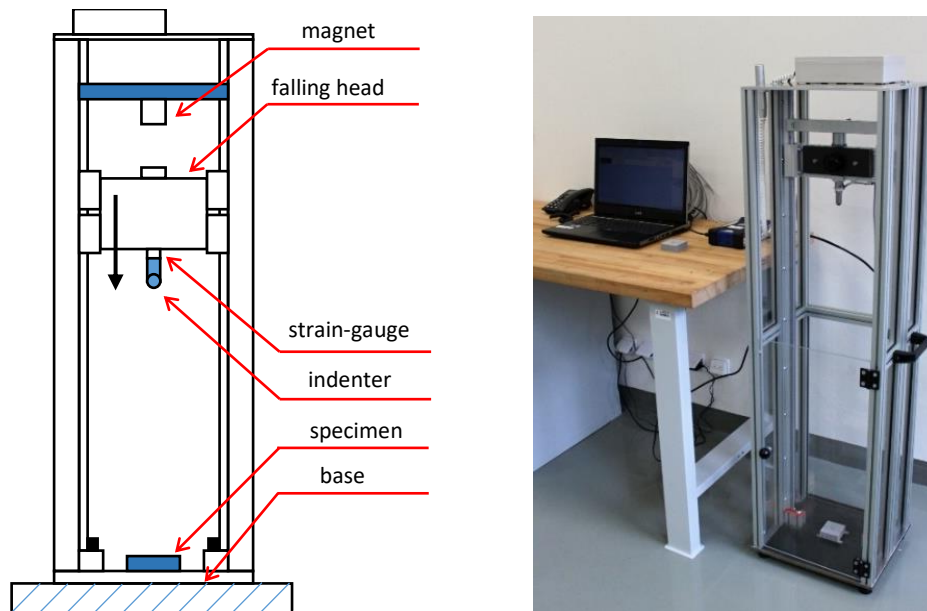


Fig. 6.1. Experimental device for impact tests

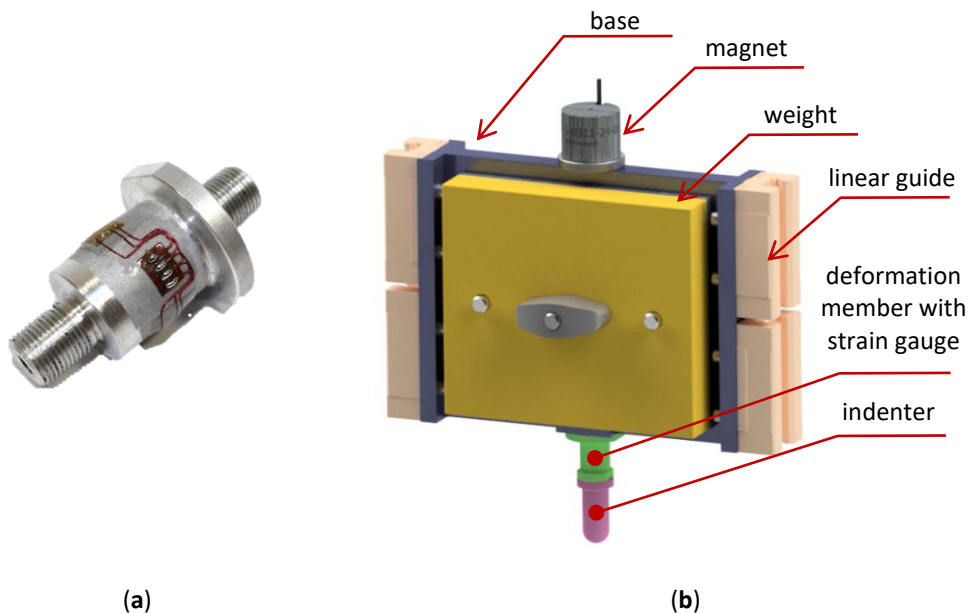


Fig. 6.2. (a) The deformation member with strain gauges; (b) The Falling head

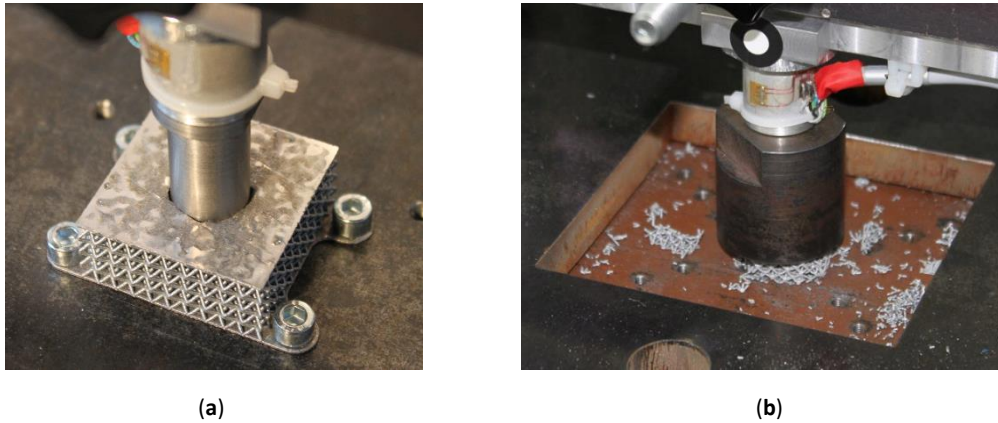


Fig. 6.3. (a) impact resistance testing; (b) fast compression test

6.1.2 Design of the measuring chain

To verify the correct results of the strain-gauge, it was calibrated by the universal device for mechanical testing - Zwick Z020. The load was increased up to 20 000 N, by step 1000 N. The results showed that the linearity has been confirmed in the entire range. For strain-gauge setup in measuring software, the calibration [equation 6.2](#) was obtained:

$$F = -22797 \cdot U + 2695,3 \quad (6.2)$$

Next, several dozens of tests were carried out in the configuration of the strain gauge, accelerometer, and high-speed camera where the deviations of the values of the individual sensors were examined. The results confirmed the correct measurement of the strain-gauge even during the impact loading (force impulse) and the need to add a high-speed camera to the measuring chain. An accelerometer is not needed due to satisfactory results obtained from the strain-gauge. The final measuring chain is shown in [Figure 6.4](#).

During impact measurement, the obtained values from the strain-gauge are recorded using a QuantumX MX410B measuring station at a sampling frequency of 96 kHz. A high sampling frequency is needed because the impact duration is in the order of 10^{-3} s. Data from the high-speed camera Phantom V710 were recorded in Phantom software with a maximal sampling frequency of 48 kHz because higher sampling frequencies allow for measurements across only a very small area.

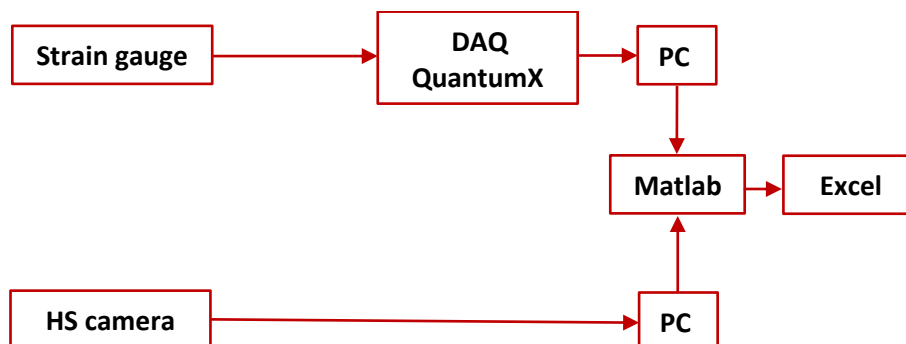


Fig. 6.4. Scheme of measuring chain

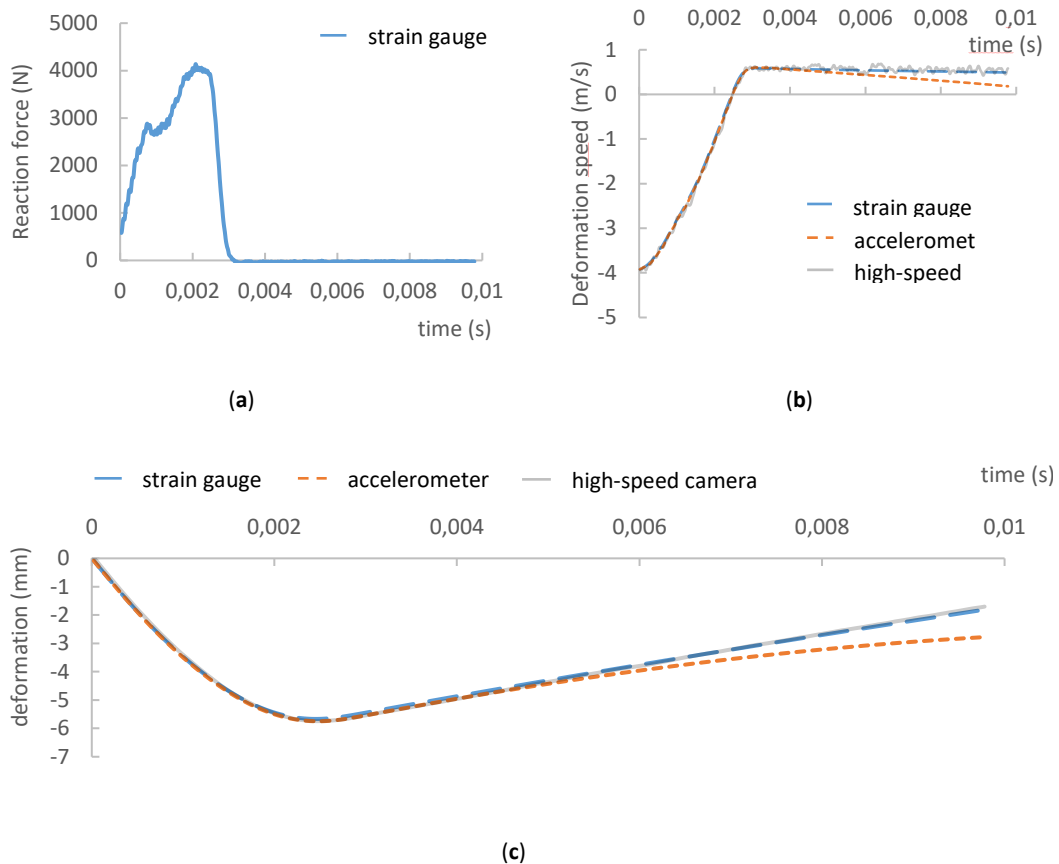


Fig. 6.5. (a) Data recorded from strain gauge, (b) Integration of deceleration a ($\text{m}\cdot\text{s}^{-2}$) by time t (s), (c) Second integration of deceleration path a ($\text{m}\cdot\text{s}^{-2}$) by time t (s)

6.1.3 Data processing software in MATLAB

Mechanical properties of the lattice structure were estimated based on kinematic characteristics of the impact test. To effectively evaluate data records from HS camera and strain-gauge and to achieve high accuracy of the results, the semi-automatic software was created in MATLAB. The final output are the dependences of position, speed, acceleration and force on time and deformation in the excel file.

The software combines the data on the position (HS camera) and force (strain gauge) in time. These data are used for creation of the base dependences and for calculation of another kinematic characteristic. Using both records jointly, the cumulative errors caused by double-integration were eliminated.

Image analysis

A set of 8-bit images from the **HS** camera with stuck round target on the falling head (Figure 6.3b) is used to estimate the trajectory of the falling head. The images were captured especially shortly before, during, and shortly after the impact with 48 kHz frequency. The images from the **HS** camera are relatively noisy due to high ISO; therefore, it was necessary to use a large round target of approx. 10 mm (50 px in diameter in the **HS** image). Further, the image analysis was used to find the target

centre position in every image - the following steps were carried out during software calculation:

- **Conversion of the colour image** to the grayscale image (8-bit)
- **Image crop** - Because of high capturing frequency, the target position change between the frames is low. Therefore, the position of the target centre from the previous image is used to crop the image to the size of 104 x 120 px. It significantly saves the computation time and contributes to better reliability.
- **Application of the Canny edge detection** - Canny edge detector [61, 62] was chosen to binarize the images. The standard deviation of the Gaussian filter is set to $\sqrt{2}$ to reduce the image noise by blurring of the image, the sensitivity is set by the user as one of the parameters prior to the calculation.

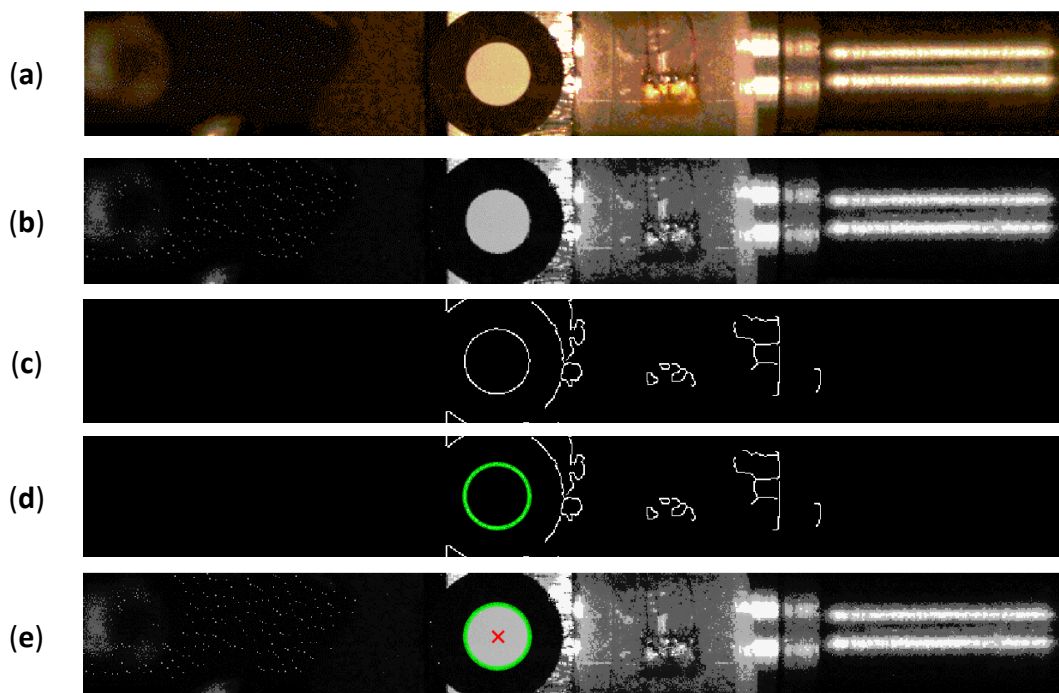


Fig. 6.6. Image analysis (a) 8-bit colour image; (b) 8-bit grayscale image; (c) Canny edge detector application; (d) Target boundary classification; (e) Ellipse fitting - target centre coordinates computation

- **Boundary line thinning and selection** – Also a part of Canny edge detection
- **Classification of connected edges according to their properties** - the aim is to find an ellipse-shaped object which fulfils the user-defined values of following criteria in the binary images:
 - o Minimum length of the major axis
 - o Minimum length of the minor axis
 - o Maximum convex area to filled area ratio
 - o Maximum residual of the fit of the best-fit ellipse

If an edge fulfils all the criteria, it is considered as the target boundary. If no target is found (or two or more targets are found), the centre position is neglected.

- **Data interpolation** – The linear data interpolation was used to find the position in case of neglecting the image in the previous step. Finally, all the data were interpolated to reach the 96 kHz sampling frequency of images (elimination of different data sampling frequencies -*HS* 48kHz, strain-gauge 96kHz)
- **Filtration** – To reduce the effects of noise, Savitzky-Golay filtering is carried out (frame length 51, polynomial order 3).
- **Calibration** – The calibration is carried out using two sets of images (at least 100 images each). The first set represents the zero position when the falling head is in the lowest position and the indenter is in contact with the base plate. The second set represents the calibration position when the object of known height h is inserted between the plate and falling head, and it is in contact with calibration object. The averaged target position of zero position $\bar{X}_0 = [\bar{x}_0; \bar{y}_0]$ and of calibration position $\bar{X}_1 = [\bar{x}_1; \bar{y}_1]$ were found. As the falling head moves on the straight line parallel to the y axis, the px to mm ratio k is computed as follows:

$$(\bar{y}_1 - \bar{y}_0) \cdot k = h \quad (6.3)$$

- **Position data transformation** – The position data in pixels were transferred to millimetres using [equation 6.3](#). During transformation, the x position is neglected and the basis (\bar{y}_0) is subtracted.

Strain - gauge data processing

The data from the strain-gauge are recorded with 96 kHz frequency for 1.5 seconds. The measurement starts when the measured force underflows the threshold value of 50N. Data processing is carried out in the following steps:

- **Filtration** – to reduce the effects of noise, the Savitzky-Golay filtration is used (frame length 21, polynomial order 3)
- **Initiating Impact Index determination** –the index where the measured force overflows the threshold (100 N) for the first time
- **Impact Ending Index determination** – the index beyond the initiating index where the measured force underflows the threshold (100 N).
- **Data cropping** – Only the data between the initiating and ending indexes are further processed

Kinematic characteristics computation

Kinematic characteristics are computed in the following steps:

- **Association of the reaction force data with the timescale, calculation of the impact duration** – The impact duration is the period when the strain-gauge records the reaction force during the experiment. This time and the timescale

of the strain-gauge data are computed based on the strain-gauge sampling frequency. The reaction force data are associated with the timescale.

- **Acceleration data computation, association with the timescale** – The acceleration is computed by dividing the reaction force data by the weight of the falling head. The acceleration data are assigned to the timescale.
- **Associating the trajectory data from the camera with the timescale** – The impact starts when the indenter hits the specimen (threshold 100 N). In the data from the *HS* camera, the nearest data specimen index, where the position of the falling head is equal to the specimen height, is the initiating index. The ending index is determined based on the measured impact duration. Further, the data are associated with the timescale, and the specimen height is subtracted from it as a bias. From these data, the depth of the impact in the specimen can be calculated

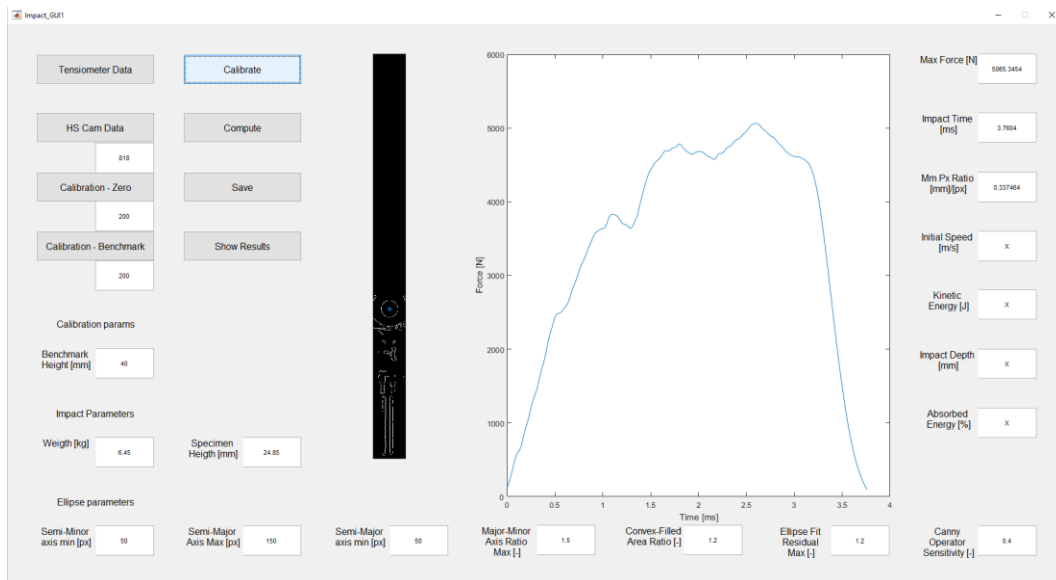


Fig. 6.7. Impact tester software GUI

- **Computation of the spike speed, kinetic energies** – Velocity of the falling head during the impact is calculated from the trajectory using the first numerical derivative – central difference. The data are filtered using Savitzky-Golay filter (frame length 51, polynomial order 3). Kinetic energy of the falling head before the impact is calculated based on the average velocity obtained from 100 values directly before the impact. Kinetic energy of the falling head after the impact is calculated based on the average velocity obtained from 100 values shortly after the impact. From the difference between E_i and E_{out} , the absorbed energy is calculated.
- **Computation of the trajectory data from the acceleration data (validation)** – To check the validity of the calculations based on the image analysis, a trajectory is also calculated from the acceleration data (derived from the force

data measured by the strain-gauge) using double numerical integration. The constants of the integration initial position ($x=0$) and initial velocity from the **HS** camera are used to reduce the deviation. The data are associated with the timescale and plotted against the trajectory derived from the **HS** camera. The deviation of the curves is calculated (the tolerance is assessed by the user). Finally, important kinematic characteristics are computed and validated. All the data are associated with the same timescale, so it is possible to draw desired graphs.

6.1.4 GUI and Results

The GUI was created to make the software more user-friendly. It allows the user to insert all the important data, start the computation and check or save the results (Figure 6.7). These results were used to confirm a developed numerical model in published Paper B.

6.2 Laser strategy for lattice structure fabrication - Paper A

6.2

The SLM technology is a complex process which is defined by dozens of process parameters (laser speed, laser power, thickness of the powder bed layer, pre-heating temperature, atmosphere, etc.) and many types of laser tracking strategies. Simultaneously, the process parameters and laser strategy have a significant influence on the mechanical properties; their change can affect the resulting behaviour of the parts.

Due to a high number of possible combinations of SLM process parameters, their optimisation for specific applications is very time-consuming and costly; therefore, in practice, one universal setup for all types of parts is used; it is usually appropriate for 80% of them. However, the lattice structure is a complex shape, often composed of thin struts, and if the universal process parameters are used for fabrication, various imperfections can occur, e.g. improper dimension accuracy, internal porosity, roughness and depending on this also degradation of mechanical properties. Therefore, a unique contour SLM strategy was developed for lattice structure production along with a set of process parameters. The advantage of the contour strategy is that the strategy is managed only with laser power, laser speed, and contour hatch distance. Due to this, it is possible to keep constant condition using various combination of **LP** and **LS** process parameters and to produce a lattice structure with expected material and mechanical properties in high dimensional accuracy.

In this chapter, only the main results will be presented. All results and conclusions can be found in the attached full-test Paper A.

6.2.1 Single weld test

The results of the width of the single tracks welds experiment are shown in Figure 6.8. The values were averaged from six measurements against and six measurements in the atmosphere flow direction. The values marked with red colour were excluded due to the worse quality of the welds (nonuniformity of width and insufficient

continuity). Based on the weld quality, the limit value of $E_{lin} = 0.25 \text{ J.mm}^{-1}$ was found for continuous welds by [equation 6.4](#).

$$E_{lin} = LP/LS \tag{6.4}$$

6.2.2 Struts experiment I

From the perspective area below (coloured green), 16 combinations of process parameters were selected for the following initial struts experiment. The initial strut experiment was aimed at finding the optimal overlap (**OL**) between the neighbouring laser welds according to the initial porosity analysis using the image analysis of top view captures from a light-microscope. In the experiment, specimens were produced in two inclinations (**OR**) according to the platform during SLM production. For evaluation of the most appropriate **OL** value, a dependence of the porosity vs. input energy E_{in} was used.

w (µm)		Laser speed (mm/s)																				
E_{lin} (J/mm)		200	300	400	500	600	700	800	900	1000	1100	1200	1300	1400	1500	1600	1700	1800	1900	2000		
Laser power (W)	175	354	310	261	290	246	221	214	199	223												
		0.88	0.58	0.44	0.35	0.29	0.25	0.22	0.19	0.18												
	200	401	343	303	286	317	271	240	210	201	210											
		1.00	0.67	0.50	0.40	0.33	0.29	0.25	0.22	0.20	0.18											
	225	374	309	271	255	214	203	199	174	163	145											
		0.75	0.56	0.45	0.38	0.32	0.28	0.25	0.23	0.20	0.19											
	250	344	314	270	253	233	223	201	180	161	163	159										
		0.83	0.63	0.50	0.42	0.36	0.31	0.28	0.25	0.23	0.21	0.19										
	275	380	346	332	289	262	277	235	227	221	201	149										
		0.69	0.55	0.46	0.39	0.34	0.31	0.28	0.25	0.23	0.21	0.20										
	300	305	325	308	267	260	232	223	202	211	193	183	192	186								
		0.75	0.60	0.50	0.43	0.38	0.33	0.30	0.27	0.25	0.23	0.21	0.20	0.19								
	325	333	316	275	274	262	258	207	199	200	196	189	176	145								
		0.65	0.54	0.46	0.41	0.36	0.33	0.30	0.27	0.25	0.23	0.22	0.20	0.19								
	350	358	336	328	317	300	261	259	259	205	200	199	209	205	352							
		0.70	0.58	0.50	0.44	0.39	0.35	0.32	0.29	0.27	0.25	0.23	0.22	0.21	0.19							
375	317	308	201	372	370	272	267	250	287	230	237	239	223	217								
	0.63	0.54	0.47	0.42	0.38	0.34	0.31	0.29	0.27	0.25	0.23	0.22	0.21	0.20								
400	357	332	358	301	273	234	236	223	214	206	223	216	212	201	210							
	0.67	0.57	0.50	0.44	0.40	0.36	0.33	0.31	0.29	0.27	0.25	0.24	0.22	0.21	0.20							

Fig. 6.8. The average width of the single welds (coloured cells); Line energy (colour-free cells)

In the charts above, three groups of porosity (three types of symbol in charts) regarding the **OL** parameter were identified in both cases of struts inclination ([Figure 6.9](#)). The data were interpolated with quadratic polynomial function, and the minimum of the porosity function was determined (black cross in chart). The position of the crisis is placed in area of the **OL** 25% groups in both cases; therefore, it was selected as the optimal value for struts production.

6.2.3 Struts experiment II

The aim of the following struts experiment was mainly a profound analysis of the internal porosity and surface roughness using μ CT technology, and determination of the effects of individual laser parameters **LS** and **LP** on the occurrence of the imperfections.

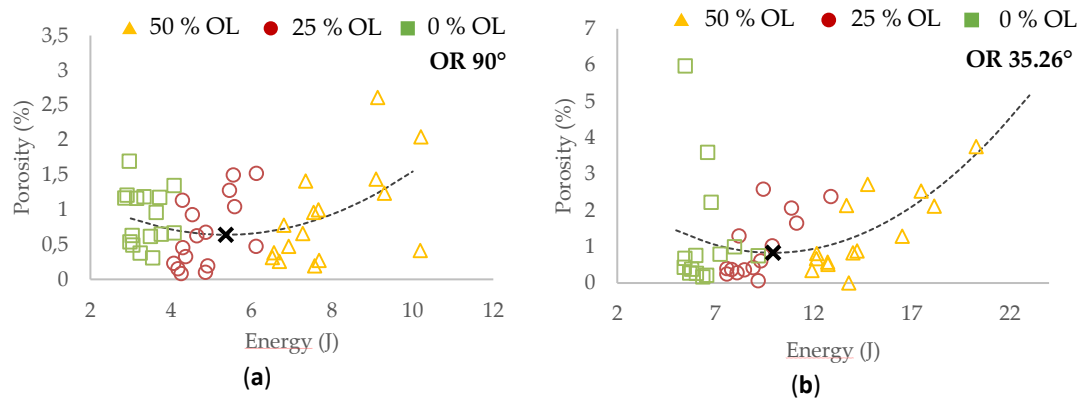


Fig. 6.9. Porosity vs. input energy dependence (a) for inclination 90°; (b) for inclination 35.26°

Porosity analysis

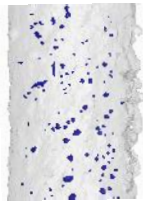
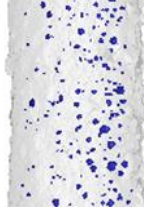
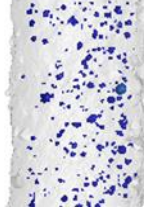
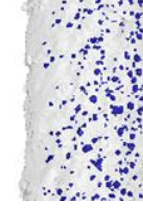
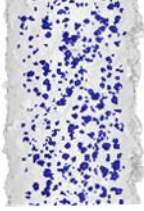
The dependence of the internal porosity measured by μ CT vs. input energy E_{in} generally shows a similar trend as in the initial results of the previous experiment. However, in this case, a significant cumulation of results at the porosity level 0,4% occurs in the range for E_{in} of $8 \div 10$ J and for E_{lin} of $0.15 \div 0.4$ J.mm⁻¹ (Figure 6.10). Even though the low porosity level of linear energy E_{lin} in the range $0.15 \div 0.25$ J.mm⁻¹ is this area is also unsuitable due to the creation of a small number of large irregular pores (Table 6.1). They decrease the strut cross-section, create stress concentrators, and finally, significantly affect mechanical properties.

Regarding the dependencies in Figure 6.10, the parameters LP of $225 \div 275$ W, LS of $900 \div 1400$ mm.s⁻¹ with E_{in} of $8 \div 10.5$ J, E_{lin} of $0.25 \div 0.4$ J.mm⁻¹, and OL 25% were selected as perspective ones from the porosity point of view.

Table 6.1 shows the 3D images of the μ CT analysis with various shapes and levels of porosity. Based on these results, the required minimum values of linear energy E_{lin} of 0.25 J.mm⁻¹ and input energy E_{in} of 8 J were identified for strut production without creating of large irregular pores. The results of these images confirm the charts in Figure 6.10.

Tab. 6.1 The porosity level of the strut specimens—3D renders with pores shape; the pores in the entire volume were projected to the plane of the view

LP 225 W	LP 250 W	LP 300 W	LP 350 W	LP 400 W
LS 1200 mm.s ⁻¹ E_{in} 7.28 J E_{lin} 0.19 J.mm ⁻¹	LS 1400 mm.s ⁻¹ E_{in} 9.17 J E_{lin} 0.18 J.mm ⁻¹	LS 500 mm.s ⁻¹ E_{in} 13.54 J E_{lin} 0.6 J.mm ⁻¹	LS 500 mm.s ⁻¹ E_{in} 15.43 J E_{lin} 0.7 J.mm ⁻¹	LS 1700 mm.s ⁻¹ E_{in} 7.56 J E_{lin} 0.24 J.mm ⁻¹
Por. - 0.17 %	Por. - 0.27 %	Por. - 1.38 %	Por. - 2.26 %	Por. - 0.63 %

LS 700 mm.s ⁻¹ <i>E_{in}</i> 9.02 J <i>E_{lin}</i> 0.32 J.mm ⁻¹	LS 700 mm.s ⁻¹ <i>E_{in}</i> 9.84 J <i>E_{lin}</i> 0.36 J.mm ⁻¹	LS 900 mm.s ⁻¹ <i>E_{in}</i> 9.37 J <i>E_{lin}</i> 0.33 J.mm ⁻¹	LS 1100 mm.s ⁻¹ <i>E_{in}</i> 8.91 J <i>E_{lin}</i> 0.32 J.mm ⁻¹	LS 900 mm.s ⁻¹ <i>E_{in}</i> 10.17 J <i>E_{lin}</i> 0.44 J.mm ⁻¹
				
Por. - 0.17%	Por. - 0.31%	Por. - 0.42%	Por. - 0.43%	Por. - 0.81%

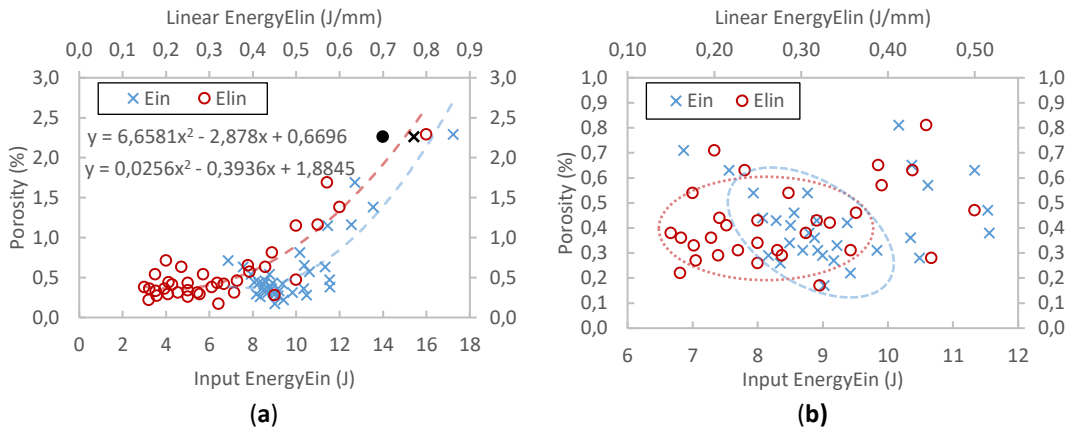


Fig. 6.10. (a) μ CT porosity vs. input and linear energy dependences, black mark represents the universal SLM process parameters; (b) focused area of results up to 1% porosity level with marked perspective areas.

The influence of the main process parameters **LS** and **LP** on porosity is presented in Figure 6.11. In the charts, the areas with stable and unstable results of porosity can be identified. Based on it, a recommended range of the process parameters for struts production is consistent with stable areas.

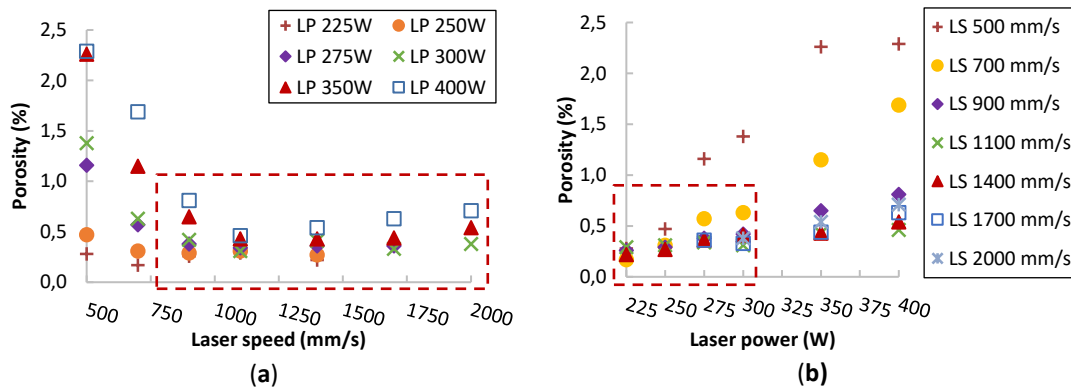


Fig. 6.11. (a) The influence of various **LS** levels on porosity; (b) The influence of various **LP** levels on porosity.

Surface roughness analysis

To digitized strut surface, the μ CT analysis was used; therefore, it was possible to obtain the surface roughness on the side and also on the down-skin strut surface (Figure 6.12). The results show a lower roughness in the area with lower input and linear energy. It is mainly caused by transferring of heat energy to the surrounding powder and sticking of the partly melted particles on the down skin surface of the strut. The chart of surface roughness vs. linear energy E_{lin} dependence shows a significant linear trend of the strut-side roughness.

The best results were cumulated in ranges between E_{in} of $8 \div 10$ J and E_{lin} of $0.15 \div 0.4$ J.mm⁻¹ with the level of about Ra 30 μ m on the strut-side surface and about Ra 40 μ m on the down-skin surface.

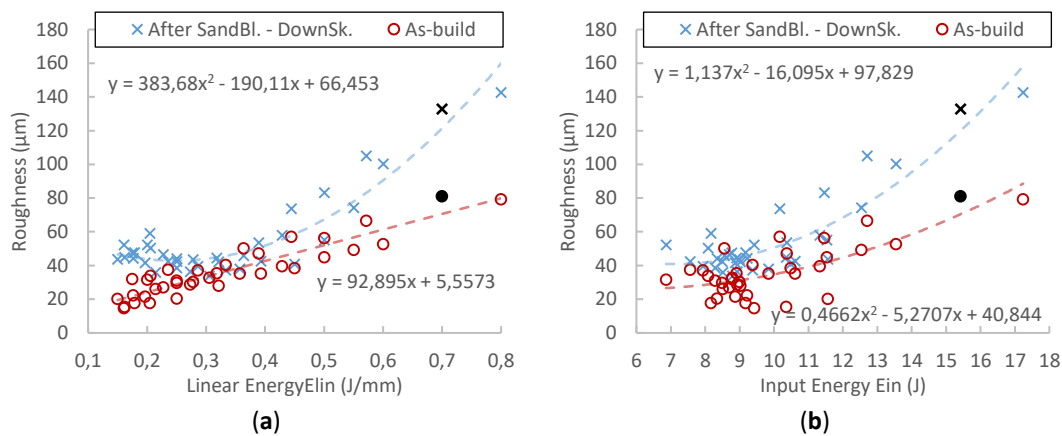


Fig. 6.12. (a) Surface roughness vs. linear energy dependence – on the side and down-skin struts surface, black marks represent the universal SLM process parameters.; (b) surface roughness vs. input energy dependence

The influence of the main process parameters LS and LP on surface roughness is presented in Figure 6.13. In the chart of LS vs roughness dependence, two linear trends can be identified. The recommended stable one is marked in the chart. In the chart of LP vs. roughness dependence, the trend is quite linear at all LP levels.

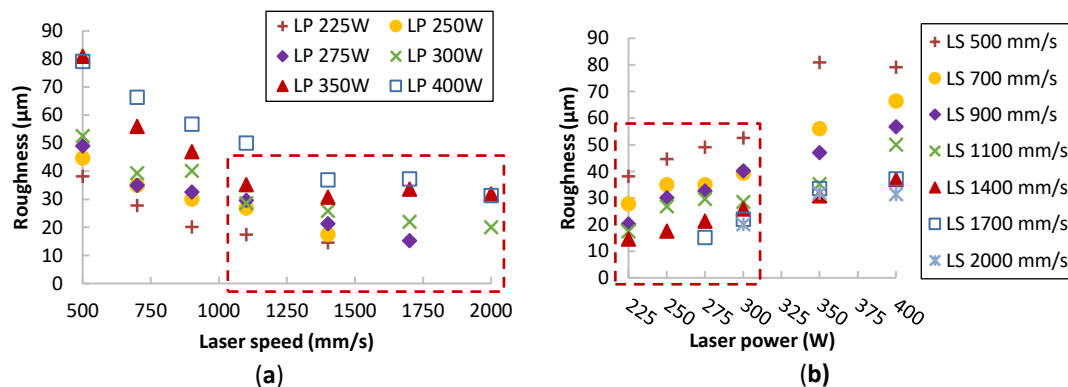


Fig. 6.13. (a) The influence of various LS levels on surface roughness; (b) The influence of various LP levels on surface roughness

Metallographic analysis

A metallographic analysis for evaluation of the microstructure was performed. Standard methods were used for metallographic specimen preparation, i.e. wet grinding and polishing with the use of diamond pastes. A microstructure of the struts was analysed in the etched state (Fuss etchant) and evaluated by metallographic light microscope (Olympus GX 51, Japan). Orientation of the micrographs is parallel to the strut axis (Figure 6.14a). The microstructure of the struts is inhomogeneous, consisting of single welds separated by fusion boundaries. Differences in the microstructure can be seen in the layers close to the down-skin surface of the struts (area B in Figure 6.14a) in comparison with the up-skin surface (area A). Different shapes of porosity depend on the E_{in} parameter. Due to overheating of the material, gas pores with a spherical shape were created (Figures 6.14b,c). No cracks were found in the microstructure of evaluated specimens.

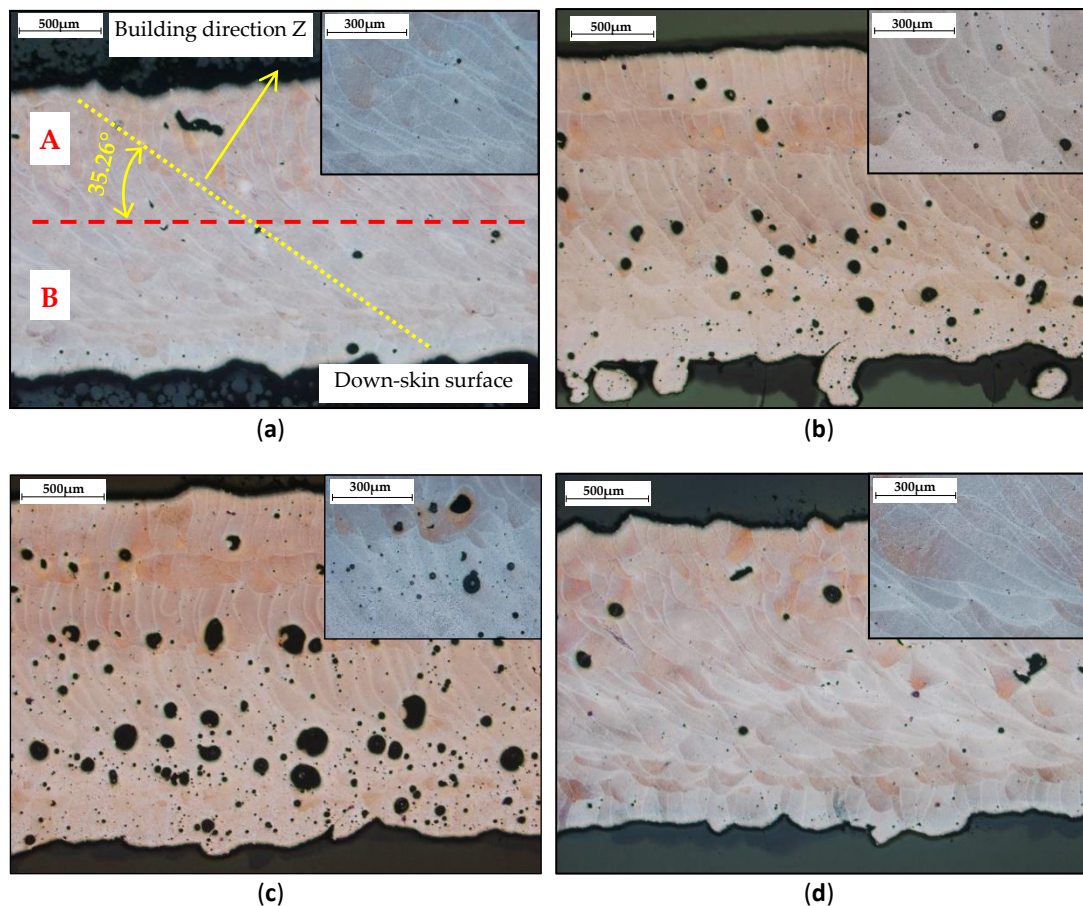


Fig. 6.14. Microstructure of the struts (a) LP of 250 W, LS of 1400 mm.s⁻¹, E_{in} of 9.17 J, E_{lin} of 0.18 J.mm⁻¹ with description common for all pictures; (b) LP of 300 W, LS of 500 mm.s⁻¹, E_{in} of 13.54 J, E_{lin} of 0.6 J.mm⁻¹ (c) LP of 350 W, LS of 500 mm.s⁻¹, E_{in} of 15.43 J, E_{lin} of 0.7 J.mm⁻¹; (d) LP of 400 W, LS of 1700 mm.s⁻¹, E_{in} of 7.56 J, E_{lin} of 0.24 J.mm⁻¹

6.3 Script for designing of the strut contour strategy

The main idea of developed contour strategy is to keep a constant overlap in all strut cross-sections during production of different struts diameters; i.e. between the

neighbouring laser welds but also in the centre of the struts. It is important to achieve a constant material and mechanical properties in the whole struts/lattice structure volume. Using only one universal laser strategy and one combination of process parameters is not possible, as is shown in Figure 6.15. For this purpose, the basic script was developed to allow for the selection of the most appropriate combination of process parameters for production of the required diameter and shape of lattice structure. This script also improves a dimensional accuracy [22] and can predict the porosity and surface roughness level .

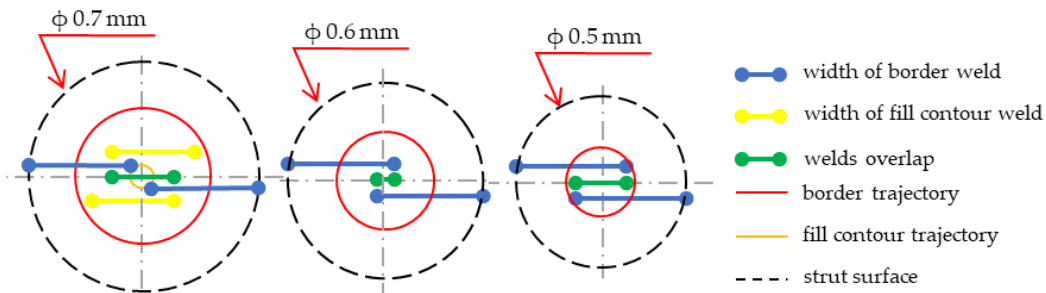


Fig. 6.15. SLM Solutions universal struts laser strategy

The example for strut diameter $d = 0.8$ mm is present in Figure 6.17. In the analysis, the recommended OL parameter in the range between of 25% - 35% was required in whole strut volume. In Figure 6.17, it is shown that this requirement is met only by a few recommended combinations from Paper A – for OL of 25%, it is a combination of $LP = 275$ W; $LP = 900$ mm.s⁻¹, $BC = 123$ μ m; $CH = 184$ μ m, $N = 2$; for $OL = 30\%$, it is a combination of $LP = 250$ W; $LP = 1000$ mm.s⁻¹, $BC = 90$ μ m, $CH = 124$ μ m, $N = 3$.

The script input parameters are the weld width, lattice structure geometry and main SLM process parameters such as laser power (LP), laser speed (LS) and layer thickness (LT). Based on input data, the script checks when an expected overlap is achieved in the centre of the struts, or the centre is re-melted (overheated; in the case of high OL parameter).

6.3.1 Algorithm of the contour strategy analysis

For fully-dense strut production, the script uses two approaches of contour strategy generation according to the strut dimensions and the used weld width - Elliptical/circular single tracks; Elliptical/circular and line single tracks (Figures 6.16 and 6.18).

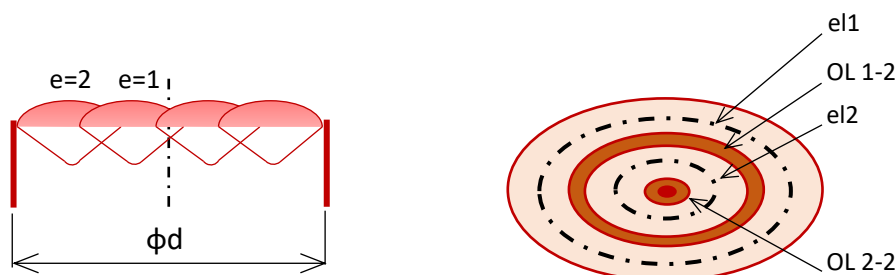


Fig. 6.16. Schema of elliptical/circular strategy

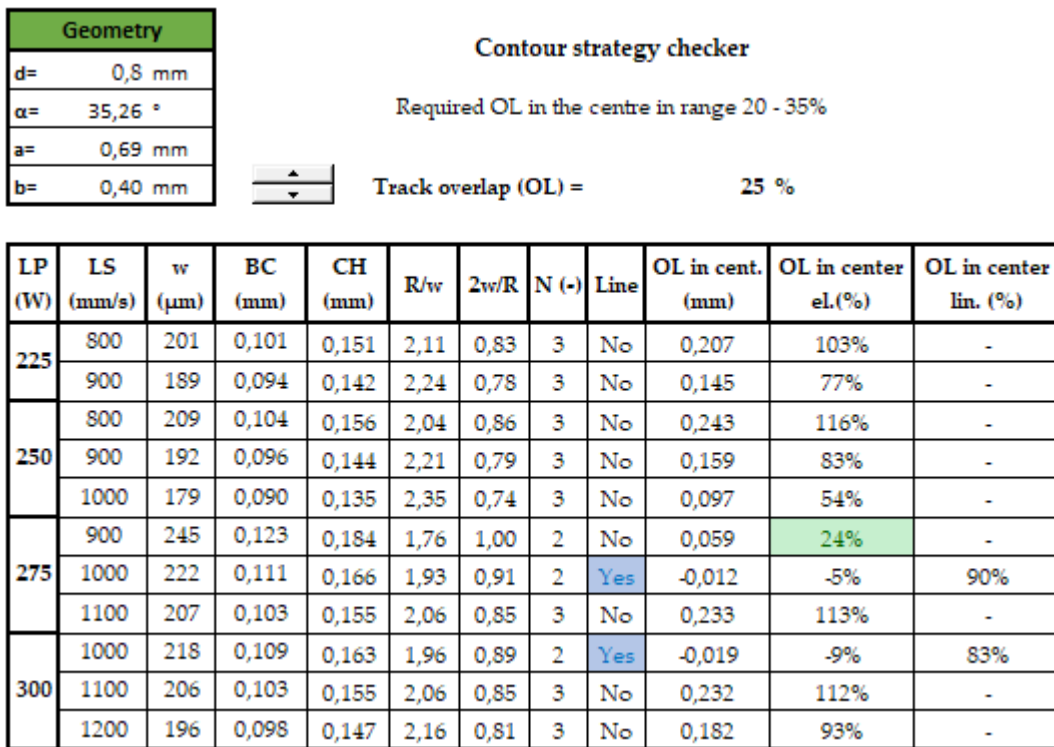


Fig. 6.17. Script for designing of the contour strategy

Parameters of the script

- **R/w ratio** – This parameter determines if the chosen combination of process parameters allows for production of a strut using a single laser path. **R** is a strut radius increase about a half of the overlap area of the weld width:

$$R = r + 0.5 \cdot OL \cdot w \tag{6.4}$$

If $R/w \leq 1$, the script uses the algorithm for single laser track calculation. If $R/w > 1$, the strut cross-section cannot melt using only one single track; therefore, a multi-track approach must be used (Figure 6.19a,b).

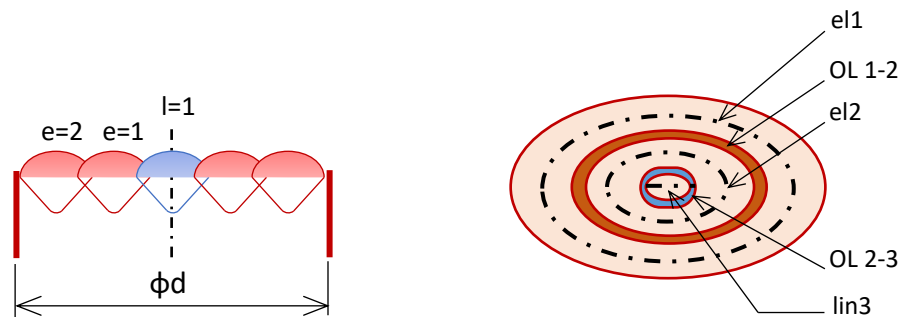


Fig. 6.18. Schema of elliptical/circular and line strategy

- **2w/R ratio** – This parameter is mainly used to describe a transition area between single and multi-track approach. For fully melted strut using the

multi-tracks strategy without over-melted areas, the following conditions must be observed:

$$R/w > 1 \text{ and } 2w/R \leq 1 \quad (6.5)$$

If the condition is met and $2w/R < 1$, a formation of non-melted area x is also checked and eventually the one-line laser track is added to the centre of the strut (Figure 6.19c).

- **Beam Compensation (BC)** – The parameter is important for dimensional accuracy and is calculated as a half of the weld width according to the used combination of process parameters:

$$BC = 0.5 \cdot w \quad (6.6)$$

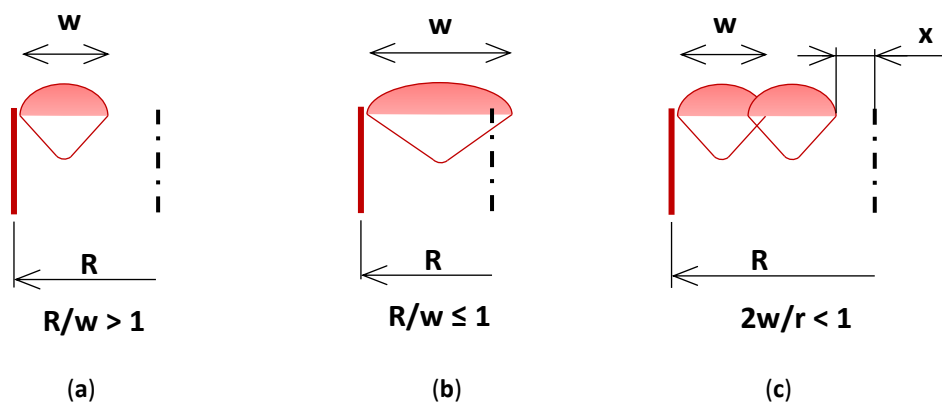


Fig. 6.19. Schematic view of the parameters of the script

- **Contour Hatch (CH)** – It is the distance between two neighbouring weld tracks and its value is dependent on the actually used weld width and required **OL** parameter. Based on the Paper A, the recommended value is **OL** = 25%.

$$CH = w \cdot (1 - OL) \quad (6.7)$$

- **N** – It is the number of used contour tracks. The algorithm of its calculation depends on the R/w and $2w/R$ ratios.
- **Laser path length** – The laser path length is used for input energy (E_{in}) calculation and is expressed by equation 5.4.
- **Porosity and surface roughness prediction** – The prediction of porosity and surface roughness is available based on the results of Paper A, and the script calculates it according to the linear energy (E_{lin}). Actual results (Figures 6.10 and 6.12) allow to use it only for strut diameter of 2 mm and track **OL** 25%.

6.4 Development of Low-velocity Impact Numerical Model - Paper B

Use of numerical modelling during a component design phase is a very effective approach as it reduces the time and number of needed experiments. One of many advantages of SLM produced lattice structures compared to other porous materials is defined core topology. It allows for the use of FEA to support the design of the impact energy absorber and predict its mechanical properties. However, nowadays, the material model which defines behaviour of AlSi10Mg lattice structure for this type of analysis is not available.

The lattice structure is a complex shape composed of thin struts which mechanical properties are highly affected by internal porosity and surface roughness. These imperfections occur during SLM process, especially if inappropriate process parameters are used for fabrication, but even the optimal parameters are used, some imperfections occur; therefore, it is necessary to include them to the numerical model. In this study, the multi-strut tensile specimens and lattice structure compression cube specimens were used to obtain mechanical properties of the thin strut including those imperfection. These results were used for creation of the micro-struts lattice structure numerical model.

6.4.1 Shape and dimensions analysis

Lattice structure specimens

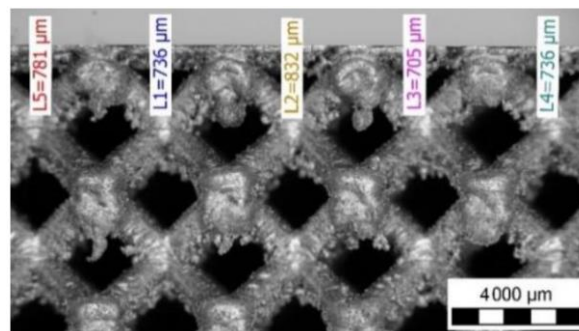


Fig. 6.20. Side view on the impact specimen using the lighting microscope

Tab. 6.2 Optical measurement by Atos Triple Scan system (lattice cubes; nom. diameter $d = 0.8$ mm).

	d_{gauss}	d_{in}	d_{out}	Ellipse	
				Minor Axis	Major Axis
S1	0.95	0.73	1.21	0.79	1.12
S2	0.96	0.74	1.22	0.79	1.12
S3	0.91	0.71	1.18	0.76	1.06
S4	0.97	0.74	1.31	0.84	1.16
\bar{x}	0.95	0.73	1.23	0.80	1.11

The optical system Atos Triple Scan III (GOM GmbH, Germany) was used for detailed measurements of the lattice structure shape and dimensions. A commonly used elementary shape for description of the lattice structure for FEA is a cylinder [11, 15]; however, the results show significant differences between the measured

inscribed and circumscribed cylinders of the lattice single struts (Table 6.2, Figures 6.20); it is not clear which diameter is appropriate for the lattice structure description in a numerical model. Therefore, a basic comparison of real weight and ideal weight of CAD model was performed using the measured diameters (Table 6.3). The CAD computed weight using $d_{gauss} = 0.95$ mm matches best the real weight; therefore, this diameter was chosen to represent the nominal diameter $d = 0.8$ mm in the numerical model.

Tab. 6.3 The comparison of real and ideal weight of the specimen

(Avg. Values)	Measured				CAD				
	h (mm)	t_{UpP} (mm)	m (g)	$\bar{\rho}$ (%)	h_{CAD} (mm)	$m_{CAD,0.8}$ (g)	$m_{CAD,0.95}$ (g)	$\bar{\rho}_{CAD,0.8}$ (%)	$\bar{\rho}_{CAD,0.95}$ (%)
\bar{x}	21.04	0.75	6.97	31	20.80	4.72	6.94	21	31

Along with commonly used cylindrical shape, the elliptical strut cross-section was identified and measured (Figure 6.21). This cross-section represents the lattice structure topology more appropriately and can reflect improvement of mechanical properties as sticking the surrounding metal particles on the down-skin surface of the struts. The results are presented in Table 6.2. Based on the light microscope measurement, also the height of the upper covered plate was changed to 0.75 mm (Figure 6.20).

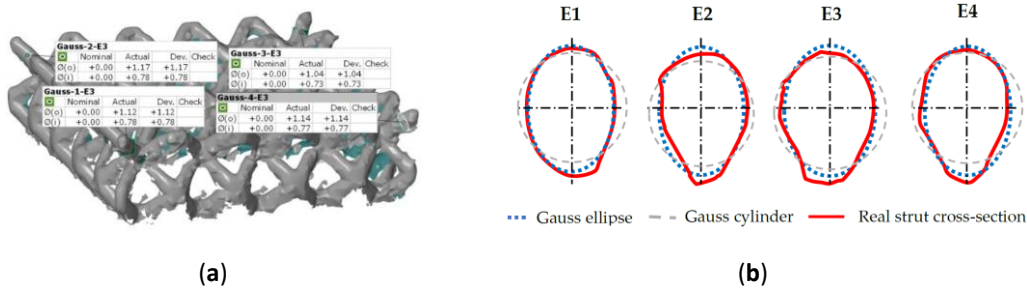


Fig. 6.21. Comparison of the real and ideal cylinder cross-section: (a) shape analysis in the GOM Inspect software and (b) real cross-section in four corner struts.

6.4.2 Quasi-static mechanical testing

Tensile specimen

The tensile specimens were also digitized to find out their precise dimensions because they are input parameters for evaluation of stress-strain curve. In the case of both shapes of specimens (struts - TS, bulk - TB), the average d_{gauss} values were used for evaluation of mechanical properties (Table 6.4).

From the stress-strain curves (Figure 6.22a), yield strength $YTS_{0.2\%}$, Young's Modulus E , and tangent modulus E_T were evaluated. $YTS_{0.2\%}$ was carried out as an intersection of the stress-strain curve and the parallel line to the linear part of the curve (Hook area) in the strain value of 0.002. E_T tangent modulus was obtained as an interpolation of the part of the plastic area in a stress-strain curve by a line. The same evaluation process was used in the case of bulk material specimens (TB-series). The obtained average values are shown in Table 6.4. From the compressive stress-

strain curves (Figure 6.22b), the plastic strain $\epsilon_{\sigma_{max}}$ in the maximum engineering stress was obtained.

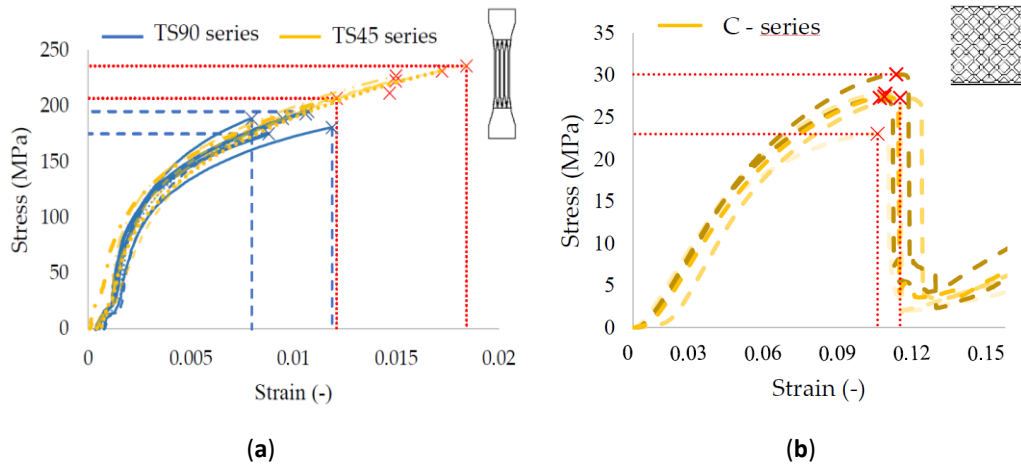


Fig. 6.22. (a) Quasi-static stress-strain curves of the struts tensile specimens; and (b) Quasi-static stress-strain curves of the compression specimens.

Tab. 6.4 The mechanical properties of the tensile specimens

<i>Spec.</i>	F_{max} (N)	χ_{Fmax} (mm)	σ_{max} (MPa)	$\epsilon_{\sigma_{max}}$ (-)	E (GPa)	$YTS_{0.2\%}$ (MPa)	UTS (MPa)	E_T (MPa)
TS45	2270	0.462	-	0.015	71.6	131.6	224.2	6649
TS90	1934	0.297	-	0.010	103.7	116.6	186.8	8701
TB45	7625	1.030	-	0.026	96.1	227.0	382.2	4858
TB90	6453	0.809	-	0.020	147.5	187.4	326	5753.3
C	10,860	2.133	27.2	0.103	483.5	-	-	-

6.4.3 Low-velocity impact test – Flat indenter

To find out the deformation characteristic during the impact energy absorption of the BCC lattice structure and for validation of the developed numerical model, the low-velocity impact tests were carried out at flat indenter (surface loading) configuration using the developed drop-weight low-velocity impactor.

All tested specimens were produced jointly in one-build job using the SLM 280^{HL} machine to ensure the same conditions during fabrication; however, significant differences in mechanical properties, such as maximum reaction force F_{max} , maximum deformation χ_{Dyn} or duration t_{def} , can be observed (Figure 6.23b). These differences could be caused by a local damage of the lattice structure which can occur due to the material imperfection created during SLM, such as surface roughness or internal porosity. This can change a symmetrical bending of dominant deformation process, which is typical for BCC structures, to an asymmetrical mechanical response [63]. Therefore, in the case of the lattice structure, it is necessary to consider the average values of the mechanical properties.

For comparison purposes, the average curves of dependences of the force vs. deformation and initial speed vs. deformation were created (Figure 6.23c,d). All the results are shown in Table 6.5; it shows that mechanical properties, such as maximum

reaction F_{max} and stiffness of the specimens under dynamic loading k_{Dyn} (in the elastic area), increase linearly with struts diameter.

Tab. 6.5 The average results of the low-velocity flat impact.

#	F_{max} (N)	t_{def} (ms)	x_{Dyn} (mm)	v_{In} (m·s ⁻¹)	E_I (J)	E_{Abs} (J)	v_{Up} (m·s ⁻¹)	k_{Dyn} (N·mm ⁻¹)	P_{Abs} (J·s ⁻¹)
IT 0.6	5089	4.92	8.70	2.96	31.87	31.48	0.32	9005	6.41
IT 0.8	10,343	3.48	5.22	2.96	31.88	31.42	0.35	19,417	9.15
IT 1.0	16,988	2.19	3.47	3.13	35.57	35.17	0.31	29,371	16.41
IT 1.2	24,297	1.56	2.55	3.20	37.13	35.38	0.68	39,006	23.17

Absorbed energy E_{Abs} was evaluated regarding the real measured initiating velocity v_{In} and residual rebounding velocity v_{Up} . From Table 6.5, it is obvious that most of the specimens absorbed more than 99% of impact energy, and only in the case of the specimens with nominal diameter $d = 1.2$ mm, there was a small decline. Therefore, the parameter absorption power P_{Abs} (J·s⁻¹), which reflects the deformation and absorbed energy, was defined.

$$P_{Abs} = E_{Abs}/t_{def} \tag{6.8}$$

The lattice structure with the low value of P_{Abs} can absorb energy for long time and through a large lattice structure deformation. It is important e.g. in the automotive industry where the car deformation area must be designed for overload not damaging the human body.

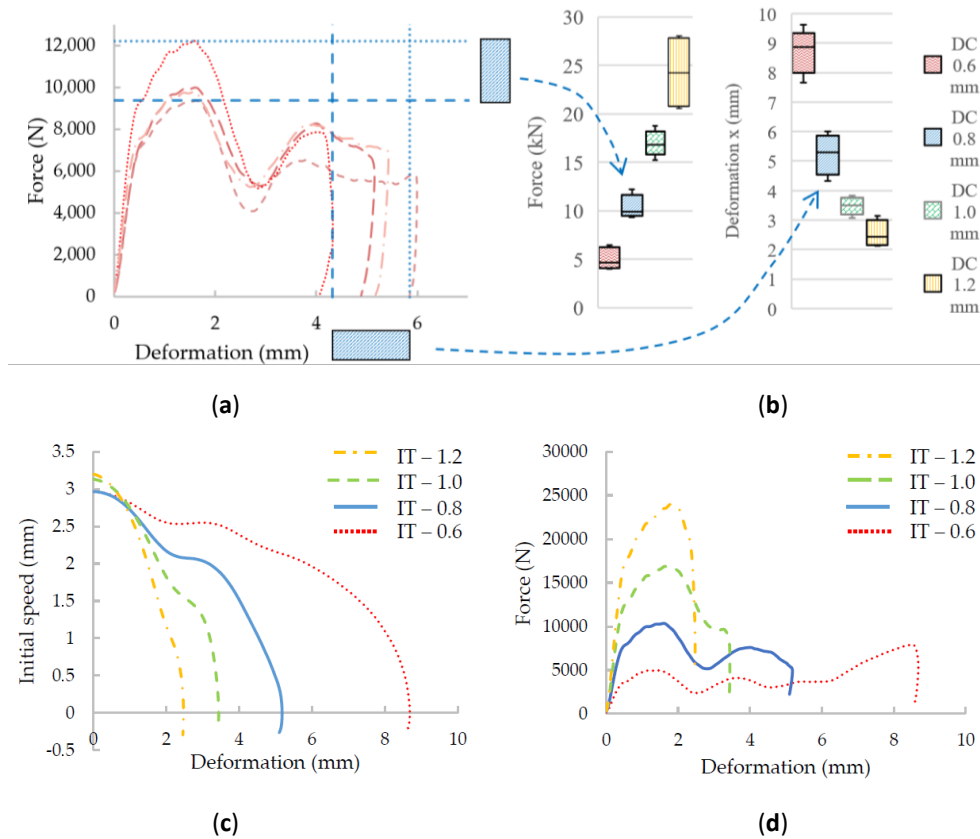


Fig. 6.23. The results from low-velocity impact testing: (a) Single IT-series with diameter $d = 0.8$ mm; (b) variance of force and deformation of all IT-series; (c) average initial speed, deformation curves; and (d) average force-deformation curves.

6.4.4 Finite Element Analysis (FEA)

FEA Material Models

Based on the quasi-static results, the material model (BL-I) of the BCC lattice structure from AlSi10Mg was created (Table 6.6). The parameters E , $YTS_{0.2\%}$ and E_T of the TS45-series were used to create the *Bilinear isotropic hardening material model* due to a similar strut build inclination, as in the case of the BCC lattice structure (35.26°) [30]. A damage criterion was obtained from the C-series as the maximum equivalent plastic strain $\epsilon_{\sigma max}$. The material model (BL-II) of the upper and bottom plate was created using mechanical parameters of the bulk material specimens. The other needed parameters were taken from the Ansys material library as the default values.

Tab. 6.6. Material models used for lattice structure specimens FEA.

Parameters	BL-I (BCC)	BL-II (Plate)	Unit
Density	2680	2680	kg·m ⁻³
Isotropic Elasticity	-	-	-
Young's Modulus	70,723	96,100	MPa
Poisson's Ratio	0.334	0.334	-
Bulk Modulus	7.1×10^{10}	9.6×10^{10}	Pa
Shear Modulus	2.7×10^{10}	3.6×10^{10}	Pa
Bilinear Isotropic Hardening	-	-	-
Yield Strength	135	227	MPa
Tangent Modulus	6586	4858	MPa
Plastic Strain Failure	-	-	-
Max. Equivalent Plastic Strain EPS	0.1025	0.1025	-

FEA Material Models

The results from FEA, which uses the quarter numerical model of the low-velocity dynamic loading, and both material models (BL-I and BL-II) are shown in Figure 6.24. The force-time curve of the numerical model with the elliptical cross-section (Figure 6.24b) corresponds more appropriately to the experimental results than the curve with the circular cross-section (Figure 6.24a).

In the case of FEA, using the circular cross-section shape, and comparing the low-velocity mechanical testing, the predicted duration of deformation is longer than measured 5 ms, a decrease of the transmitted force after the first F_{max} (after deformation of the first layer) is significantly lower as well as the level of the transmitted force in the middle part of the force-time curve (between 1.5 – 4 ms). In the case of FEA considering the elliptical cross-section shape, all observed parameters achieve better values as is shown in Table 6.7.

The deviations between FEA and the experiment were compared using four positions in the chart - F_{max1} value in the first force peak, F_{min} value at the end of the first progressive collapse, F_{max2} value in the second peak and the duration of deformation. The values from FEA were compared to the average values from five experimentally tested specimens. The results in Table 6.6 show that e.g. the relative error of FEA with circular cross-section is 14%, while with an elliptical cross-section, it is only 5%. As is shown, expect the t_{Fmin} value, the elliptical geometry reaches better

or the same results as the circular geometry. Elliptical model also can more accurate predict the end of the deformation duration. Therefore, the numerical model with elliptical cross-section will be used for future analysis.

Tab. 6.7 Relative error comparison between different strut-cross sections.

#	F_{max} (N)	t_{Fmax} (ms)	F_{min} (N)	t_{Fmin} (ms)	F_{max2} (N)	t_{Fmax2} (ms)	t_{def} (ms)
Experiment (Avg value from 5 measurement $d = 0.8$ mm)	10341	0.58	5153	1.15	7589	1.78	4.75
Elliptical cross-section	9830	0.50	2552	1.0	8999	1.74	5.132
vs. experiment	-5 %	-16%	-102%	-15%	+16%	-2%	+7%
Circular cross- section	-9040	0.66	1188	1.2	6879	1.74	6.11
vs. experiment	+14%	+12%	-333%	-4%	-10%	-2%	+22%

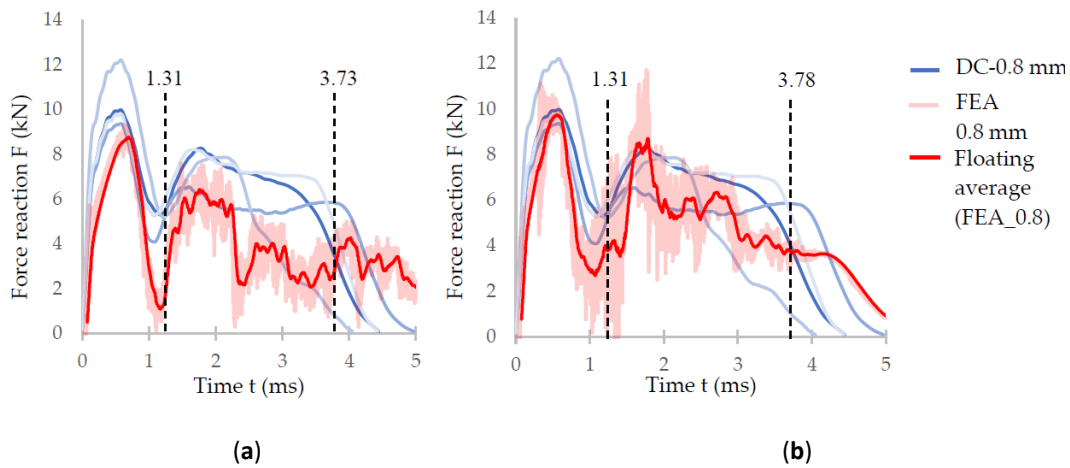


Fig. 6.24. Comparison of the results of the IT-0.8 series and the numerical simulation with (a) circular cross-section; and (b) elliptical cross-section.

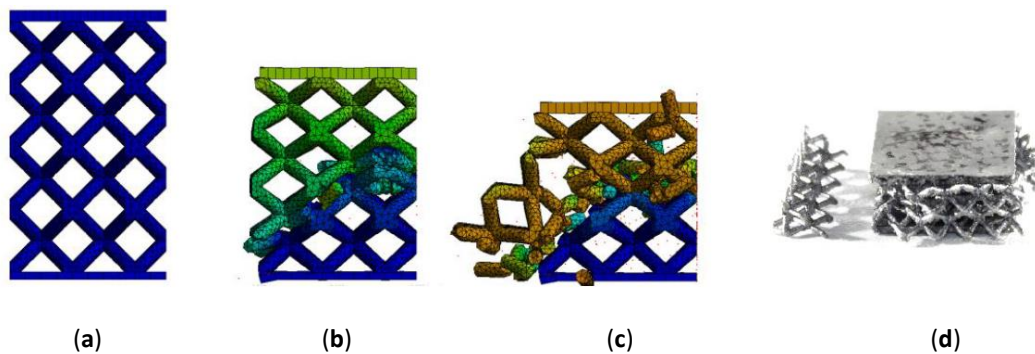


Fig. 6.25. Gradual deformation of the specimen with circular strut cross-section in time —(a) 0 ms; (b) 1.31 ms; (c) 3.73 ms; (d) real damage of the specimen IT-2 after low-velocity impact test.

6.5 Study about influence of the strut diameter size on the BCC lattice structure mechanical behaviour using FEA

The material model used in FEA was created for the lattice structure with specific nominal diameter $d = 0.8$ mm; therefore, all specimens, such as those for optical

measurement or quasi-static testing, were fabricated with this nominal diameter. To allow for prediction of a deformation behavior of the commonly used lattice structure with non-tested strut size in the range between of 0.6 and 1.2 mm, the actual results about ellipticity was supplemented with previous study about influence of the strut inclination on its dimensions [11].

6.5.1 Influence of the strut inclination on its dimensions

The “cage” specimens were digitized by Atos Triple Scan and evaluated in GOM Inspect software by fitting ideal cylinders to digitized surface data. The results show that the diameters sizes under $d = 0.4$ mm and strut orientations α between of 0° and 25° are non-manufacturable from AISi10Mg. The courses of all analysed orientations are similar; the inscribed, Gauss and circumscribed cylinders are larger than the required nominal diameter; the deviation of real and required diameter is decreasing with rising nominal diameter (Figure 6.27). All results of this analysis were published in [11].

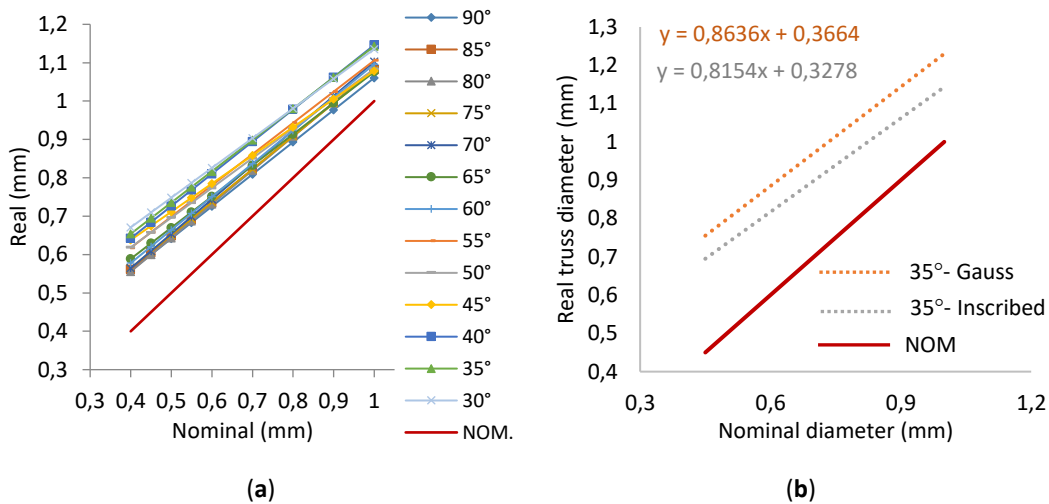


Fig. 6.26. (a) Real size of the inscribed diameter vs. real diameter of the struts from AISi10Mg; (b) Influence of 35° strut inclination on strut size of d_{Gauss} and d_{in} ; this orientation is similar as in BCC lattice structure

6.5.2 Definition of strut ellipticity for strut diameter in the range between of 0.6 and 1.2 mm

To create the FEM geometry for the non-tested struts diameters, the actual results ellipticity were supplemented with the results of the study above (Figure 6.26b). The geometry modification is was performed as follows.

The results in Table 6.3 show that, based on the weight comparison, the value of real elliptical strut cross-section is similar to the circular cross-section with d_{Gauss} . It was used along with the elliptical ratio $e = 0.714$ evaluated from the O-series as the ratio between the minor and major axes of the elliptical cross-section. The calculation is described using the equations (6.9 – 6.13).

$$A_{Dgauss} = A_{ellipse} \quad (6.9)$$

$$\pi \frac{d_{gauss}^2}{4} = \pi \cdot a \cdot b \quad (6.10)$$

$$e = \frac{a}{b} = \frac{0.795/2}{1.114/2} = 0.714 \quad (6.11)$$

$$b = \sqrt{d_{gauss}^2/4 \cdot e} \quad (6.12)$$

$$a = e \cdot b \quad (6.13)$$

The results of FEA were verified by drop-weight impact mechanical testing. A comparison can be seen in Figure 6.27 along with the differences between the numerical models with circular and elliptical cross-section. For more accurate results or for diameters larger than 1.2 mm, it is necessary to repeat all performed analyses.

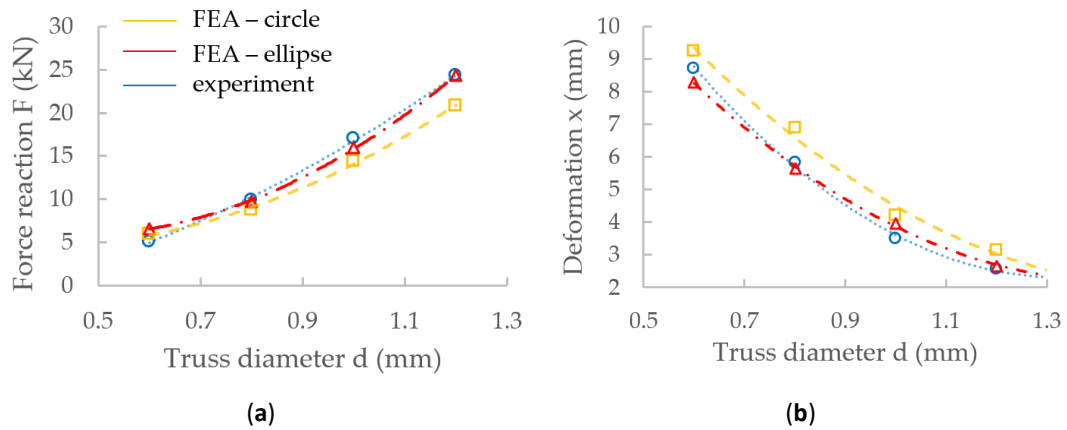


Fig. 6.27. Comparison of FEA results and experiment for different strut diameters; (a) reaction force; and (b) deformation.

6.6 Study of the lattice structure local impact

6.6

Another type of dynamic loading is penetration (break-through) of the lattice structure with a small object with high energy. For this purpose, the drop-weight impact experiment with ball indenter ($d = 16$ mm) was performed. The experiment conditions were the same as in the case of previous impact absorption measurement for comparison of the mechanical properties. The results were used for validation of the FEA analysis and are shown in Table 6.8 and Figure 6.28.

Tab. 6.8 The average results of the low-velocity flat impact.

#	F_{max} (N)	t_{def} (ms)	x_{Dyn} (mm)	v_{In} (m·s ⁻¹)	E_I (J)	E_{Abs} (J)	v_{Up} (m·s ⁻¹)	P_{Abs} (J·s ⁻¹)
ITS 0.6	8135	4.08	7.65	3.17	36.39	36.37	0.31	8.91
ITS 0.8	12,104	2.72	5.00	3.06	33.94	33.83	0.4	12.44
ITS 1.0	18,062	2.14	4.15	3.19	36.87	36.71	0.45	17.15
ITS 1.2	21,215	1.78	3.33	3.15	36.09	35.86	0.51	20.15

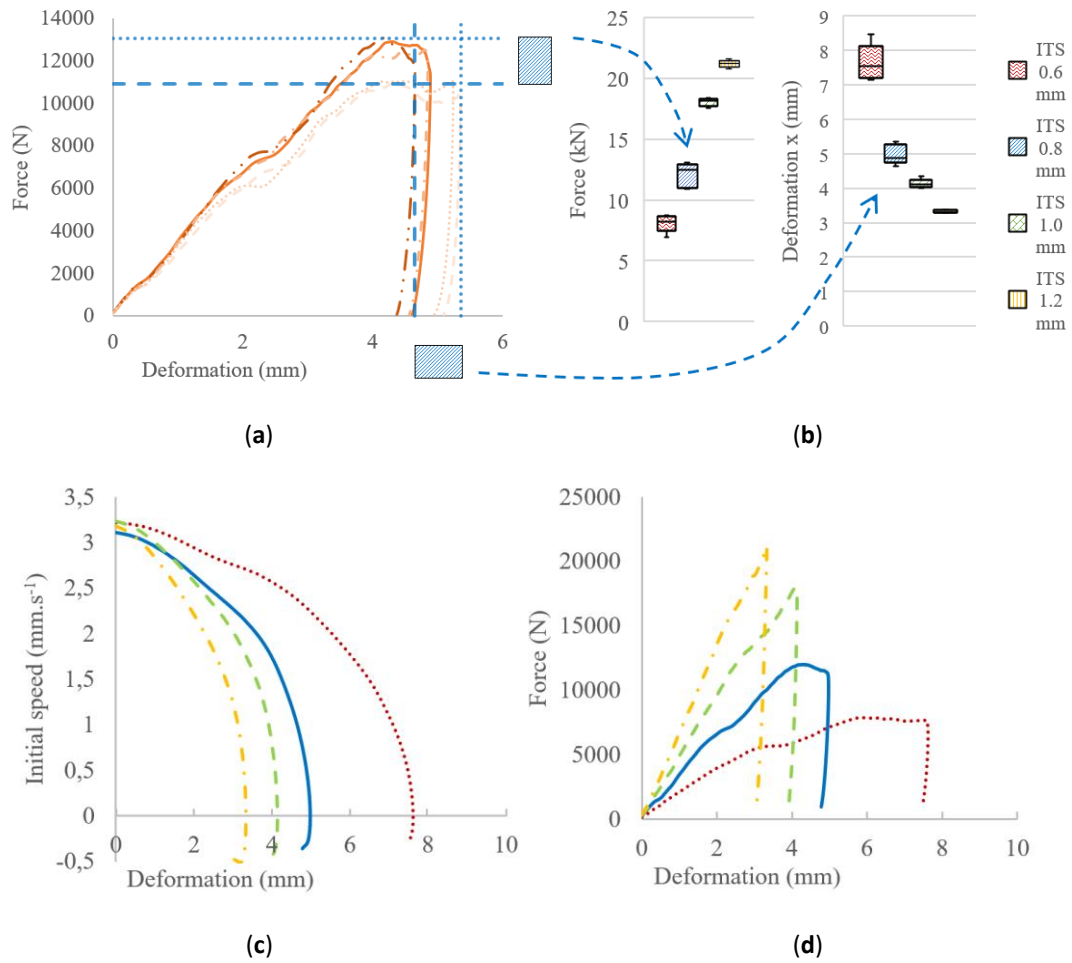


Fig. 6.28. The results from low-velocity impact with tip indenter: (a) Single ITS-series with diameter $d = 0.8$ mm; (b) variance of force and deformation of all ITS-series; (c) average initial speed vs. deformation curves; and (d) average force vs. deformation curves.

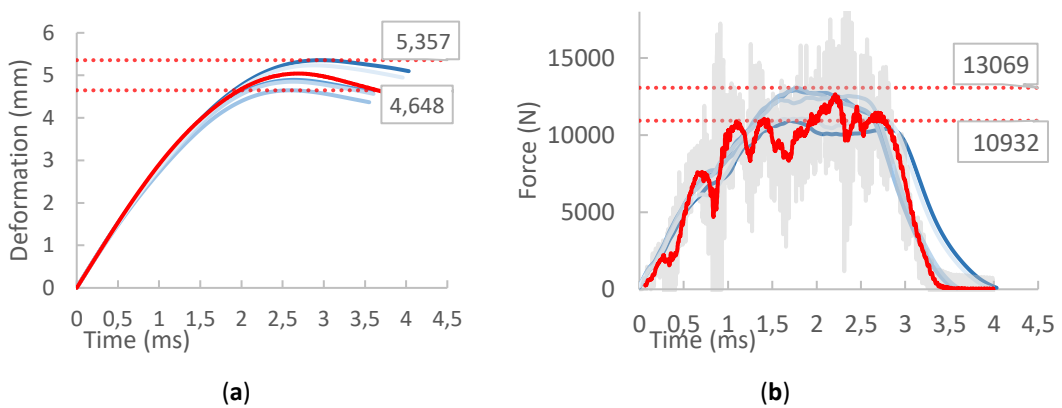


Fig. 6.29. Comparison of the measured data of the ITS-0.8 series and the numerical simulation (a) deformation vs. time dependence; and (b) reaction force vs. time dependence.

The final numerical model using the geometry with the elliptical cross-section for nominal diameter $d = 0.8$ mm and the lattice structure material model was used for the initial FEA. The results show large deviations compared to the measured data and

prediction. Based on this, the *EPS* parameter was optimized using a parametric task in Ansys software to obtain comparable results of maximum penetration and reaction forces in the range between 10% and 25%, in step 2.5%. The best match was obtained with *EPS* = 20 %, as is shown in Figure 6.29. For verification, the analysis was also performed for struts diameters of 0.6, 1.0, and 1.2 mm.

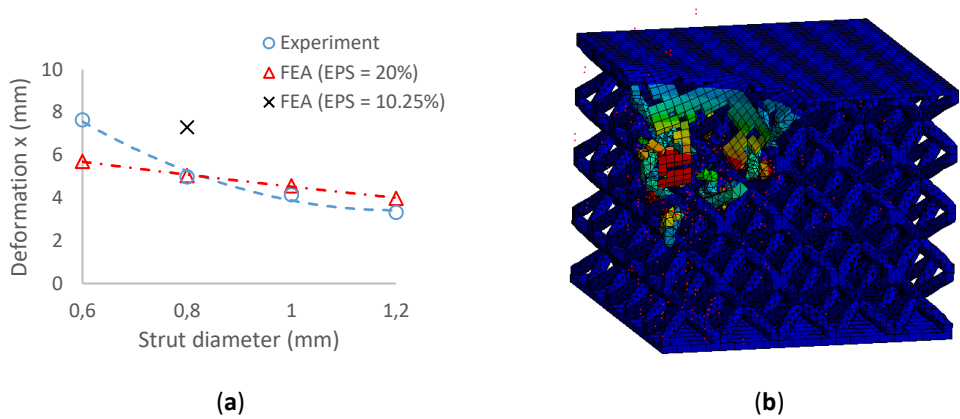


Fig. 6.30. (a) Comparison of FEA results and experiment for different strut diameters; (b) specimen deformation after impact with tip in FEA

7 DISCUSSION

7.1 Laser strategy for lattice structure fabrication

7.1.1 Linear energy limit

The results of the single tracks welds experiment show $E_{lin} = 0.25 \text{ J.mm}^{-1}$ as a limit value for consistent welds. The obtained value is higher than that in the case of [23] where the determined limit was 1.5 J.mm^{-1} . The differences were caused by parameters of the laser and the parameters of the experiment. In the study [23], the laser was focused to $70 \mu\text{m}$ spot size and the single welds were produced directly on the platform while in the present study, the laser was focused to $82 \mu\text{m}$ and the single welds were produced on the 5 mm solid block. This reflects more appropriately a real layer by layer production and an increase in thickness of the deposited powder (LT) during the formation of the first few layers because, after laser melting, the produced layer has usually a height lower than that of the originally spread layer of $50 \mu\text{m}$. Then, the next deposited layer has a higher thickness and a quality of weld and the required linear energy E_{lin} can be changed [49]. The comparison also shows that the SLM process strongly depends on many process parameters and only other authors' results obtained under the same condition can be used as a research background.

The results also show that the required linear energy for production of the single weld and the strut is the same. From this, it follows that the needed linear energy is not dependent on the geometry of the produced part.

7.1.2 The influence of the residual heat energy during strut-lattice structure production

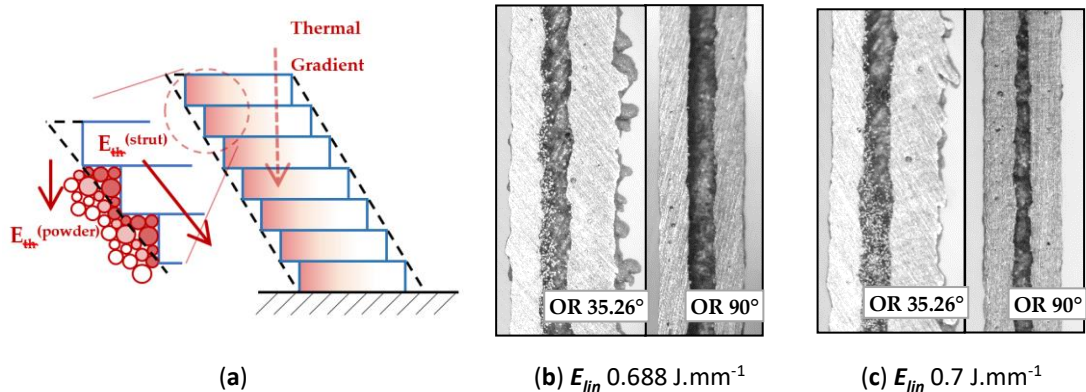


Fig. 7.1 (a) Scheme of the heat transfer; Comparison of inclined and perpendicular strut (b) for parameters $LP 275 \text{ W}$, $LP 400 \text{ J.mm}^{-1}$; (c) $LP 350 \text{ W}$, $LP 500 \text{ J.mm}^{-1}$.

The results of the initial surface roughness (on the strut side) show that the roughness strongly depends on the strut inclination [21]. It is caused by worse heat transfer where after layer production, a part of the residual heat energy is transferred through the struts to the platform, another part is gradually spread to the surrounding metal powder in the thermal gradient direction, and the rest of it is accumulated in the strut and causes its overheating. Accumulation of the thermal

energy is caused by much lower thermal conductive performance of the powder vs. solid material due to only the point contact of the powder particles between themselves.

Due to overheating, the change of the microstructure of the AlSi10Mg material significantly increases the porosity at close to the down-skin of the struts (Figure 6.14c) [28] and the single weld width, as is shown in the hollow struts results (in full-text Paper B) and partly in the results of the *OL* parameter (Figure 6.9). Wider single welds can significantly affect the dimensional accuracy of the produced struts (Figure 7.1 b,c). The residual heat energy, transferred to the surrounding powder, increases the strut cross-section by sticking powder on the strut down-skin surface (Figure 7.1a), as was confirmed in Paper B (Figure 6.21) and also in previous studies [11, 15, 25].

These effects of heat transfer to the surrounding powder due to the strut inclination cannot be eliminated but only reduced by using a suitable combination of process parameters with lower input energy E_{in} . The effect is higher for materials with relatively lower melting temperature, as in the case of AlSi10Mg.

7.1.3 Input energy calculation

The input energy E_{in} was defined to describe different conditions during production of two struts with the same geometry but different inclination. Using standard approaches for energy calculation as $E = P/(t \cdot h \cdot v)$ or E_{lin} , the same energy values are obtained for both cases; however, two different cross-sections with different length of the laser trajectories and energy levels actually occur. From this, it follows that for achieving of equal porosity level of *OR* 90° and *OR* 35.26°, it is necessary to use a different combination of the process parameters; with lower energy level for *OR* 35.26°. The result of the input energy obtained in this study are applicable only for strut diameter $d = 2$ mm; for other dimensions, the optimal level must be found.

7.1.4 Porosity formation

The performed analyses show a different level and shape of porosity according to the input energy E_{in} and the linear energy E_{lin} . While the low energy setup is used, E_{lin} up to 0.25 J. mm⁻¹ and E_{in} up to 8 J, the porosity is often formed by lack of fusion porosity which is usually represent by a small number of larger irregular pores located in **close to the up-skin surface** (Table 6.1). Their formation is related to the thermal transfer in the inclined struts where the residual thermal energy is accumulated at the down-skin surface [28]; therefore, even with the use of lower energies, the neighbouring laser tracks are connected in down-skin area and the porosity occurred rather in upper part of the strut. Based on the results, the minimum value $E_{lin} = 0.25$ J. mm⁻¹, which ensures sufficient linear energy for connection of the neighbouring laser tracks in the whole volume, was determined.

If a high energy setup is used, E_{lin} over 0.4 J. mm⁻¹ and E_{in} over 10 J, the porosity is mainly formed by a lot of small spherical pores in the whole volume with higher concentration close to the down-skin surface. For future mechanical properties, mainly the large irregular pores are problematic (Figure 7.2).

Porosity – 0.21 %
 $E_{lin} = 0.18 \text{ J.mm}^{-1}$
 $E_{in} = 9.2 \text{ J}$
 Lack of fusion porosity

Porosity – 0.41 %
 $E_{lin} = 0.32 \text{ J.mm}^{-1}$
 $E_{in} = 10.2 \text{ J}$
 Gas pores

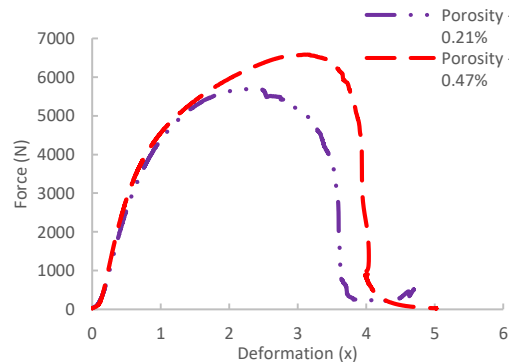
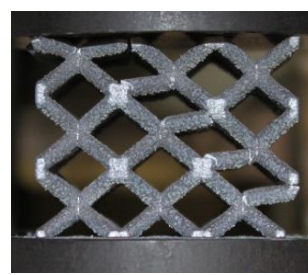
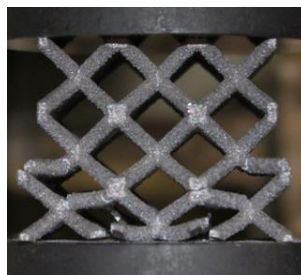
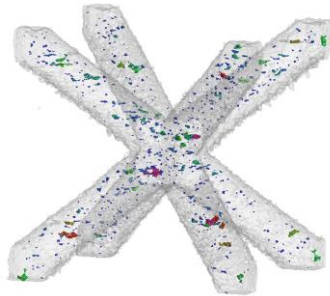


Fig. 7.2 Initial analysis of influence of the internal porosity on the mechanical properties of the lattice structure

7.1.5 The porosity and surface roughness dependence on the main process parameters **LP** and **LS**

The current results of strut experiments clearly show that the porosity and surface roughness are affected by the input energy E_{in} as well as linear energy E_{lin} ; both of them include the laser power **LP** and the laser speed **LS**. It follows that the number of internal defects and level of surface roughness can be significantly reduced using appropriate laser process parameters.

The charts of the dependences of **LP** and **LS** on the porosity (Figure 6.11) demonstrate a different influence of the parameters on porosity formation. The chart **LP** vs porosity shows that the porosity increases with higher **LP** at all **LS** levels linearly. The chart **LS** vs porosity shows non-linear results with the lowest porosity in the range

of $900 \div 1400 \text{ mm}\cdot\text{s}^{-1}$. With higher **LS**, the porosity seems to be stable and at constant levels. With the **LSs** up to $1000 \text{ mm}\cdot\text{s}^{-1}$, porosity rapidly increases. It is caused by too high E_{in} and formation of gas pores in the material due to its overheating (Figure 6.14c).

The dependences of **LS** and **LP** on the surface roughness has a similar character as that on the porosity in the case of input energy E_{in} . Linear energy E_{lin} dependence shows the pronounced linear dependence of as-built surface roughness. Figure 6.13a shows two approximately linear areas. In the first area, up to $1400 \text{ mm}\cdot\text{s}^{-1}$, the surface roughness increases with higher **LS**, while in the other one, between $1400 \text{ mm}\cdot\text{s}^{-1}$ and $2000 \text{ mm}\cdot\text{s}^{-1}$, the roughness level is stable. The dependence of **LP** vs. roughness is linear for all tested laser speeds. Generally, the results show a low surface roughness with lower E_{in} and E_{lin} .

7.1.6 The ranges of the suitable values of LS and LP

Based on all above results, the perspective area which meets all conditions for low porosity and surface roughness levels was found.

LS/ LP	500		600		700		800		900		1000		1100		1200		1300		1400	
	E_{lin}	E_{in}	E_{lin}	E_{in}	E_{lin}	E_{in}	E_{lin}	E_{in}	E_{lin}	E_{in}	E_{lin}	E_{in}	E_{lin}	E_{in}	E_{lin}	E_{in}	E_{lin}	E_{in}	E_{lin}	E_{in}
225	0.45	9.78	0.38	9.53	0.32	9.33	0.28	9.16	0.25	9.01										
250							0.31	9.75	0.28	9.48	0.25	9.24								
275									0.31	9.98	0.28	9.77	0.25	9.59						
300											0.30	9.87	0.27	9.54	0.25	9.26				
325											0.33	-	0.30	0.27	0.25					
350											0.35	9.97	0.32	9.48	0.29	9.05	0.27	8.67	0.25	8.34
375											0.38	-	0.34	-	0.31	-	0.29	-	0.27	-
400											0.40	9.98	0.36	9.35	0.33	8.80	0.31	8.33		

Fig. 7.3 The perspective area for struts fabrication - linear energy E_{lin} ($\text{J}\cdot\text{mm}^{-1}$) (green cells) and input energy to the layer E_{in} (J) (red cells)

7.2 Low-velocity Impact Numerical Model and Its Application

7.2.1 Substitution of the Strut Real Cross-Section

A deformation behaviour of the developed numerical model with the circular cross-section geometry of $d = 0.8 \text{ mm}$ (nominal diameter) showed large deviations to the experiment during initial tests. Therefore, the strut cross-section and the weight of fabricated specimens were compared with the CAD model. The results showed significant differences; therefore, the nominal diameter in the CAD model was changed to the measured d_{Gauss} which matches best with the weight and cross-section of specimens. This approach is in line with the study of Stuart et al. [15], where the diameter in the area between d_{in} and d_{out} was chosen according to FEM analysis of the real μCT strut geometry (Figure 2.11a).

As was already mentioned above, due to a residual heat transfer into the surrounding powder, the real shape of the lattice structure struts similar to “water drop” was found using optical measurement (Figure 5.5). A partially melted powder modifies the strut shape into an elliptical cross-section resulting in an increase of

mechanical properties in the build direction (axis Z). For good agreement of the FEM model and experiment, it is necessary to include this geometry. If an equivalent circular cross-section is used, the mechanical properties of the lattice structure are increase equally in all directions but not sufficiently in Z direction. It can be seen during a comparison of the progressive collapse of the FEA and the experiment (Figure 6.24). The results show that the elliptical cross-section is more suitable for a description of the whole deformation process and the circular cross-section can only be used for the estimation of approximate F_{max} reaction force when the lattice structure starts to be damaged.

7.2.2 Evaluation of mechanical properties of thin struts produced by SLM

A lattice structure is a complex shape which is usually composed of many thin struts. As was described above, the material properties of the struts produced by SLM are strongly influenced by internal porosity and surface roughness [14, 34]. Therefore, the mechanical properties of the bulk material cannot be used as the input information for the FEA material model, and the mechanical tests of the “strut shape” specimens must be performed; therefore, the lattice structure specimens were used for compressive loading (Figure 5.12), and the multi-struts specimens for tensile testing (Figure 5.11). This shape was developed to attain the similar condition for tensile testing as for compression loading of lattice structure where many of single struts transfer the load simultaneously. To obtain the correct mechanical properties during evaluation of strut mechanical properties, it is necessary to use the real dimensions measured e.g., optical measurement [11, 15].

The results of tensile testing show that specimens fabricated by SLM with of **OR** 45° have different mechanical properties in comparison with those of **OR** 90°, specifically: $YTS_{0.2\%} + 10\%$; $UTS + 20\%$; Young’s modulus $E + 40\%$; and Tangent modulus $E_t - 30\%$. Generally better mechanical properties in case of **OR** 45° could be due to a higher porosity level inside the strut in the case of **OR** 90° orientation.

The strut mechanical properties were also compared with bulk material which is not too affected by internal defects. The results show much lower strut mechanical properties and more brittle material, specifically: $YTS_{0.2\%} - 40\%$; $UTS - 30\%$; Young’s modulus $E - 30\%$ and Tangent modulus $E_t + 30 \div 50\%$. It may be mainly caused by significant surface roughness and almost two times higher surface of multi-strut specimens compare to bulk specimens (970/565 mm², calculated using the Gaussian diameter for specimens T45-series $d_{Gauss} = 0.89$ mm.). The size of specimen’s surface is also connected with close to the surface porosity.

7.2.3 Variance of low-velocity impact results

The results of the flat impact loading show a high variance in the results which is caused mainly due to material imperfection of SLM fabricated lattice structures such as surface roughness or internal porosity and their influence on the brittle AlSi10Mg material. The imperfections can change symmetrical bending of dominant deformation process, which is typical for BCC structures, to an asymmetrical mechanical response [63].

In comparison with the results of ball (local) impact loading, the variance of the results is significantly higher. It is mainly due to the surrounding non-deformed lattice structure which stabilized the deformation process and significantly reduced the influence of material imperfection in the case of local impact test. For future design of lattice structure specimens for flat impact testing, the solid thin wall ($t = 0.3 \text{ mm}$) on the lattice structure sides is recommended to stabilise the deformation process.

7.2.3 Lattice structure local impact analysis – Ball indenter (FEA)

The results of local impact analysis show that the developed material model of lattice structure can be used for flat impact loading, even for different struts diameters; but for the local impact analysis, the model needs to be modified, especially as for the damage criterion **EPS**.

This criterion represents a true strain of the lattice structure at the area of damage and its value could not be measured using available methods; therefore, an alternative method was used and the **EPS** = 0.1025 (Table 6.6) was obtained as the global strain of lattice structure at the first peak F_{max} in the compression test. In FEA, this parameter defines the state when the element is excluded (element erosion) and no longer contributes to load transfer.

For the local impact analysis, the alternative parametric optimization was performed using the Ansys numerical model with elliptical strut cross-section and the nominal diameter $d = 0.8$. The value **EPS** = 0.2 was found as the best corresponding with the results of the experiment; therefore, this value was used for other tested diameters (in FEA).

The correct, but complicated, approach how to find the **EPS** value is to perform a numerical simulation to identify the true stress-strain curve of the elements at damage area [64] and also to find out a fracture model of strut damage [65]. This issue will be solved in the future publication in co-operation with department of Solid Mechanics, Mechatronics and Biomechanics.

8 CONCLUSIONS

The present thesis deals with three areas of the research which are needed to achieve the global aim which is the development of the SLM produced lattice structure energy absorber (protective mechanism) with defined mechanical behaviour in the future. These areas are as follows: a design of the drop-weight impact tester, the development of the numerical model of the impact loading of lattice structure and development of the contour strategy for the lattice structure production.

In order to study the mechanical behaviour of the BCC lattice structure produced by SLM, the drop-weight impact tester with maximal theoretical impact energy about of 120 J was developed. The maximal impact velocity is up to 4 m.s^{-1} , thus the device belongs to the low-velocity category. The device allows changing the shape of the indenter based on the required loading – flat (surface), ball (local). The impact tester is equipped with the strain-gauge and the HS camera which allows measuring the needed mechanical properties with the sampling frequency of 96 kHz. The strain-gauge is used to obtain the force vs. time dependence during specimen's deformation and the HS camera is used to obtain precise information on the impact energy, deformation of the tested specimen and eventually non-absorbed residual rebounded energy. The HS camera data record is evaluated using the image analysis in the developed software in MATLAB and subsequently, both records are jointly analysed to obtain the absorption properties of the lattice structure specimens. The obtained results were necessary for identification of the boundary condition of the FEA for validation of the numerical model.

As is clear from previous studies, mechanical and material properties of the lattice structures produced by SLM are strongly dependent on used SLM process parameters and laser strategy due to formation of an internal porosity and surface roughness. Using appropriate combination of the process parameters, these imperfections can be reduced; therefore, mechanical properties can be significantly improved, and better match of the numerical model and experiment can occur [29]. On the other hand, there is no presented study specifically on laser strategy for lattice structure. Therefore, the research in the field of influence of the main process parameters was performed and subsequently, the contour strategy for the lattice structure production from AlSi10Mg powder was developed.

An experimental study was divided into two parts – the first part, an analysis of single laser welds in a wide range of **LP** and **LS** process parameters was performed. The results were used to find out perspective combinations of process parameters for continuous and uniform welds production, the widths of the welds were used as the base information to design the contour strategy. The second part was performed directly on the strut shape specimens and was aimed at the analysis of the **LP**, **LS** and **OL** parameters and their influence on the formation of the internal porosity and surface roughness. The results were implemented to the basic semi-automated script for contour strategy designing. The future aim is to develop the software which automatically chooses the suitable combination of the process parameters depending on the porosity and surface roughness for struts diameters in the range of

0.5 – 1.2 mm. The actual results were published in the Materials Journal ([Paper A](#), IF=2.467). Simultaneously, this research continues, and another publication is preparing with colleagues from DAP department at RWTH Aachen. Then, it will be possible to implement the all results into presented numerical model. The main conclusions are as follows:

- To produce the micro strut–lattice structure, the contour strategy seems to be perspective, mainly because of the possibility to use various laser process combinations based on different strut dimensions to achieve a fully melted strut with a constant **OL** 25% parameter.
- The heat transfer condition in the inclined struts significantly influences all material and dimensional parameters of the struts (lattice structure). During the production with high E_{in} , heat energy is accumulated in the down-skin part of the strut and higher roughness, higher porosity and change of the material microstructure occur. Therefore, the production at lower E_{in} levels leads to more stable results with lower porosity and roughness.
- E_{in} calculated on the basis of the real laser trajectory in the strut describes well the amount of porosity and roughness in the strut specimens ($d = 2\text{ mm}$). Another necessary condition for struts production without large and irregular internal pores is the minimum level of linear energy E_{lin} 0.25 J.mm^{-1} . The perspective areas of process parameters are presented in [Figure 7.2](#).

In order to study the mechanical behaviour of the SLM produced BCC lattice structure under impact loading, the two numerical models were developed in ANSYS Explicit – for surface impact and local impact loading. Both use the bilinear isotropic hardening material model which defines the mechanical behaviour of the AlSi10Mg BCC lattice structure in the FEA. The material model was developed based on a quasi-static tensile test of the multi-strut specimens and a quasi-static compression test of the lattice structure cube specimens.

Based on the results of the optical measurement, two lattice structure geometries were used in numerical model – the one using circular cross-section with the measured strut diameter d_{gauss} and the one using the elliptical cross-section which better corresponds with the experimental results. The both geometries were tested in the range of the lattice structure nominal diameter 0.6 – 1.2 mm.

The results show that in the case of local impact, the material model must be further supplemented with the fracture model of damage and the **EPS** parameter obtained from the numerical simulation. In the case of surface impact, the numerical model with elliptical cross-section well corresponds with experimental results in the range of the nominal diameters above. It confirms that the presented numerical model can be used for prediction of the deformation behaviour of the lattice structure; this approach can be used for a precise design of the absorber in high-performance applications. The main results were published in the Materials Journal ([Paper B](#), IF=2,467). The main conclusions are as follows:

- The elliptical shape of the lattice structure significantly decreases a deviation between the FEA and the measured results compared to the circular cross-section (about 10%, measured in the first force peak).

- To find the correct mechanical properties for FEA material model, it is necessary to use the multi-strut specimens with appropriate orientation during production due to the influence of internal porosity and surface roughness.
- The shape of the BCC lattice structure was analysed using optical methods. A distinct “water drop” shape was found. It is caused by sticking of the powder on the down-skin strut area due to heat transfer to the surrounding powder.
- A weight comparison of the CAD design and the produced lattice structure shows that for circular simplification of the strut “water drop” shape, the Gaussian strut diameter should be used.

Regarding the scientific questions, the obtained knowledge can be summarized in the following concluding remarks:

- The material porosity is strongly dependent on the input laser energy represented by **LS**, **LP**, **OL**, **OR** and the geometry of the lattice structure. In the case of inclined struts, the porosity is influenced especially by thermal gradient which directs to the platform (down to a surrounding powder) and not in the strut axis direction. It causes accumulation of the thermal energy in the strut and its overheating followed by the change of the microstructure and creation of the gas pores especially close to the down-skin surface. **(The hypothesis H1 was confirmed).**
- During micro-strut lattice structure production, the thin-strut geometry creates more difficult conditions for a transfer of thermal energy from melt pool. It is mainly caused due to a limited amount of energy that the thin cross-section can transfer per unit of time. Therefore, the lattice structure production is more sensitive to suitable SLM process parameters setup in right energy level. **(The hypothesis H2 was confirmed).**
- As was written above, the orientation of the strut changes the direction of the thermal gradient. Using a wrong combination of the SLM process parameters, especially those that provide high energy levels, significant shape changes of the strut cross-section occur in the thermal gradient direction. On the other hand, if the suitable parameters are used, the change of the cross-section will be small. Therefore, the main influence on the change of the shape has input energy E_{in} . **(The hypothesis H3 was falsified).**
- Based on the multi-strut tensile test, **the hypothesis H4 was confirmed** (Figure 6.22). The results show that the main difference is in the elongation at break parameter. It can be caused by a lot of factors, e.g. the specimen in **OR** 90° are higher in axis Z; therefore, they are longer influenced by thermal energy and a material aging occurs. Another reason could be size and shape of struts cross-section in single layers. The elliptical cross-section in case of OR 45° has larger surface and therefore the influence of close the surface porosity can be smaller.

9 LIST OF PUBLICATIONS

Papers published in journals with impact factor

VRÁNA, R.; KOUTNÝ, D., PALOUŠEK, D., PANTĚLEJEV, L., JAROŠ, J., ZIKMUND, T. and KAISER, J. Selective Laser Melting Laser Strategy for Fabrication of Thin Struts Usable in Lattice Structures. *Materials* **2018**, 11 (9), ISSN 1996-1944.

- *Materials MDPI* - **IF 2.467**, Q2

VRÁNA, R.; ČERVINEK, O., MAŇAS, P., KOUTNÝ, D. and PALOUŠEK, D. Dynamic Loading of Lattice Structure Made by Selective Laser Melting - Numerical Model with Substitution of Geometrical Imperfections. *Materials* **2018**, 11(11), ISSN 1996-1944.

- *Materials MDPI* - **IF 2.467**, Q2

Papers published in peer-reviewed journals (WoS or Scopus)

VRANA, R.; KOUTNY, D.; PALOUSEK, D.; ZIKMUND, T. Impact Resistance of Lattice Structure Made by Selective Laser Melting from AlSi12 Alloy. *MM Science Journal*, **2015**, 2015 (4), s. 852-855. ISSN: 1805- 0476.

VRANA, R.; KOUTNY, D.; PALOUSEK, D. Impact Resistance of Different Types of Lattice Structures manufactured by SLM. *MM Science Journal*, **2016**, roč. 2016, č. 6, s. 1579-1585. ISSN: 1803-1269.

Papers in conference proceedings (WoS or Scopus)

VRANA, R.; PALOUSEK, D.; KOUTNY, D.; KOUKAL, O.; ZIKMUND, T.; KREJCI, P. Impact resistance of lattice structure made by Selective Laser Melting technology. In *Euro PM2015 Proceedings*. Reims, France, **2015**. s. 1-6. ISBN: 978-1-899072-47-7.

KOUKAL, O.; KOUTNY, D.; PALOUSEK, D.; **VRANA, R.;** ZIKMUND, T.; PANTELEJEV, L. Research about the Influence of Process Parameters of Selective Laser Melting on Material EN AW 2618. In *Euro PM2015 Proceedings*. Reims, France, **2015**. s. 1-6. ISBN: 978-1-899072-47-7.

VRANA, R.; KOUTNY, D.; PALOUSEK, D.; ZIKMUND, T. Influence of Selective Laser Melting Process Parameters on Impact Resistance of Lattice Structure made from AlSi10Mg. In *World PM2016 Proceedings*. Hamburk, Germany, **2016**, ISBN: 978-189907248-4.

MANAS, P.; **VRANA, R.;** HEJMAL, Z.; DUBEC, B. Determination of the material properties of recycled rubber for explicit FEM simulation. In *ICSMESP 2017 Proceedings*. Prague, Czech Republic, 2017. s. 1-7. ISSN: 2367-2544.

VRANA, R.; VOSYNEK, P., KOUTNY, D., NAVRAT, T., PALOUSEK, D. Evaluation of mechanical behaviour of 3D printed lattice structure by SLM: Experiment and FEA. In *EAN 2018 Proceedings*. Harachov, Czech Republic, **2018**. s. 443-449. ISBN: 978-802704062-9

VAVERKA, O., KOUTNY, D., **VRANA, R.;** PANTELEJEV, L., PALOUSEK, D. Effect of heat treatment on mechanical properties and residual stresses in additively manufactured

parts. In *Engineering Mechanics 2018 24th international conference*. Svatka, Czech Republic, 2018. pp. 897-900. ISBN 978-80-86246-91-8

Papers in other conference proceedings

KOUTNY, D.; **VRANA, R.**; PALOUSEK, D. Dimensional accuracy of single beams of AlSi10Mg alloy and 316L stainless steel manufactured by SLM. In *5th International Conference on Additive Technologies iCAT2014*. Ljubljana: Interesansa, **2014**. s. 142-147. ISBN: 978-961-281-579-0.

VRANA, R.; KOUKAL, O.; KOUTNY, D.; PALOUSEK, D.; KREJCI, P. Device for Testing Impact Resistance of Lattice Structures Panels Produced by the Selective Laser Melting. In *Book of Proceedings of 56th International Conference of Machine Design Department*. První. **2015**. s. 144-149. ISBN: 978-80-552-1377-4.

10 LITERATURE

- [1] DECKARD, Carl R. Apparatus for producing parts by selective sintering. 1984.
- [2] MEINERS WILHELM, WISSENBACH KONRAD, Gasser Andres. Shaped body especially prototype or replacement part production. 1996.
- [3] *SLM Solutions GmbH - History*. 2015.
- [4] *Výrobky z hliníkové pěny* [online]. 2007. Dostupné z: <http://www.mmspektrum.com/clanek/vyrobky-z-hlinikove-peny.html>
- [5] *Apologetics Press* [online]. Dostupné z: <http://www.apologeticspress.org/ApPubPage.aspx?pub=1&issue=581&article=625>
- [6] ŠMARDA JAN. *Biologie pro psychology a pedagogy*. 2007. ISBN 978-80-7367-343-7.
- [7] YADROITSEV, Igor. *Selective laser melting: Direct manufacturing of 3D-objects by selective laser melting of metal powders*. B.m.: LAP LAMBERT Academic Publishing, 2009. ISBN 383-831-794-7.
- [8] *Next Eurostar E3000 satellite to feature Airbus 3D printed aluminum parts | 3D Printer News & 3D Printing News* [online]. [vid. 2018-12-07]. Dostupné z: <https://www.3ders.org/articles/20150321-next-eurostar-e3000-satellite-to-feature-airbus-3d-printed-aluminum-parts.html>
- [9] WEHMÖLLER, M., P. H. WARNKE, C. ZILIAN a H. EUFINGER. Implant design and production-a new approach by selective laser melting. *International Congress Series* [online]. 2005, **1281**, 690–695. ISSN 05315131.
- [10] BRANDL, Erhard, Ulrike HECKENBERGER, Vitus HOLZINGER a Damien BUCHBINDER. Additive manufactured AlSi10Mg samples using Selective Laser Melting (SLM): Microstructure, high cycle fatigue, and fracture behavior. *Materials and Design* [online]. 2012, **34**, 159–169 [vid. 2018-07-05].
- [11] KOUTNÝ, D.; VRÁNA, R.; PALOUŠEK, D. Dimensional accuracy of single beams of AlSi10Mg alloy and 316L stainless steel manufactured by SLM. In: *In 5th International Conference on Additive Technologies iCAT2014* [online]. 2014, s. s. 142-147.
- [12] KEMPEN, K., L. THUIS, J. VAN HUMBEECK a J. P. KRUTH. Mechanical Properties of AlSi10Mg Produced by Selective Laser Melting. *Physics Procedia* [online]. 2012, **39**, 439–446. ISSN 18753892.
- [13] VRÁNA, Radek, Daniel KOUTNÝ, David PALOUŠEK a Tomáš ZIKMUND. Influence of Selective Laser Melting Process Parameters on Impact Resistance of Lattice Structure made from AlSi10Mg. In: *World PM2016 Proceedings* [online]. 2016, s. 6.
- [14] TSOPANOS, S., R. A. W. MINES, S. MCKOWN, Y. SHEN, W. J. CANTWELL, W. BROOKS a C. J. SUTCLIFFE. The Influence of Processing Parameters on the Mechanical Properties of Selectively Laser Melted Stainless Steel Microlattice Structures. *Journal of Manufacturing Science and Engineering* [online]. 2010, **132**(4), 041011. ISSN 10871357.
- [15] SUARD, Mathieu, Pierre LHUISSIER, Rémy DENDIEVEL, Frédéric VIGNAT, Jean-Jacques BLANDIN a François VILLENEUVE. Impact of EBM Fabrication Strategies on Geometry and Mechanical Properties of Titanium Cellular Structures. In: *DDMC 2014 Fraunhofer Direct Digital Manufacturing Conference* [online]. 2014, s. 1–6 [vid. 2018-07-05].
- [16] YAP, C. Y., C. K. CHUA, Z. L. DONG, Z. H. LIU, D. Q. ZHANG, L. E. LOH a S. L. SING. Review of selective laser melting: Materials and applications. *Applied Physics Reviews* [online]. 2015, **2**(4). ISSN 19319401.
- [17] SCHLEIFENBAUM, H., W. MEINERS, K. WISSENBACH a C. HINKE. Individualized production by means of high power Selective Laser Melting. *CIRP Journal of Manufacturing Science and Technology* [online]. 2010, **2**(3), 161–169. ISSN 17555817.
- [18] D. D. GU, W. MEINERS, K. WISSENBACH a R. POPRAWA. Laser additive manufacturing of ceramic components: Materials, processes, and mechanisms. *Laser Additive Manufacturing: Materials, Design, Technologies, and Applications* [online]. 2016, **6608**, 163–180. ISSN 0950-6608.
- [19] SLM Solutions [online]. nedatováno. Dostupné z: <https://slm-solutions.com/>
- [20] *Powder material fabrication* [online]. 2018. Dostupné z: <https://www.ald->

- vt.com/portfolio/engineering/vacuum-metallurgy/vacuum-induction-melting-inert-gas-atomization/
- [21] LEARY, Martin, Maciej MAZUR, Joe ELAMBASSERIL, Matthew MCMILLAN, Thomas CHIRENT, Yingying SUN, Ma QIAN, Mark EASTON a Milan BRANDT. Selective laser melting (SLM) of AlSi12Mg lattice structures. *Materials & Design* [online]. 2016, **98**, 344–357. ISSN 02641275.
- [22] ABELE, Eberhard, Hanns a. STOFFREGEN, Klaus KLIMKEIT, Holger HOCHÉ a Matthias OECHSNER. Optimisation of process parameters for lattice structures. *Rapid Prototyping Journal* [online]. 2015, **21**(1), 117–127. ISSN 1355-2546.
- [23] WEI, Pei, Zhengying WEI, Zhen CHEN, Jun DU, Yuyang HE, Junfeng LI a Yatong ZHOU. The AlSi10Mg samples produced by selective laser melting: single track, densification, microstructure and mechanical behavior. *Applied Surface Science* [online]. 2017, **408**, 38–50. ISSN 01694332.
- [24] YAN, Chunze, Liang HAO, Ahmed HUSSEIN, Philippe YOUNG a David RAYMONT. Advanced lightweight 316L stainless steel cellular lattice structures fabricated via selective laser melting. *Materials and Design* [online]. 2014, **55**, 533–541. ISSN 18734197.
- [25] QIU, Chunlei, Sheng YUE, Nicholas J E ADKINS, Mark WARD, Hany HASSANIN, Peter D LEE, Philip J WITHERS a Moataz M ATTALLAH. Influence of processing conditions on strut structure and compressive properties of cellular lattice structures fabricated by selective laser melting. *Materials Science & Engineering A* [online]. 2015, **628**, 188–197 [vid. 2018-07-05].
- [26] YU, Guanqun, Dongdong GU, Donghua DAI, Mujian XIA, Chenglong MA a Qimin SHI. On the role of processing parameters in thermal behavior, surface morphology and accuracy during laser 3D printing of aluminum alloy. *Journal of Physics D: Applied Physics* [online]. 2016, 15pp [vid. 2018-08-22].
- [27] QIU, Chunlei, Sheng YUE, Nicholas J.E. ADKINS, Mark WARD, Hany HASSANIN, Peter D. LEE, Philip J. WITHERS a Moataz M. ATTALLAH. Influence of processing conditions on strut structure and compressive properties of cellular lattice structures fabricated by selective laser melting. *Materials Science and Engineering: A* [online]. 2015, **638**, 228–231. ISSN 09215093.
- [28] DELROISSE, Pauline, Pascal J. JACQUES, Eric MAIRE, Olivier RIGO a Aude SIMAR. Effect of strut orientation on the microstructure heterogeneities in AlSi10Mg lattices processed by selective laser melting. *Scripta Materialia* [online]. 2017, **141**, 32–35 [vid. 2018-08-22]. ISSN 1359-6462.
- [29] AMANI, Yasin, Sylvain DANCETTE, Pauline DELROISSE, Aude SIMAR a Eric MAIRE. Compression behavior of lattice structures produced by selective laser melting: X-ray tomography based experimental and finite element approaches. *Acta Materialia* [online]. 2018, **159**, 395–407. ISSN 13596454.
- [30] HITZLER, Leonhard, Christoph JANOUSCH, Jochen SCHANZ, Markus MERKEL, Burkhard HEINE, Florian MACK, Wayne HALL a Andreas ÖCHSNER. Direction and location dependency of selective laser melted AlSi10Mg specimens. *Journal of Materials Processing Technology* [online]. 2017, **243**, 48–61. ISSN 09240136.
- [31] HITZLER, L., C. JANOUSCH, J. SCHANZ, M. MERKEL, F. MACK a A. ÖCHSNER. Non-destructive evaluation of AlSi10Mg prismatic samples generated by selective laser melting: Influence of manufacturing conditions. *Materialwissenschaft und Werkstofftechnik* [online]. 2016, **47**(5–6), 564–581 [vid. 2018-12-09]. ISSN 09335137.
- [32] BAGHERIFARD, Sara, Niccolò BERETTA, Stefano MONTI, Martina RICCIO, Michele BANDINI a Mario GUAGLIANO. On the fatigue strength enhancement of additive manufactured AlSi10Mg parts by mechanical and thermal post-processing. *Materials and Design* [online]. 2018, **145**, 28–41. ISSN 18734197.
- [33] MATWEB. *Matweb materials data* [online]. 2012 [vid. 2012-05-04]. Dostupné z: <http://www.matweb.com/>
- [34] DONG, Zhichao, Xiaoyu ZHANG, Wenhua SHI, Hao ZHOU, Hongshuai LEI a Jun LIANG. Study of Size Effect on Microstructure and Mechanical Properties of AlSi10Mg Samples Made by Selective Laser Melting. *Materials* [online]. 2018, **11**(12), 2463. ISSN 1996-1944.
- [35] YAHAYA, Ma, D RUAN, G LU a MS DARGUSCH. Response of aluminium honeycomb sandwich panels subjected to foam projectile impact e An experimental study. *International Journal of Impact Engineering* [online]. 2015, **75**, 100–109 [vid. 2018-07-05].
- [36] HEB SUR, Mohan G., Ronald D. NOEBE a Duane M. REVILOCK. Impact resistance of lightweight

- hybrid structures for gas turbine engine fan containment applications. *Journal of Materials Engineering and Performance* [online]. 2003, **12**(4), 470–479. ISSN 10599495.
- [37] SHEN, Yiou, Wesley CANTWELL, Robert MINES a Yan LI. Low-velocity impact performance of lattice structure core based sandwich panels. *Journal of Composite Materials* [online]. 2014, **48**(25), 3153–3167. ISSN 1530793X.
- [38] MINES, R. A.W., S. TSOPANOS, Y. SHEN, R. HASAN a S. T. MCKOWN. Drop weight impact behaviour of sandwich panels with metallic micro lattice cores. *International Journal of Impact Engineering* [online]. 2013, **60**, 120–132. ISSN 0734743X.
- [39] SWANSON, Stephen R. Limits of quasi-static solutions in impact of composite structures. *Composites Engineering* [online]. 1992, **2**(4), 261–267 [vid. 2018-12-12]. ISSN 0961-9526.
- [40] MINES, Robert A.W., Sozohn TSOPANOS a S.T. MCKOWN. Verification of a Finite Element Simulation of the Progressive Collapse of Micro Lattice Structures. *Applied Mechanics and Materials* [online]. 2011, **70**, 111–116. ISSN 1662-7482.
- [41] *LS-Dyna User's Manual*. 2003.
- [42] LABEAS, G. Investigation of sandwich structures with innovative cellular metallic cores under low velocity impact loading. *Plastics, Rubber and Composites* [online]. 2013, **42**(5), 194–202. ISSN 1465-8011.
- [43] WANG, Yonghui, J.Y. Richard LIEW, Siew Chin LEE a Wei WANG. Experimental and analytical studies of a novel aluminum foam filled energy absorption connector under quasi-static compression loading. *Engineering Structures* [online]. 2017, **131**, 136–147 [vid. 2017-05-03]. ISSN 01410296.
- [44] KOPANIDIS, A., A. THEODORAKAKOS, E. GAVAISES a D. BOURIS. 3D numerical simulation of flow and conjugate heat transfer through a pore scale model of high porosity open cell metal foam. *International Journal of Heat and Mass Transfer* [online]. 2010, **53**(11–12), 2539–2550. ISSN 00179310.
- [45] SHIMIZU, T, K MATSUZAKI, H NAGAI a N KANETAKE. Production of high porosity metal foams using EPS beads as space holders. *Materials Science & Engineering A* [online]. 2012, **558**, 343–348 [vid. 2018-07-05].
- [46] ZHU, Ling, Kailing GUO, Yinggang LI, T. X. YU a Qingwen ZHOU. Experimental study on the dynamic behaviour of aluminium foam sandwich plates under single and repeated impacts at low temperature. *International Journal of Impact Engineering* [online]. 2018, **114**(December 2017), 123–132. ISSN 0734743X.
- [47] BANHART, J. Manufacture, characterisation and application of cellular metals and metal foams. *Progress in Materials Science* [online]. 2001, **46**(6), 559–632. ISSN 00796425.
- [48] KARAGIOZOVA, D. Dynamic buckling of elastic–plastic square tubes under axial impact—I: stress wave propagation phenomenon ARTICLE IN PRESS. *International Journal of Impact Engineering* [online]. 2004, **30**(2), 143–166 [vid. 2018-07-05].
- [49] ABOULKHAIR, Nesma T., Nicola M. EVERITT, Ian ASHCROFT a Chris TUCK. Reducing porosity in AlSi10Mg parts processed by selective laser melting. *Additive Manufacturing* [online]. 2014, **1–4**, 77–86. ISSN 22148604.
- [50] ZHANG, Baicheng, Lucas DEMBINSKI a Christian CODDET. The study of the laser parameters and environment variables effect on mechanical properties of high compact parts elaborated by selective laser melting 316L powder. *Materials Science and Engineering A* [online]. 2013, **584**, 21–31. ISSN 09215093.
- [51] YAN, Chunze, Liang HAO, Ahmed HUSSEIN a David RAYMONT. Evaluations of cellular lattice structures manufactured using selective laser melting. *International Journal of Machine Tools and Manufacture* [online]. 2012, **62**, 32–38 [vid. 2018-08-22].
- [52] SMITH, M., Z. GUAN a W. J. CANTWELL. Finite element modelling of the compressive response of lattice structures manufactured using the selective laser melting technique. *International Journal of Mechanical Sciences* [online]. 2013, **67**, 28–41. ISSN 00207403.
- [53] USHIJIMA, K., W. J. CANTWELL, R. A.W. MINES, S. TSOPANOS a M. SMITH. An investigation into the compressive properties of stainless steel micro-lattice structures. *Journal of Sandwich Structures and Materials* [online]. 2011, **13**(3), 303–329. ISSN 10996362.
- [54] GRYTEN, F., T. BØRVIK, O.S. HOPPERSTAD a M. LANGSETH. Low velocity perforation of AA5083-H116 aluminium plates. *International Journal of Impact Engineering* [online]. 2009,

- 36(4)**, 597–610 [vid. 2018-07-05]. ISSN 0734-743X.
- [55] GRYTEN, F, B HOLMEDAL, O S HOPPERSTAD a T BØRVIK. Evaluation of identification methods for YLD2004-18p. *International Journal of Plasticity* [online]. 2008, **24**, 2248–2277 [vid. 2018-07-05].
- [56] LI, Xin, Peiwen ZHANG, Zhihua WANG, Guiying WU a Longmao ZHAO. Dynamic behavior of aluminum honeycomb sandwich panels under air blast: Experiment and numerical analysis. *Composite Structure* [online]. 2014, **108**, 1001–1008 [vid. 2018-08-29].
- [57] MOHMMED, Ramadan, Azzam AHMED, Mohamed Ahmed ELGALIB a Hashim ALI. Low Velocity Impact Properties of Foam Sandwich Composites : A Brief Review. *International Journal of Engineering Science and Innovative Technology* [online]. 2014, **3(2)**, 579–591.
- [58] MOHMMED, Ramadan, Fa ZHANG, Baozhong SUN a Bohong GU. Finite element analyses of low-velocity impact damage of foam sandwiched composites with different ply angles face sheets. *Materials and Design* [online]. 2013, **47**, 189–199 [vid. 2018-07-05].
- [59] OZDEMIR, Zuhail, Andrew TYAS, Russell GOODALL a Harm ASKES. Energy absorption in lattice structures in dynamics: Nonlinear FE simulations. *International Journal of Impact Engineering* [online]. 2017, **102**, 1–15. ISSN 0734743X.
- [60] PALOUSEK, David, Milan OMASTA, Daniel KOUTNY, Josef BEDNAR, Tomas KOUTECKY a Filip DOKOUPIL. Effect of matte coating on 3D optical measurement accuracy. *Optical Materials* [online]. 2015, **40**, 1–9 [vid. 2018-07-05]. ISSN 09253467.
- [61] BHADARIA, H S, Annapurna SINGH a Anuj KUMAR. Comparison between Various Edge Detection Methods on Satellite Image. *International Journal of Emerging Technology and Advanced Engineering*. 2013, **3(6)**, 324–328.
- [62] SHRIVAKSHAN, G T.
A_Comparison_of_various_Edge_Detection_Techniques_used_inImage_Processing_IJCSI-9-5-1-269-276_September_2012. 2012, **9(5)**, 269–276. ISSN 1694-0814; 1694-0784.
- [63] RAVARI, Mohammad Reza Karamooz, Mahmoud KADKHODAEI a Abbas GHAEI. Effects of asymmetric material response on the mechanical behavior of porous shape memory alloys. *Journal of Intelligent Material Systems and Structures* [online]. 2016, **27(12)**, 1687–1701. ISSN 15308138.
- [64] JENÍK, Ivan, Petr KUBÍK, František ŠEBEK, Jiří HŮLKA a Jindřich PETRUŠKA. Sequential simulation and neural network in the stress–strain curve identification over the large strains using tensile test. *Archive of Applied Mechanics* [online]. 2017, **87(6)**, 1077–1093. ISSN 14320681.
- [65] ŠEBEK, František, Petr KUBÍK, Jindřich PETRUŠKA a Jiří HŮLKA. Extremely Low-Stress Triaxiality Tests in Calibration of Fracture Models in Metal-Cutting Simulation. *Metallurgical and Materials Transactions A: Physical Metallurgy and Materials Science* [online]. 2016, **47(11)**, 5302–5312. ISSN 10735623.

LIST OF FIGURES AND TABLES

List of Figures

Fig. 1.1. (a) Absorbers of impact energy from metal foam [4]; (b) inner structure of bone [5]	12
Fig. 1.2. Lattice structure bracket for space application (a) ESA, BUT, LKE; (b) Airbus [8]	13
Fig. 2.1. Concept of SLM process. (a) High-power laser melts selective areas of the powder bed; (b) Process is repeated for successive layers; (c) Surrounding powder is removed [16].	14
Fig. 2.2. SLM 280 ^{HL} machine from SLM Solution GmbH [19]	15
Fig. 2.3. Schema of the gas atomization [20]	15
Fig. 2.4. (a) Gyroid unit; (b) Schematic illustration of the SLM manufacturing process of the circular strut [24]	16
Fig. 2.5. (a) Variation of porosity within the struts as a function of laser power at a traverse speed of 7000 mm.s ⁻¹ ; (b) Magnified view of the strut surface [25]	16
Fig. 2.6. Positioning of the laser spot relative to the nominal contour using different laser spot displacements [22]	17
Fig. 2.7. Representative optical microscope image of the lower and upper faces of 35.26°, 45° and 90° struts [21]	17
Fig. 2.8. (a) Uniaxial compression stress-strain responses of tested lattice specimens; (b) Von Mises stress and relative stiffness, k_R , both normalised to data for unconstrained BCC [21]	18
Fig. 2.9. (a) Real AlSi10Mg beam diameter in dependence on beam inclination; Evaluation of dimensional accuracy of individual beams, (b) minimum circumscribed cylinder, (c) maximum inscribed cylinder (left) [11]	19
Fig. 2.10. (a) Comparison of FEA analysis using various strut diameter and the real CT shape; (b) Tomographic reconstruction of a 1mm strut with the inscribed cylinder (dark) inside the real strut (bright) [15]	19
Fig. 2.11. (a) Comparison of surface roughness contour plots at different processing conditions; (b) The linear shrinkage ratio of different laser power in the simulation and experiments [26]	20
Fig. 2.12. Motion trail of single gas pore and the velocity vector plots around the pore in the molten pool at different time: (a) $t = 62 \mu\text{s}$; (b) $t = 102 \mu\text{s}$; (c) $t = 142 \mu\text{s}$ [27]	20
Fig. 2.13. (a) Influence of incident laser power and scanning speed on the relative density of SLM-processed specimens; (b) Influence of hatch spacing on the relative density of SLM-processed specimens under the laser power of $P = 180 \text{ W}$, scanning speed of $v = 1000 \text{ mm} \cdot \text{s}^{-1}$ and hatch spacing of $50 \mu\text{m}$ [23].	21
Fig. 2.14. Comparison of the microstructure of (a) a vertical and (b) an inclined strut (c) Porosity in zone A and B of (b) observed by 3D X-ray tomography along virtual parallelepiped oriented along the axis of the strut [28].	21
Fig. 2.15. (a) Local cavities in red and AlSi10Mg phase in transparent gray; (b) One diagonal slice of the 3D tomographic image [29]	22
Fig. 2.16. Contour plots of VVF resulting from FE simulations of the homogeneous (a) or heterogeneous GTN models (b) of the thin-strut specimen, at a nominal strain of 0.066 corresponding to experimental plastic collapse strain [29]	22
Fig. 2.17. Stress-strain curves obtained by in-situ/ex-situ compression, FE simulations of the (a) thin-strut and (b) thick-strut specimens. The dotted blue, dashed red and solid green lines correspond to FE simulations with non-porous J2 plasticity, homogeneous GTN and heterogeneous GTN models, respectively [29]	23
Fig. 2.18. (a) The specimens' orientation during SLM production; (b) SLM laser strategy and its influence on the close to surface porosity [12]	23
Fig. 2.19. The specimens' orientation during SLM production [10]	24

Fig. 2.20. (a) Schema of the configurations in the build space; (b) Young’s modulus dependency of AlSi10Mg for tensile loading in regard to the orientation during the SLM process [30]	24
Fig. 2.21. (a) The engineering stress-strain curves for AB and HT specimen’s series; (b) the applied T6 heat treatment (HT) [32].....	25
Tab. 2.2 The mechanical properties for SLM specimens compared with convent. cast material [32].....	25
Fig. 2.22. (a) SEM micrographs of failure surfaces of 316L struts; (b) tensile mechanical testing of wire [14]	27
Fig. 2.23. Effect of build size on the mechanical performance of AlSi10Mg specimens: (a) EM and EL; (b) <i>UTS</i> and <i>YS</i> [34].....	27
Fig. 2.24. Impact experimental set-up.[35]	28
Fig. 2.25. The drop-weight rig used to characterise the dynamic properties of specimens [37]	28
Fig. 2.26. Impactor load - displacement curves of sandwich panels based on (a) the Ti64 lattice core and (b) the aluminium honeycomb core for corner supported low velocity impact tests. Stainless steel 316L data shown for comparison; (c) Load vs impactor displacement for various impact energies for 316L stainless steel core sandwich panel under four-point support [38]	29
Fig. 2.27 Struts SEM images of SS316L lattice structure blocks manufactured using (a) P=140W, T=500 ms and (b) P=70W, T=1000 ms [37].	30
Fig. 2.28 (a) Permanent indentation vs. absorbed energy plots of SS316L lattice sandwich panels fully supported, strain rate ranged from $2 \times 10^{-4} \text{ s}^{-1}$ to $3 \times 10^2 \text{ s}^{-1}$; (b) Ti64 #2 and #5 following impact tests at velocity of 3 m.s^{-1} [37].	31
Fig. 2.29 (a) Perforation and simulation, (b) Behaviour of a specific micro strut (A) [40]	31
Fig. 2.30 (a) Quarter panel FE model with symmetrical boundary conditions; (b) Mesh (FE) of skin and core of homogenised core FE model [42]	33
Fig. 2.31 (a) bcc-LV2 (99 J); (b) bcc-LV3 (20 J) [42]	33
Fig. 2.32 Example of application of energy absorption connector [43].....	34
Fig. 2.33 Determination of densification displacement.[43]	35
Fig. 5.1. SLM powder characteristics - (a) particle size distribution chart; (b)shape of particles (SEM)	44
Fig. 5.2. The specimen after basic grinding; (a) the top view images captured by lighting microscope; (b) three areas of the struts after converting of the colours in ImageJ software.....	45
Fig. 5.3. Struts analysis - (a) surface roughness evaluation in GOM Inspect software; (b) group of four specimens measured together in VGStudio MAX software; (c) transparent 3D render of the strut with the lowest porosity of 0.17% (d) transparent 3D render of the strut with the highest porosity of 2.93%.	45
Fig. 5.4. Schema of the elliptic laser tracks trajectory	46
Fig. 5.5. (a) Measurement of the elliptical cross-section; (b) Visual 2D representation of elements used for dimensional struts analysis.....	47
Fig. 5.6. (a) Orientation of specimen with support structures; (b) Produced specimen fixed on the platform.....	47
Fig. 5.7. Mechanical testing using Zwick Z020 machine (a) tensile test, (b) compression test	48
Fig. 5.8. (a) Low-velocity impact tester; (b) Geometry of the flat indenter; (c) Geometry of the ball indenter	48
Fig. 5.9. (a) Shape of the single-track weld specimen; (b) measurement of the width of the single welds; (c) One combination of process parameters produced in and against atmosphere flow.....	49
Fig. 5.10. (a) Shape of the specimen shapes with inclination of 90° ; (b) used overlap strategy	50
Fig. 5.11. Specimens for (a) quasi-static tensile testing of bulk material (TB-series); (b) quasi-static tensile testing of multi-strut specimens (TS-series).....	51
Fig. 5.12. Specimens for (a) quasi-static compressive (C-series) and low-velocity impact testing (IT-series); (b) optical analysis (O-series).....	51

Fig. 5.13. Numerical model in the Ansys software (a) quarter model with bodies and constrains; (b) finite element mesh quality	52
Fig. 6.1. Experimental device for impact tests	55
Fig. 6.2. (a) The deformation member with strain gauges; (b) The Falling head	55
Fig. 6.3. (a) impact resistance testing; (b) fast compression test.....	56
Fig. 6.4. Scheme of measuring chain	56
Fig. 6.5. (a) Data recorded from strain gauge, (b) Integration of deceleration a ($m.s^{-2}$) by time t (s), (c) Second integration of deceleration path a ($m.s^{-2}$) by time t (s)	57
Fig. 6.6. Image analysis (a) 8-bit colour image; (b) 8-bit grayscale image; (c) Canny edge detector application; (d) Target boundary classification; (e) Ellipse fitting - target centre coordinates computation.....	58
Fig. 6.7. Impact tester software GUI	60
Fig. 6.8. The average width of the single welds (coloured cells); Line energy (colour-free cells)	62
Fig. 6.9. Porosity vs. input energy dependence (a) for inclination 90° ; (b) for inclination 35.26°	63
Fig. 6.10. (a) μ CT porosity vs. input and linear energy dependences, black mark represents the universal SLM process parameters; (b) focused area of results up to 1% porosity level with marked perspective areas.	64
Fig. 6.11. (a) The influence of various LS levels on porosity; (b) The influence of various LP levels on porosity.	64
Fig. 6.12. (a) Surface roughness vs. linear energy dependence – on the side and down-skin struts surface, black marks represent the universal SLM process parameters.; (b) surface roughness vs. input energy dependence.....	65
Fig. 6.13. (a) The influence of various LS levels on surface roughness; (b) The influence of various LP levels on surface roughness.....	65
Fig. 6.14. Microstructure of the struts (a) LP of 250 W, LS of 1400 mm.s^{-1} , E_{in} of 9.17 J, E_{lin} of 0.18 J.mm^{-1} with description common for all pictures; (b) LP of 300 W, LS of 500 mm.s^{-1} , E_{in} of 13.54 J, E_{lin} of 0.6 J.mm^{-1} (c) LP of 350 W, LS of 500 mm.s^{-1} , E_{in} of 15.43 J, E_{lin} of 0.7 J.mm^{-1} ; (d) LP of 400 W, LS of 1700 mm.s^{-1} , E_{in} of 7.56 J, E_{lin} of 0.24 J.mm^{-1}	66
Fig. 6.15. SLM Solutions universal struts laser strategy	67
Fig. 6.16. Schema of elliptical/circular strategy	67
Fig. 6.17. Script for designing of the contour strategy	68
Fig. 6.18. Schema of elliptical/circular and line strategy.....	68
Fig. 6.19. Schematic view of the parameters of the script.....	69
Fig. 6.20. Side view on the impact specimen using the lighting microscope	70
Fig. 6.21. Comparison of the real and ideal cylinder cross-section: (a) shape analysis in the GOM Inspect software and (b) real cross-section in four corner struts.....	71
Fig. 6.22. (a) Quasi-static stress-strain curves of the struts tensile specimens; and (b) Quasi- static stress-strain curves of the compression specimens.	72
Fig. 6.23. The results from low-velocity impact testing: (a) Single IT-series with diameter $d =$ 0.8 mm ; (b) variance of force and deformation of all IT-series; (c) average initial speed, deformation curves; and (d) average force-deformation curves.	73
Fig. 6.24. Comparison of the results of the IT-0.8 series and the numerical simulation with (a) circular cross-section; and (b) elliptical cross-section.	75
Fig. 6.25. Gradual deformation of the specimen with circular strut cross-section in time — (a) 0 ms ; (b) 1.31 ms ; (c) 3.73 ms ; (d) real damage of the specimen IT-2 after low- velocity impact test.	75
Fig. 6.26. (a) Real size of the inscribed diameter vs. real diameter of the struts from AISi10Mg; (b) Influence of 35° strut inclination on strut size of d_{Gauss} and d_{in} ; this orientation is similar as in BCC lattice structure	76
Fig. 6.27. Comparison of FEA results and experiment for different strut diameters; (a) reaction force; and (b) deformation.....	77

Fig. 6.28. The results from low-velocity impact with tip indenter: (a) Single ITS-series with diameter $d = 0.8$ mm; (b) variance of force and deformation of all ITS-series; (c) average initial speed vs. deformation curves; and (d) average force vs. deformation curves. 78

Fig. 6.29. Comparison of the measured data of the ITS-0.8 series and the numerical simulation (a) deformation vs. time dependence; and (b) reaction force vs. time dependence. 78

Fig. 6.30. (a) Comparison of FEA results and experiment for different strut diameters; (b) specimen deformation after impact with tip in FEA..... 79

Fig. 7.1 (a) Scheme of the heat transfer; Comparison of inclined and perpendicular strut (b) for parameters LP 275 W, LP 400 J.mm⁻¹; (c) LP 350 W, LP 500 J.mm⁻¹. 80

Fig. 7.2 Initial analysis of influence of the internal porosity on the mechanical properties of the lattice structure 82

Fig. 7.3 The perspective area for struts fabrication - linear energy E_{lin} (J.mm⁻¹) (green cells) and input energy to the layer E_{in} (J) (red cells) 83

List of Tables

Tab. 2.1 Averaged results for the mechanical properties, tensile test in accordance to the DIN EN ISO 6892-1:2009–12 [30]..... 25

Tab. 2.3 Fatigue strength corresponding to 3 million cycles for all series [32] 26

Tab. 2.4 Comparison of averaged mechanical properties for AlSi10Mg; all results refer to samples without additional post heat-treatment [30] 26

Tab. 5.1 Comparison of different laser strategies applied on thin struts - the developed contour strategy and standard SLM strategy 50

Tab. 6.1 The porosity level of the strut samples—3D renders with pores shape; the pores in the entire volume were projected to the plane of the view 63

Tab. 6.2 Optical measurement by Atos Triple Scan system (lattice cubes; nom. diameter $d = 0.8$ mm)..... 70

Tab. 6.3 The comparison of real and ideal weight of the specimen 71

Tab. 6.4 The mechanical properties of the tensile specimens 72

Tab. 6.5 The average results of the low-velocity flat impact..... 73

Tab. 6.6. Material models used for lattice structure specimens FEA. 74

Tab. 6.7 Relative error comparison between different strut-cross sections. 75

Tab. 6.8 The average results of the low-velocity flat impact..... 77

LIST OF SYMBOLS AND ABBREVIATIONS

SLM		selective laser melting technology
DMLS		direct metal laser sintering
FEM		finite element method
CAD		computer aided design
YLR		ytterbium fibre lasers
BCC		body centred cubic
FCC		face centred cubic
BCCZ		body centred cubic with z strut
FBC CZ		face body centred cubic with z strut
μ CT		micro computed tomography
3D		three-dimensional
FEA		finite element analysis
HT		heat treatment
AB		as-built state
SB		sand blasted
SP		shoot peening
SEM		scanning electron microscope
EBM		electron-beam melting
FH		falling head
HS		high-speed
LP	W	laser power
LS	mm.s^{-1}	laser speed
OR	$^{\circ}$	strut inclination
d	mm	nominal diameter
V_{ef}	-	effective strut volume
UTS	MPa	ultimate tensile strength
YTS	MPa	yield tensile strength
$YTS_{0.2\%}$	MPa	yield tensile strength at strain 0.2%
E	MPa	young's modulus
E_T	MPa	tangent modulus
ν	-	poisson's ration
ρ	-	relative density
w	μm	width of the single weld
OL	%	overlap of the laser welds
BC	μm	beam compensation
CH	μm	contour hatch
E_{lin}	J.mm^{-1}	linear energy
E_{in}	J	input energy
l	mm	length of the laser tracks
N	-	number of contours

o	mm	circumference of the single track
a_{BCC}	mm	length of the BCC unit cell
d_{in}	mm	diameter of inscribed cylinder
d_{Gauss}	mm	diameter of Gauss cylinder
d_{out}	mm	diameter of circumscribed cylinder
d_r	mm	real measured diameter
t	mm	thickness
m	kg	mass of the loading element
h	m	height of the fall
v_{in}	$\text{m}\cdot\text{s}^{-1}$	impact velocity
E_{I}	J	impact energy
E_{out}	J	rebounced energy
EPS	-	equivalent plastic strain
F_{min}	N	minimum force during impact
F_{max}	N	maximum force during impact
		deformation of the specimen at
X_{Fmax}	mm	maximum force
σ_{max}	MPa	maximum engineering stress
		strain at the maximum engineering
$\epsilon_{\sigma\text{max}}$	-	stress
t_{Fmin}	ms	time at minimum force
t_{Fmax}	ms	time at maximum force
t_{def}	ms	duration of deformation
		deformation of the specimens under
X_{Dyn}	mm	dynamic loading
E_{Abs}	J	absorbed energy
v_{Up}	$\text{mm}\cdot\text{s}^{-1}$	speed of the rebound
		average stiffness of the specimens
k_{Dyn}	$\text{N}\cdot\text{mm}^{-1}$	under dynamic loading
		absorption power of the specimens
P_{Abs}	$\text{J}\cdot\text{s}^{-1}$	under dynamic loading

LIST OF APPENDICES

- 1) **Paper A** - Selective Laser Melting Laser Strategy for Fabrication of Thin Struts Usable in Lattice Structures
- 2) **Paper B** - Selective Laser Melting Laser Strategy for Fabrication of Thin Struts Usable in Lattice Structures

Article

Selective Laser Melting Strategy for Fabrication of Thin Struts Usable in Lattice Structures

Radek Vrána ^{1,*}, Daniel Koutný ¹, David Paloušek ¹, Libor Pantělejev ², Jan Jaroš ¹, Tomáš Zikmund ³ and Jozef Kaiser ³

¹ Brno University of Technology, Faculty of Mechanical Engineering, Institute of Machine and Industrial Design, Technická 2896/2, 616 69 Brno, Czech Republic; Daniel.Koutny@vut.cz (D.K.); David.Palousek@vut.cz (D.P.); Jan.Jaros@vut.cz (J.J.)

² Brno University of Technology, Faculty of Mechanical Engineering, Institute of Materials Science and Engineering, Technická 2896/2, 616 69 Brno, Czech Republic; Libor.Pantelejev@vut.cz

³ Brno University of Technology, Central European Institute of technology BUT, Purkyňova 123, 612 00 Brno, Czech Republic; Tomas.Zikmund@vut.cz (T.Z.); Jozef.Kaiser@vut.cz (J.K.)

* Correspondence: Radek.Vrana@vut.cz; Tel.: +420-541-144-927

Received: 30 August 2018; Accepted: 12 September 2018; Published: 18 September 2018



Abstract: This paper deals with the selective laser melting (SLM) processing strategy for strut-lattice structure production which uses only contour lines and allows the porosity and roughness level to be managed based on combination of the input and linear energy parameters. To evaluate the influence of a laser scanning strategy on material properties and surface roughness a set of experiments was performed. The single welds test was used to find the appropriate processing parameters to achieve continuous welds with known width. Strut samples were used to find a suitable value of weld overlapping and to clarify the influence of input and linear laser energy on the strut porosity and surface roughness. The samples of inclined hollow struts were used to compare the wall thickness with single welds width; the results showed about 25% wider welds in the case of a hollow strut. Using the proposed SLM strategy it is possible to reach a significantly lower porosity and surface roughness of the struts. The best results for struts with an inclination of 35.26° were achieved with 25% track overlapping, input energy in the range from 9 J to 10.5 J and linear energy E_{lin} from 0.25 to 0.4 J/mm; in particular, the relative density of 99.83% and the surface roughness on the side of the strut of Ra 14.6 μm in an as-built state was achieved.

Keywords: selective laser melting (SLM); AlSi10Mg aluminum alloy; scanning strategy; porosity; roughness; contour strategy; melt-pool size; linear energy; input energy

1. Introduction

Nowadays, metallic porous materials such as cellular structures or foams have a wide range of applications. Metal foams are mostly used for energy-absorbing applications or as filling material of the conventionally produced profiles for weight reduction. Their most significant advantage is relatively cheap mass production. However, the regularity and shape of the foam structure cannot be precisely controlled [1–5]. On the other hand, the additively manufactured cellular lattice structures are mostly used for special parts in aerospace, space, cooling or biomedical applications [6–8]. The most important advantages of the lattice structure are their shape regularity and a wide range of possible materials that can be used [9,10]. One of the suitable additive technologies for lattice structure production is selective laser melting (SLM).

SLM is a layer-based metal additive technology allowing for rapid fabrication of prototypes and lightweight components with complex geometry [11–14]. Fabrication, using SLM, is affected by many

process parameters which have a significant effect on the final material properties. The main SLM process parameters are laser power (*LP*), laser speed (*LS*), thickness of the applied powder layer, distance between laser tracks, diameter of the laser beam, and scanning direction [15]. Its influence on the final mechanical properties was examined, especially for solid-based production; however, for lattice structures, this has not been well investigated.

Qiu et al. [8] investigated the influence of the laser power (*LP*) and the scanning (*LS*) speed on the diameter, shape and porosity of the struts made of AlSi10Mg material. The linear dependence between the strut diameter and the increasing *LP* was found. The authors used *LS* of 3500 mm/s while the *LP* was changed in the range from 150 W to 400 W. The diameter of strut changed from 260 μm to 500 μm for the nominal diameter of 300 μm . Due to the number of struts in the lattice structure, the mechanical properties can significantly change. The dependence of the main process parameters on the strut porosity was evaluated, but only for one *LP* and *LS* level. Abele et al. [16] dealt with dimensional accuracy of the strut structure. The authors tested a laser strategy for lattice structure production focused on high dimensional accuracy of very thin struts ($d = 0.2 \text{ mm}$). These struts were produced by only one laser path, and therefore the authors investigated primarily the offset of the laser contour paths. The linear energy E_{lin} (J/mm) and laser spot diameter were used as the main parameters. The authors defined the struts' size limitation as two times laser spot diameter. Leary et al. [17] investigated a manufacturability and surface roughness of the struts with the orientation typical for struts–lattice structures. They found that the surface roughness on the strut down-skin surface is significantly higher due to a heat transfer and sticking of the surrounding powder on the strut down-skin. The surface roughness is strongly dependent on the strut orientation which was also described by other authors [10,16,17]. Yan et al. [10] explained the higher surface roughness on the down-skin surface by the “stair effect” after slicing of the strut to the single layers. This effect increases at a lower strut inclination, where a greater part of the layer is produced directly on the powder. However, a lower height of layer thickness could decrease this effect. Koutný et al. [18] examined the influence of the strut orientation on the strut size. The samples were measured by a 3D optical scanner and evaluated by maximum inscribed cylinders inside the struts. Correction parameters for the struts' production with the accurate size were proposed.

Yu et al. [19,20] investigated the influence of the laser power and the scanning speed on the width of the single track. The scanning speed was found to be more influential in relation to the final width than the laser power. Samples fabricated with high energy density had a high porosity in the upper layers because the previous layers were re-melted and gas pores moved up to the current layer. Parts with full density were produced with high laser energy density. Wei et al. [21] showed that the weld samples produced in the linear energy density range of 1.5–1.875 J/cm had a continuous scan track with a relatively smooth surface without intertrack pores. Delroisse et al. [22] studied the influence of strut orientation on the microstructure. They found a heterogenous microstructure in case of inclined struts, while the vertical struts had a fully homogenous structure. The differences were explained by worse heat transfer in the bottom zone of the strut caused by strut orientation.

Koutný et al. [18] also examined the influence of the strut orientation on the strut size for samples made of stainless steel (*SS*) material. The results of *SS* material were different compared to aluminum alloy; while the samples of *SS* material had the diameter smaller than nominal, the samples of aluminum alloy had a larger diameter. Attar et al. [23] examined commercially pure titanium alloy (CP-Ti) from powder with a wide grain size range up to 100 μm . The authors experimentally investigated the SLM process parameter to produce nearly full dense (>99.5%) CP-Ti cylindrical samples with diameter $d = 4 \text{ mm}$ without any post-treatment.

The present study deals with SLM scanning strategy for struts fabrication using concentric contour laser paths in the entire strut cross-section instead of volume strategy [16]. The main aim is to allow for fabrication of struts–lattice structures with expected mechanical and material properties with high repeatability. This is very important for designing components for aerospace or space industries using finite element method (FEM) analysis [24] and topology optimization with great strength to weight

ratio. Due to a large number of the struts in the lattice structure, even a low increase in the single strut dimension can significantly change the mechanical properties of the lattice structure [8,25–28]. Also, the influence of the *LS* and *LP* process parameters on the struts' surface roughness and porosity are described.

2. Materials and Methods

2.1. Metal Powder Analysis

The AlSi10Mg aluminum alloy metal powder (TLS Technik GmbH, Bitterfeld, Germany) was used in all experiments. The metal powder was produced using a gas atomization in nitrogen atmosphere and its particles were almost spherical in shape (Figure 1b). A particle size distribution was analyzed (Horiba LA-960, Horiba, Kyoto, Japan) for powder quality verification. The results can be seen in the chart (Figure 1a). The particle mean size was 41.41 μm , median size was 40.7 μm and standard deviation was 12.9 μm . The particle size up to 25.2 μm represents 10% and the particle size up to 58 μm represents 90% of particle size distribution. Depending on the particle size distribution, a 50 μm layer was applied.

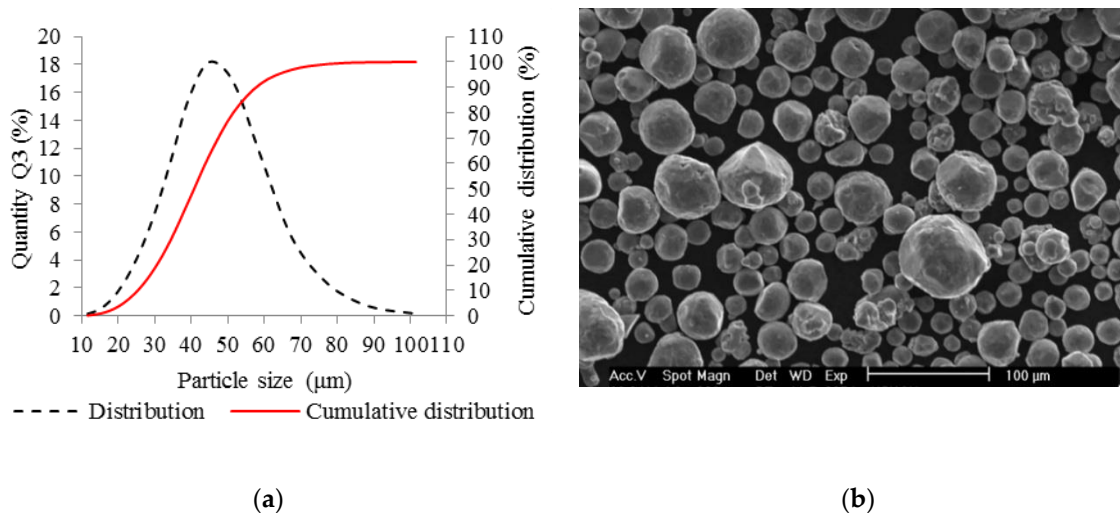


Figure 1. Selective laser melting (SLM) powder characteristics; (a) chart of particle size distribution; (b) shape of powder particles (scanning electron microscopy (SEM)).

2.2. Roughness Analysis

The struts samples were digitized by the optical measurement system (Atos Triple Scan III, GOM GmbH, Braunschweig, Germany) to find out the surface roughness on the strut side. The optical system was equipped with two 8 Mpx cameras and MV60 lens (resolution 17 μm). The samples were coated with a thin layer of TiO_2 powder (thickness of around 3 μm) [29] before the scanning process and digitized separately one by one for a more detailed measurement. After digitization, the data were polygonised using a “more detailed” option in GOM Atos software. With the optical measurement, the down-skin surface cannot be sufficiently digitized. Therefore, data of micro-computed tomography were used.

The GOM Inspect software was employed to evaluate the surface roughness by comparing the section line of digitized strut surface and the best-fitted computer-aided design (CAD). (Figure 3a). Obtained values were used for calculation of the R_a surface roughness according to Equation (1).

$$Ra = \frac{1}{n} \sum_{i=1}^n |z_i| = \frac{|z_1| + |z_2| + \dots + |z_n|}{n} (\mu\text{m}) \quad (1)$$

2.3. Porosity Analysis

Software Image J was used for the initial porosity analysis of the top view sample images (8-bites) after basic grinding with the use a hand grinder (GP-2 Grinder, Sinowon, Dongguan, China). The image area for the analysis was cropped out using the rectangle window without inclusion of the rough border of the strut. Then, the colors were converted to black and white using the automatic threshold to reach a repeatability for all samples. The results of the porosity were evaluated as the percentage of black in the color white (Figure 2).

Internal porosity was also analyzed using the micro-computed tomography (μ CT, GE phoenix v|tome|x L240, GE, Wunstorf, Germany). The main parameters of the X-ray tube used were the voltage of 130 kV, current of 100 μ A, and filter of 0.5 mm copper plate. Within two μ CT measurements, two groups of four samples were jointly analyzed (Figure 3b). The measured data were obtained with the 15 μ m linear voxel size resolution and were reconstructed (using the back-projection algorithm) in the Datos reconstruction software. All subsequent post-processing was performed in the software VGStudio MAX 3.1.

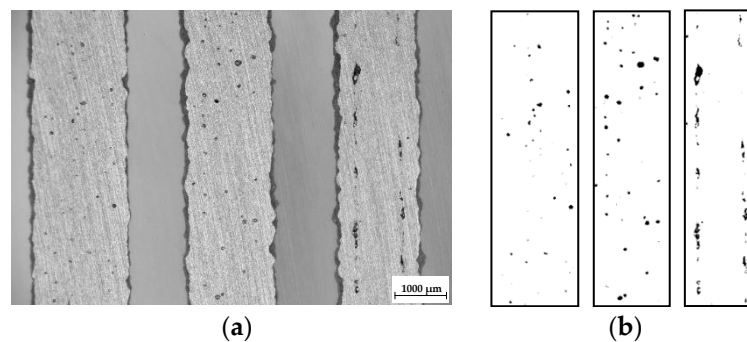


Figure 2. The samples after basic grinding to the struts mid-plane; (a) the top view images captured by light microscope; (b) three areas of the struts after converting of the colors in ImageJ software.

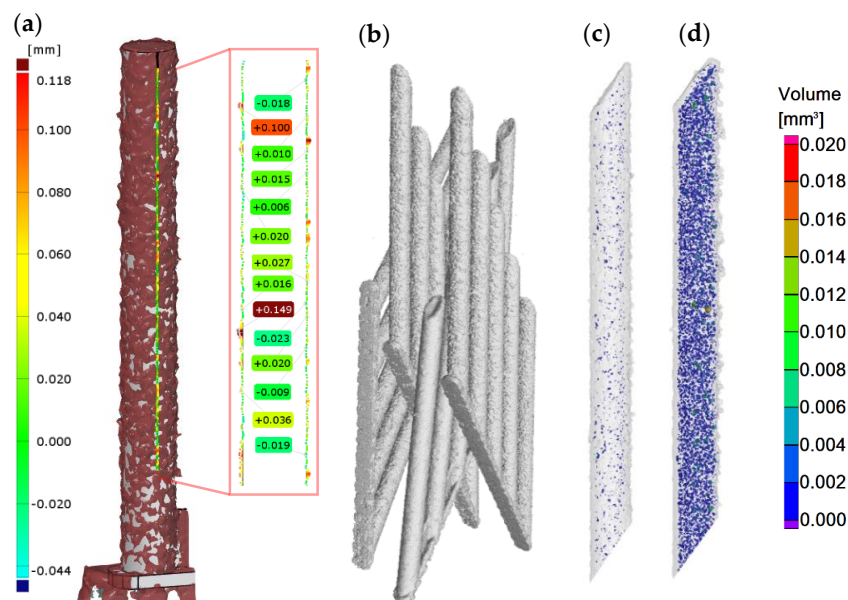


Figure 3. Struts analysis—(a) surface roughness evaluation in GOM Inspect software after optical measurement; (b) group of four samples measured together in VGStudio MAX software; (c) transparent 3D render of the strut with the lowest porosity 0.17% (d) transparent 3D render of the strut with the highest porosity 2.93%.

During the software analysis, the reconstructed data were divided into single struts and then each sample was independently analyzed in the porosity analysis module. The software detection of the air pores is based on the thresholding method that determines the boundary between the material and the air (background). This threshold was calculated automatically by software to reach comparability between both measurements. The results of the porosity analysis were between 0.17 and 2.93% (Figure 3c,d).

2.4. Input Energy Calculation

The input energy to the current layer (E_{in}) was obtained by Equation (2). It is based on the real laser paths in the actual layer, and on beam compensation and hatch distance parameters, which depended on actual process parameters and their single welds. The total length of the laser paths in the layer l was calculated based on the ellipse circumference o and the numbers of laser tracks N (Equation (3), Table 1), LS and LP were the main laser parameters.

$$E_{in} = \frac{LP}{LS} \cdot (J) \quad (2)$$

$$l = \sum_{i=1}^n o_1 + o_2 + \dots + o_n \text{ (mm)} \quad (3)$$

$$o \approx \frac{\pi}{2} \left[a + b + \sqrt{2(a^2 + b^2)} \right] \text{ (mm)} \quad (4)$$

$$a = \frac{d}{2}; b = \left(\frac{d}{2} \right) \cdot \cos(54,74^\circ) \text{ (mm)} \quad (5)$$

2.5. Samples Fabrication

All samples were manufactured using a SLM machine (SLM 280^{HL}, Lübeck, Germany) equipped with 400 W Ytterbium fiber lasers (YLR) laser. The laser beam was focused to the diameter of 82 μm and had a Gaussian shape. Laser scanning speed may reach up to 10,000 mm/s. During the production process, N_2 atmosphere was used in the chamber and the oxygen level was kept under 0.2%. The platform temperature was 150 $^\circ\text{C}$.

To find the most suitable material and surface properties of AlSi10Mg struts produced by SLM, several tests were used:

- Single welds test;
- Struts test;
- Struts test II;
- Hollow struts test.

2.5.1. Single Welds Test

The aim of the single welds experiment was to find a suitable combination of the main process parameters (LP , LS) for the production of consistent single welds and to find out the width of single welds for a specific combination of process parameters.

To prepare the real condition during layer by layer production, single welds were produced on the top of 5 mm solid material block (Figure 4a). The influence of the laser direction on the single welds condition was also observed; therefore, all single welds were produced in and against atmosphere flow direction (Figure 4b). Images of the welds from the top view were captured by light microscope (Olympus SZX7, Olympus, Tokyo, Japan) and used for width measuring and a visual evaluation of the continuity and uniformity (Figure 4c). Their width was measured in six points along each single weld and one average value for both directions was used. For the experiment, the following process parameters were changed— LP in the range between 175 and 400 W in steps 25 W and LS in the range between 200 and 2000 mm/s in steps 100 mm/s.

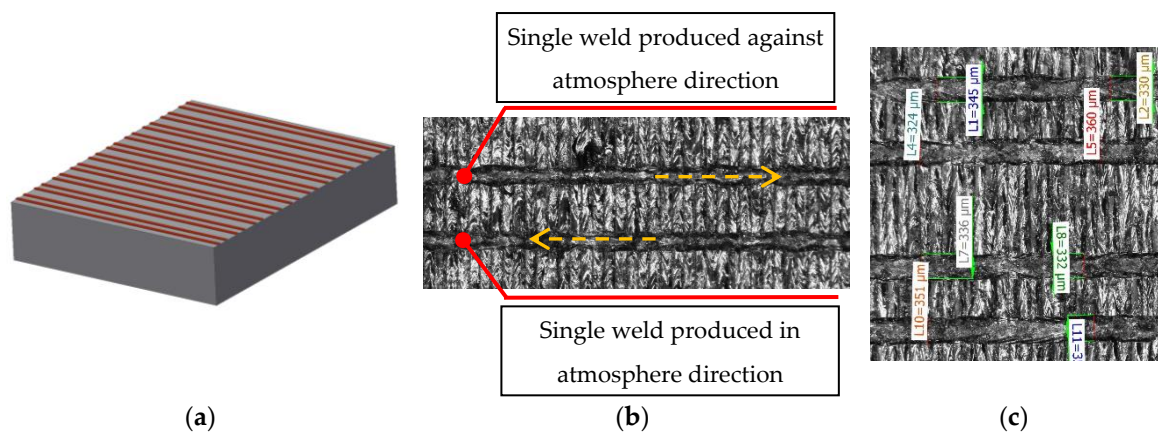


Figure 4. (a) Shape of the single welds samples; (b) one combination of process parameters produced in and against the atmosphere flow; (c) measurement of width of the single welds.

2.5.2. Strut Test

The aim of the test was to narrow the process parameter window of the single weld test depending on the porosity and surface roughness of the struts and to find the most suitable overlap (OL) parameter from the porosity point of view. The samples consisted of five struts with diameter $d = 2$ mm were produced in two orientations (OR) compared to the platform OR 90° and OR 35.26° . The strut diameter was chosen to be sufficiently large to set OL in the range from OL -50% to OL 50% of the weld width (Figure 5b). The beam compensation parameter (BC , a distance between the strut surface and the first laser path) was applied as a half of the weld width. Laser process parameters were changed as follows— LP in the range from 225 to 350 W, and LS in the range from 400 to 2000 mm/s.

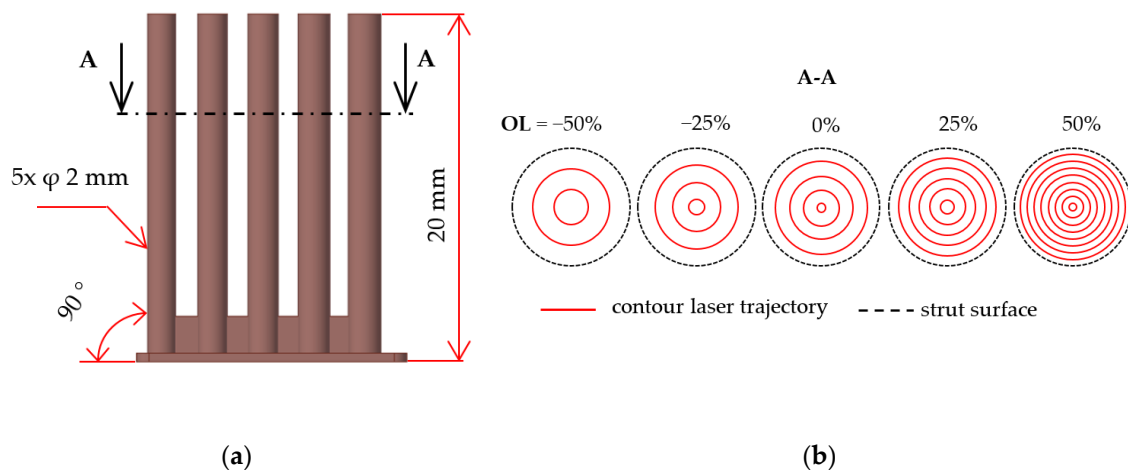


Figure 5. (a) Shape of the samples with inclination of 90° ; (b) contour strategy with different overlap parameter.

In this experiment, the laser strategy for lattice structure production created only by contour lines was tested (Table 1). The main idea is the possibility to produce fine lattice structure using various combinations of the process parameters (low/high energy) to manage surface roughness or internal porosity and to allow for production of very thin struts. An advantage is an easy optimization of the strategy for the elimination of non-melted or over-melted areas in struts and for improving dimension accuracy.

Table 1. Laser strategies of the strut with inclination of 35.26° (orientation in body centered cubic (BCC) lattice structure).

Strategy/d (mm)	0.5 mm	0.6 mm	0.7 mm	0.8 mm	0.9 mm
Contour					
Standard					

After fabrication, samples were ground to the mid-plane of the struts using a hand metallographic grinder (GP-2 Grinder, Sinowon, Dongguan, China), and the images of the samples from the top view were taken by light microscope (Olympus SZX7, Tokyo, Japan). For the initial porosity analysis ImageJ software was used. Porosity was analyzed only on the samples with *OL* 0%, 25% and 50%.

2.5.3. Strut Test II

The aim of the experiment was to find the influence of *LP* and *LS* on the internal porosity and surface roughness. The following process parameters were selected: *LP* in the range between 225 W and 400 W and *LS* in the range between 500 mm/s and 2000 mm/s with respect to the perspective area of previous strut test. The strut samples with *OR* 35.26° only were used in the experiment. The samples were analyzed using μ CT to obtain more accurate results of porosity and full surface data for down-skin roughness evaluation.

2.5.4. Hollow Struts Test

Samples of hollow strut shape; created with only one single weld in each layer, were produced (Figure 6). The cross-section of the hollow strut sample was designed to ensure evaluation of correct width of the wall without distortion caused by grinding in the inclined plane. The primary aim of the hollow strut test was to compare the width of the single welds on the solid block and the width of the wall of hollow struts (the shape close to the real strut). The combinations of the process parameters were selected also to obtain the influence of the width of wall on *LP* and *LS*. For this experiment, the following process parameters were changed—*LP* (225, 250, 275, 300, 350, 400 W); *LS* (500, 900, 1400 mm/s). After fabrication, the 37 samples were ground to the mid-plane of the struts using a hand metallographic grinder (GP-2 Grinder, Sinowon, Dongguan, China) and the images of the ground surface from the top view were captured by light microscope (Olympus SZX7, Olympus, Tokyo, Japan).

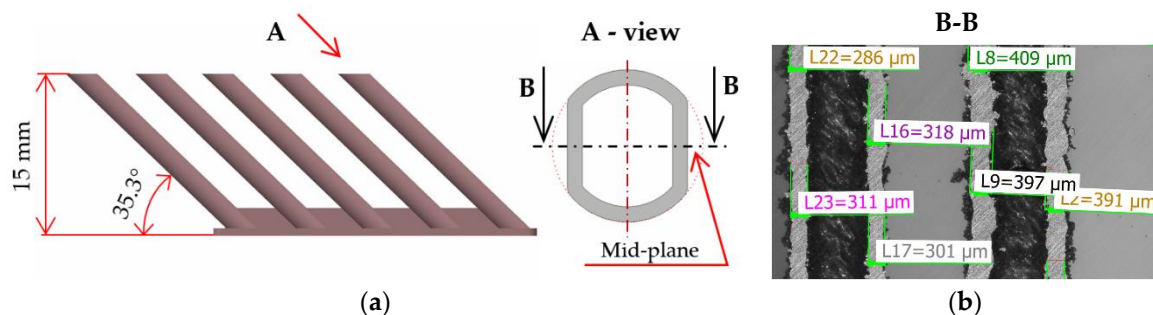


Figure 6. (a) A special shape of strut designed for evaluation of the width of hollow strut walls without distortion caused by inclined grinding plane; (b) wall width measurement using macro images captured by the light microscope.

3. Results

3.1. Single Welds Test

The results of the width of single welds are shown in Figure 7. The final values were averaged from six measurements against and six measurements in the atmosphere flow direction. The values marked in red color were excluded due the worse quality of the welds (non-uniformity of width and bad continuity). For the input linear energy calculation, Equation (6) was used and the limit value of around 0.25 J/mm was found for continuous welds.

$$E_{lin} = LP/LS \quad (\text{J/mm}) \tag{6}$$

w (μm)		Laser speed (mm/s)																				
E _{lin} (J/mm)		200	300	400	500	600	700	800	900	1000	1100	1200	1300	1400	1500	1600	1700	1800	1900	2000		
Laser power (W)	175	354	310	261	290	246	221	214	199	223												
		0.88	0.58	0.44	0.35	0.29	0.25	0.22	0.19	0.18												
	200	401	343	303	286	317	271	240	210	201	210											
		1.00	0.67	0.50	0.40	0.33	0.29	0.25	0.22	0.20	0.18											
	225	374	309	271	255	214	203	199	174	163	145											
		0.75	0.56	0.45	0.38	0.32	0.28	0.25	0.23	0.20	0.19											
	250	344	314	270	253	233	223	201	180	161	163	159										
		0.83	0.63	0.50	0.42	0.36	0.31	0.28	0.25	0.23	0.21	0.19										
	275	380	346	332	289	262	277	235	227	221	201	149										
		0.69	0.55	0.46	0.39	0.34	0.31	0.28	0.25	0.23	0.21	0.20										
	300	305	325	308	267	260	232	223	202	211	193	183	192	186								
		0.75	0.60	0.50	0.43	0.38	0.33	0.30	0.27	0.25	0.23	0.21	0.20	0.19								
	325	333	316	275	274	262	258	207	199	200	196	189	176	145								
		0.65	0.54	0.46	0.41	0.36	0.33	0.30	0.27	0.25	0.23	0.22	0.20	0.19								
	350	358	336	328	317	300	261	259	205	200	199	209	205	352								
		0.70	0.58	0.50	0.44	0.39	0.35	0.32	0.29	0.27	0.25	0.23	0.22	0.21	0.19							
375	317	308	201	372	370	272	267	250	287	230	237	239	223	217								
	0.63	0.54	0.47	0.42	0.38	0.34	0.31	0.29	0.27	0.25	0.23	0.22	0.21	0.20								
400	357	332	358	301	273	234	236	223	214	206	223	216	212	201	210							
	0.67	0.57	0.50	0.44	0.40	0.36	0.33	0.31	0.29	0.27	0.25	0.24	0.22	0.21	0.20							

Figure 7. The average width of the single welds in and against atmosphere flow (colored cells); line energy (color free cells).

Figure 8a shows the frequency of the continuous single welds widths from 145 μm to 401 μm in all tested process window. Different widths of single welds are useful for ensuring the dimension accuracy and material properties during production of the struts using a contour line strategy (especially thin struts). Therefore, for the next experiments, the welds across the entire perspective process window were selected as follows—the consistent welds were categorized into 11 classes according to weld widths. From each class, one combination of process parameters was chosen depending on the amount of linear energy E_{lin} in the (Equation (6)). The combination of LP and LS with the linear energy level closest to the average energy level of the class was selected. A few more combinations, e.g., laser parameters corresponding with standard process parameters or the parameters from previous studies, were chosen. Finally, 16 combinations of LS and LP were tested.

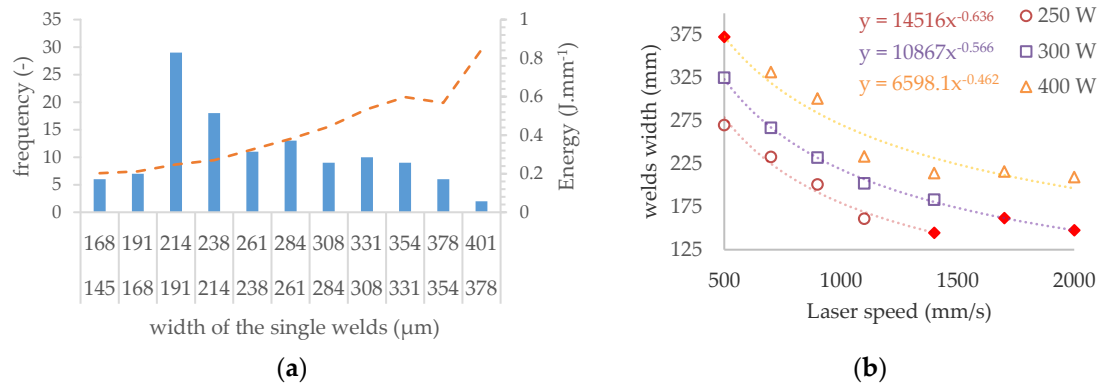


Figure 8. The results of the single welds test (a) histogram of the width frequency of single welds, (b) the prediction of weld width for non-tested combinations of process parameters.

3.2. Struts Test

3.2.1. Determining the Overlap Parameter

The samples were ground to the mid-plane of the struts to measure the internal porosity and to check the weld overlap (*OL*). The internal porosity was analyzed on the struts with *OL* from 50% to 0% to prevent distortion of the results due to a disconnection between the neighboring single welds. For evaluation of the most suitable *OL* value, a dependence of the porosity vs. input energy E_{in} was used (Figure 9a,b).

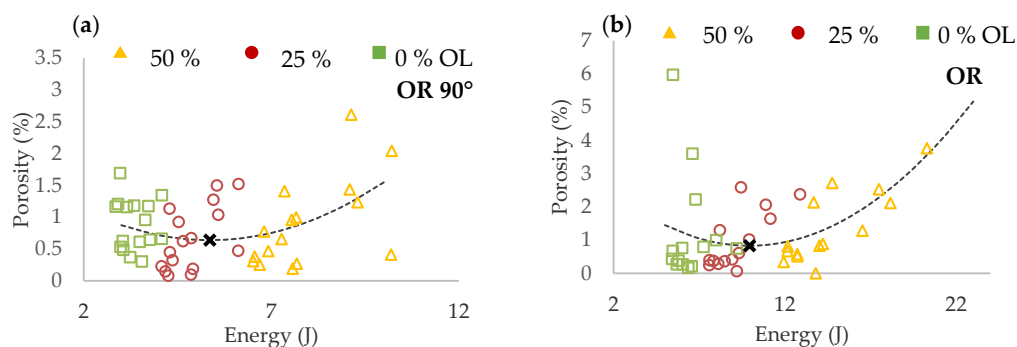


Figure 9. Porosity vs. input energy dependence (a) for inclination 90°; (b) for inclination 35.26°.

In the charts, three groups of porosity regarding the *OL* parameter were identified in both cases of struts inclination. To find out the *OL* parameter with the lowest porosity level, the results were interpolated with quadratic polynomial function and the minimum of the function was determined (black cross in Figure 9).

In the results of both strut inclination, the overlap *OL* 50% shows a higher porosity level. It occurs due to a large overlap area where the material is overheated. Higher porosity level is also at *OL* 0% where it could be caused by theoretically no overlap and insufficient connection between the neighboring welds. The lowest porosity level was reached at *OL* 25% in both orientations; therefore, for the next experiments, the *OL* 25% was selected as the most suitable. In the case of *OR* 35.26°, higher porosity values were identified compared to *OR* 90°.

3.2.2. Initial Roughness Analysis

Results of surface roughness on the strut side show different trends based on struts inclination (Figure 10). For the struts of *OR* 90°, roughness decreases with higher E_{in} while for *OR* 35.26°, roughness significantly increases with higher E_{in} . The worse surface quality at *OR* 35.26° is caused by

approximately 40% higher E_{in} and heat transfer to the surrounding powder particles and caused by strut inclination.

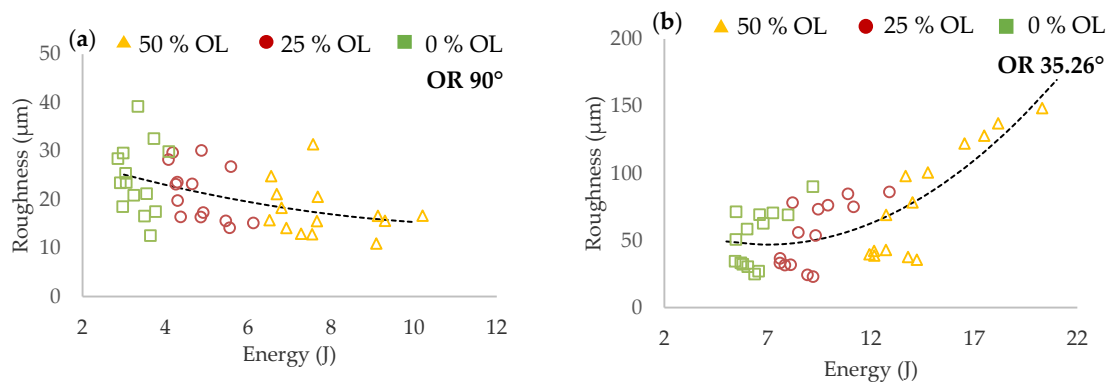


Figure 10. Surface roughness vs. input energy dependence (a) for inclination of 90°; (b) for inclination of 35.26°.

The images captured by light microscope (Olympus SZX7, Tokyo, Japan) confirm the previous results. Figure 11 shows two combinations of process parameter. The former with high E_{in} — LP 275 W, LS 400 mm/s (Figure 11a,b), and the latter with low E_{in} — LP 300 W, LS 1400 mm/s (Figure 11c,d). In the case of the struts at OR 90° produced with higher E_{in} , the surface quality was smooth, with no partially melted powder (Figure 11b). The struts produced with lower E_{in} were characterized by visually rough struts surface (Figure 11d). In the case of the struts at OR 35.26° produced with higher E_{in} , the top surface also seems to be smooth; however, a lot of partially melted powder appeared on the strut down-skin surface (Figure 11a). The struts produced with lower E_{in} had a significantly smaller amount of partially melted powder on the strut down-skin surface (Figure 11c).

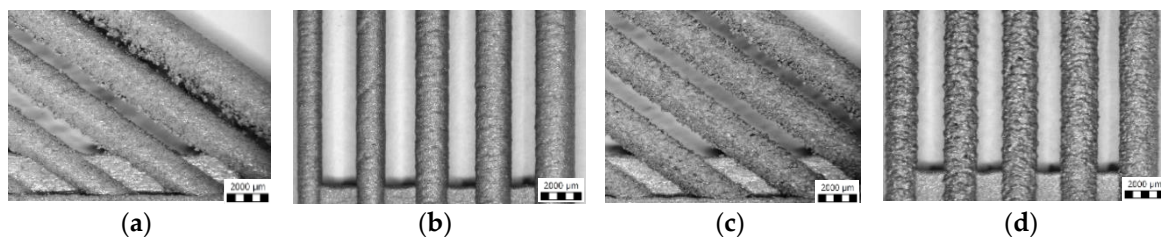


Figure 11. Struts surface quality—produced with higher E_{in} (a) at orientation (OR) 36.26°; (b) at OR 90°; produced with lower E_{in} (c) at OR 36.26°; (d) at OR 90°.

The results of porosity and surface roughness were jointly used to narrow the perspective area of the process parameters for struts production in 3D contour graph (Statistica software). Based on the results, the laser parameters were narrowed as follows— LP between 225 W and 300 W, LS over 1000 mm/s.

3.3. Struts Test II

3.3.1. Interpolation of Welds Width

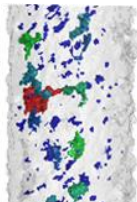
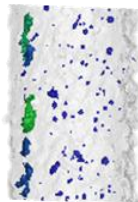
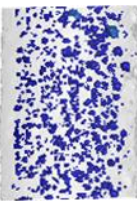
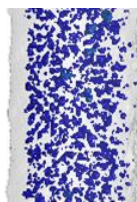
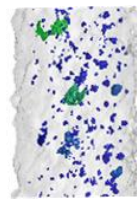
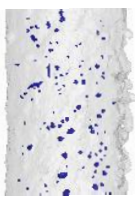
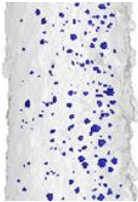
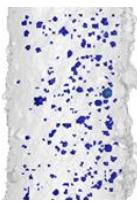
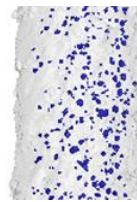
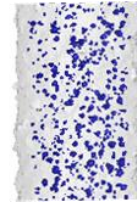
The aim of the struts test II mainly was to determining the effects of individual parameters on surface roughness and internal porosity. In order to obtain dependencies on LP and LS , the parameters were selected with respect to perspective area of the previous strut test. Some combinations of LP and LS were not included in the single welds test and their widths were not known. To find them, the dependence between LS and width of the single weld was used for prediction (Figure 8b).

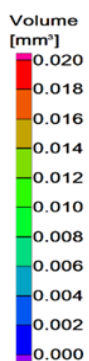
Figure 8b shows the curves of *LS* vs. welds width curves for *LP* 400, 300 and 250 W. From the results of *LP* 400 W, it is obvious that the dependence is not linear; therefore, the power functions, which best correspond to the measured data, were used for interpolation. This is also confirmed by the results for *LP* 300 W and *LP* 350 W. The calculated values are marked red.

3.3.2. Porosity Analysis

The porosity results were obtained by a micro-computed tomography (μ CT) device with voxel size of 15 μ m. The struts were individually analyzed to find out the porosity level for each combination of process parameters. However, the shape and the size of pores is also important. Table 2 shows the images of the μ CT analysis with various shapes of pores and porosity level. Based on the results, the required minimum values of linear energy E_{lin} 0.25 J/mm and input energy E_{in} 8 J were identified for strut production without creating large irregular pores.

Table 2. The porosity level of the strut samples—3D renders with pores shape; the pores in the entire volume were projected to the plane of the view; all images have the same pores scale bar.

	<i>LP</i> 225 W	<i>LP</i> 250 W	<i>LP</i> 300 W	<i>LP</i> 350 W	<i>LP</i> 400 W
	<i>LS</i> 1200 mm/s; E_{in} 7.28 J; E_{lin} 0.19 J/mm	<i>LS</i> 1400 mm/s; E_{in} 9.17 J; E_{lin} 0.18 J/mm	<i>LS</i> 500 mm/s; E_{in} 13.54 J; E_{lin} 0.6 J/mm	<i>LS</i> 500 mm/s; E_{in} 15.43 J; E_{lin} 0.7 J/mm	<i>LS</i> 1700 mm/s; E_{in} 7.56 J; E_{lin} 0.24 J/mm
					
	Por. -0.17%	Por. -0.27%	Por. -1.38%	Por. -2.26%	Por. -0.63%
	<i>LS</i> 700 mm/s; E_{in} 9.02 J; E_{lin} 0.32 J/mm	<i>LS</i> 700 mm/s; E_{in} 9.84 J; E_{lin} 0.36 J/mm	<i>LS</i> 900 mm/s; E_{in} 9.37 J; E_{lin} 0.33 J/mm	<i>LS</i> 1100 mm/s; E_{in} 8.91 J; E_{lin} 0.32 J/mm	<i>LS</i> 900 mm/s; E_{in} 10.17 J; E_{lin} 0.44 J/mm
					
	Por. -0.17%	Por. -0.31%	Por. -0.42%	Por. -0.43%	Por. -0.81%



3.3.3. Evaluation of Perspective Laser Parameters

The results of porosity levels generally show a similar trend as in the initial results of the previous test. However, in this case, the significant accumulation of results at the porosity level 0.4% occurs for E_{in} of 8 ÷ 10 J and for E_{lin} of 0.15 ÷ 0.4 J/mm (Figure 12a,b). However, the porosity level of linear energy E_{lin} in range 0.15 ÷ 0.25 J/mm is very low, and the porosity is created with a small number of large irregular pores. It can significantly decrease the mechanical properties; therefore, this area is unsuitable for the production of the struts. Regarding the charts, which show the influence of *LS* and *LP* on the porosity (Figure 13a,b) and the previous porosity analysis, the parameters *LP* of 225 ÷ 275 W, *LS* of 900 ÷ 1400 mm/s with E_{in} of 8 ÷ 10.5 J, E_{lin} of 0.25 ÷ 0.4 J/mm, and *OL* 25% were selected as the perspective for struts production from the porosity point of view.

The results of surface roughness were obtained by μ CT measurement in this experiment; therefore, it was possible to analyze the results on the side and also down-skin strut surface (Figure 12c,d).

The results show a similar trend as the results of porosity except for the pronounced linear dependence of as-built surface roughness on linear energy E_{lin} . The best results were accumulated between E_{in} 8 ÷ 10 J and E_{lin} of 0.15 ÷ 0.4 J/mm with the level of about Ra 30 μm on the strut-side surface and about Ra 40 μm on the down-skin surface.

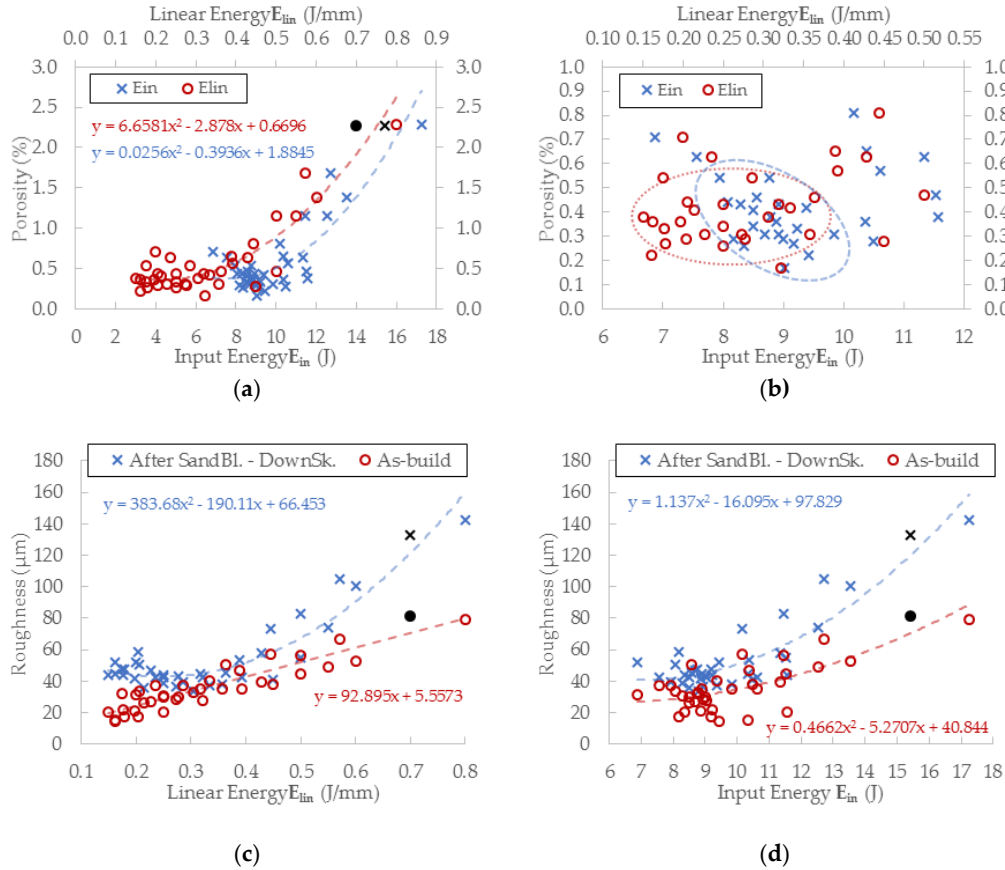


Figure 12. (a) μCT porosity vs. input and linear energy dependences, black mark represents the universal SLM process parameters; (b) focused results area up to 1% porosity level with marked perspective areas; (c) surface roughness vs. linear energy dependence—on the side and down-skin struts surface, black marks represent the universal SLM process parameters.; (d) surface roughness vs. input energy dependence.

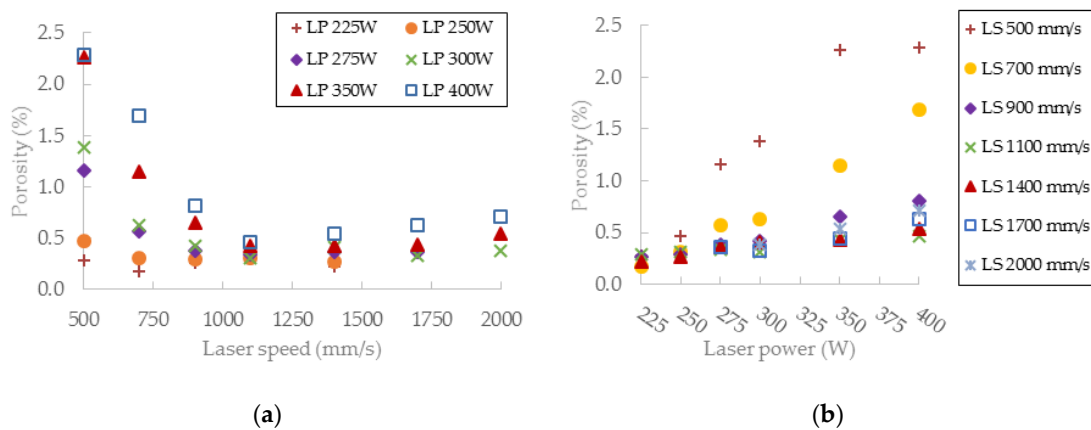


Figure 13. Cont.

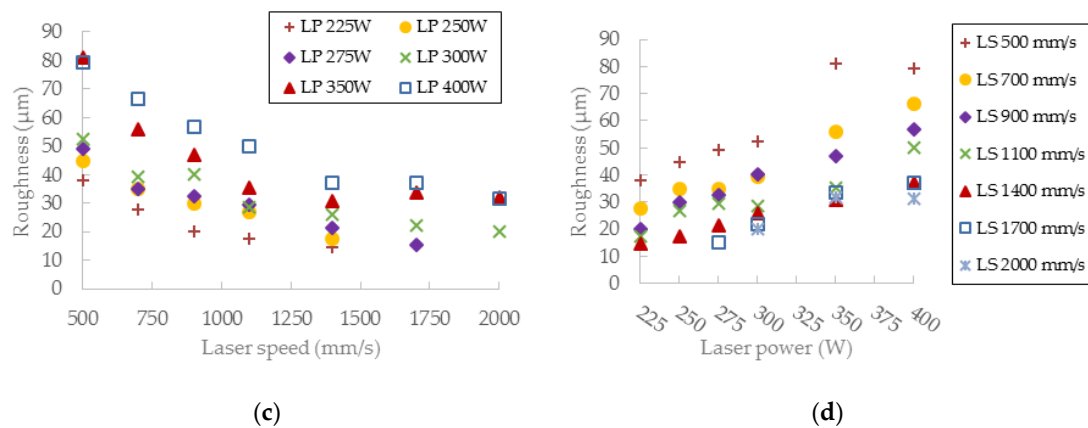


Figure 13. (a) The influence of various laser speed (LS) levels on porosity; (b) the influence of various laser power (LP) levels on porosity; (c) the influence of various LS levels on surface roughness; (d) the influence of various LP levels on surface roughness.

Regarding the charts, which show the influence of LS and LP on the roughness (Figure 13c,d), parameters LP in the range of 225 ÷ 300 W, LS in the range of 900 ÷ 2000 mm/s with E_{in} of 8 ÷ 10 J, Elin of 0.15 ÷ 0.4 J/mm and OL 25% were selected as the perspective for lattice structure production with a low roughness level.

3.4. Wall Width Analysis

Simultaneously with the strut samples, hollow strut samples were fabricated. The hollow strut shape was used because of similar heat transfer conditions as those in the case of struts production. The width of the wall at $OR\ 35.26^\circ$ was of about 25% higher on average than that in the case of the single welds on a solid block (Figure 14). The results confirm the trends of the weld widths from a single weld test. The influence of LP seems to be more linear than that of LS.

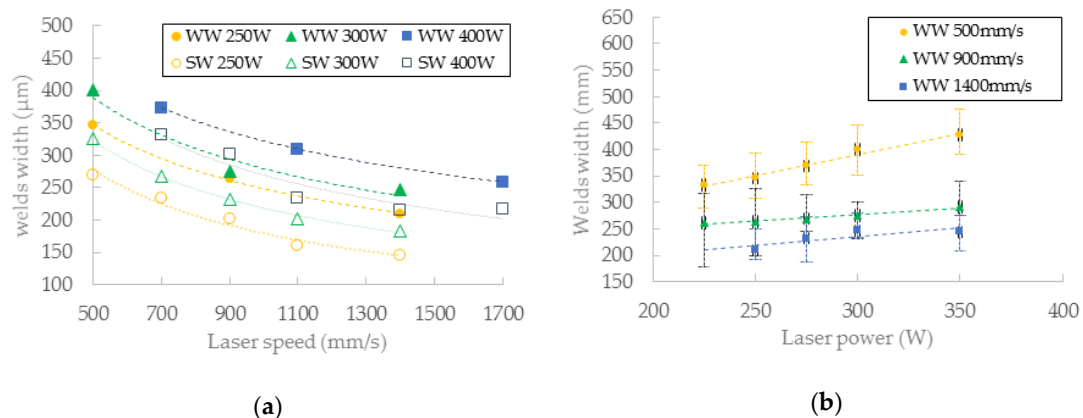


Figure 14. (a) Comparison of single welds and walls width according to LS—in chart (SW) single weld width; (WW) wall width; (b) the wall width according to LP.

3.5. Metallographic Analysis

A metallographic analysis for evaluation of the microstructure was performed. Standard methods were used for metallographic sample preparation, i.e., wet grinding and polishing with use of diamond pastes. A microstructure of the struts was analyzed in an etched state (Fuss etchant) and evaluated by metallographic light microscope (Olympus GX 51, Tokyo, Japan). Orientation of the micrographs is parallel to the strut axis (Figure 15a). The microstructure of the struts is inhomogeneous, consisting of single welds separated by fusion boundaries. Differences in the microstructure can be seen in the

layers close to the down-skin surface of the struts (B area in Figure 15a) in comparison with the up-skin surface (A area). Different shapes of porosity depend on the E_{in} parameter. Due to overheating of the material, gas pores with a spherical shape were created (Figure 15b,c). No cracks were found in the microstructure of the evaluated samples.

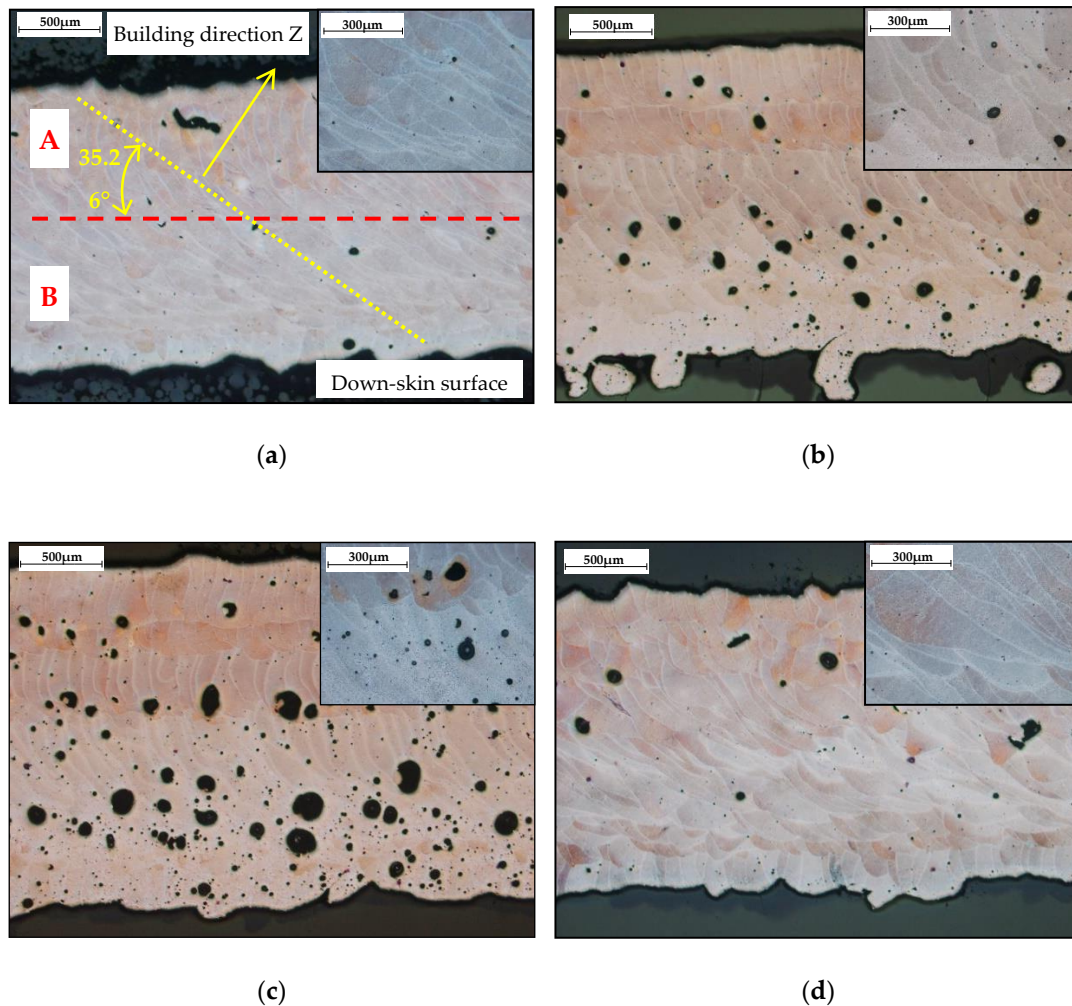


Figure 15. Microstructure of the struts (a) LP 250 W, LS 1400 mm/s, E_{in} 9.17 J, E_{lin} 0.18 J/mm with description common for all pictures; (b) LP 300 W, LS 500 mm/s, E_{in} 13.54 J, E_{lin} 0.6 J/mm (c) LP 350 W, LS 500 mm/s, E_{in} 15.43 J, E_{lin} 0.7 J/mm; (d) LP 400 W, LS 1700 mm/s, E_{in} 7.56 J, E_{lin} 0.24 J/mm.

4. Discussion

4.1. Comparison of the Linear Energy Needed for Consistent Single Weld

The results of the single welds experiment show as a limit value E_{lin} 0.25 J/mm for consistent welds. The value is higher than that in the case of [21], where the determined limit was 1.5 J/cm. The difference is caused by the shape of the used sample. In [21], the single welds were fabricated directly on the platform. In the present study, the sample, which simulates real production and the increase of thickness of the deposited powder during the first few layers, was used. After melting, the produced layer has a height usually lower than that of the originally spread layer of 50 μ m. Then, the next deposited layer has higher thickness and a quality of weld and the required linear energy E_{lin} can be changed [30].

4.2. Benefits of Contour Lines Laser Strategy

The state that led to the design of a contour scanning strategy is shown in Figure 16. There are examples of the laser strategy internally developed by SLM Solutions universal process parameters. In the cases of diameters of 0.5 and 0.6 mm, only one contour line was generated while in the case of 0.7 mm diameter, one more fill contour line was generated. Using the results of the single weld test, it is possible to calculate the theoretical dimensional accuracy and re-melting area.

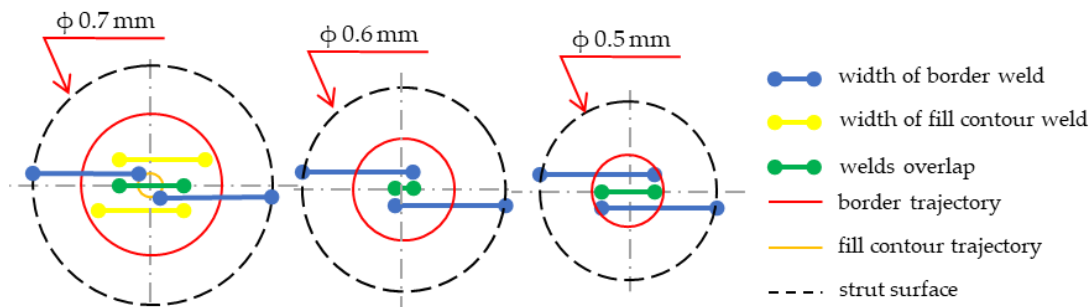


Figure 16. SLM Solutions universal struts laser strategy.

The laser parameters of universal process parameters are as follows: contour line *LP* 350 W, *LS* 500 mm/s; fill contour offset *LP* 250 W, *LS* 555 mm/s, and *LF* = −4). During production of a 0.5 mm strut, the diameter will be theoretically about 0.116 mm (23%) larger because of a combination of the beam compensation parameter of 0.15 mm and the weld width of 0.358 mm. A theoretical overlap area is 0.158 mm (44% of the weld width). In the case of a 0.6 mm strut, the diameter will also be larger (about $d = 0.116$ mm; 19%) and a theoretical overlap area is 0.058 mm (16% of the weld width). The diameter of 0.7 mm will also be about 0.116 mm larger; as can be seen in Figure 16, from the contour line, no overlap area is created. Therefore, a fill contour track in the distance of 0.17 mm from the contour line is added. Due to the fill contour line and its distance from the contour path, an unfavorable state with large overlap of 0.31 mm (87% of the weld width) is created in the center of the strut. Its trajectory is also on the already produced contour weld and thus the material is re-melted, which can cause internal defects in the struts (Figure 16; $d = 0.7$ mm). The aim of the proposed contour strategy is to create uniform conditions for different strut diameters and improve the dimension accuracy using single welds results.

Using the previous results of the single welds experiment, the hollow strut experiment and a designed script in Excel, the contour strategy for production of the struts with low porosity, and surface roughness, were designed (Table 3). The obtained weld widths from the single weld experiment which meet the required linear energy E_{lin} and input energy E_{in} were used only (Figure 19a). These values were increased by about 25% (parameter from the hollow strut test, Figure 19b) and then used to define the beam compensation *BC* parameter ($(\text{single width} \times 1.25)/2$). The goal of the Excel script was to find a suitable combination of laser parameters which achieve the overlap in the center of the struts as close as possible to the value around *OL* 25%. The results are shown in Table 3. For the diameters of 0.5 and 0.6 mm, the combinations with the required *OL* parameter have been found. In the case of the diameter 0.7 mm, the best results were obtained with *LP* 225 W, *LS* 900 mm/s and *LP* 250 W, *LS* 1000 mm/s, however the *OL* parameter between neighboring welds must increase to 29% and 34%. For values closer to *OL* 25%, it would be necessary to discover other combinations of parameters around these two; however, the expected levels of porosity and roughness using these combinations will be significantly lower compared to standard SLM strategy (Figure 12).

Table 3. Various suitable combination of process parameters for production of the struts with diameters 0.5–0.7 mm, (N (-) is number of the used contour, w (μm) is single width $\times 1.25$).

d (mm)	OL (%)	LP (W)	LS (mm/s)	w (μm)	BC (μm)	N (-)	OL in Center (μm)	OL in Center (%)
0.5	-	225	600	295	147	1	89	30%
	-	325	1000	293	147	1	86	29%
	-	350	1300	285	143	1	70	25%
	-	375	1200	294	147	1	88	30%
0.6	-	400	1000	339	170	1	78	23%
0.7	34%	225	900	236	118	2	84	36%
	29%	250	1000	224	112	2	67	30%

4.3. The Heat Transfer during Strut Fabrication

The first strut experiment in this study was also designed for comparison of the conditions during production the struts with OR 90° and OR 35.26° . The difference is caused by worse heat transfer in the inclined strut. It can lead to wider single welds than expected; therefore, the successful results of porosity at OL 0% were discovered (Figure 9, Figure 18b). This was verified by the hollow struts experiment which confirmed this hypothesis. The width of the wall was increased on average by about 25% (Figure 14a). At higher energy levels (over 0.5 J/mm), the effect of the wider bottom part of the wall also appeared (Figure 17). It was caused by the thermal gradient during SLM production of struts with inclination and shows the heat energy transfer well. To describe the energy conditions during the struts' production, this must be considered:

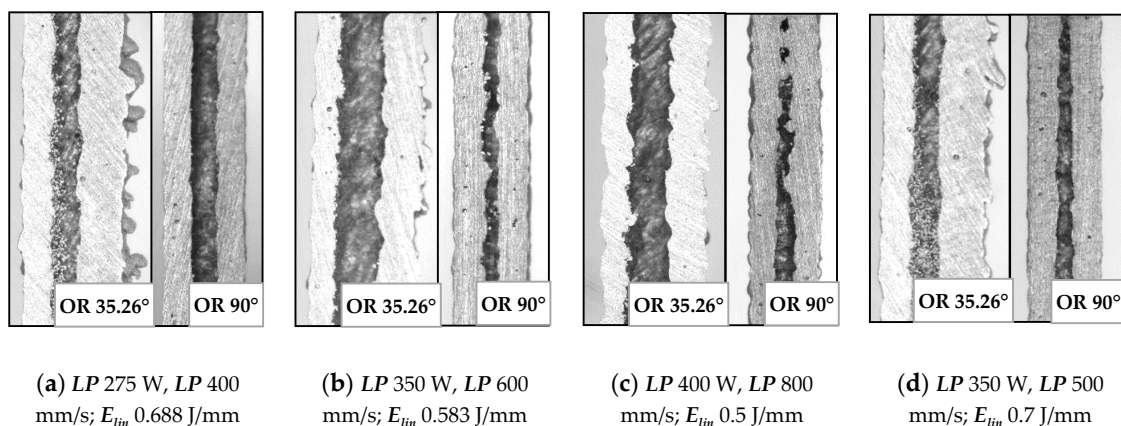


Figure 17. Comparison of inclined and perpendicular strut (a) for parameters LP 275 W, LP 400 mm/s; (b) LP 350 W, LP 600 mm/s; (c) LP 400 W, LP 800 mm/s; (d) LP 350 W, LP 500 mm/s.

- (1) Due to the point contact of the powder particles between themselves, the metal powder has much lower heat conductive performance and works as an insulator compared to the solid material.
- (2) Due to the strut inclination, the cross-section with a higher area occurs in every layer. Using the energy calculation in Equation (2), it is possible to calculate the increase of the input energy E_{in} and compare OR 35.26° and OR 90° ; it is about 40% higher in the case of OR 35.26° .
- (3) The thermal gradient points in the direction $-Z$. Due to the inclination of the struts, the heat transfer is slower than in the case of the strut with the axis directed in thermal gradient direction.

After melting of each layer of the strut, the heat energy flows straight down in thermal gradient direction. There are two parts of each produced layer with different energy transmission, the part produced on the previous layer and overhanging part produced on the powder (Figure 18). In the former case of the part on the previous layer, the energy flows through the strut. Because the thermal gradient has a different direction than the strut, heat transfer is slower compared to the strut with OR 90° .

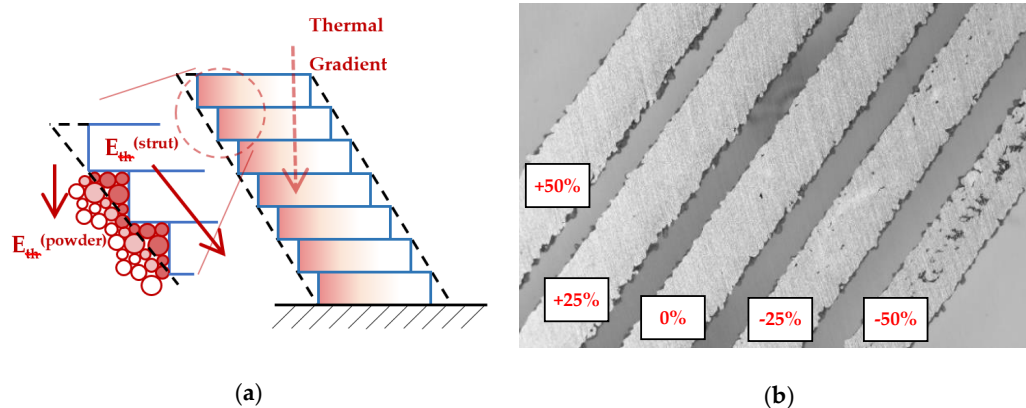


Figure 18. (a) Scheme of the heat transfer during SLM additive manufacturing; (b) The ground sample to the mid-plane of the struts.

In the latter, the thermal energy flows to the powder which is in contact with the strut down-skin surface and the powder particles are overheated because there is only a point contact between neighboring powder particles, and only poor heat transmission to the powder bed. Affected particles are melted on the down-skin surface which causes larger dimensions of the struts [8,18] or a wider bottom part of the hollow struts samples, as well as a higher surface roughness on the down-skin surface of the strut (Figure 17). The heat energy is also accumulated in overhanging part of the layer and the material structure is changed [22] (Figure 15).

4.4. Porosity and Roughness Analysis

The results of μ CT show a different shape and level of porosity according to the input energy E_{in} and the linear energy E_{lin} . The porosity in the struts with the lowest porosity level is often formed by a small number of larger pores which are located close to the top surface (Table 2). Formation of the large irregular pores is related to the heat transfer in the inclined struts where more heat energy is accumulated at the bottom part of the strut. Due to the low linear energy, there is no overheating area in the bottom part of the strut (the spherical porosity is very small); however, on the upper side, the state is an unstable because of a lack of linear energy. This causes the occasional disconnection of neighboring welds and formation of larger pores. The minimum value E_{lin} 0.25 J/mm was determined; it is in line with the results of single welds.

A lack of E_{in} causes porosity in the center of the struts. During production of the laser tracks close to the strut surface, heat transfer is lower due to the surrounding powder. During production of single welds in the center of the strut, heat transfer is higher due to the neighboring welds; an unstable state occurs with occasional disconnection of the welds and formation of larger pores. The minimum value E_{in} 9 J was determined. Also, the inside-out order of single welds production is recommended.

4.5. Porosity and Roughness

The current results of strut experiments clearly show that the porosity and surface roughness is affected by the input energy E_{in} as well as linear energy E_{lin} ; these both include the laser power LP and the laser speed LS . It follows that for strut production free of internal defects and a rough surface, appropriate laser process parameters must be chosen. The charts of the dependences of LP and LS on the porosity (Figure 13) demonstrate a different influence of the parameters on porosity forming. The chart shows that the porosity increases with higher LP at all LS levels linearly, except for LS level of 500 mm/s, which shows unstable results. The LS parameter shows non-linear results with the lowest porosity in the range of 1000 ÷ 1250 mm/s. With higher LS , the porosity seems to be stable and at the constant level, except for LP 400W where the porosity increases. LS s up to 1000 mm/s are

unstable and the porosity significantly increases. It could be caused by too high E_{in} and formation of gas pores in the material due to its overheating material (Figure 15c).

The influence of LS and LP on the surface roughness has a similar character as that on the porosity in case of input energy E_{in} . Linear energy E_{lin} dependence shows the pronounced linear dependence of as-built surface roughness. In Figure 13c, it is possible to find two approximately linear areas. The first area, up to 1400 mm/s, where there are significant changes in roughness values, and the other one, between 1400 mm/s and 2000 mm/s, where there is a significantly lower and stable roughness level. The dependence of LP vs. roughness is linear for all tested laser speeds. Generally, the results show a low surface roughness with lower E_{in} and E_{lin} .

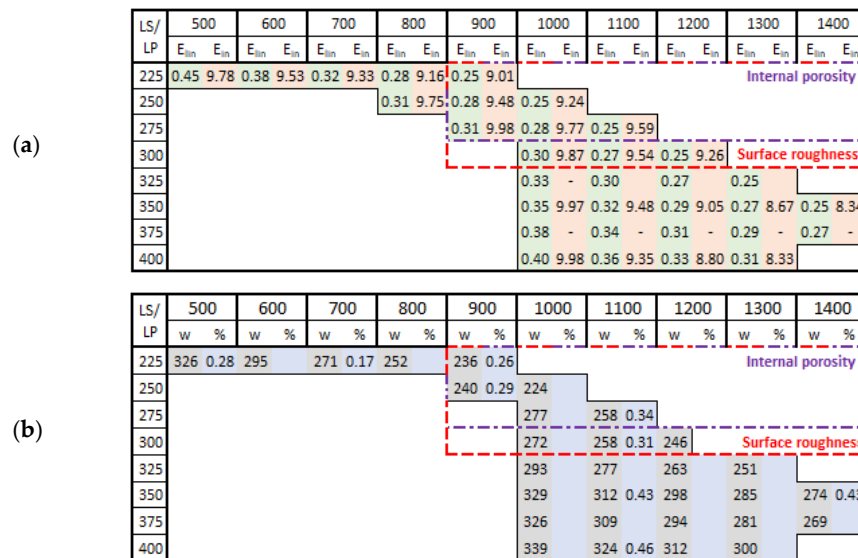


Figure 19. The perspective area (a) linear energy E_{lin} (J/mm) (green cells) and input energy to the layer E_{in} (J) (red cells); (b) width of single welds in (μm) multiplied $\times 1.25$ (parameter from hollow strut test) (grey cells) and porosity level (blue cells).

5. Conclusions

In this article, an experimental study was conducted to investigate the influence of a proposed contour line laser strategy for an SLM lattice structure on internal porosity and surface roughness of the single struts, which significantly affects the mechanical properties of the lattice structure. Based on the dependence of porosity vs. input E_{in} and linear energy E_{lin} , the influence of the laser speed LS and laser power LP was found and the perspective areas of suitable process parameters for the struts–lattice structure were defined. In the present study, the main conclusions are as follows:

- For the production of the struts–lattice structure, the contour strategy seems to be perspective, mainly because of the possibility to use various laser process combinations based on the required width of single welds of the different strut dimensions to achieve a fully melted strut with a constant OL 25% parameter.
- The heat transfer condition in the inclined struts significantly influences all material and shape parameters of the struts (lattice structure). During the strut production with high E_{in} , heat energy is accumulated in the down-skin part of the strut and higher roughness, higher porosity and change of the material microstructure occur. Therefore, the production at lower E_{in} levels leads to more stable results with lower porosity and roughness.
- E_{in} calculated based on the real laser trajectory in the strut describes the amount of the porosity (P) and roughness (R) in the strut samples ($d = 2$ mm) well. Another necessary condition for struts production without large and irregular internal pores is the minimum level of linear energy E_{lin} 0.25 J/mm. The perspective areas of process parameters based on P and R were defined as

follows— E_{in} of $8 \div 10$ J; E_{lin} of $0.25 \div 0.4$ J/mm, LP of $225 \div 300$ W, LS of $1250 \div 1750$ mm/s and OL $20\% \div 30\%$. Figure 19 shows the perspective area which meets all conditions for low porosity and surface roughness levels. The presented weld widths are combinations of single weld values multiplied by the parameter obtained from the hollow strut test ($\times 1.25$).

Author Contributions: Conceptualization, R.V. and D.K.; Data curation, R.V.; Formal analysis, R.V.; Funding acquisition, D.P. and J.K.; Investigation, R.V., L.P., J.J. and T.Z.; Methodology, R.V. and D.K.; Project administration, R.V.; Resources, D.P. and J.K.; Supervision, D.K. and D.P.; Validation, R.V., D.K., D.P., L.P. and T.Z.; Visualization, R.V.; Writing—original draft, R.V., D.K. and L.P.; Writing—review and editing, R.V., D.K. and L.P.

Funding: This research was funded by [NETME Centre] grant number [CZ.1.05/2.1.00/01.0002], [NETME Centre Plus] grant number [LO1202], [Architected materials designed for additive manufacturing] grant number [CZ.02.1.01/0.0/0.0/16_025/0007304], [BUT] grant number [FSI-S-17-4144], [CEITEC 2020] grant number [LQ1601] and the APC was funded by [BUT open access fund].

Acknowledgments: This work is an output of research and scientific activities of the NETME Centre, the regional R&D centre built with the financial support from the Operational Programme Research and Development for Innovations within the project NETME Centre (New Technologies for Mechanical Engineering), Reg. No. CZ.1.05/2.1.00/01.0002 and, in the follow-up sustainability stage, supported through NETME CENTRE PLUS (LO1202) by financial means from the Ministry of Education, Youth and Sports under the “National Sustainability Programme I”. The study was further supported by the ESIF, EU Operational Programme Research, Development and Education within the research project “Architected materials designed for additive manufacturing”, Reg. No.: CZ.02.1.01/0.0/0.0/16_025/0007304, by the project FSI-S-17-4144 and by the Ministry of Education, Youth and Sports of the Czech Republic under the project CEITEC 2020 (LQ1601).

Conflicts of Interest: The authors declare no conflict of interest. The founding sponsors had no role in the design of the study; in the collection, analyses, or interpretation of data; in the writing of the manuscript, and in the decision to publish the results.

References

- Kopanidis, A.; Theodorakakos, A.; Gavaises, E.; Bouris, D. 3D numerical simulation of flow and conjugate heat transfer through a pore scale model of high porosity open cell metal foam. *Int. J. Heat Mass Transf.* **2010**, *53*, 2539–2550. [[CrossRef](#)]
- Mohammed, R.; Ahmed, A.; Elgalib, M.A.; Ali, H. Low Velocity Impact Properties of Foam Sandwich Composites: A Brief Review. *Int. J. Eng. Sci. Innov. Technol.* **2014**, *3*, 579–591.
- Mohammed, R.; Zhang, F.; Sun, B.; Gu, B. Finite element analyses of low-velocity impact damage of foam sandwiched composites with different ply angles face sheets. *Mater. Des.* **2013**, *47*, 189–199. [[CrossRef](#)]
- Shimizu, T.; Matsuzaki, K.; Nagai, H.; Kanetake, N. Production of high porosity metal foams using EPS beads as space holders. *Mater. Sci. Eng. A* **2012**, *558*, 343–348. [[CrossRef](#)]
- Zhu, L.; Guo, K.; Li, Y.; Yu, T.X.; Zhou, Q. Experimental study on the dynamic behaviour of aluminium foam sandwich plates under single and repeated impacts at low temperature. *Int. J. Impact Eng.* **2018**, *114*, 123–132. [[CrossRef](#)]
- Harris, J.A.; Winter, R.E.; McShane, G.J. Impact response of additively manufactured metallic hybrid lattice materials. *Int. J. Impact Eng.* **2017**, *104*, 177–191. [[CrossRef](#)]
- Mines, R.A.W.; Tsopanos, S.; Shen, Y.; Hasan, R.; McKown, S.T. Drop weight impact behaviour of sandwich panels with metallic micro lattice cores. *Int. J. Impact Eng.* **2013**, *60*, 120–132. [[CrossRef](#)]
- Qiu, C.; Yue, S.; Adkins, N.J.E.; Ward, M.; Hassanin, H.; Lee, P.D.; Withers, P.J.; Attallah, M.M. Influence of processing conditions on strut structure and compressive properties of cellular lattice structures fabricated by selective laser melting. *Mater. Sci. Eng. A* **2015**, *628*, 188–197. [[CrossRef](#)]
- Attar, H.; Ehtemam-Haghighia, S.; Kent, D.; Dargusch, M.S. Recent developments and opportunities in additive manufacturing of titanium-based matrix composites: A review. *Int. J. Mach. Tools Manuf.* **2018**, *133*, 85–102. [[CrossRef](#)]
- Yan, C.; Hao, L.; Hussein, A.; Young, P.; Raymont, D. Advanced lightweight 316L stainless steel cellular lattice structures fabricated via selective laser melting. *J. Mater. Des.* **2014**, *55*, 533–541. [[CrossRef](#)]
- Brandl, E.; Heckenberger, U.; Holzinger, V.; Buchbinder, D. Additive manufactured AlSi10Mg samples using Selective Laser Melting (SLM): Microstructure, high cycle fatigue, and fracture behavior. *J. Mater. Des.* **2012**, *34*, 159–169. [[CrossRef](#)]

12. Kempen, K.; Thijs, L.; van Humbeeck, J.; Kruth, J.-P. Mechanical Properties of AlSi10Mg Produced by Selective Laser Melting. *Phys. Procedia* **2012**, *39*, 439–446. [[CrossRef](#)]
13. Thijs, L.; Kempen, K.; Kruth, J.-P.; van Humbeeck, J. Fine-structured aluminium products with controllable texture by selective laser melting of pre-alloyed AlSi10Mg powder. *Acta Mater.* **2013**, *61*, 1809–1819. [[CrossRef](#)]
14. Yadroitsev, I. *Selective Laser Melting: Direct Manufacturing of 3D-Objects by Selective Laser Melting of Metal Powders*; LAP Lambert: Saarbrücken, Germany, 2009; ISBN 3838317947.
15. Koutny, D.; Palousek, D.; Pantelejev, L.; Hoeller, C.; Pichler, R.; Tesicky, L.; Kaiser, J. Influence of scanning strategies on processing of aluminum alloy EN AW 2618 using selective laser melting. *Materials* **2018**, *11*, 298. [[CrossRef](#)] [[PubMed](#)]
16. Abele, E.; Stoffregen, H.A.; Klimkeit, K.; Hoche, H.; Oechsner, M. Optimisation of process parameters for lattice structures. *Rapid Prototyp. J.* **2015**, *21*, 117–127. [[CrossRef](#)]
17. Leary, M.; Mazur, M.; Elambasseril, J.; McMillan, M.; Chirent, T.; Sun, Y.; Qian, M.; Easton, M.; Brandt, M. Selective laser melting (SLM) of AlSi12Mg lattice structures. *Mater. Des.* **2016**, *98*, 344–357. [[CrossRef](#)]
18. Koutny, D.; Vrana, R.; Paloušek, D. Dimensional accuracy of single beams of AlSi10Mg alloy and 316L stainless steel manufactured by SLM. In Proceedings of the 5th International Conference on Additive Technologies iCAT2014, Vienna, Austria, 16–17 October 2014; pp. 142–147.
19. Yu, G.; Gu, D.; Dai, D.; Xia, M.; Ma, C.; Shi, Q. On the role of processing parameters in thermal behavior, surface morphology and accuracy during laser 3D printing of aluminum alloy. *J. Phys. D Appl. Phys.* **2016**, *1*–15. [[CrossRef](#)]
20. Yu, G.; Gu, D.; Dai, D.; Xia, M.; Ma, C.; Chang, K. Influence of processing parameters on laser penetration depth and melting/re-melting densification during selective laser melting of aluminum alloy. *Appl. Phys. A* **2016**, *122*, 1–12. [[CrossRef](#)]
21. Wei, P.; Wei, Z. The AlSi10Mg samples produced by selective laser melting: Single track, densification, microstructure and mechanical behavior. *Appl. Surf. Sci.* **2017**, *408*, 38–50. [[CrossRef](#)]
22. Delroisse, P.; Jacques, P.J.; Maire, E.; Rigo, O.; Simar, A. Effect of strut orientation on the microstructure heterogeneities in AlSi10Mg lattices processed by selective laser melting. *Scr. Mater.* **2017**, *141*, 32–35. [[CrossRef](#)]
23. Attar, H.; Calin, M.; Zhang, L.C.; Scudino, S.; Eckert, J. Manufacture by selective laser melting and mechanical behavior of commercially pure titanium. *Mater. Sci. Eng. A* **2014**, *593*, 170–177. [[CrossRef](#)]
24. Vrana, R.; Vosynek, P.; Koutny, D.; Navrat, T.; Palousek, D. Evaluation of mechanical behavior of 3D printed lattice structure by SLM: Experiment and FEA. In Proceedings of the Engineering Mechanics 2018 24th International Conference, Svratka, The Czech Republic, 14–17 May 2018; pp. 897–900.
25. Vrana, R.; Koutny, D.; Paloušek, D.; Zikmund, T. Influence of selective laser melting process parameters on impact resistance of lattice structure made from AlSi10Mg. In Proceedings of the World PM 2016 Congress and Exhibition, Hamburg, Germany, 9–13 October 2016; ISBN 978-189-907-248-4.
26. Vrana, R.; Koutny, D.; Paloušek, D. Impact Resistance of Different Types of Lattice Structures Manufactured by SLM. *MM Sci. J.* **2016**, *2016*, 1579–1585. [[CrossRef](#)]
27. Vrana, R.; Koutny, D.; Paloušek, D.; Zikmund, T. Impact resistance of lattice structure made by selective laser melting from AlSi12 alloy. *MM Sci. J.* **2015**, *2015*, 1579–1585. [[CrossRef](#)]
28. Vrana, R.; Koutny, D.; Paloušek, D.; Koukal, O.; Zikmund, T.; Krejci, P. Impact resistance of lattice structure made by selective laser melting technology. In Proceedings of the Euro PM 2015: International Power Metallurgy Congress and Exhibition, Reims, France, 4–7 September 2015; ISBN 978-189-907-247-7.
29. Palousek, D.; Omasta, M.; Koutny, D.; Bednar, J.; Koutecky, T.; Dokoupil, F. Effect of matte coating on 3D optical measurement accuracy. *Opt. Mater.* **2015**, *40*, 1–9. [[CrossRef](#)]
30. Aboulkhair, N.T.; Everitt, N.M.; Ashcroft, I.; Tuck, C. Reducing porosity in AlSi10Mg parts processed by selective laser melting. *Addit. Manuf.* **2014**, *1*, 77–86. [[CrossRef](#)]



Article

Dynamic Loading of Lattice Structure Made by Selective Laser Melting-Numerical Model with Substitution of Geometrical Imperfections

Radek Vrána ¹, Ondřej Červínek ^{1,*}, Pavel Mañas ², Daniel Koutný ¹ and David Paloušek ¹

¹ Institute of Machine and Industrial Design, Faculty of Mechanical Engineering, Brno University of Technology, Technická 2896/2, 616 69 Brno, Czech Republic; Radek.Vrana@vut.cz (R.V.); Daniel.Koutny@vut.cz (D.K.); David.Palousek@vut.cz (D.P.)

² Department of Engineer Technology, Faculty of Military Technology, University of Defence, Kounicova 65, 662 10 Brno, Czech Republic; Pavel.Manas@unob.cz

* Correspondence: Ondrej.Cervinek@vut.cz; Tel.: +420-541-143-256

Received: 9 October 2018; Accepted: 25 October 2018; Published: 29 October 2018



Abstract: Selective laser melting (SLM) is an additive technology that allows for the production of precisely designed complex structures for energy absorbing applications from a wide range of metallic materials. Geometrical imperfections of the SLM fabricated lattice structures, which form one of the many thin struts, can lead to a great difference in prediction of their behavior. This article deals with the prediction of lattice structure mechanical properties under dynamic loading using finite element method (FEA) with inclusion of geometrical imperfections of the SLM process. Such properties are necessary to know especially for the application of SLM fabricated lattice structures in automotive or aerospace industries. Four types of specimens from AlSi10Mg alloy powder material were manufactured using SLM for quasi-static mechanical testing and determination of lattice structure mechanical properties for the FEA material model, for optical measurement of geometrical accuracy, and for low-velocity impact testing using the impact tester with a flat indenter. Geometries of struts with elliptical and circular cross-sections were identified and tested using FEA. The results showed that, in the case of elliptical cross-section, a significantly better match was found (2% error in the F_{max}) with the low-velocity impact experiments during the whole deformation process compared to the circular cross-section. The FEA numerical model will be used for future testing of geometry changes and its effect on mechanical properties.

Keywords: finite element analysis (FEA); low-velocity impact; numerical model; lattice structure; material model; ANSYS Workbench; aluminum alloy AlSi10Mg; energy absorption

1. Introduction

Energy absorbers made of porous materials are currently used to absorb mechanical energy caused by impact or high velocity deformation due to their high efficiency of energy absorption and low weight [1–3]. There are several types of commercially produced porous materials, e.g., hexagonal honeycomb structures [4], metal foams [5–7], or laminated composite fiber blocks [8]. Mostly, the aluminum foams are used. They usually have porosity about 75–95% with a large amount of closed gas pockets and irregular porous structure. This material is usually used in the form of sandwich panels to achieve a higher absorption effect through uniform distribution of stress during loading.

An alternative way to produce porous materials with precisely controlled shape of porous geometry is the SLM technology [9]. SLM uses a layer-based production which allows for the manufacturing of the porous material with a complex shape that can be designed directly for the

expected amount of impact energy. Using SLM, it is also possible to integrate screw holes or other fixation elements to the porous material. Unlike conventionally produced materials, SLM allows the production of the porous material from various alloys such as titanium or tool steels alloys [10]. The most commonly used shape of lattice structure produced by SLM is BCC (Body Centered Cubic) [9,11]. BCC geometry corresponds to body diagonals of the cube. It consists of eight struts intersecting in its center. Orientation of the struts in BCC structure is 35.26° compared to xy plane.

During SLM production of the lattice structure, geometrical imperfections occur. They are caused by struts orientation and heat transfer to the surrounding metal powder. Consequently, the laser process parameter needs to be optimized for SLM production of lattice structure [12–19]. Vrana et al. [19] deal with the SLM processing strategy for strut-lattice structure production, which uses only contour lines and various combinations of main process parameters. The authors focused on the evaluation of the influence of a laser scanning strategy on material properties and surface roughness. The best results were achieved with 25% track overlapping, input energy E_{imp} in the range from 9 J to 10.5 J and linear energy E_{lin} from 0.25 to 0.4 J/mm; in particular, the relative density of 99.83% and the surface roughness on the side of the strut of Ra 14.6 μm in an as-built state was achieved. Geometrical imperfections are mainly shape deviations created by sticking of the partly melted powder particles onto the down skin side of struts [19–21], high surface roughness, and internal porosity. Sticking of powder was also dealt with by Koutny et al. [20]. These authors studied the influence of SLM production orientation on the real diameter of struts. The results show a dependence between the struts diameter and production orientation. In the case AlSi10Mg, the diameter of the struts was always larger, and their true diameter changed with orientation of the strut (compared to the platform). Qui et al. [14] also examined the influence of laser process parameters onto the strut diameter. The results show that single struts manufactured by SLM had a larger diameter than nominal. The diameter increased monotonically with higher laser power and it significantly improved compression mechanical properties of the lattice structure compared to the assumption. Similar results were achieved by Vrana et al. [22] in the case of lattice structure under low-velocity impact loading. The results from mechanical testing show a significant improvement of the impact resistance due to the strut diameter increase.

For efficient design of energy absorber, it is necessary to use FEA to predict mechanical properties of the part during impact load. There are two main approaches to the numerical models of porous materials. The former uses a homogenized model of geometry and the latter uses a simplified model of real geometry [2,4,23–27]. The method of how to simplify the real shape of the lattice struts for FEA was described by Suard et al. [21]. They studied the shape of the lattice structure struts produced by EBM technology. A Computed tomography (CT) analysis was used for a detailed 3D scan of the strut surface. For geometry simplification in FEA, the effective volume corresponding with the maximum cylinder inscribed in the strut was defined. Koutny et al. [20] measured the shape of struts specimens using optical measurement. Similar to the previous author, the maximum inscribed diameter was used for the evaluation of mechanical properties.

Porous materials have a specific impact loading behavior due to the topology of core geometry. Therefore, in the case of homogenized geometry, it is necessary to use a suitable material model that considers its deformation behavior. Material models of porous structures, such as honeycomb or metal foam, are usually included in the material library of the FEA software, and it is possible to also use them for lattice structure [10,26–28]. According to Mohammed et al. [26], a crushable foam material model is suitable for simulation of penetration of porous foam blocks with a damage criterion describing the occurrence of breakdowns between the core and plates. Input material constants can be obtained from uniaxial compression tests according to ASTM D5308. Labeas et al. [27] used both ways; the material model Mat-26 Honeycomb (LS-Dyna) to create a dynamic FEM simulation with a homogenized micro-lattice core and the bilinear (multilinear) material model with micro-lattice BCC structure geometry. The results showed that the simplified core is only suitable for prediction of the first progressive collapse of the lattice structure, while the beam geometry allows for the prediction

of the whole deformation process due to the preserving topology of the core. Based on previous studies [10,26,27], it is possible to determine boundary conditions, type and density of polygonal mesh, type of contact between bodies. It is necessary to consider the difference between the core and plate material model and the damage criterion [19,24,29,30] that needs to be added.

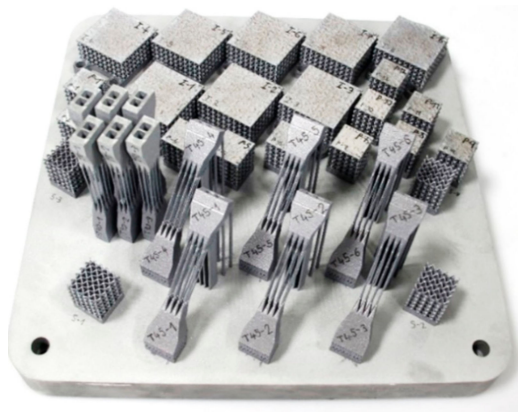
The authors [31–33] examined mechanical properties of AlSi10Mg alloy produced by SLM technology. As tensile specimens, the standard or flat specimens in the as-build or machined condition were usually used. Kempen et al. [33] showed various mechanical properties depending on the SLM production orientation. Specimens with xy orientation achieved a higher elongation compared to the z direction. The influence of the strut shape and SLM process parameters was dealt with by Tsopanos et al. [34]. In their study, the single struts from 316L alloy were tested. The results showed significant differences between the mechanical properties of struts with internal porosity or non-melted particles compared to the well melted struts. It is caused by small dimensions of struts compared to the standard tensile specimens. Therefore, special multi-strut tensile specimens were designed in this study.

Porous materials as honeycomb or metal foams are already used as a highly effective absorber in industry. Currently, metal additive technologies such as SLM can be used as one of the ways for production of energy absorbers. Thanks to the additive production, it is possible to customize the absorbers for specific impact loading by the structure shape design (various areas with a different type of structure, gradient structure [35], etc.) or by the used material. SLM technology also has a few technological limitations that should be considered in FEA. In the case of thin struts production, small shape deviations can occur. Due to the high number of the struts inside the lattice structure, these imperfections can influence mechanical properties of whole structure. Therefore, this study deals with the influence of SLM technology imperfections during struts production and their mechanical response in FEA.

2. Materials and Methods

2.1. Specimens Fabrication Using SLM

All sets of specimens were manufactured using SLM 280HL machine (SLM Solutions GmbH, Lübeck, Germany) which is equipped with a 400 W Ytterbium fiber laser (YLR-laser) with Gaussian shape of energy distribution and spot diameter 82 μm . Laser scanning speed may reach up to 10.000 $\text{mm}\cdot\text{s}^{-1}$. During SLM process, the N_2 atmosphere was used in a chamber which provides 280 \times 280 \times 350 mm build envelope. To ensure the same conditions during the manufacturing process, each set of specimens were produced in one build job (Figure 1a). Standard process parameters (SLM Solutions) were used (Figure 1b).



(a)

Selective Laser Melting Process Parameters	
Laser power	350 W
Laser speed – borders	500 $\text{mm}\cdot\text{s}^{-1}$
Laser speed – volume	930 $\text{mm}\cdot\text{s}^{-1}$
Beam compensation	150 μm
Layer thickness	50 μm
Hatch distance	150 μm
Platform preheating	150 $^{\circ}\text{C}$
Laser spot size	ϕ 82 μm
Oxygen level	up to 0.2 %
Atmosphere	N_2

(b)

Figure 1. (a) Single series of mechanical specimens after SLM manufacturing; (b) SLM laser process parameters used for specimen fabrication.

2.2. Metal Powder Analysis

AlSi10Mg aluminum alloy powder (TLS Technik GmbH, Bitterfeld, Germany) was used for manufacturing all types of specimens. The powder material with almost spherical shape of particles was produced using a gas atomization technology in nitrogen atmosphere (Figure 2b). For quality verification, the particle size distribution was analyzed (Horiba LA-960, Horiba, Kyoto, Japan). Main parameters of the particle size distribution were as follows—median size was 40.7 μm , mean size was 41.4 μm , and standard deviation was 12.9 μm . The particle size up to 25.2 μm represents 10% and the particles up to size of 58 μm represents 90% of particles (Figure 2a). Depending on the particle size distribution of the metal powder, a 50 μm layer was used for fabrication of all specimens.

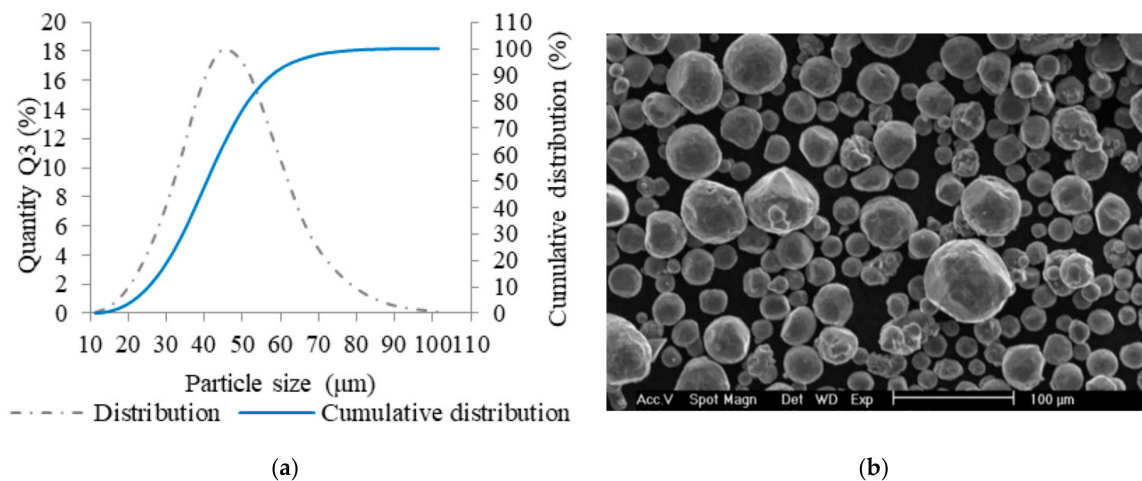


Figure 2. Selective laser melting (SLM) powder characteristics; (a) chart of particle size distribution; (b) shape of powder particles (scanning electron microscopy (SEM)).

2.3. Specimens for Mechanical Testing

2.3.1. Tensile Specimens

Mechanical properties of thin struts are highly affected by surface roughness and internal material porosity, which locally reduces the strut cross-section and mechanical properties [34]. Therefore, a special (multi-struts) shape of tensile specimens was designed for quasi-static mechanical testing (TS-series; Figure 3d). The multi-strut specimens were composed of 12 struts with diameters of $d = 0.8$ mm and strut lengths of $l = 29$ mm. To describe the material properties depending on specimen's inclination during SLM layer-based fabrication, they were fabricated in orientation of 90° and 45° (relative to the platform). To compare the struts and bulk mechanical properties, standard bulk material specimens (TB-series; Figure 3b) were also fabricated in orientation of 90° and 45° (relative to the platform). All specimens were tested in the as-built condition.

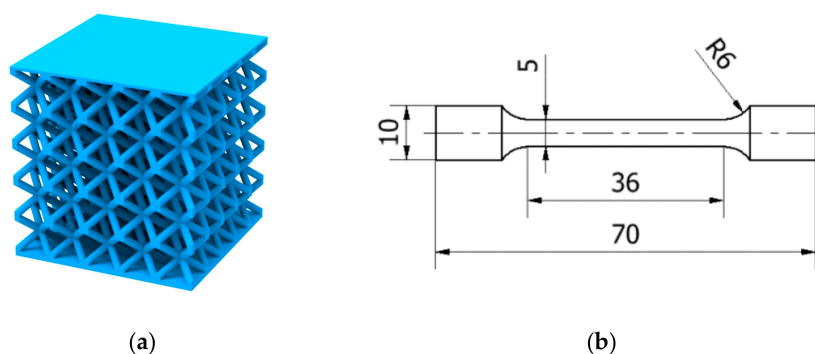


Figure 3. Cont.

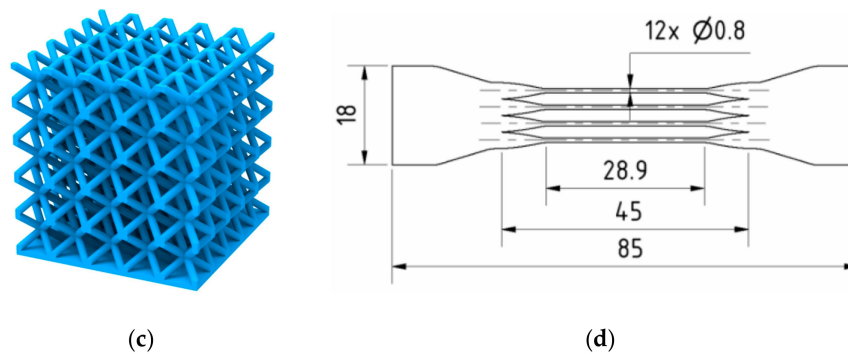


Figure 3. Specimens for (a) quasi-static compressive (C-series) and low-velocity impact testing (IT-series); (b) quasi-static tensile testing of bulk material (TB-series); (c) optical analysis (O-series); and (d) quasi-static tensile testing of multi-strut specimens (TS-series).

2.3.2. Lattice Structure Specimens

For quasi-static compression tests, BCC lattice structure core specimens with dimensions of $20 \times 20 \times 20.8$ mm were used (C-series; Figure 3a). The BCC unit cell was composed of eight struts with diameter $d = 0.8$ mm and side length $a_{BCC} = 4$ mm. On the bottom and upper side, the specimens were covered with thin plates $t = 0.3$ mm. For low-velocity impact testing, a specimen with dimensions of $20 \times 20 \times 16.8$ mm and the same shape of the unit cell was used (IT-series; Figure 3a). To verify the material model based on parameters obtained from quasi-static testing, specimens for low-velocity impact testing with diameters of 0.6, 0.8, 1.0, and 1.2 mm were produced. Specimens for optical measurement were similar to the specimens for mechanical testing but manufactured without the upper plate for better access to the lattice structure core during the optical measurement process (O-series; Figure 3c).

2.4. Shape of the Struts Analysis

To determine the actual dimensions of BCC lattice structure and multi-strut tensile specimens, O-series and TS-series of the specimens were analyzed by ATOS Triple Scan (GOM GmbH, Braunschweig, Germany) optical 3D scanner (MV170 lens; calibration was carried out according to VDI/VDE 2634, Part 3). Before the scanning process, specimens were coated with a thin layer of titanium dioxide powder (approx. $3 \mu\text{m}$) [36]. Due to the complex shape of specimens, only four-corner struts could be digitized in the required quality.

The actual dimensions were measured by fitting the ideal cylinders and ellipses into the surface geometry in GOM Inspect software (SR1, GOM GmbH, Braunschweig, Germany, Figure 4)—diameter d_{in} (inscribed cylinder) shows the largest diameter of homogeneous strut without geometrical imperfection and surface roughness; diameter d_{out} (circumscribed cylinder) defines the strut diameter including surface roughness and partially melted powder on the down skin strut surface; diameter d_{gauss} shows the value with the Gaussian distribution.

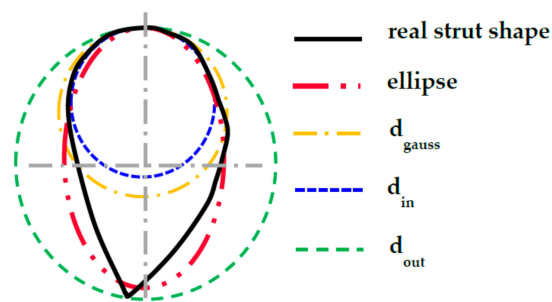


Figure 4. Visual 2D representation of elements used for dimensional struts analysis.

To include the partially melted powder on the down skin side to the strut geometry, the ellipse geometry, which very well reflects the real shape of the strut cross-section, was used. Ellipse dimensions were measured in three points on the single corner struts, and the average value was used. Measured diameters were used for dimensional analysis of the lattice structure and for the creation of real lattice structure geometry in FEA.

2.5. Mechanical Testing

2.5.1. Quasi-Static Mechanical Testing

Zwick Z020 device, (Zwick Z020, ZwickRoell GmbH & Co. KG, Ulm, Germany) a universal machine for mechanical testing with maximum force of 20 kN, was used for tensile (TS-series, TB-series) and compression test (C-series). Specimens were pre-loaded with 20 N and loaded with standard loading speed of $2 \text{ mm} \cdot \text{min}^{-1}$. During tensile testing, specimens were clamped into the jaws and loaded until all struts were broken.

During the pressure testing, the samples were placed between two plates in the testing device. The bottom plate was fixed attached to the device, thereby, movement of the sample in the vertical axis or its rotation was avoided. The upper movable plate was hinged with a rotary joint. This type of connection allowed a slight rotation of the upper (loading) plate during contacting with the sample's surface. This eliminates the possible effect of uneven loads caused by inclined grinding of the sample surface (Figure 5).

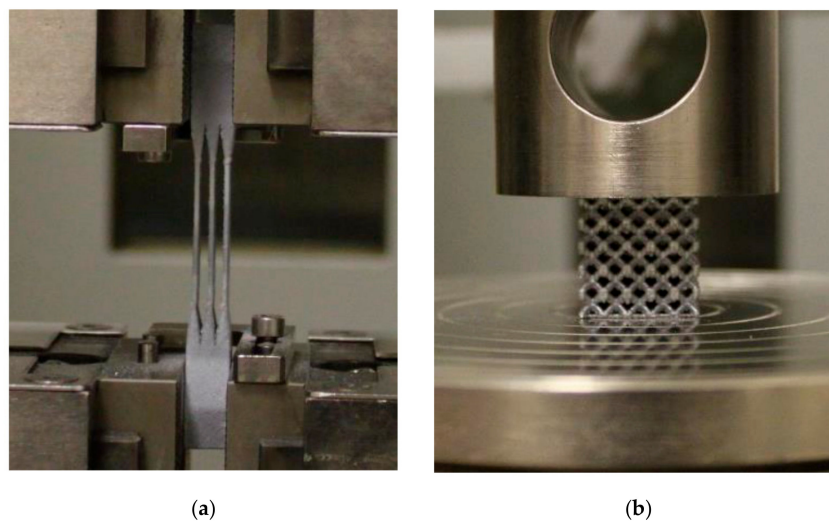


Figure 5. Mechanical testing using Zwick Z020 machine (a) tensile test; and (b) compression test.

2.5.2. Low-Velocity Impact Test

Low-velocity impact testing of the IT-series was performed on the drop weight impact tester developed at Brno University of Technology (Figure 6a). The system is equipped with high-speed camera Phantom V710 and strain-gauge (XY31-3/120). The strain-gauge measures the reaction force during deformation of the lattice specimens, the high-speed camera measures the position of the marker on the falling head. Signals from the strain gauge were recorded using the data acquisition system Quantum X MX410B (HBM GmbH) with a sampling frequency of 96 kHz, data from the high-speed camera were recorded in Phantom software with a sampling frequency of 48 kHz. Both records were jointly evaluated in MATLAB software. The main output of measurements are the following dependencies: Force reaction, time (deformation), velocity of falling head, time (deformation), maximum specimen deformation, and deformation duration. The device allows to change the shape of impact body—flat indenter (surface contact; Figure 6b) and ball indenter (point contact; $d = 16 \text{ mm}$). During impact testing, the weight of the falling head was $m = 7.252 \text{ kg}$ and

the drop height was $h = 1$ m. For these parameters, the falling head achieves the maximum drop speed $v_{In} = 3.2 \text{ m}\cdot\text{s}^{-1}$ with maximum energy $E_{In} = 71.1 \text{ J}$. The testing device belongs to the group of low-velocity test devices [7,25,26].

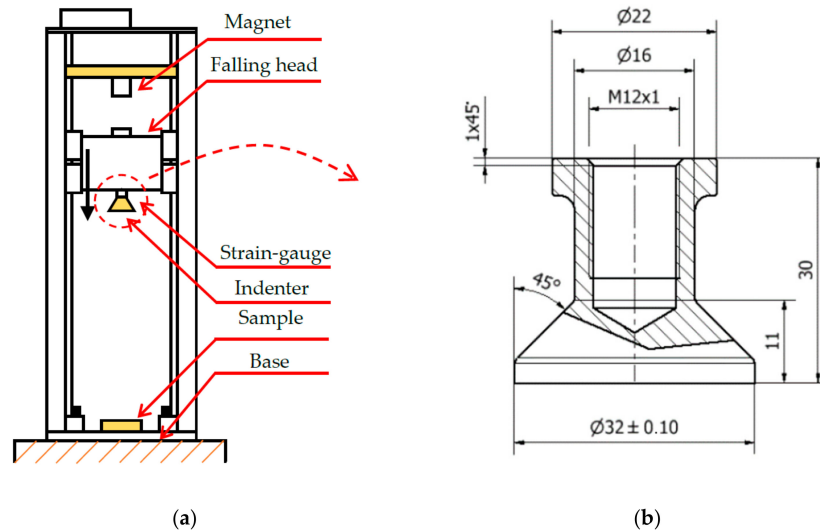


Figure 6. (a) Schema of the low-velocity impact tester; and (b) Geometry of the flat indenter.

2.6. FEM Numerical Model

The numerical model of the low-velocity impact test was created in ANSYS Workbench 18.2 software, module Explicit dynamic. Based on previous studies [2,4,23–27], the material model Bilinear isotropic hardening was selected for definition of mechanical properties of lattice core. The geometry was composed of five bodies according to Figure 7a, where the body (3) represents the lattice structured core; bodies (2) and (4) represent bottom and upper plates of the specimen; the body (1) is the indenter, and the body (5) is a solid base.

The initial drop weight impact test was performed to find out the strain rate values for various struts diameters. The obtained results were in range of $80\text{--}120 \text{ s}^{-1}$. Based on the initial results along with the loading velocity of about of $3 \text{ m}\cdot\text{s}^{-1}$, the elastic-plastic material model was selected. This model did not further consider sensitivity in the strain-rate effect.

Input parameters for definition of lattice structure core material model were determined from quasi-static tensile and compression tests of the specimen TS- and C-series, specifically from stress-strain curves, which were created based on force—displacement testing data and the geometry results from optical measurement of the specimens (see Section 3.3.1). Mechanical parameters of plates were determined from the tensile test of bulk material (TB-series). The material model was also supplemented with the criterion of damage obtained from the lattice quasi-static compression test. The used limit value corresponds with strain at the maximum stress point ($\epsilon_{\sigma_{max}}$) before the progressive collapse of the lattice structure. For the indenter and the base body, the standard Structural Steel material model was used in the case of the indenter with rigid behavior.

Numerical model constrains were based on a quarter symmetry in x and y directions. From the bottom to the top in Figure 7a, between the base (5) and the bottom plate (4), the frictional contact with static frictional coefficient (0.61), and dynamic frictional coefficient of 0.47 were defined. The bottom and upper plates (4, 2) are connected with the lattice core (3) by the bonded contacts. Body self-interaction was involved. To achieve a comparable result with the experiment, only the base body (5), which represents the base plate in the testing device, was limited in x, y, z direction (rotation was not suppressed). To define the boundary conditions, parameters of the low-velocity impact experiment were used. The falling head ($m = 7.25 \text{ kg}$) was represented by the indenter in the numerical model. As in reality, the weight of the indenter is very low compared to the falling head; therefore, the

weight of the indenter was increased using a higher density value ($\rho_{Ind} = 899,306 \text{ kg}\cdot\text{m}^{-3}$) to match the weight of the real falling head. The impact velocity was determined using high-speed camera $v = 3.1 \text{ m}\cdot\text{s}^{-1}$. For all bodies, the standard gravitational acceleration $g = 9.806 \text{ m}\cdot\text{s}^{-2}$ was adopted.

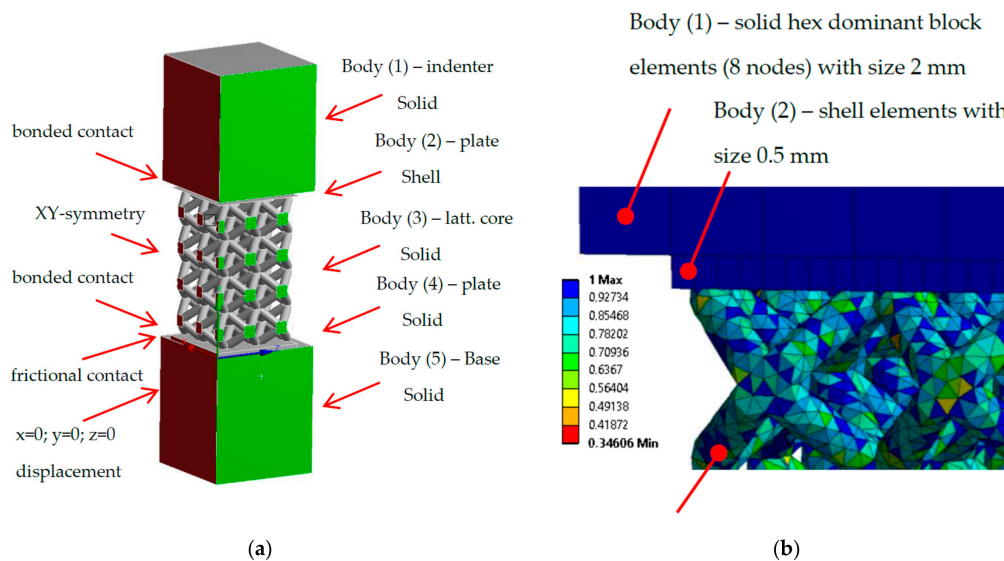


Figure 7. Numerical model in the Ansys software (a) quarter model with bodies and constrains; (b) finite element mesh quality.

A finite element mesh was created with several element types (Figure 7a)—the base and indenter bodies (1, 5) were formed by Hex dominant block elements (8 nodes) with size 2 mm, the bottom plate (4) with Hex Dominant block elements (8 nodes) with a size of 1 mm, the lattice core (3) with solid Tetrahedron (4 nodes) elements, which also well represents the surface roughness of the struts (Figure 7b). Their size was managed by the diameter of struts and the mesh quality parameter. In the case of circular cross-section shape with diameter $d = 0.95 \text{ mm}$, tetrahedron element size was 0.4 mm. The shell elements with size of 0.5 mm were used for upper plate (2) to prevent the Hourglass effect (Figure 8a).

In the case of a mid-surface representation, all physical and geometrical information are represented only by the surface of shell elements without thickness (Figure 8b). For the correct physical representation and constrain application between the upper plate and indenter, the shell thickness factor was considered and set to $STF = 0.95$. This parameter ensures a contact surface in real distance from the mid-surface (Figure 8c).

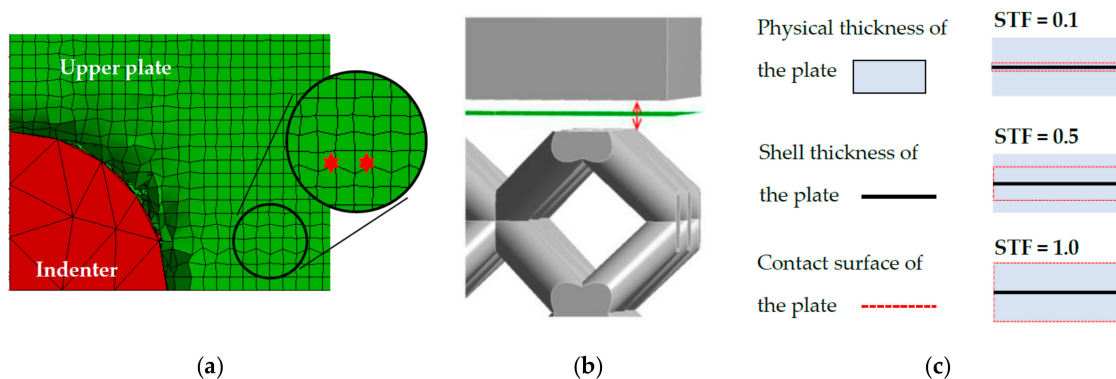


Figure 8. (a) Hour-glassing energy error; Shell thickness factor—(b) Shell mid-surface of the upper plate; and (c) Description of the contact surface.

3. Results

In presented study, there are a lot of used abbreviations, therefore, the table which summarizes them was created (Table 1).

Table 1. The list of used abbreviation.

Shortcut	Description	Shortcut	Description
SLM	Selective laser melting technology	d_{in}	Maximum inscribed cylinder into the strut
FEA	Finite element analysis	d_{out}	Minimum circumscribed cylinder on the strut surface
FEM	Finite element method	A_r	Cross-section area of real strut
YLR	Ytterbium fiber laser	A_{Din}	Cross-section area of maximum inscribed cylinder into a strut
BCC	Body centered cubic	A_{Dgauss}	Cross-section area of Gauss strut cylinder
NM	Numerical model	A_{Dout}	Cross-section area of minimum circumscribed cylinder fitted on a strut surface
STF	Shell thickness factor	$A_{ellipse}$	Cross-section area of an ellipse fitted to the strut surface
CAD	Computer aided design	a	Ellipse minor axes
EPS	Equivalent Plastic Strain	b	Ellipse major axes
BL-I	Bilinear isotropic hardening model of lattice core	e	Ellipse ratio
BL-II	Bilinear isotropic hardening model of bottom and upper plates	F_{max}	Maximum force
EBM	Electron beam melting	x_{Fmax}	Deformation of the specimen at maximum force
CT	Computed tomography	σ_{max}	Maximum engineering stress
a_{BCC}	Length of BCC cell edge	$\epsilon_{\sigma max}$	Strain at the maximum engineering stress
l	Length of the struts in the multi-strut tensile specimen	E	Young's Modulus
d	Nominal lattice structure strut diameter	E_T	Tangent Modulus
t	Specimen's upper plate thickness	$YTS_{0.2\%}$	Offset yield strength at strain 0.2%
h	Height of the C-series specimens	UTS	Ultimate tensile strength
h_{CAD}	Nominal CAD height of the specimen	E_{In}	Initiating impact energy, energy just before impact
t_{UpP}	Thickness of the upper plate	v_{In}	Initiating speed, speed just before impact
m_C	Weight of the C-series specimens	m	Weight of the falling head
$m_{CAD_{0.8}}$	CAD weight of the C-series specimen with nominal struts diameter	t_{def}	Duration of deformation
$m_{CAD_{0.95}}$	CAD weight of the C-series specimen with Gauss struts diameter and real upper plate thickness	x_{Dyn}	Deformation of the specimens under dynamic loading
$\bar{\rho}$	Measured relative density of C-series	E_{Abs}	Absorbed energy
$\bar{\rho}_{CAD_{0.8}}$	Calculated relative density of the CAD model with nominal diameter $d = 0.8$ mm	v_{Up}	Speed of the rebound
$\bar{\rho}_{CAD_{0.95}}$	Calculated relative density of the CAD model with measured Gaussian diameter $d = 0.8$ mm	k_{Dyn}	Average stiffness of the specimens under dynamic loading
d_{gauss}	Ideal struts Gauss cylinder	P_{Abs}	Absorption power of the specimens under dynamic loading
n	Number of the struts in the multi-strut specimen	h_{ef}	Effective length of the tensile specimen
ρ_{Ind}	deliberately increased density of the indenter to represent the weight of the whole falling head	E_{inp}	Input energy to the current layer of the lattice structure
SEM	Scanning electron microscopy	E_{lin}	Linear energy—(laser power/laser speed)

3.1. The Analysis of Initial Weight and Height

After SLM fabrication, the basic parameters, such as weight and height of C-series, were carried out (nominal struts diameter $d = 0.8$ mm). The results showed that the weight of the specimens was almost twice as high and the relative density $\bar{\rho}$, which was found comparing the real weight and the theoretical weight of the solid cube, was about 10% higher than that expected by CAD. Therefore, the lattice structure numerical model must have struts diameter larger than the nominal diameter $d = 0.8$ mm. The deviation was caused by SLM production of larger struts of the lattice structure, as was also described in the study in Reference [14]. Based on these results (Table 2), more detailed analyses using optical measurement were performed.

Table 2. The initial analysis of the C-series.

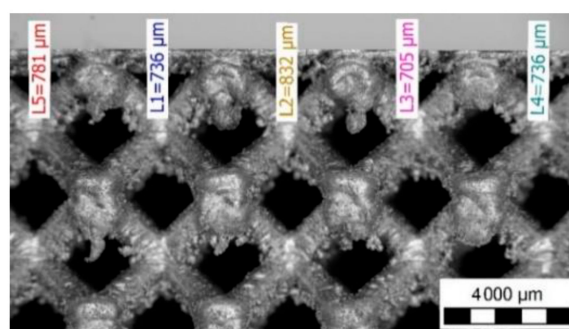
(Avg. Values)	Measured					CAD			
	h (mm)	t_{UpP} (mm)	m (g)	$\bar{\rho}$ (%)	h_{CAD} (mm)	$m_{CAD_{0.8}}$ (g)	$m_{CAD_{0.95}}$ (g)	$\bar{\rho}_{CAD_{0.8}}$ (%)	$\bar{\rho}_{CAD_{0.95}}$ (%)
\bar{x}	21.04	0.75	6.97	31	20.80	4.72	6.94	21	31

3.2. Optical Measurement of the Lattice Structure

The optical system Atos Triple Scan III (GOM GmbH, Braunschweig, Germany) and the lighting microscope Olympus SZX7 (Olympus, Tokyo, Japan) were used for more detailed measurements of the lattice structure. The result shows that there were significant differences between the inscribed and circumscribed cylinders (Table 3, Figures 4 and 9).

Table 3. Struts diameter measured using the Atos Triple Scan optical system (O-series; nominal diameter $d = 0.8$ mm).

(mm)	Corner Strut	d_{gauss}	d_{in}	d_{out}	Ellipse			
					Minor Axis		Major Axis	
S1	1	0.94	0.74	1.26	0.79	1.1	0.79	1.12
	2	0.99	0.75	1.19	0.81	1.17		
	3	0.93	0.7	1.24	0.79	1.14		
	4	0.93	0.72	1.16	0.78	1.09		
S2	1	0.96	0.76	1.18	0.8	1.2	0.79	1.12
	2	0.92	0.75	1.09	0.79	1.03		
	3	1.02	0.73	1.36	0.8	1.06		
	4	0.94	0.72	1.23	0.77	1.17		
S3	1	0.86	0.69	1.08	0.78	1.08	0.76	1.06
	2	0.91	0.69	1.26	0.77	1.05		
	3	0.94	0.76	1.2	0.76	1.13		
	4	0.91	0.7	1.17	0.73	0.97		
S4	1	0.97	0.82	1.27	0.86	1.27	0.84	1.16
	2	0.96	0.73	1.31	0.89	1.15		
	3	1.01	0.74	1.43	0.83	1.04		
	4	0.93	0.67	1.23	0.77	1.18		
\bar{x}		0.945	0.729	1.229	0.795	1.114		

**Figure 9.** Side view on the C-series specimen using the lighting microscope.

3.3. Mechanical Properties

3.3.1. Quasi-Static Mechanical Testing

For evaluation of mechanical properties, the average dimensions of d_{gauss} were used (Table 4; Figure 10). From the stress-strain curves, yield strength $YTS_{0.2\%}$, Young's Modulus E , and tangent modulus E_T were evaluated. $YTS_{0.2\%}$ was carried out as an intersection of the stress-strain curve and the parallel line to the linear part of the curve (Hook area) in the strain value 0.002. E_T tangent modulus was obtained as an interpolation of the part of the plastic area in a stress-strain curve by a line.

The same evaluation process was used in the case of bulk material specimens (TB-series). The obtained average values are shown in Table 5.

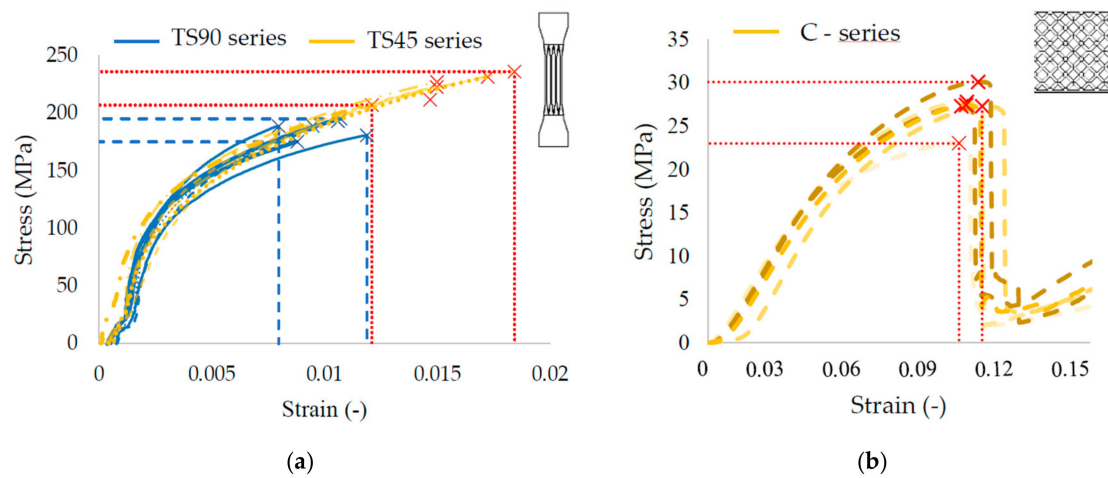


Figure 10. (a) Quasi-static stress-strain curves of the struts tensile specimens; and (b) Quasi-static stress-strain curves of the compression specimens.

Table 4. The dimensions of the tensile specimen specimens (multi-struts tensile specimens TS-series; bulk tensile specimens TB-series).

(mm)	TS45			TS90			TB45			TB90		
	d_{gauss}	d_{in}	d_{out}	d_{gauss}	d_{in}	d_{out}	d_{gauss}	d_{in}	d_{out}	d_{gauss}	d_{in}	d_{out}
1	0.88	0.66	1.07	0.78	0.61	1.09	5.05	4.91	5.49	5.03	4.94	5.36
2	0.88	0.69	1.14	0.79	0.68	1.03	5.04	4.89	5.66	5.02	4.9	5.45
3	0.89	0.72	1.15	-	-	-	5.03	4.85	5.6	5.01	4.93	5.57
4	0.9	0.74	1.19	0.79	0.71	0.88	-	-	-	-	-	-
5	0.9	0.7	1.34	0.8	0.69	1.06	-	-	-	-	-	-
6	0.91	0.71	1.29	0.78	0.69	0.87	-	-	-	-	-	-
\bar{x}	0.89	0.70	1.20	0.79	0.68	0.99	5.04	4.88	5.58	5.02	4.92	5.46

Table 5. The dimensions of the tensile specimen specimens with different orientation to the platform (multi-struts tensile specimens TS-series; bulk tensile specimens TB-series).

Spec.	F_{max} (N)	x_{Fmax} (mm)	σ_{max} (MPa)	$\epsilon_{\sigma_{max}}$	E (GPa)	YTS _{0.2%} (MPa)	UTS (MPa)	E_T (MPa)
TS45	2270	0.462	-	0.015	71.6	131.6	224.2	6649
TS90	1934	0.297	-	0.010	103.7	116.6	186.8	8701
TB45	7625	1.030	-	0.026	96.1	227.0	382.2	4858
TB90	6453	0.809	-	0.020	147.5	187.4	326	5753.3
C	10,860	2.133	27.2	0.103	483.5	-	-	-

3.3.2. Low-Velocity Impact Test Results

To find out the absorption characteristics of the BCC lattice structure material and FEA for validation, the low-velocity impact test of the IT-series was carried out using the low-velocity impactor. As was described above, the specimens were produced together in the one build job; however, significant differences in mechanical properties in single sets of specimens, such as maximum reaction force F_{max} , maximum deformation x_{Dyn} or duration t_{def} can be observed (Figure 11b). These differences could be caused by a local damage of the lattice structure under loading, the structure which can occur by the material imperfection of SLM fabricated lattice structures such as surface roughness or internal porosity. It can change symmetrical bending of dominate deformation process, which is typical for BCC structures, to an asymmetrical mechanical response [37]. Therefore, in the case of the lattice

structure, it is necessary to work with average values of the mechanical properties. For comparison purposes, the average curves of the force-deformation and initial speed-deformation were created (Figure 11c,d). All the low-velocity impact results are shown in Table 6; there is shown that mechanical properties of sets of specimens, such as maximum reaction F_{max} and stiffness of the specimens under dynamic loading $k_{D_{yn}}$, increase linearly with struts diameter.

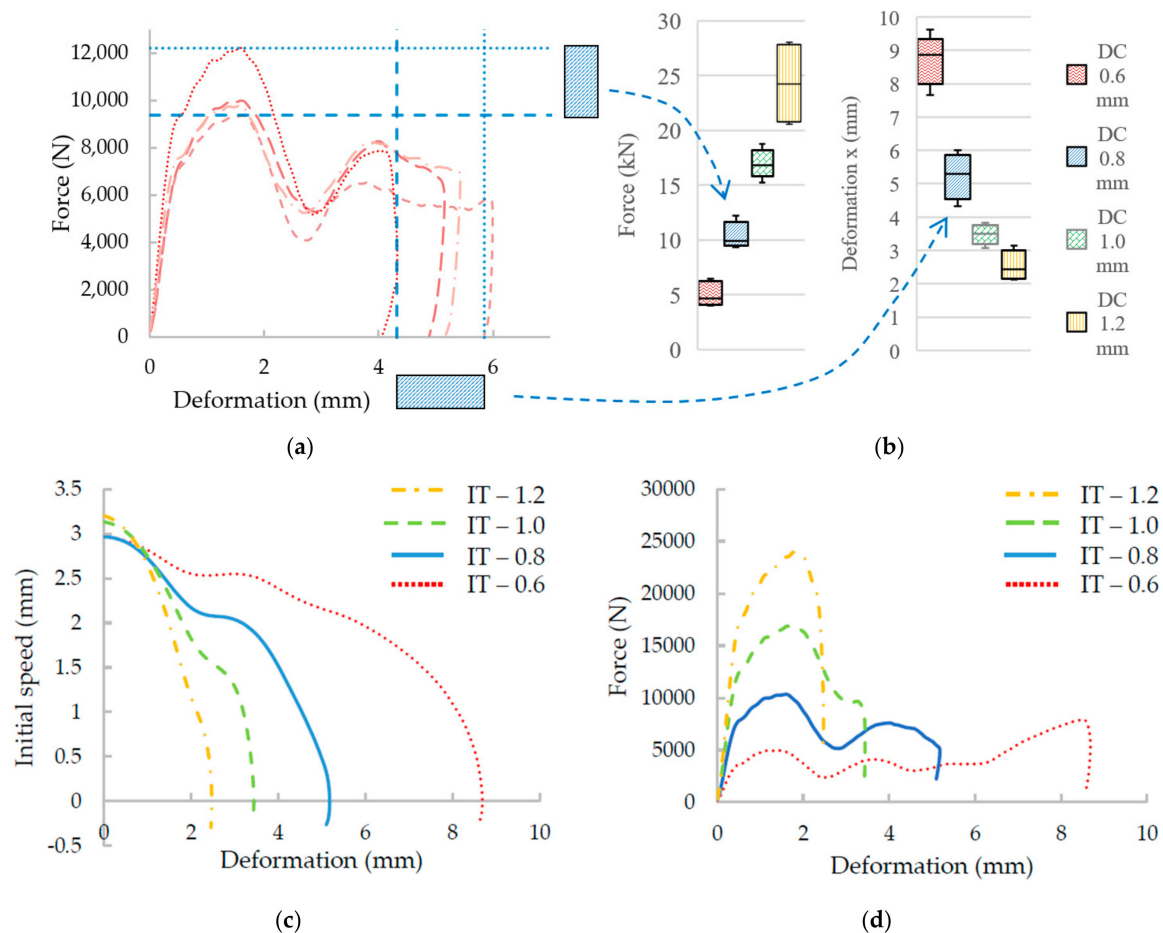


Figure 11. The results from low-velocity impact testing: (a) Single IT-series with diameter $d = 0.8$ mm; (b) variance of force and deformation of all IT-series; (c) average initial speed, deformation curves; and (d) average force-deformation curves.

Absorbed energy E_{Abs} was evaluated regarding the real measured initiating speed v_{In} and initiating impact energy E_{In} for each specimen. From Table 5, it is obvious that most of specimens absorbed more than 99% of impact energy, and only in the case of the specimens with nominal diameter $d = 1.2$ mm, there was a small decline. Therefore, the parameter absorption power P_{Abs} ($J \cdot s^{-1}$), which reflects the deformation and absorbed energy, was defined.

$$P_{Abs} = E_{Abs} / t_{def} \tag{1}$$

The lattice structure with low value of P_{Abs} can absorb energy through long duration and large deformation. It is important e.g., in automotive industry where the car deformation area must be designed for overload not damaging the human body.

Table 6. The results of the low-velocity impact.

#	F_{max} (N)	t_{def} (ms)	x_{Dyn} (mm)	v_{In} (m·s ⁻¹)	E_{In} (J)	E_{Abs} (J)	v_{Up} (m·s ⁻¹)	k_{Dyn} (N·mm ⁻¹)	P_{Abs} (J·s ⁻¹)
IT 0.6	4252	4.94	9.07	3.02	33.10	32.47	0.42	9005	6.58
	6479	4.64	7.67	2.95	31.51	31.19	0.30		6.73
	4005	5.29	9.61	2.93	31.19	30.87	0.30		5.83
	4660	5.04	8.86	2.95	31.48	31.20	0.28		6.19
	6047	4.71	8.31	2.97	32.08	31.68	0.33		6.73
\bar{x}	5089	4.92	8.70	2.96	31.87	31.48	0.32	-	6.41
IT 0.8	-	-	-	-	-	-	-	-	-
	9989	3.41	5.15	2.97	32.03	31.58	0.35	19,417	9.27
	9368	4.05	6.00	2.93	31.91	31.71	0.24		7.82
	12,218	2.94	4.32	>2.96	31.87	31.31	0.39		10.66
	9795	3.52	5.43	2.96	31.72	31.08	0.42		8.83
\bar{x}	10,343	3.48	5.22	2.96	31.88	31.42	0.35	-	9.15
IT 1.0	15,223	2.79	3.83	3.07	34.22	33.89	0.30	29,371	12.14
	17,625	2.03	3.30	3.13	35.45	35.28	0.22		17.37
	16,437	2.16	3.66	3.15	36.09	35.56	0.38		16.49
	18,796	1.80	3.08	3.16	36.09	35.29	0.47		19.58
	16,859	2.18	3.50	3.15	35.98	35.83	0.20		16.46
\bar{x}	16,988	2.19	3.47	3.13	35.57	35.17	0.31	-	16.41
IT 1.2	24,205	1.49	2.43	3.19	36.93	34.87	0.75	39,006	23.41
	28,067	1.31	2.17	3.22	37.61	35.22	0.81		26.84
	20,597	1.89	3.14	3.21	37.30	36.44	0.48		19.33
	27,627	1.31	2.13	3.21	37.28	34.92	0.81		26.61
	20,990	1.80	2.87	3.17	36.54	35.41	0.56		19.65
\bar{x}	24,297	1.56	2.55	3.20	37.13	35.38	0.68	-	23.17

3.4. Finite Element Analysis (FEA)

3.4.1. FEA Material Models

Based on the quasi-static results, the material model (BL-I) of the BCC lattice structure from AlSi10Mg alloy was created (Table 7). The parameters E , $YTS_{0.2\%}$ and E_T of the TS45-series were used to create the Bilinear isotropic hardening material model due to a similar strut build inclination, as in the case of the BCC lattice structure (35.26°) [33]. A damage criterion was obtained from the C-series as the maximum equivalent plastic strain $\epsilon_{\sigma max}$. The material model (BL-II) of the upper and bottom plate was created using mechanical parameters of the bulk material. The other needed parameters were used from the Ansys material library as the default values.

Table 7. Materials model used for lattice structure specimens FEA.

Parameters	BL-I (BCC)	BL-II (Plate)	Unit
Density	2680	2680	kg·m ⁻³
Isotropic Elasticity	-	-	-
Young's Modulus	70,723	96,100	MPa
Poisson's Ratio	0.334	0.334	-
Bulk Modulus	7.1×10^{10}	9.6×10^{10}	Pa
Shear Modulus	2.7×10^{10}	3.6×10^{10}	Pa
Bilinear Isotropic Hardening	-	-	-
Yield Strength	135	227	MPa
Tangent Modulus	6586	4858	MPa
Plastic Strain Failure	-	-	-
Max. Equivalent Plastic Strain EPS	0.1025	0.1025	-

3.4.2. FEM Model

The results from FEA using the numerical model (NM) of the low-velocity dynamic loading (described above) are shown in Figure 12. From the figure, it is obvious that the force-time curve of the NM with ellipse cross-section (Figure 12b) corresponds better to the experimental results than that with circular cross-section (Figure 12a). The largest deviations can be seen in the middle (between 1.5–4 ms) and towards the end (between 4–5 ms) of the force-time curve. In the case of FEA considering the circular cross-section shape, the deformation time exceeded 5 ms, and the specimen was continually deformed. It does not correspond with the results of the low-velocity testing where the deformation ended at 5 ms. In the case of FEA considering the ellipse cross-section shape, duration and deformation ended at the end of 5 ms. The real and predicted damage of the specimens after low-velocity impact testing is shown in Figures 13 and 14.

The deviations between FEA and the experiment were compared using the maximum force value in the first force peak in the case of FEA, and the average maximum force from the five experimentally tested specimens. The results show that the relative error of FEA with circular cross-section is 12%, while with elliptical cross-section, it is 2% in the case of IT-0.8 series.

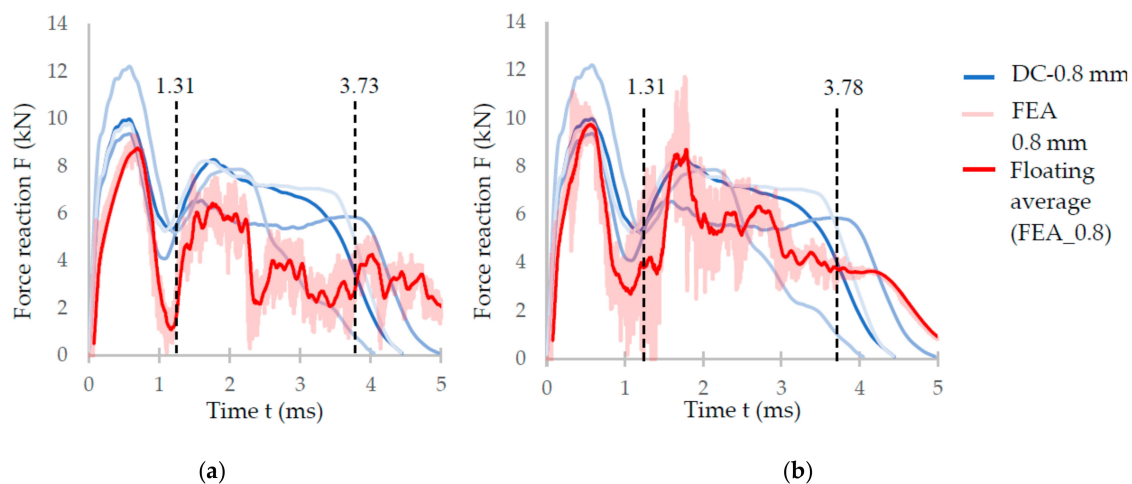


Figure 12. (a) Comparison of the results of the IT-0.8 series and the numerical simulation with (a) circular cross-section; and (b) elliptical cross-section.

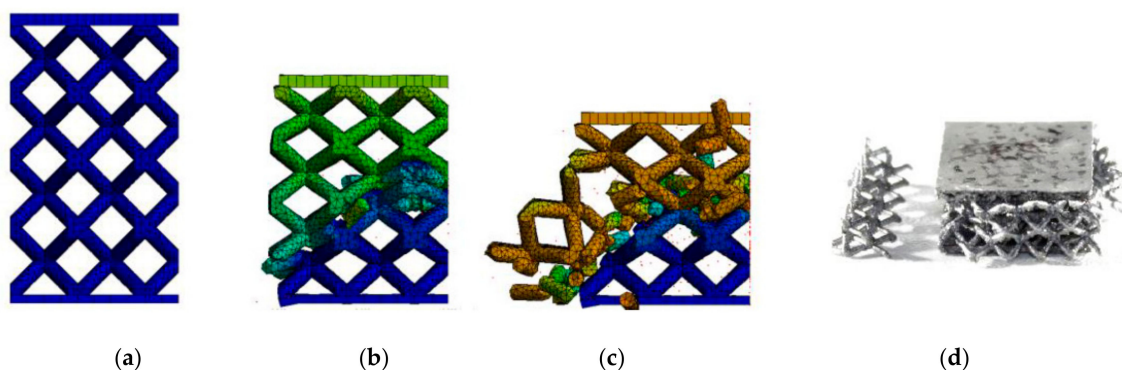


Figure 13. Gradual deformation of the specimen with circular strut cross-section in time—(a) 0 ms; (b) 1.31 ms; (c) 3.73 ms; (d) real damage of the specimen IT-2 after low-velocity impact test.

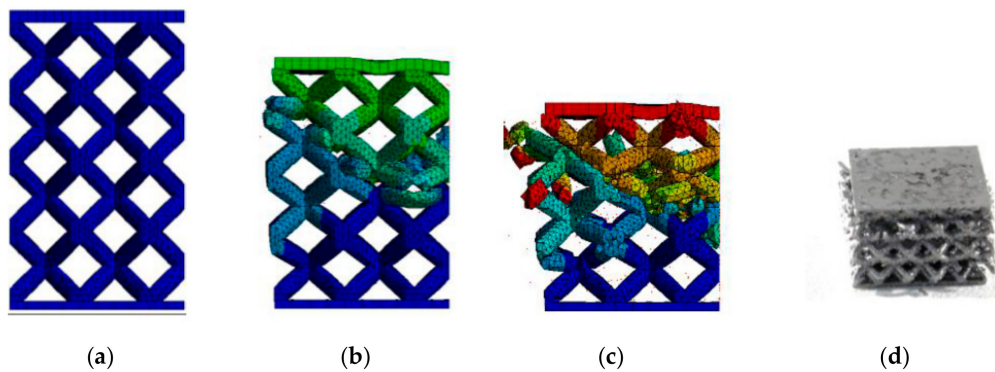


Figure 14. Gradual deformation of the specimen with elliptical strut cross-section in time: (a) 0 ms; (b) 1.31 ms, (c) 3.78 ms; and (d) real damage of the specimen IT-2 after low-velocity impact test.

4. Discussion

4.1. Substitution of the Strut's Real Cross-Section with the Ideal Cross-Section

The deformation behavior of numerical model (NM) with the ideal circular cross-section geometry of $d = 0.8$ mm (nominal diameter) showed large differences to the experiment during initial tests. Therefore, the results from weighing and optical measuring of the C-series (Figure 15a) were used for finding ideal diameter for using in NM for prediction of the real behavior of the lattice structure.

From the 3D scanned data of the lattice structure (C-series), a cross-section area of the real single strut was calculated (Figure 15b; $A_r = 0.712$ mm²) and compared with the cross-section area of the fitted ideal cylinders to the strut in the GOM Inspect software ($A_{Din} = 0.417$ mm²; $A_{Dgauss} = 0.701$ mm²; $A_{Dout} = 1.186$ mm²). The results show that the best match is in the case of d_{Gauss} . Therefore, this diameter seems to be appropriate to represent the designed diameter $d = 0.8$ mm in the NM.

A similar result was obtained from weight comparison where the weight of the lattice structure CAD model with d_{Gauss} and the measured weight were compared (Table 2). To the weight of CAD model ($m_{CAD_{0.95}}$), the larger thickness of the plates from the lighting microscope was also added. The result shows that weight m and $m_{CAD_{0.95}}$ are almost identical. Based on these basic analyses, the strut diameter d_{Gauss} was selected for lattice structure simplification using ideal circular cross-section in the numerical model. This result differs from the results of Suart et al. [21], where the diameter equal to d_{In} was used.

During the evaluation of optical measurement, the real shape of the lattice structure struts similar to “water drop” was found (Figure 15b). On the down skin strut surface, surroundings metal powder was melted due to struts orientation and heat transfer [19]. The partially melted powder modifies the strut shape into an elliptical cross-section resulting in an increase of mechanical properties under compression loading (Figure 12). Therefore, if only equivalent circular cross-section is used, the mechanical properties are increase in all directions instead of only Z direction. This will be reflected especially in the FEM model response during the progressive collapse of the lattice structure where deviations from the actual behavior occur, as is shown in Figure 12a. The results of experiment and FEA comparison show that the elliptic cross-section is more suitable for a description of the whole deformation process via FEA (Figure 12b). The circular cross-section can only be used for the estimation of approximate F_{max} reaction force when the lattice structure starts to be damaged.

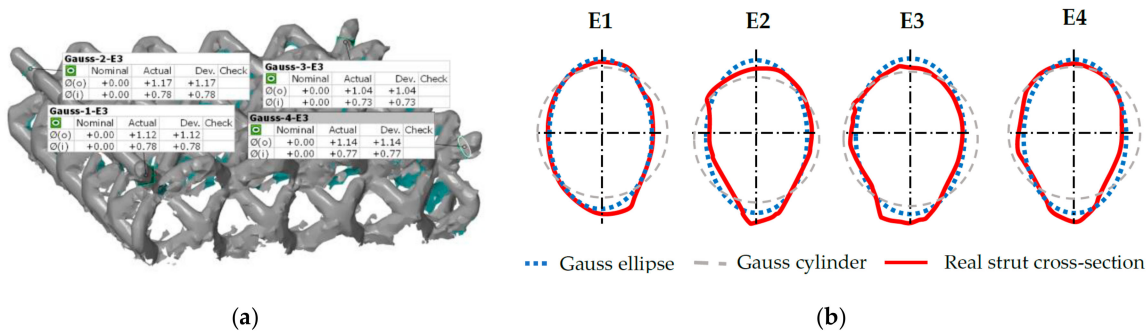


Figure 15. Comparison of the real and ideal cylinder cross-section: (a) shape analysis in the GOM Inspect software and (b) real cross-section in four corner struts.

4.2. Application of Numerical Model to BCC Lattice Structures with Struts Diameter between 0.6–1.2 mm

The material model was created directly for the lattice structure with 0.8 mm nominal diameter; therefore, the other specimens, such as those for optical measurement or quasi-static testing, were fabricated only for this nominal diameter. However, as is shown in Figure 16, the material model of the lattice structure can also be used for diameters between 0.6–1.2 mm, which are commonly used dimensions of lattice structure struts.

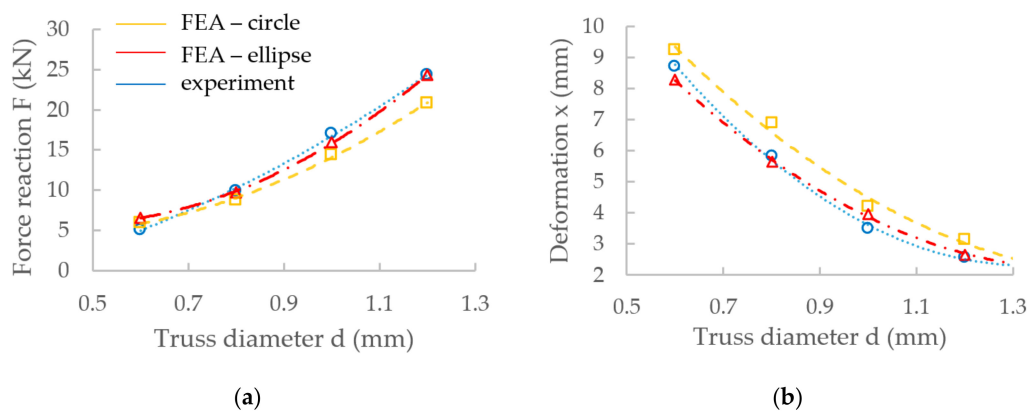


Figure 16. Comparison of FEA results and experiment for different strut diameters; (a) reaction force; and (b) deformation.

To create the FEM geometry in Ansys software, real strut diameters of nominal diameters 0.6, 1.0 and 1.2 mm were obtained from the previous study [20] where the relation between the designed and real strut diameter after SLM processing was described. In order to use the elliptical shape for these diameters (0.6–1.2 mm), the ellipse ratio e from the O-series ($d = 0.8$ mm) was evaluated and applied to other strut sizes using Equation (6). The d_{gauss} cylinder values from the line equation (Figure 17) [20] were used to calculate the circle cross-section area. Then the elliptical ratio $e = 0.71$ and the equivalent sizes of circular and elliptical cross-sections were used for calculation of minor and major axes of the ellipse. The elliptical ratio was identified as a ratio between the average minor and major ellipse axes in the O-series test. The re-calculation process is described in Equations (2)–(6). The results also confirm a better compliance with the ellipse cross-section than with the circular one (Figure 16).

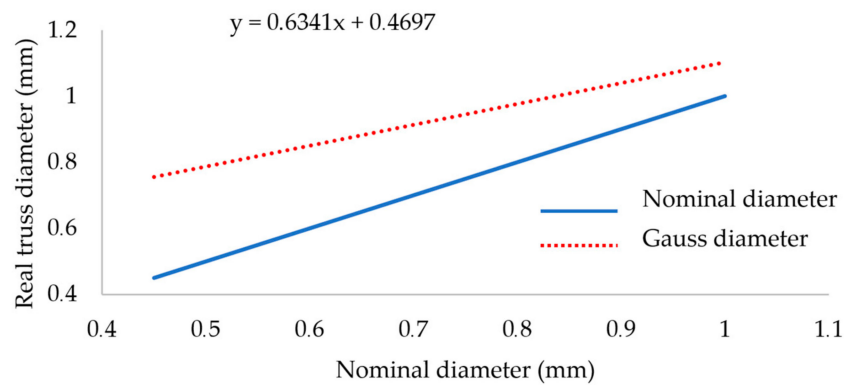


Figure 17. Increase of the real strut diameter fabricated by SLM described in the study [20].

$$A_{Dgauss} = A_{ellipse} \quad (2)$$

$$\pi \frac{d_{gauss}^2}{4} = \pi \cdot a \cdot b \quad (3)$$

$$e = \frac{a}{b} = \frac{0.795/2}{1.114/2} = 0.714 \quad (4)$$

$$b = \sqrt{d_{gauss}^2 / 4 \cdot e} \quad (5)$$

$$a = e \cdot b \quad (6)$$

4.3. Mechanical Testing

In their study [34], the Tsopanos et al. tested single struts of 316L with diameters of about 0.2 mm. The mechanical properties of struts were half as compared to the standard material because the mechanical properties of a single strut mainly decrease porosity and surface roughness. From this, it follows that to find the correct mechanical properties for the numerical model of lattice structure, it is not suitable to use the bulk material tensile specimens.

Nevertheless, during compression loading, a lot of single struts transfer the load in the lattice structure. Therefore, multi-strut tensile specimen, where more struts are also loaded simultaneously were designed. The results of tensile testing show that specimens fabricated by SLM with of 45° orientation have different mechanical properties in comparison with those of 90° orientation – $YTS_{0.2\%} + 10\%$; $UTS + 20\%$; $E + 40\%$; and $E_t - 30\%$. It could be due to a higher porosity level inside the strut in the case of 90° orientation. To obtain the correct mechanical properties during evaluation of strut mechanical properties, it is necessary to use the real dimensions measured e.g., by optical measurement. The strut mechanical properties were compared with bulk material which is not too affected by internal defects. The results show much lower strut mechanical properties and more brittle material. ($YTS_{0.2\%} - 40\%$; $UTS - 30\%$; Young's modulus $E - 30\%$ and Tangent modulus $E_t + 30 \div 50\%$). It may be mainly caused by significant surface roughness and almost two times higher surface of multi-strut specimens compare to bulk specimens (970/565 mm², calculated using Gaussian diam. for specimens T45-series $d_{Gauss} = 0.89$ mm.). The size of specimen's surface is also connected with close to surface porosity which can be expressed using parameter CtS and Equation (7) (for one truss of multi-strut spec., it is of 130; for bulk spec., it is of 29). This parameter expresses the ratio between the surface of the specimen or struts in multi-strut specimen S (mm²) and cross-section of the specimen or strut A (mm²). Its value shows susceptibility to failure due to close to surface porosity.

$$CtS = \frac{S}{A} = \frac{n \cdot \pi \cdot d \cdot h_{ef}}{n \cdot \pi \frac{d^2}{4}} = \frac{4h_{ef}}{d} = 28.8 \quad (7)$$

where n is number of the struts of the specimens (for bulk shape $n = 1$), d is the strut or bulk specimens' diameter and h is the effective area of the specimen (see Figure 3).

4.4. Criterion of Damage

A damage criterion is the Ansys parameter which defines when the element is excluded from calculation (element erosion) and no longer contributes to load transfer. In the case of presented numerical model, the Equivalent Plastic Strain $EPS = 0.1025$ was used (Table 6). It means that if the element is deformed more than 10.25%, it is removed.

The true strain value at the area of the damage of tensile specimen is required as input for this criterion in Ansys. From the strut tensile testing, only the global specimen's strain without considering the local damage in the critical area was obtained. There are two reasons: Firstly, it was an atypical shape of the specimens where it was problematic to measure the narrowing of the single struts in the damaged area. Secondly, the used material is very brittle; therefore, the narrowing of the struts was very small and could not be measured with available equipment. For this reason, an alternative method was used; EPS was represented by the strain at the first peak F_{max} in the compression test.

5. Conclusions

In this study, all processes of material model creation and final FEA analysis were presented. The results show that the SLM technology allows to produce energy absorbers from AlSi10Mg alloy, which can effectively absorb energy through self-deformation. Due to a good accordance between the numerical model and the experiment, it was possible to use the numerical model of lattice structure for precise design of the absorber in high-performance applications. This model will be used for future testing of geometry changes and their impact on mechanical properties. The presented process of finding the material model can be employed for various materials used for SLM production.

- The numerical model of BCC micro-lattice structure under dynamic loading with the elliptic strut shape was developed. The results show that the elliptic shape of the lattice structure significantly decreases a deviation between FEA and the measured results compared to the circular cross-section (10%, measured in the first force peak).
- To find the correct mechanical properties for FEA material model, it is necessary to use the struts specimens with appropriate orientation during production due to the influence of internal porosity and surface roughness.
- The orientation during SLM production significantly influences the mechanical properties.
- The shape of the BCC lattice structure was analyzed using optical methods. A distinct "water drop" shape was found in the case of AlSi10Mg alloy.
- A weight comparison of the CAD design and the produced lattice structure shows that for simplification of the "water drop" shape of the strut, the Gaussian strut diameter should be used.
- The results of quasi-static mechanical testing show that the differences between mechanical properties of the 90° and 45° orientation are mainly in the plastic area of deformation and may be caused by the significant surface roughness.

Author Contributions: Conceptualization, R.V.; Data curation, R.V. and O.Č.; Formal analysis, R.V., P.M. and D.K.; Funding acquisition, D.P.; Investigation, R.V. and O.Č.; Methodology, R.V. and P.M.; Project administration, R.V.; Resources, D.P.; Supervision, P.M., D.K. and D.P.; Validation, R.V., O.Č., P.M., D.K. and D.P.; Visualization, R.V.; Writing—original draft, R.V., O.Č. and D.K.; Writing—review & editing, R.V. and O.Č.

Funding: This research was funded by the ESIF, EU Operational Programme Research, Development and Education within the research project [Architected materials designed for additive manufacturing] grant number [CZ.02.1.01/0.0/0.0/16_025/0007304].

Conflicts of Interest: The authors declare no conflict of interest.

References

1. Karagiozova, D. Dynamic buckling of elastic-plastic square tubes under axial impact—I: Stress wave propagation phenomenon. *Int. J. Impact Eng.* **2004**, *30*, 143–166. [[CrossRef](#)]
2. Li, X.; Zhang, P.; Wang, Z.; Wu, G.; Zhao, L. Dynamic behavior of aluminum honeycomb sandwich panels under air blast: Experiment and numerical analysis. *Compos. Struct.* **2014**, *108*, 1001–1008. [[CrossRef](#)]
3. Olabi, A.G.; Morris, E.; Hashmi, M.S.J. Metallic tube type energy absorbers: A synopsis. *Thin Walled Struct.* **2007**, *45*, 706–726. [[CrossRef](#)]
4. Dharmasena, K.P.; Wadley, N.G.; Xue, Z.; Hutchinson, J.W. Mechanical response of metallic honeycomb sandwich panel structures to high-intensity dynamic loading. *Int. J. Impact Eng.* **2008**, *35*, 1063–1074. [[CrossRef](#)]
5. Kopanidis, A.; Theodorakakos, A.; Gavaises, E.; Bouris, D. 3D numerical simulation of flow and conjugate heat transfer through a pore scale model of high porosity open cell metal foam. *Int. J. Heat Mass Transf.* **2010**, *53*, 2539–2550. [[CrossRef](#)]
6. Shimizu, T.; Matsuzaki, K.; Nagai, H.; Kanetake, N. Production of high porosity metal foams using EPS beads as space holders. *Mater. Sci. Eng. A* **2012**, *558*, 343–348. [[CrossRef](#)]
7. Zhu, L.; Guo, K.; Li, Y.; Yu, T.X.; Zhou, Q. Experimental study on the dynamic behaviour of aluminium foam sandwich plates under single and repeated impacts at low temperature. *Int. J. Impact Eng.* **2018**, *114*, 123–132. [[CrossRef](#)]
8. Sun, B.; Zhang, R.; Zhang, Q.; Gideon, R.; Gu, B. Drop-weight impact damage of three-dimensional angle-interlock woven composites. *J. Compos. Mater.* **2013**, *47*, 2193–2209. [[CrossRef](#)]
9. Vrana, R.; Koutny, D.; Paloušek, D. Impact Resistance of Different Types of Lattice Structures Manufactured by SLM. *MM Sci. J.* **2016**, *2016*, 1579–1585. [[CrossRef](#)]
10. Mines, R.A.W.; Tsopanos, S.; Shen, Y.; Hasan, R.; McKown, S.T. Drop weight impact behaviour of sandwich panels with metallic micro lattice cores. *Int. J. Impact Eng.* **2013**, *60*, 120–132. [[CrossRef](#)]
11. Harris, J.A.; Winter, R.E.; McShane, G.J. Impact response of additively manufactured metallic hybrid lattice materials. *Int. J. Impact Eng.* **2017**, *104*, 177–191. [[CrossRef](#)]
12. Yadroitsev, I. *Selective Laser Melting: Direct Manufacturing of 3D-Objects by Selective Laser Melting of Metal Powders*; LAP Lambert: Saarbrücken, Germany, 2009.
13. Thijs, L.; Kempen, K.; Kruth, J.-P.; van Humbeeck, J. Fine-structured aluminium products with controllable texture by selective laser melting of pre-alloyed AlSi10Mg powder. *Acta Mater.* **2013**, *61*, 1809–1819. [[CrossRef](#)]
14. Qiu, C.; Yue, S.; Adkins, N.J.E.; Ward, M.; Hassanin, H.; Lee, P.D.; Withers, P.J.; Attallah, M.M. Influence of processing conditions on strut structure and compressive properties of cellular lattice structures fabricated by selective laser melting. *Mater. Sci. Eng. A* **2015**, *628*, 188–197. [[CrossRef](#)]
15. Koutny, D.; Palousek, D.; Pantelejev, L.; Hoeller, C.; Pichler, R.; Tesicky, L.; Kaiser, J. Influence of scanning strategies on processing of aluminum alloy EN AW 2618 using selective laser melting. *Materials* **2018**, *11*, 298. [[CrossRef](#)] [[PubMed](#)]
16. Han, X.; Zhu, H.; Nie, X.; Wang, G.; Zeng, X. Investigation on Selective Laser Melting AlSi10Mg Cellular Lattice Strut: Molten Pool Morphology, Surface Roughness and Dimensional Accuracy. *Materials* **2018**, *11*, 392. [[CrossRef](#)] [[PubMed](#)]
17. Ilcik, J.; Koutny, D.; Palousek, D. Geometrical accuracy of the metal parts produced by selective laser melting: Initial tests. In Proceedings of the 54th International Conference of Machine-Design-Departments (ICMD), Hejnice, Czech Republic, 10–12 September 2013; pp. 573–582.
18. Skalicky, P.; Koutny, D.; Pantelejev, L.; Palousek, D. Processing of aluminum alloy EN AW 7075 using selective laser melting: Initial study. In Proceedings of the 58th International Conference of Machine-Design-Departments (ICMD2017), Prague, Czech Republic, 6–8 September 2017; pp. 330–335.
19. Vrana, R.; Koutny, D.; Palousek, D.; Pantelejev, L.; Jaros, J.; Zikmund, T.; Kaiser, J. Selective laser melting strategy for fabrication of thin struts usable in lattice structures. *Materials* **2018**, *11*, 1763. [[CrossRef](#)] [[PubMed](#)]
20. Koutny, D.; Vrana, R.; Paloušek, D. Dimensional accuracy of single beams of AlSi10Mg alloy and 316L stainless steel manufactured by SLM. In Proceedings of the 5th International Conference on Additive Technologies (iCAT2014), Vienna, Austria, 16–17 October 2014; pp. 142–147.

21. Suard, M.; Lhuissier, P.; Dendievel, R.; Vignat, F.; Blandin, J.J.; Villeneuve, F. Impact of EBM fabrication strategies on geometry and mechanical properties of titanium cellular structures. In Proceedings of the Fraunhofer Direct Digital Manufacturing Conference (DDMC 2014), Berlin, Germany, 12–13 March 2014.
22. Vrana, R.; Koutny, D.; Paloušek, D.; Zikmund, T. Influence of selective laser melting process parameters on impact resistance of lattice structure made from AlSi10Mg. In Proceedings of the World PM 2016 Congress and Exhibition, Hamburg, Germany, 9–13 October 2016.
23. Grytten, F.; Børvik, T.; Hopperstad, O.S.; Langseth, M. Low velocity perforation of AA5083-H116 aluminium plates. *Int. J. Impact Eng.* **2009**, *36*, 597–610. [[CrossRef](#)]
24. Grytten, F.; Holmedal, B.; Hopperstad, O.S.; Børvik, T. Evaluation of identification methods for YLD2004-18p. *Int. J. Plast.* **2008**, *24*, 2248–2277. [[CrossRef](#)]
25. Mohammed, R.; Ahmed, A.; Elgalib, M.A.; Ali, H. Low Velocity Impact Properties of Foam Sandwich Composites: A Brief Review. *Int. J. Eng. Sci. Innov. Technol.* **2014**, *3*, 579–591.
26. Mohammed, R.; Zhang, F.; Sun, B.; Gu, B. Finite element analyses of low-velocity impact damage of foam sandwiched composites with different ply angles face sheets. *Mater. Des.* **2013**, *47*, 189–199. [[CrossRef](#)]
27. Labeas, G.; Ptochos, E. Investigation of sandwich structures with innovative cellular metallic cores under low velocity impact loading. *Plast. Rubber Compos.* **2013**, *42*, 194–202. [[CrossRef](#)]
28. Ozdemir, Z.; Tyas, A.; Goodall, R.; Askes, H. Energy absorption in lattice structures in dynamics: Nonlinear FE simulations. *Int. J. Impact Eng.* **2017**, *102*, 1–15. [[CrossRef](#)]
29. Banerjee, A.; Dhar, S.; Acharyya, S.; Datta, D.; Nayak, N. Determination of Johnson cook material and failure model constants and numerical modelling of Charpy impact test of armour steel. *Mater. Sci. Eng. A* **2015**, *640*, 200–209. [[CrossRef](#)]
30. Milani, A.S.; Dabboussi, W.; Nemes, J.A.; Abeyaratne, R.C. An improved multi-objective identification of Johnson–Cook material parameters. *Int. J. Impact Eng.* **2009**, *36*, 294–302. [[CrossRef](#)]
31. Brandl, E.; Heckenberger, U.; Holzinger, V.; Buchbinder, D. Additive manufactured AlSi10Mg samples using Selective Laser Melting (SLM): Microstructure, high cycle fatigue, and fracture behavior. *J. Mater. Des.* **2012**, *34*, 159–169. [[CrossRef](#)]
32. Vaverka, O.; Koutný, D.; Vrána, R.; Pantělejev, L.; Paloušek, D. Effect of heat treatment on mechanical properties and residual stresses in additively manufactured parts. In Proceedings of the Engineering Mechanics 2018 24th International Conference, Svratka, Czech Republic, 14–17 May 2018.
33. Kempen, K.; Thijs, L.; van Humbeeck, J.; Kruth, J.-P. Mechanical properties of AlSi10Mg produced by selective laser melting. *Phys. Procedia* **2012**, *39*, 439–446. [[CrossRef](#)]
34. Tsopanos, S.; Mines, R.A.W.; Mckown, S.; Shen, Y.; Cantwell, W.J.; Brooks, W.; Sutcliffe, C.J. The influence of processing parameters on the mechanical properties of selectively laser melted stainless steel microlattice structures. *J. Manuf. Sci. Eng.* **2010**, *132*, 1–12. [[CrossRef](#)]
35. Xiao, L.; Song, W. Additively-manufactured functionally graded Ti-6Al-4V lattice structures with high strength under static and dynamic loading: Experiments. *Int. J. Impact Eng.* **2018**, *111*, 255–272. [[CrossRef](#)]
36. Palousek, D.; Omasta, M.; Koutny, D.; Bednar, J.; Koutecky, T.; Dokoupil, F. Effect of matte coating on 3D optical measurement accuracy. *Opt. Mater.* **2015**, *40*, 1–9. [[CrossRef](#)]
37. Ravari, M.R.K.; Kadkhodaei, M.; Ghaei, A. Effects of asymmetric material response on the mechanical behavior of porous shape memory alloys. *J. Intell. Mater. Syst. Struct.* **2016**, *27*, 1687–1701. [[CrossRef](#)]

